University of Alberta

Determination of the elastic constants of orthorhombic and transversely isotropic materials: Experimental application to a kerogen rich rock

by

Marko Mah

A thesis submitted to the Faculty of Graduate Studies and Research in partial
fulfillment of the requirements for the degree of Doctor of Philosophy
in
Geophysics

Department of Physics

Edmonton, Alberta

Fall 2005

Library and
Archives Canada

Published Heritage
Branch

395 Wellington Street
Ottawa ON K1A 0N4
Canada

Bibliothèque et
Archives Canada

Direction du
Patrimoine de l'édition

395, rue Wellington
Ottawa ON K1A 0N4
Canada

0-494-08687-4

Your file Votre référence
ISBN:
Our file Notre reference
ISBN:

NOTICE:
The author has granted a non-exclusive license allowing Library and Archives Canada to reproduce, publish, archive, preserve, conserve, communicate to the public by telecommunication or on the Internet, loan, distribute and sell theses worldwide, for commercial or non-commercial purposes, in microform, paper, electronic and/or any other formats.

The author retains copyright ownership and moral rights in this thesis. Neither the thesis nor substantial extracts from it may be printed or otherwise reproduced without the author's permission.

AVIS:
L'auteur a accordé une licence non exclusive permettant à la Bibliothèque et Archives Canada de reproduire, publier, archiver, sauvegarder, conserver, transmettre au public par télécommunication ou par l'Internet, prêter, distribuer et vendre des thèses partout dans le monde, à des fins commerciales ou autres, sur support microforme, papier, électronique et/ou autres formats.

L'auteur conserve la propriété du droit d'auteur et des droits moraux qui protège cette thèse. Ni la thèse ni des extraits substantiels de celle-ci ne doivent être imprimés ou autrement reproduits sans son autorisation.

In compliance with the Canadian Privacy Act some supporting forms may have been removed from this thesis.

While these forms may be included in the document page count, their removal does not represent any loss of content from the thesis.

Conformément à la loi canadienne sur la protection de la vie privée, quelques formulaires secondaires ont été enlevés de cette thèse.

Bien que ces formulaires aient inclus dans la pagination, il n'y aura aucun contenu manquant.

Canada

Security is mostly a superstition. It does not exist in nature, nor do the children of men as a whole experience it. Avoiding danger is no safer in the long run than outright exposure. Life is either a daring adventure or nothing.

– Helen Keller

University politics are vicious precisely because the stakes are so small.

– Henry Kissinger

Dedication

To family and friends

Abstract

Co-planar arrays of specially constructed near-point ultrasonic transducers of differing polarizations were used to generate and record ultrasonic waveforms travelling at a variety of different angles within a number of different planes. Using a well-tested $\tau - p$ plane wave decomposition technique, the elastic constants of a block of isotropic soda-lime glass as well as an anisotropic medium were determined.

This method was used to try and obtain ultrasonic phase velocities in an oil shale from the Piceance Basin, Colorado, USA after its composition and structure have been determined. The composition and structure of the oil shale was determined through the use of thin sections, pyrolysis, powder X-ray diffraction, scanning electron microscope, and electron microprobing. Due to problems with inhomogeneities and dispersion, elastic constants as a function of pressure for the oil shale were determined using the conventional pulse transmission method.

Acknowledgements

I would first like to thank Douglas Schmitt for his supervision, guidance, and support. During my stay at the University of Alberta it has been a pleasure discussing the various aspects of anisotropy and all its implications with him.

This work was supported by NSERC and the Petroleum Research Fund administered by the American Chemical Society. Technical assistance and sample preparation were greatly assisted by L. Tober, C. Ryder, D. Collis, R. Hunt, and R. Tomski. The work of Drs. Kebaili and Molz prepared the way for the present experiment. I would also like to thank Joe Dellinger for the use of his computer programs that check the transverse isotropy and orthorhombicity of elastic constants. The assistance of the Alberta Microelectronics Centre in cutting the ceramic transducers is greatly appreciated. The use of the computer equipment and software of the Downhole Seismic Imaging Consortium and the Seismic Heavy Oil Consortium during the preparation of this thesis is appreciated.

The presentation of part of this work at the 2002 Fall AGU in San Francisco was supported by a Gordon Kaplan Travel Award and a Student Conference Travel Award as administered by the Institute for Geophysical Research.

I would like to thank S. Matveev for help in electron microprobing, D. Caird in X-ray diffraction, Dong Chan Li for help with the scanning electron microscope, D. Resultay for help with thin sections, and Dean Rokosh for his work with the soxhlet analysis and sedigraph. I would also like to thank the many numerous people not already mentioned who have made my stay here enjoyable.

Preface

The work presented in this thesis was carried out at the Department of Physics at the University of Alberta, Edmonton and at the Institute for Geophysical Research. The work was done under the supervision of Douglas R. Schmitt. Results from Chapter 3 have been published in the following articles:

- Mah, M., and Schmitt, D. R., 2001, Near point-source longitudinal and transverse mode ultrasonic arrays for material characterization: IEEE Transactions on Ultrasonics, Ferroelectrics, and Frequency Control, **48**, 691-698.
- Mah, M., and Schmitt, D.R., 2000, Use of compressional and shear wave ultrasonic arrays for material characterization: GeoCanada2000 Conference CD.
- Mah, M., and Schmitt, D.R., 2000, Use of compressional and shear wave ultrasonic arrays for material characterization: 4th Downhole Seismic Imaging Consortium Annual Meeting Technical Program

The majority of the results from Chapter 4 have been published in the following articles:

- Mah, M., and Schmitt, D. R., 2003, Determination of the complete elastic stiffnesses from ultrasonic phase velocity measurements: Journal of Geophysical Research-Solid Earth, **108(B1)**, art. no. 2016.
- Mah, M., and Schmitt, D.R., 2002, Determination of the complete elastic stiffnesses from ultrasonic phase velocity measurements: 2002 CSEG National Convention.

Part of Appendix A was published previously in my M.Sc. thesis:

- Mah, M., 1999, Experimental determination of the elastic coefficients of anisotropic materials with the slant-stack method, M. Sc. thesis, University of Alberta.

and is contained here and expanded upon only for completeness.

Table of Contents

1 **Overview** **1**

2 **Introduction** **4**
- 2.1 Background . . . 4
- 2.2 Properties of shales . . . 6
- 2.3 Brief review of anisotropy . . . 8
- 2.4 Causes of velocity anisotropy . . . 13
  - 2.4.1 Clay minerals . . . 14
  - 2.4.2 Microcracks and oriented pores . . . 16
  - 2.4.3 Kerogen . . . 18
- 2.5 Velocity measurements of shales . . . 19
- 2.6 Determination of elastic constants of shales . . . 22
- 2.7 The $\tau - p$ method . . . 27
- 2.8 Oil shale characterization . . . 30

3 **$\tau - p$ methodology** **43**
- 3.1 Abstract . . . 43
- 3.2 Introduction . . . 44
- 3.3 Background . . . 45
  - 3.3.1 Plane-wave Decomposition . . . 45
  - 3.3.2 Experimental Method . . . 48
  - 3.3.3 Point-source transducers . . . 49
- 3.4 Results and discussion . . . 54
  - 3.4.1 Determination of Phase Velocities . . . 54
- 3.5 Conclusions . . . 62

4 **Determination of the elastic stiffnesses** **65**
- 4.1 Abstract . . . 65
- 4.2 Introduction . . . 66
- 4.3 Background . . . 67
  - 4.3.1 Phase Velocities and Elasticity . . . 67

4.3.2 Theoretical Relations 68
4.4 Experimental Phase-Velocity Measurements 76
4.4.1 Plane-wave Decomposition 76
4.4.2 Sample Characterization 78
4.4.3 Experimental Configuration 79
4.5 Results and Discussion 81
4.5.1 Phase Velocities 81
4.5.2 Inversion for Elastic Coefficients 89
4.6 Conclusions 101

5 Rock Sample Characterization **108**
5.1 Abstract 108
5.2 Introduction 108
5.2.1 Background 112
5.2.2 Sample Analysis 113
5.3 Thin section 115
5.4 X-ray diffraction 119
5.4.1 What is X-ray diffraction? 119
5.4.2 Powder X-ray diffraction results 122
5.4.3 Oriented X-ray diffraction results 126
5.5 Pyrolysis and whole-rock analysis 130
5.5.1 What is pyrolysis and whole-rock analysis? 130
5.5.2 Pyrolysis and whole-rock analysis results 131
5.6 Scanning electron microscope 136
5.6.1 What is scanning electron microscopy? 136
5.6.2 SEM results on the oil shale samples 137
5.7 Electron microprobe 148
5.7.1 What is electron microprobing? 148
5.7.2 Electron microprobe results 151
5.8 Summary of density, composition, and structure 206

6 Elastic Anisotropy of Oil Shale **219**
6.1 Abstract 219
6.2 Introduction 219
6.3 Background 220
6.4 Causes of Anisotropy 222
6.4.1 Intrinsic Anisotropy 222
6.4.2 Microcracks and oriented pores 223
6.4.3 Layering 223
6.5 Experimental configuration 224
6.5.1 Laboratory Set-up 225

6.6 Experimental results and analysis 231
6.6.1 Crush tests and heterogeneity tests 231
6.6.2 Velocity versus pressure 232
6.6.3 Elastic Constants with Pressure 251
6.6.4 Thomsen's parameters 262
6.7 Conclusions 277

7 Conclusions **286**
7.1 Summary 286
7.2 Future Work 288
7.2.1 $\tau - p$ methodology 288
7.2.2 3rd order elastic constants 289
7.2.3 Backus modelling 289
7.2.4 Anisotropic turning ray 290

A Elastic constant formula derivation **293**
A.1 Theory 293
A.2 Relationship between stiffness and anisotropic velocities 299
A.3 Isotropic case: 2 elastic constants 304
A.4 Cubic case: 3 elastic constants 305
A.5 Hexagonal case: 5 elastic constants 307
A.5.1 Proof of hexagonal symmetry is equivalent to transverse isotropy 310
A.6 Orthorhombic case: 9 elastic constants 323
A.7 Monoclinic case: 13 elastic constants 327

B Christoffel Symbols **331**
B.1 Theory 331
B.2 Expanded Christoffel terms for a few example directions 333

List of Figures

2.1 Distinction between group and phase velocities. 10
2.2 Coordinate axes with respect to layering in a TI medium. 12
2.3 Particle motions of the 3 propagation modes in a TI medium. . . 13
2.4 Development of oriented pores and microcracks during diagenesis. 17
2.5 Development of flattened layers of kerogen during diagenesis. . . . 18
2.6 Cores taken at various angles to bedding. 23
2.7 Walk-away VSP. 28

3.1 Illustration of $\tau - p$ methodology using sources of a known distance apart. 46
3.2 Ideal particle motion imparted and received by the piezoelectric transducers. 50
3.3 Theoretical radiation pattern for the 3 modes of propagation for source normal and parallel to the surface. 52
3.4 Frequency spectrum of data. 53
3.5 Observed P-wave trace at 10.0 cm offset on the glass block. 55
3.6 Observed P-wave traces on the glass block and corresponding $\tau - p$ transform. 55
3.7 Observed SV wave trace at 4.0 cm offset on the glass block. . . . 56
3.8 Analysis of the SV mode arrivals. 57
3.9 Observed SH wave trace at 0.5 cm offset on the glass block. . . . 58
3.10 Analysis of the SH mode arrivals. 58
3.11 Vertical slowness versus horizontal slowness in glasss. 59
3.12 Summary of the phase velocities versus phase propagation angle. . 61

4.1 Sagittal plane containing sources and receivers. 78
4.2 Cross-section of the phenolic sample. 80
4.3 The five planes on the composite block in which arrays were prepared and designated. 82
4.4 The P-wave results from the $xz - y$ plane. 83
4.5 Unprocessed SV mode arrivals before muting, windowing, and bandpass filtering. 84

4.6 The SV-wave results from the $xz - y$ plane. 85
4.7 The SH-wave results from the $xz - y$ plane. 86
4.8 A composite of phase velocities in the x-z, y-z, and x-y planes. . . 87
4.9 A composite of phase velocities in the xy-z, y-z, and xz-y planes. . 88

5.1 Oil shale facility map. 109
5.2 Close up of oil shale sample (Penny diameter = 19.08 mm). 115
5.3 Oil shale sample with respect to coordinate axes. 116
5.4 Thin section of oil shale taken in 3 perpendicular directions. . . . 117
5.5 Bragg diffraction 121
5.6 X-ray diffractometer 121
5.7 Powder X-ray diffraction of calcite and dolomite 123
5.8 Powder X-ray diffraction of oil shale sample. 124
5.9 Powder X-ray diffraction signature of illite. 125
5.10 Powder X-ray diffraction signature of illite and illite-montmorillonite clay minerals. 127
5.11 X-ray diffraction of oil shale sample 129
5.12 Schematic of scanning electron microscope. 137
5.13 Low resolution SEM view of layering in the $y - z$ plane. 139
5.14 Low resolution SEM view of layering in the $x - z$ plane. 140
5.15 High resolution SEM view of structureless material in the $y - z$ plane. 141
5.16 High resolution SEM view of layering in the $x - z$ plane. 142
5.17 High resolution SEM view of a void in the $y - z$ plane. 143
5.18 Low resolution SEM view of layering in the $x - y$ plane. 144
5.19 High resolution SEM view of layering in the $x - y$ plane. 145
5.20 High resolution SEM view of dolomite chunk in the $y - z$ plane. . 146
5.21 High resolution SEM view of quartz grain in the $x - z$ plane. . . . 147
5.22 Diagram of electron microprobe. 149
5.23 Electron beam - sample interaction. 151
5.24 Electron microprobe image of aluminium in the $y - z$ plane 156
5.25 Electron microprobe image of calcium in the $y - z$ plane 157
5.26 Electron microprobe image of carbon in the $y - z$ plane 158
5.27 Electron microprobe image of iron in the $y - z$ plane 159
5.28 Electron microprobe image of magnesium in the $y - z$ plane . . . 160
5.29 Electron microprobe image of potassium in the $y - z$ plane 161
5.30 Electron microprobe image of silicon in the $y - z$ plane 162
5.31 Electron microprobe image of sodium in the $y - z$ plane 163
5.32 Electron microprobe image of sulfur in the $y - z$ plane 164
5.33 Processed image of albite in the $y - z$ plane 165
5.34 Processed image of anorthoclase in the $y - z$ plane 166

5.35 Processed image of calcite in the $y - z$ plane 167
5.36 Processed image of dawsonite in the $y - z$ plane 168
5.37 Processed image of dolomite in the $y - z$ plane 169
5.38 Processed image of a ferromagnesium mineral in the $y - z$ plane . 170
5.39 Processed image of illite in the $y - z$ plane 171
5.40 Processed image of pyrite in the $y - z$ plane 172
5.41 Processed image of quartz in the $y - z$ plane 173
5.42 Electron microprobe image of calcium in the $x - z$ plane 175
5.43 Electron microprobe image of carbon in the $x - z$ plane 176
5.44 Electron microprobe image of iron in the $x - z$ plane 177
5.45 Electron microprobe image of magnesium in the $x - z$ plane . . . 178
5.46 Electron microprobe image of sulfur in the $x - z$ plane 179
5.47 Electron microprobe image of titanium in the $x - z$ plane 180
5.48 Processed image of calcite in the $x - z$ plane 181
5.49 Processed image of dolomite in the $x - z$ plane 182
5.50 Processed image of a ferromagnesium mineral in the $x - z$ plane . 183
5.51 Processed image of ilmenite in the $x - z$ plane 184
5.52 Processed image of pyrite in the $x - z$ plane 185
5.53 Electron microprobe image of aluminium in the $x - y$ plane . . . 188
5.54 Electron microprobe image of calcium in the $x - y$ plane 189
5.55 Electron microprobe image of carbon in the $x - y$ plane 190
5.56 Electron microprobe image of iron in the $x - y$ plane 191
5.57 Electron microprobe image of magnesium in the $x - y$ plane . . . 192
5.58 Electron microprobe image of potassium in the $x - y$ plane 193
5.59 Electron microprobe image of silicon in the $x - y$ plane 194
5.60 Electron microprobe image of sodium in the $x - y$ plane 195
5.61 Electron microprobe image of sulfur in the $x - y$ plane 196
5.62 Processed image of albite in the $x - y$ plane 197
5.63 Processed image of anorthoclase in the $x - y$ plane 198
5.64 Processed image of calcite in the $x - y$ plane 199
5.65 Processed image of dawsonite in the $x - y$ plane 200
5.66 Processed image of dolomite in the $x - y$ plane 201
5.67 Processed image of a ferromagnesium mineral in the $x - y$ plane . 202
5.68 Processed image of illite in the $x - y$ plane 203
5.69 Processed image of pyrite in the $x - y$ plane 204
5.70 Processed image of quartz in the $x - y$ plane 205

6.1 P-wave waveform acquired using methodology described in Mah & Schmitt (2001a, 2001b, and 2003). 225
6.2 Multifaceted cube of oil shale. 226
6.3 Measurements taken at 6 different orientations to layering. 227

6.4 Pressure vessel. 229
6.5 Sample before and after recutting. 230
6.6 Locations investigated in heterogeneity test. 236
6.7 Waveforms acquired at locations C and E. 237
6.8 P-wave waveforms versus pressure. 238
6.9 Amplitude spectrum of P-wave waveforms. 239
6.10 S-wave waveforms versus pressure. 240
6.11 Amplitude spectrum of S-wave waveforms. 241
6.12 P-wave travelling in (1 0 0) direction. 242
6.13 P-wave and S-wave velocities versus pressure. 243
6.14 P-wave velocity versus pressure in the (1 0 0), (0 1 0), and (0 0 1) direction. 244
6.15 P-wave velocity versus pressure in the $(\frac{1}{\sqrt{2}}\ \frac{1}{\sqrt{2}}\ 0)$ direction. 245
6.16 P-wave velocity versus pressure in the $(\frac{1}{\sqrt{2}}\ 0\ \frac{1}{\sqrt{2}})$ direction. 246
6.17 P-wave velocity versus pressure in the $(0\ \frac{1}{\sqrt{2}}\ \frac{1}{\sqrt{2}})$ direction. 247
6.18 S-wave velocity versus pressure in the (0 1 0) direction. 248
6.19 S-wave velocity versus pressure in the (1 0 0) direction. 249
6.20 S-wave velocity versus pressure in the (1 0 0) direction. 250
6.21 Elastic constants C12, C13, and C23 versus pressure. 255
6.22 Elastic constants C11, C22, and C33 versus pressure. 256
6.23 Elastic constant hysteresis versus pressure. 257
6.24 Elastic constants C44, C55, and C66 versus pressure. 258
6.25 Difference between elastic constants C11 and C22 versus pressure. 259
6.26 Difference between elastic constants C13 and C23 versus pressure. 260
6.27 Difference between elastic constants C44 and C55 versus pressure. 261
6.28 Velocity surfaces using various combinations of δ and ϵ. 263
6.29 Elastic coefficient $\epsilon 1$ versus pressure. 265
6.30 Elastic coefficient $\epsilon 2$ versus pressure. 266
6.31 Elastic coefficient $\delta 1$ versus pressure. 268
6.32 Elastic coefficient $\delta 2$ versus pressure. 271
6.33 Elastic coefficient $\delta 3$ versus pressure. 274
6.34 Elastic coefficient $\gamma 1$ versus pressure. 276
6.35 Elastic coefficient $\gamma 2$ versus pressure. 277

A.1 Unit cube showing stress directions 295
A.2 Unit cube showing relative faces. 296

List of Tables

2.1 Composition of shales studied in various contributions (Percentage by weight) . . . 7
2.2 Elastic constants of shale sample as derived by various papers (GPa) 24

3.1 Comparison of velocities . . . 49

4.1 General summary of how various elastic constants are determined for isotropic and cubic media. . . . 71
4.2 General summary of how various elastic constants are determined for a hexagonal media. . . . 72
4.3 General summary of how various elastic constants are determined in an orthorhombic medium. . . . 73
4.4 General summary of how various elastic constants are determined in monoclinic and triclinic media. . . . 74
4.5 Elastic constants before rotation. . . . 75
4.6 Elastic constants after rotation. . . . 75
4.7 Elastic stiffnesses as calculated in Case 1. . . . 92
4.8 Elastic stiffnesses as calculated in Case 2. . . . 93
4.9 Elastic stiffnesses as calculated in Case 3. . . . 94
4.10 Elastic stiffnesses as calculated in Case 4. . . . 95

5.1 Pyrolysis of oil shale sample . . . 132
5.2 Whole-rock analysis of oil shale sample. . . . 133
5.3 Relative amounts of non-kerogenous minerals in oil shale sample. . 135
5.4 Overall composition of oil shale sample as deduced by whole-rock analysis. . . . 135
5.5 Relative amounts of non-kerogenous minerals in oil shale sample in $y - z$ plane sample. . . . 153
5.6 Relative amounts of minerals in oil shale sample in $y - z$ plane sample. . . . 153
5.7 Relative amounts of non-kerogenous minerals in oil shale sample in $x - y$ plane sample. . . . 187

5.8 Relative amounts of minerals in oil shale sample in $x - y$ plane sample. 187
5.9 Relative amounts of minerals in oil shale sample. 208

6.1 Velocities from heterogeneity test. 232
6.2 Distance and velocity at 0, 10, and 20 MPa pressure. 235
6.3 Elastic constants at 0, 10, and 20 MPa pressure. 254

2

Chapter 1

Overview

In general, elastic wave anisotropy describes the changes in the character of both compressional and shear waves with direction through materials. This anisotropy has been observed in a wide variety of rocks and especially in shales. The anisotropy seen in rocks is caused by both the composition and finer structures present in the rock itself. In Chapter 2, a brief review of anisotropy and causes of anisotropy is presented. Due to their importance in sedimentary basins, a survey of the anisotropic measurements performed in shales is given. This review shows that only a limited amount of research has been performed exploring the causes of seismic anisotropy in shale.

In order to determine the anisotropy of a material, one must be able to accurately measure the velocities in a variety of well chosen directions. In Chapter 3, the $\tau - p$ methodology, first described by Kebaili & Schmitt (1996), is employed to measure the P-wave and S-wave velocities in an isotropic glass block using specially constructed near point-source transducers. The $\tau - p$ methodology had not been previously applied to determine S-wave velocities. It was found that the measured P-wave and S-wave velocities were accurate to within 1 % (Mah & Schmitt, 2001). In Chapter 4, the $\tau - p$ methodology was applied to the anisotropic synthetic composite material phenolic (Mah & Schmitt, 2003). Both P-wave and S-wave velocities, 779 in total, were determined in a variety of well chosen directions. This allowed all anisotropic parameters of the phenolic to be determined using a new bootstrap inversion. This bootstrap inversion was applied to various subsets of the P-wave and S-wave velocities assuming differing levels of symmetry. These bootstrap inversions showed that that the phenolic is orthorhombic in nature. In Chapters 3 and 4, it is shown that the $\tau - p$ methodology can be used to successfully determine all the anisotropic parameter for a manmade material.

The results of Chapters 3 and 4 established that the anisotropy of an easily characterized manmade material can be determined using the $\tau - p$ method. The method was attempted on a more complex, real sedimentary 'oil shale'. In Chapter 5, a Colorado oil shale was characterized using a variety of methods that included thin sectioning, whole-rock analysis, X-ray diffraction, scanning electron microscopy, and electron microprobing. This allowed the composition and structure of the oil shale to be determined. Of some interest was the observation that the layering, a source of the anisotropy, appeared at all scales from a few microns to those visible to the naked eye.

In Chapter 6, velocities in some well chosen directions were determined in the oil shale using the pulse transmission methodology since the $\tau - p$ methodology was unable to give accurate results. This allowed the anisotropic parameters of the oil shale to be determined. The anisotropic parameters were different from what was expected from its structure as determined in Chapter 5. Some of this discrepancy may be due to heterogeneity of the sample as shown in ultrasonic tests involving P-wave and S-wave measurements at a variety of locations. The velocity measurements were conducted inside a pressure vessel which allowed the anisotropy of the oil shale to be determined as a function of pressure or burial depth. Such measurements had not been previously performed on oil shales. All 9 orthorhombic elastic constants were determined allowing us to observe how the anisotropy of the oil shale changes with pressure.

References

Kebaili, A., and Schmitt, D. R., 1997, Ultrasonic anisotropic phase velocity determination with the Radon transform, Journal of the Acoustical Society of America, **101**, 3278-3286.

Mah, M., and Schmitt, D. R., 2001, Near point-source longitudinal and transverse mode ultrasonic arrays for material characterization, IEEE Transactions on Ultrasonics, Ferroelectrics, and Frequency Control, **48**, 691-698.

Mah, M., and Schmitt, D. R., 2003, Determination of the complete elastic stiffnesses from ultrasonic phase velocity determination: J. Geophys. Res., **108(B1)** art. no. 2016.

Chapter 2

Introduction

2.1 Background

This research extends our knowledge of the elastic and seismic anisotropic properties of rocks. Only recently have the intrinsic anisotropic properties of the earth been taken into consideration when processing seismic data. These seismic data allow us to image the earth deep beneath the surface in the search for oil and gas. Such images are usually produced by the common midpoint method, a method almost exclusively based on the assumption that the earth consists of isotropic layers. However, real rocks, through which the seismic waves pass, are elastically anisotropic. In an anisotropic medium there is sideslip of energy as it propagates which leads to lateral positioning errors (Isaac & Lawton, 1999; Vestrum & Lawton, 1999). Conventional seismic processing does not take anisotropy into account and in many cases the earth is poorly imaged (Vestrum et al., 1999). This may lead to erroneous subsurface interpretations of the images of the earth and a lessened likelihood of successfully finding oil and gas.

Oil and gas deposits are typically found in sedimentary basins within which shales make up 50 % to 75 % of the volume of the rocks present. Shales generally start out as layers of clay minerals that are deposited in a marine or lacustrine environment with some organic matter as well. As this burial process continues, these sediments are geothermally heated and compressed by newly arrived sediments. This causes the sediments to become denser and expel water. During this process of diagenesis, oil and gas are also formed and expelled from the shale. These fluids then migrate from their area of initial formation until a porous and permeable medium such as sandstone or carbonate reservoir is encountered.

During this process of deposition and burial, the clay minerals are thought to undergo translation and rotation as the shale expels fluids from its pores. This causes the clay minerals to be preferentially orientated in many thin, continuous layers (Brindley, 1953; Buessem & Nagy, 1953). These preferentially oriented clay minerals are thought to in part cause velocity anisotropy in the shales (Cholach, 2004; Hornby et al., 1994; Kaarsberg, 1968; Sayers, 1994;). The formation of microcracks, elliptical shaped pores, and flattened layers of kerogen (a bituminous substance formed organic carbon) during diagenesis contributes to this velocity anisotropy as well.

This velocity anisotropy manifests itself in shales as compressional wave (P-wave) velocity variations with increasing source-receiver offset in seismic surveys. Shear wave birefringence is also observed in seismic data. Velocity anisotropy in shales and sediments has been detected in marine seismic data (Banik, 1984). Vertical seismic profile (VSP) data and cross borehole surveys have been used to detect velocity anisotropy (Kebaili & Schmitt, 1996; Winterstein & Paulsson, 1990). Velocity anisotropy is also observed in laboratory experiments on shale cores at high frequency.

If enough velocity measurements of different polarizations are taken in the proper directions, the elastic constants of the material can be determined. For shales, it has often been suggested that they are transversely isotropic (TI) on the basis of their natural texture. A transversely isotropic material has the same properties within a layer or plane but has differing properties perpendicular to this plane. One implication of this is that only 5 independent elastic constants are required to describe the material (Musgrave, 1970). Many experimental methods have been employed in order to determine these elastic constants. One is the use of measurements of P and S wave velocities taken on cores that are parallel, perpendicular, and at 45 degrees to the bedding (Johnston & Christensen, 1995; Vernik & Nur, 1992). However, when measurements are taken in directions that are neither parallel nor perpendicular to the symmetry axes of the materials (such as those at 45 degrees to bedding), erroneous velocity values of the velocity may result (Dellinger & Vernik, 1994). This may lead to inaccurate values for the calculated elastic constants.

A new method employing the $\tau-p$ transform can be used to accurately determine the variation of velocity more continuously than other methods (Kebaili & Schmitt, 1997; Mah & Schmitt, 2001a). It has been shown that if sufficient numbers of velocity measurements are taken, no assumptions need be made about the anisotropy or orientation of the shale. This allows us to determine the elastic constants with a higher level of confidence.

2.2 Properties of shales

Shales are very complex sedimentary rocks. Shales are composed of the following constituents 1) framework silicates, 2) clay minerals, 3) oxides and hydroxides, 4) carbonates, 5) sulfur materials, 6) organic materials, and 7) other constituents (Potter et al., 1980). The framework silicates tend to be in the form of quartz, feldspar, and zeolites (Potter et al., 1980). The clay minerals tend to be in the form of kaolinite, montomorillonite, sericites, smectite, illite, muscovite, chlorite, corrensite, vermiculite, sepiolite and attapulgite (Potter et al., 1980; Dunoyer de Segonzac, 1970). Oxides and hydroxides tend to be in the form of hematite, and gibbsite. Carbonates are usually in the form of calcite or dolomite. Sulfur materials are in the form of gypsum, anhydrite, barite, and pyrite. Discrete and structured organic particles along with kerogen form the organic materials present in the shale. Other minor constituents may be apatite, glass, or heavy minerals. Of these constituents, the clay minerals and quartz typically form the majority of the shales (Table 2.1). Shales also tend to be low density and relatively porous with porosities up to about to 35 % (Potter et al, 1980). Despite these high porosities, the permeability of shales tends to be quite low. For example, the shale studied by Domnesteanu et al. (2001) had a permeability of only 0.02 mD while others found permeabilities in the range of 0.08 to 3.4 mD (Potter et al., 1980).

Mineral	Domenesteanu et al. (2001)	Hornby (1995)	Hornby (1998)	Jones & Wang (1981)
quartz	49	31	30	44
clay	41	58	59	27
feldspar	7	4	7	19
pyrite	3	2	4	6
carbonate	0	2	0	4
porosity (% vol.)	14.62	10.5	10.5	16
bulk density (g/cm^3)	2.38	2.54	2.68	2.40

Table 2.1: Composition of shales studied in various contributions (Percentage by weight)

During deposition, sediments are initially laid out in low energy marine or lacustrine environments that can easily be inferred from the well-laminated bedding in the shales. Due to continued burial and possibly subsidence, the sediments undergo compaction. During this compaction, the sediments are exposed to increased pressure and temperature that causes them to "dewater". Dewatering is the process where water is forced out of the clay mineral layers. The sediments undergo diagenesis where the clay minerals are transformed. For example, smectite ($(Na,Ca)(Al,Mg)_6(Si_4O_{10})_3(OH)_6$) is transformed to a mixed smectite-illite state before eventually becoming illite ($K_{1.25}Al_4(Si_{6.75}Al_{1.25}O_{20})(OH_4)$) in the presence of K-feldspar (Dunoyer de Segonzac, 1970). The organic material present in the sediments undergoes maturation as well and oil and gas is generated and eventually expelled leaving solid bitumen or kerogen (Hunt, 1996). However, the permeability of shale is quite low. The intrapore pressure builds up and cracks the shale to form microfractures allowing the oil and gas to migrate. During, this whole process, the initial pores are gradually reduced due to compaction thereby decreasing the porosity of the shale (Hunt, 1996). The diagenesis of these sediments to form shales depends not only on the sediment source and burial depth but on the burial history as well.

2.3 Brief review of anisotropy

Materials that are isotropic and homogeneous have properties that are independent of both direction and position, respectively. The velocities of both the P-waves and S-waves do not change with the direction of propagation in an isotropic material. As well, the velocities of the two S-waves are degenerate (i.e. have the same value). It can be easily shown that it takes only 2 independent elastic constants to describe such a material. In terms of Lame's parameter λ and μ (Musgrave, 1970), the elastic matrix C_{MN} is:

$$C_{IJ} = \begin{bmatrix} \lambda + 2\mu & \lambda & \lambda & 0 & 0 & 0 \\ & \lambda + 2\mu & \lambda & 0 & 0 & 0 \\ & & \lambda + 2\mu & 0 & 0 & 0 \\ & & & \mu & 0 & 0 \\ & & & & \mu & 0 \\ & & & & & \mu \end{bmatrix} . \tag{2.1}$$

The elastic constants can easily be determined by taking P-wave and S-wave phase velocity measurements in any direction and using the following formula:

$$\nu_P = \sqrt{\frac{\lambda + 2\mu}{\rho}}\,, \tag{2.2}$$

$$\nu_S = \sqrt{\frac{\mu}{\rho}} \tag{2.3}$$

where ρ is the density, and ν_P and ν_S are the P-wave and S-wave phase velocities, respectively. λ and μ are Lame constants where λ is equal to the bulk modulus minus two-thirds of the shear modulus and μ is the shear modulus.

The situation becomes much more complicated when the material is anisotropic. This means that the velocities vary with direction. Further, the two S-waves are no longer degenerate and will not necessarily propagate with the same velocity; this phenomenon is often referred to as shear wave birefringence or shear wave splitting. As well, when velocities are measured in non-symmetry axis directions, the phase (plane wave) velocities may not coincide with the group (ray) velocities.

The velocities used in the previous equations are *phase* velocities. Phase velocities are, in one sense, associated with the propagation of a hypothetical plane wave. Generating plane waves in the real world is difficult, if not impossible, since they are affiliated with wavefronts that are planar. Group velocities are measured when point sources and point receivers and is associated with the simple time of flight from source to receiver. In an isotropic medium, group and *phase* velocities would be equal. However, group velocities and *phase* velocities are not generally the same in an anisotropic medium. To illustrate this, in Figure 2.1 a wavefront W is propagating outward after being produced by a point source at point O at time 0. At point P, the group velocity (also known as the ray velocity) is simply the distance d travelled by the wavefront divided by the time t. However, the plane wavefront F that is tangent to the wavefront at point P travels a distance D that is not necessarily the same as distance d. An observer

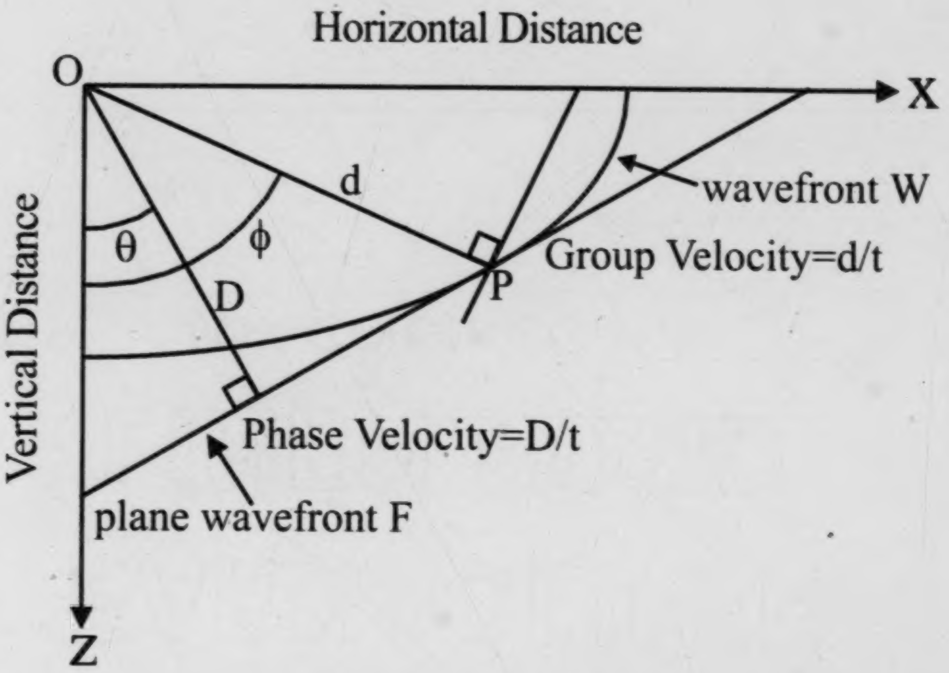
Horizontal Distance
O
X
d
wavefront W
θ
ϕ
Group Velocity=d/t
P
D
Vertical Distance
Phase Velocity=D/t
plane wavefront F
Z

Figure 2.1: Distinction between group and phase velocities in anisotropic media (after Kebaili & Schmitt, 1997). W is the wavefront propagating outward from the origin O. F is the plane wavefront propagating with a phase propagation angle θ from the $z-axis$ that is tangent to the wavefront W at the point P. ϕ is the angle from the $z-axis$ at which the distance d is measured.

at P could not distinguish whether he or she observed a plane wavefront F that passed through the origin at time $t = 0$ or the wavefront W produced by a point source at $t = 0$. This makes the *phase* velocity equal to the distance D divided by the travel time t.

Due to shales being layered in nature, some researchers assume that the shales are transversely isotropic (e.g., Levin, 1992; Miller et al., 1994; Vernik, 1993;) although this precept will be investigated in this thesis. A transversely isotropic (TI) material with a vertical axis ($z-axis$) of symmetry will have phase velocities that are the same in the $x-y$ plane (Figure 2.2). The phenomenon of shear wave birefringence will be observed and the group and phase velocities are not necessarily the same away from the $z-axis$ or $x-y$ plane. The elastic tensor will need only 5 independent elastic constants to describe it, and has the following form:

$$C_{IJ} = \begin{bmatrix} C_{11} & C_{12} & C_{13} & 0 & 0 & 0 \\ & C_{11} & C_{13} & 0 & 0 & 0 \\ & & C_{33} & 0 & 0 & 0 \\ & & & C_{44} & 0 & 0 \\ & & & & C_{44} & 0 \\ & & & & & C_{66} \end{bmatrix} \tag{2.4}$$

where $C_{12} = C_{11} - 2C_{66}$.

In principle, the elastic constants can be derived from phase velocity measurements used in the following formulas (see Appendix A):

$$C_{11} = \rho\nu_P^2 \tag{2.5}$$

$$C_{44} = \rho\nu_{SH}^2 \tag{2.6}$$

$$C_{66} = \rho\nu_{SV}^2 \tag{2.7}$$

where the phase velocities are measured in the $x-y$ plane, SH refers to the shear wave with particle motions perpendicular to the $z-axis$, and SV refers to the shear wave with particle motions parallel to the $z-axis$ (Figure 2.3).

The following elastic constants can be determined by phase velocity measurements for the wave propagating parallel to the $z-axis$ where the two S-wave

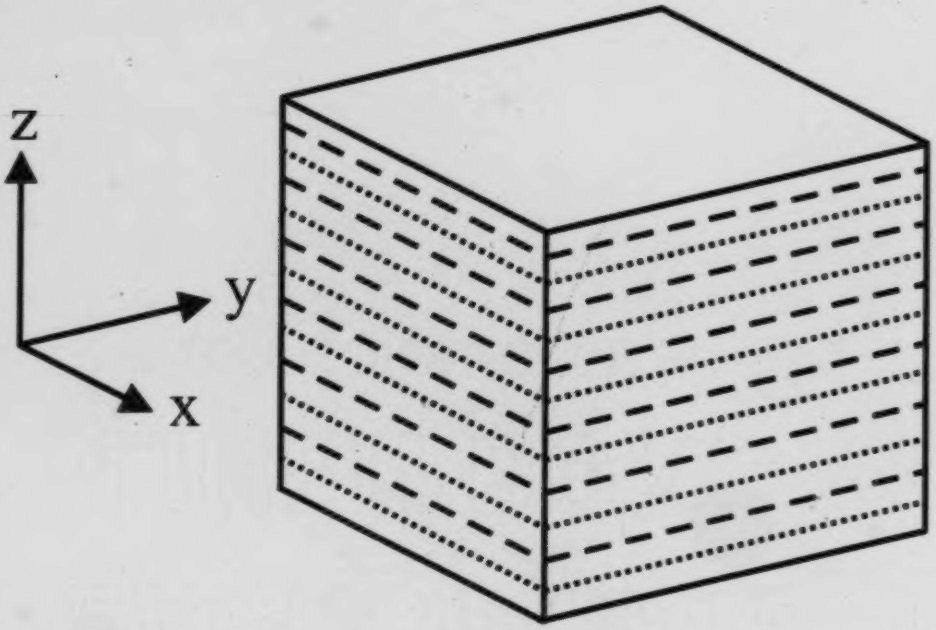

Figure 2.2: Coordinate axes with respect to layering in a transversely isotropic (TI) medium where all the properties are radially symmetric around the $z-axis$.

velocities are degenerate (i.e. they will propagate at the same speed).

$$C_{33} = \rho v_P^2 \tag{2.8}$$

$$C_{44} = \rho v_S^2 \tag{2.9}$$

This leaves the C_{13} elastic constant as yet undetermined. It can be determined by measuring the P-wave phase velocity at an off axis angle which is most conveniently in a direction 45° to bedding or to the $z - axis$. Using the following formula (as derived in Appendix A) it may be determined from the phase velocity measurement and the other elastic constants.

$$C_{13} = -C_{44} - \sqrt{(C_{11} + C_{44} - 2\rho v_P^2)(C_{33} + C_{44} - 2\rho v_P^2)} \tag{2.10}$$

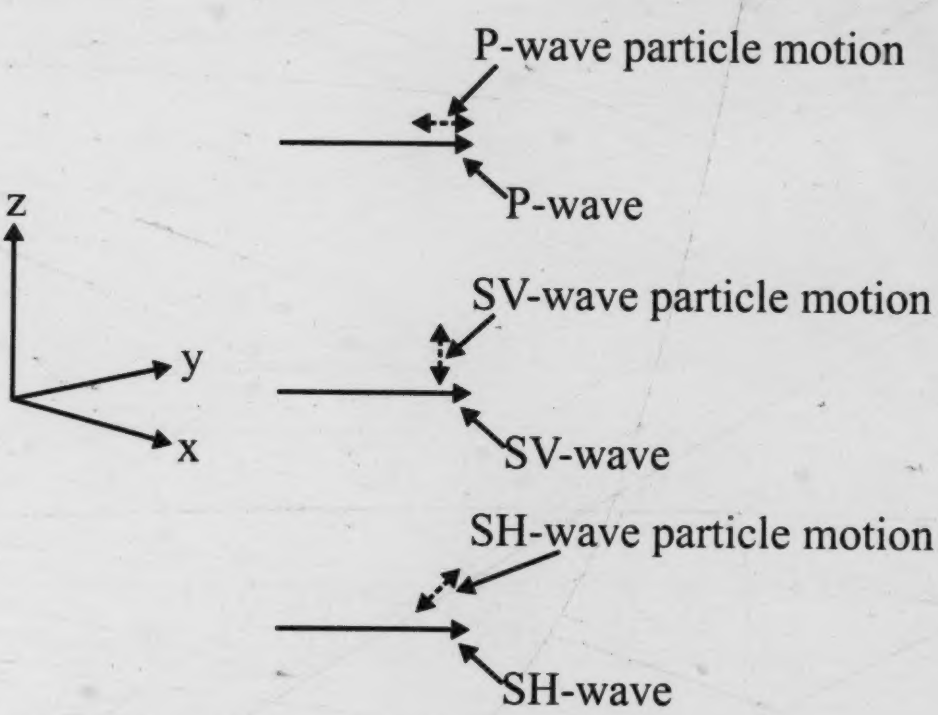
P-wave particle motion
P-wave
SV-wave particle motion
SV-wave
SH-wave particle motion
SH-wave
z
y
x

Figure 2.3: Particle motions of the 3 propagation modes in a TI medium in the $x - y$ plane. The dashed arrows represent the particles motions for the waves travelling in the $x - y$ plane for a TI medium with a vertical axis of symmetry.

where ρ is the density of the material.

However, if the P-wave velocity measurements are poor or the other elastic constants are uncertain, the propagation of errors in the calculation of C_{13} makes it difficult to accurately determine C_{13}. In many studies the C_{13} elastic constant is left unknown (e.g., Vernik & Landis, 1996).

2.4 Causes of velocity anisotropy

There are several possible sources for velocity anisotropy in shales. The most popular explanation is that the platy phyllitic minerals present in shales are preferentially aligned (Cholach, 2004; Hornby et al., 1994; Kaarsberg, 1968; Sayers, 1994;). Another plausible explanation is the presence of microcracks with planes parallel to bedding and preferentially oriented pores. Yet another possible explanation is the presence of organic kerogen. Even though kerogen itself is isotropic, it may form thin layers that can lead to TI behaviour as described by Backus (1962) and Melia & Carlson (1984).

2.4.1 Clay minerals

Shales contain a large amount of clay minerals. These can be kaolinite, montmorillonite, illite, smectite, or even chlorite. The clay minerals themselves tend to be platy and are highly anisotropic in nature (Hornby et al., 1994; Katahara, 1996; Sayers, 1994; Wang et al., 2001) although currently there are no good quantitative estimates of their elastic properties. When uniformly randomly oriented clay minerals form a conglomerate they construct an isotropic rock (Cholach, 2004; Wang et al. 2001). The clay minerals are considered to be quite rigid so that during diagenesis these minerals do not substantially deform but move and rotate relative to the direction of the greatest compressive stress. Laboratory experiments involving X-ray diagrams of the surface of clay-water mixtures have shown that an oriented texture developed through compression with the normal to basal plane of the clay minerals oriented parallel with the direction of applied pressure (Brindley, 1953; Buessem & Nagy, 1953). Interestingly, a study of cores down to 450 m burial depth in a package of shale showed no correlation between the burial depth and preferred clay mineral orientation but did show changes in clay mineralogy with depth (Gipson, 1966). X-ray measurements show that these bedding planes of flat-lying sediments have a circular symmetry for all stages of compaction with the degree of preferred orientation increasing with compaction (Kaarsberg, 1959). In other words, during compaction these clay minerals become preferentially oriented which pushes the overall symmetry of the shale to transverse isotropy with the axis of symmetry parallel to the direction of greatest stress.

Evidence of clay minerals as the source of transverse isotropy in shales is supported through laboratory experiments. Hornby et al. (1994) generated an effective-medium model that uses the clay platelet distribution as obtained from scanning electron micrographs to successfully model the anisotropic behaviour of a shale. This is confirmed by Sondergeld & Rai (1986) who go on further to state that the preferred alignment of clay minerals and visual fabric is essentially the same as that of the elastic fabric. By measuring the changes in resistivity, P-wave velocity and S-wave velocity as a function of effective pressure of a shale, Johnston (1987) concluded that these changes were more consistent with a material influenced by clay composition and total organic content (TOC) than pore shape. However, studies done by Tosaya & Nur (1982) and Freund (1992) which measured the P-wave and S-wave velocities as functions of clay content and porosity found that both influence the velocities and hence the seismic anisotropy. Kaarsberg (1959) measured the velocities versus the weight of a drying kaolinite sample where the clay minerals observed by X-ray diffraction were found to be preferentially aligned. It was found that as the kaolinite sample dried; the sample became more anisotropic thus implying that the anisotropy was determined by the aligned clay minerals present. In another similar study done by Johnston & Christensen (1995), where the seismic properties of some shales are analyzed using velocity measurements as a function of confining pressure, it was found that the anisotropy decreased with pressure due to closure of microcracks. However, the clay mineral alignment parallel to bedding as observed by X-ray diffraction and electron microprobe backscatter imaging is thought to be the primary source of anisotropy at high pressure.

2.4.2 Microcracks and oriented pores

As mentioned in the previous section, microcracks and preferentially oriented pores are another possible source of seismic anisotropy in shales. During compaction, the clay-rich sediments are not only subjected to increased pressure but to heat as well. The intra-pore pressure, controlled both by depth and burial history, increases and eventually exceeds the depth dependent fluid hydrostatic pressure (Bishop, 1979; Smith, 1971; Snarskiy, 1961). This pressure differential may cause the rock to rupture, thus forming fractures or microcracks (see Figure 2.4) that allow fluids to migrate (Vernik, 1994). This idea of microcracks is supported by the presence of stress-induced anisotropy in granite in which anisotropy is induced by applying a uniaxial stress that preferentially closes microcracks that are oriented perpendicular to the applied stress (Mavko et al., 1995; Nur & Simmons, 1969). During compaction, the pores may be deformed to preferentially oriented shapes and so cause the material to behave anisotropically (Kim et al., 1999; Wild & Crampin, 1991). This has been observed in anisotropic carbonate-bearing sediments (Carlson et al., 1984; Dey-Barsukov et al., 2000) and is thought to contribute to the anisotropy in shales. These microcracks and preferentially oriented pores are both possible sources of anisotropy and are both oriented void spaces though their origins are quite different. The oriented pores are voids that are deformed and reduced during compaction. In contrast the microcracks are formed due to the generation and expulsion of fluids.

These microcracks and preferentially oriented pores can be detected in laboratory measurements. As mentioned previously, studies done by Tosaya & Nur (1982) and Freund (1992) that measured the P-wave and S-wave velocities as functions of clay content and porosity found that both influence the velocities and hence the seismic anisotropy. Hornby (1998) determined through pressure vessel experiments on a variety of samples that the anisotropy of shales increases

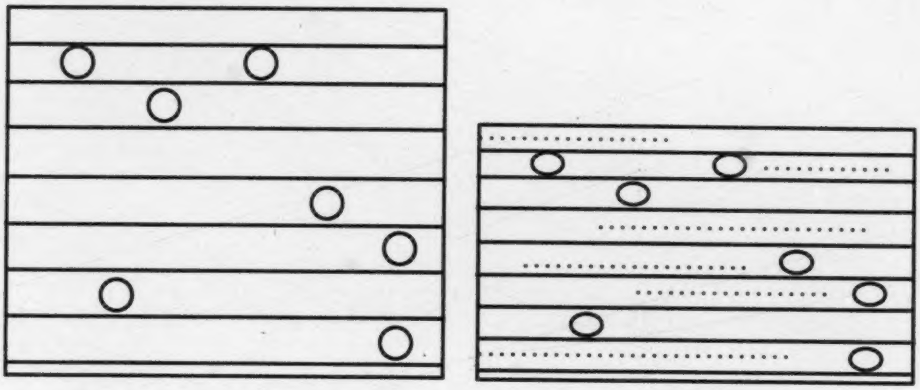

(a) Shale before diagenesis with round pores and no microcracks. Circles represent round pores.

(b) Shale after diagenesis with oriented pores and microcracks. Ovals represent the oriented pores. Dotted lines represent microcracks.

Figure 2.4: Development of oriented pores and microcracks during diagenesis.

with porosity. It was found that during the compaction process, the clay minerals are aligned which increases the anisotropy of the shale but at the same time the porosity will decrease thereby reducing the anisotropy. It was not stated which was more influential. This idea is supported by Vernik (1994) who observed a decrease in anisotropy with increased pressure due to the closure of microcracks. Johnston & Christensen (1995) found that both aligned clay minerals and microcracks contributed to the anisotropy for shales at low confining pressures. However at higher pressures, there was a decrease in the anisotropy due to closure of the microcracks. These microcracks have been detected through velocity hysteresis in velocity versus pressure graphs. This velocity hysteresis is attributed to microcracks that do not reopen at the pressure when they initially closed but remain closed until a lower pressure is reached (Jones & Wang, 1981). As well it was noticed by Jones & Wang (1981) that the velocity anisotropy is greater in lower porosity shales and these findings contrast with those of Hornby

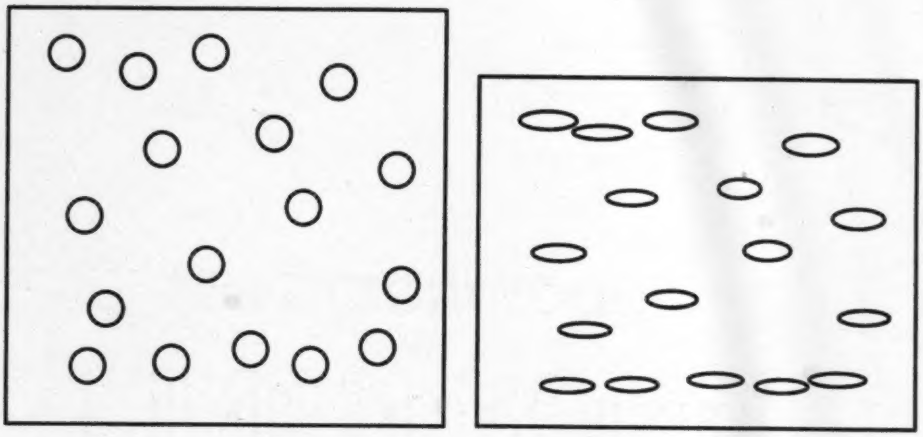

(a) Shale before diagenesis with round particles of kerogen.

(b) Shale after diagenesis with flattened particles of kerogen.

Figure 2.5: Development of flattened layers of kerogen during diagenesis.

(1998). This may indicate that the aligned clay minerals have a greater influence on velocity anisotropy than porosity. The effects of the microcracks can be estimated using the change in velocity with confining pressure (Vernik, 1993) which allows the contribution of microcracks to velocity anisotropy to be estimated.

2.4.3 Kerogen

Depending on the depositional conditions, there may be a significant amount of organic material in the form of kerogen present in shales such as oil shales. Kerogen is the solid organic material left over after the majority of the gaseous or liquid hydrocarbons have migrated out of the shales. During the compaction of the shales, the water and hydrocarbons are expelled and the pore spaces are reduced. The left over kerogen then forms thin tabular layers (Figure 2.5). Even though the kerogen may be isotropic, the layering will produce an anisotropic medium (Backus, 1962; Brittan et al., 1995; Melia & Carlson, 1984).

The occurrence of these kerogen layers is observed in Vernik & Nur (1992) and may affect the P and S-wave velocities in the shales. In Vernik & Landis (1996), Thomsen's (1986) elastic anisotropy parameter ϵ was found to change as a function of the kerogen volume. This implies kerogen may indeed be connected to the anisotropy in shales. As mentioned previously in Johnston (1987), the changes in P and S-wave velocities and resistivities with effective pressure may be influenced by the total organic content (TOC) present. As well, a model using non-spherical inclusions of kerogen predicted the elastic constants of a lean oil shale with some success (Rundle & Schuler, 1981).

In summary, it has been theorized and observed that oriented clay minerals, pores, microcracks, and kerogen layers are sources of velocity anisotropy in shales. However, not one single source of anisotropy can completely explain the anisotropy in all the shales studied. One must conclude that the anisotropy present in the shales is due to a combination of oriented clay minerals, preferentially oriented pores, microcracks, and kerogen layers. The amount of anisotropy which each contributes to the shale depends not only on the pressure under which the measurements are taken but also on the composition of the shale itself, which seems to be influenced by numerous factors.

2.5 Velocity measurements of shales

Shales are mechanically anisotropic as indicated by their strength (Ajalloeian & Lashkaripour, 2000; Nichols et al., 1986; Sargand et al., 1987) and velocity. The velocity anisotropy of shales has been observed both in the laboratory and in the field. In the field, seismic data have shown that the stacking velocities used in seismic data processing seem to change with offset or that the P-wave velocities vary with angle of propagation. Shear wave splitting is observed in both the laboratory and in the field. In the laboratory, P-wave and S-wave velocities taken parallel to bedding are different from velocities measured perpendicular to bedding.

In the field, anisotropy has manifested itself in the form of velocity variations with angle or offset. The difference in the arrival times for 2 polarizations of shear waves is also seen and is called shear wave splitting. It is also known as shear wave birefringence in reference to the optical phenomenon of birefringence in materials such as calcite whereby the two polarizations of light travel at two different velocities in the material. Some of the earliest observations of velocity variations with offset were those of Brodov et al. (1984), Cholet & Richard (1954), Crampin (1985), and Dunoyer de Segonzac & Laherrere (1959). Cholet & Richard (1954) measured velocity changes with offset from reverse VSP data in layers containing clay. Dunoyer de Segonzac & Laherrere (1959) determined that the measured velocities changed with offset from 2 sets of VSP data. More recent observations of velocity variation with offset are those of Miller et al. (1994) who determined the P-wave and S-wave velocities as functions of offset from a VSP in a submarine shale and of Kebaili & Schmitt (1996) whom measured the P-wave velocities in a walk-away VSP using the $\tau - p$ method in a shale formation. Not only have VSP data been used to observe velocity anisotropy but cross-borehole tomography has also been used for that purpose. Williamson et al. (1993) determined P-wave velocities as functions of angle and depth from sonic logs and cross-borehole tomography. VSP data show not only velocity variations with angle and depth but can show shear wave birefringence as well. Beckham (1996) observed shear wave birefringence and showed from VSP data and borehole sonic tools that there were some shear wave polarization changes with depth. As well, Harris (1996) observed shear-wave splitting in a seismic reflection survey.

Velocity variations with angle and shear wave birefringence can be observed in laboratory measurements of shale. P-wave and S-wave velocities can be measured in shales and a large difference is found between velocities parallel to bedding and velocities perpendicular to bedding (Carcione, 2000; Domnesteanu et al., 2001; Hornby, 1995; Hornby, 1998; Johnston & Christensen, 1995; Johnston & Toksoz, 1980; Jones & Wang, 1981; Kaarsberg, 1959; Kaarsberg, 1968; Lo et al., 1986; Podio et al., 1968; Sondergeld & Rai, 1986; Sondergeld et al., 2000; Vernik, 1993; Vernik,1994; Vernik & Landis, 1996; Vernik & Liu, 1997; Vernik & Nur, 1992;). Not only were velocities measured parallel and perpendicular to bedding but at off-axis angles as well (Domnesteanu et al., 2001; Hornby, 1995; Hornby, 1998; Johnston & Christensen, 1995; Jones & Wang, 1981; Kaarsberg, 1968; Lo et al., 1986; Podio et al., 1968; Pros & Babuska, 1957; Sondergeld & Rai, 1986; Vernik, 1993; Vernik & Liu, 1997; Vernik & Nur, 1992). In performing these velocity measurements, shear wave birefringence was observed (Christensen, 1971; Jones & Wang, 1981; Sondergeld & Rai, 1986). In particular, Jones & Wang (1981) measured P-wave and S-wave velocities as functions of pressure both perpendicularly and parallel to bedding for shales at different depths. It was observed that both S-wave polarization velocities were the same parallel to bedding while S-wave velocities perpendicular to bedding were about 25 % less than the SH-wave velocities parallel to bedding.

In field data of layers containing shale it has been observed that velocity variation with offset and shear wave birefringence occurs. More importantly, velocity variations with angle and shear wave birefringence have been observed in measurements of shale cores in the laboratory. It has been shown that shales are predominantly transversely isotropic with velocities parallel to bedding being faster than velocities perpendicular to bedding.

2.6 Determination of elastic constants of shales

As seen in the previous section, there are numerous methods of determining velocity as a function of propagation angle. In this section, I intend to discuss the determination of the elastic constants of materials, mainly shale rocks. Depending on the level of symmetry expressed in the sedimentary rocks, if an adequate number of phase velocity measurements are taken of the proper polarizations in an adequate number of directions, the elastic constant of the material can be determined. Through laboratory and field experiments, shales are thought to be transversely isotropic in nature.

In the laboratory, the most common method of determining the elastic constants of a shale involves obtaining 3 cores from a sample (Figure 2.6). One core parallel to bedding, one core perpendicular to bedding, and one core at some off-axis angle, usually 45°, to bedding. By measuring the P-wave and S-wave velocities on the cores parallel and perpendicular to bedding as mentioned above, the elastic constants C_{11}, C_{33}, C_{44}, and C_{66} can be determined quite accurately. The measurement of the core at 45° to bedding allows the C_{13} elastic constant to be determined. Domnesteanu et al. (2001), Hornby (1995), Hornby (1998), Johnston & Christensen (1995), Jones & Wang (1981), Kaarsberg (1968), Lo et al. (1986), Podio et al. (1968), and Vernik & Landis (1996) employed this method. A summary of the available elastic constants is shown in Table 2.2. However, it has been noted by many of these authors that there have been problems with determining the C_{13} elastic constant. Domnesteanu et al. (2001) measured angles ranging from 0° to 90° bedding instead of 45° alone but still had problems determining the C_{13} elastic constant. Hornby (1995) mentioned that there may be problems with determining the C_{13} elastic constant. Hornby (1998) tried to rectify the problem by including measurements at off-axis angles of 30°, 40°, and 62° to bedding but with only limited success. Johnston & Christensen (1995)

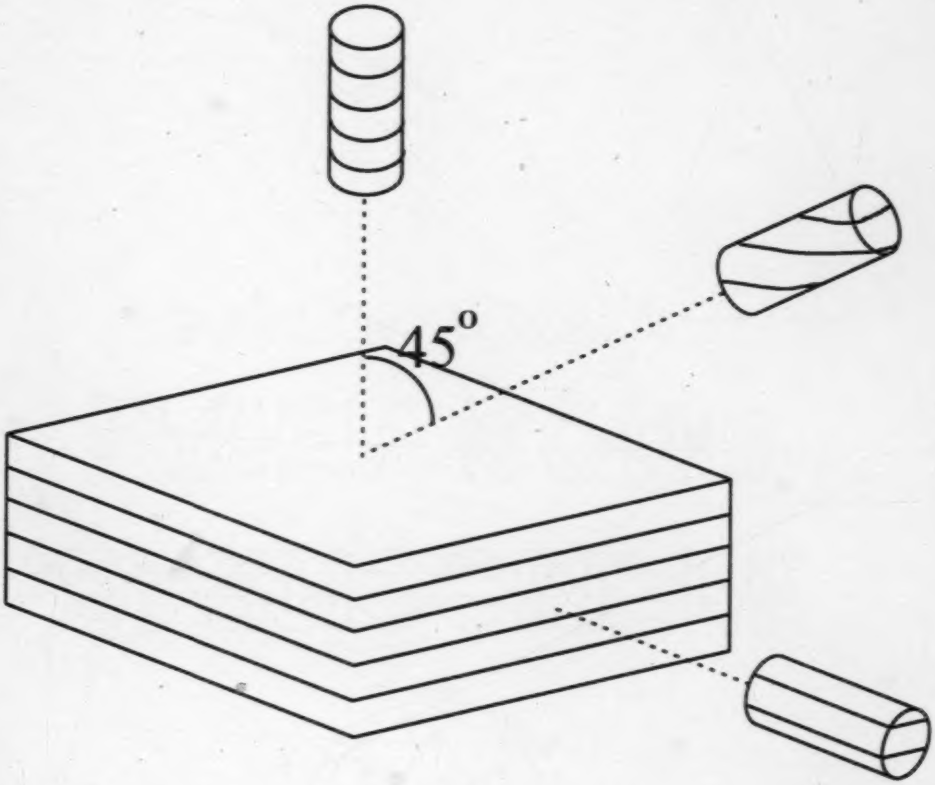

Figure 2.6: Cores taken at various angles to the bedding in the shale.

found the calculated error in the C_{13} elastic constant was about 4 times that of the other elastic constants. Kaarsberg (1968) determined the C_{11}, C_{33}, C_{44}, and C_{66} elastic constants as a function of differing densities of shale. But the C_{13} elastic constant could not be determined for all the samples. Podio et al. (1968) took cores parallel, perpendicular, 30°, 45°, and 60° to bedding. When the calculated and measured P-wave and S-wave velocities were compared as a function of angle, it was found they did not match well for intermediate angles. This indicates that the C_{13} elastic constant is not well determined. Similarly, Vernik & Landis (1996) determined all of the elastic constants as a function of the kerogen volume of a set of shales except for the C_{13} elastic constant. In particular, Jones & Wang (1981) found that the error was approximately 50 % of the value of C_{13}. This is extremely high. The problem of determining the C_{13} elastic constant may be due to ambiguities about whether group or phase velocities are being measured at off-axis angles (Dellinger & Vernik, 1994).

Paper	C_{11}	C_{33}	C_{44}	C_{66}	C_{13}
Domnesteanu et al. (2001)	Derived as function of pressure				
Hornby (1995)	Derived as function of pressure				
Hornby (1998)	Derived as function of pressure				
Johnston & Christensen (1995) for core TH-26	45.40	19.02	6.83	17.63	8.60
Jones & Wang (1981)	34.3 ± 1.4	22.7 ± 1.9	5.4 ± 0.8	10.6 ± 1.6	10.7 ± 5.4
Kaarsberg (1968)	59.5	42.5	15.3	19.7	15.8
Lo et al. (1986)	Derived as function of pressure				
Podio et al. (1968)	Derived as function of pressure				
Vernik & Landis (1996)	Derived as function of kerogen volume				

Table 2.2: Elastic constants of shale sample as derived by various papers (GPa)

In a transversely isotropic medium, the group and phase velocities are the same in directions parallel and perpendicular to the symmetry axis. In our sample, this means the group and phase velocities are coincidental perpendicular and parallel to bedding. However, this is not the case at off axis angles. Dellinger & Vernik (1994) state that away from the symmetry axis the velocities that are measured may be neither group nor phase velocities. Without careful consideration of the sample and source-receiver geometries, it may be ambiguous whether group, phase, or some intermediate velocity is determined. In the standard 3 core method of determining elastic anisotropy, the only elastic constant that needs to be determined from off axis velocity measurements is the C_{13} elastic constant. If velocity measurements are not taken carefully in the 45° to bedding direction or at any off axis angle, erroneous values of C_{13} will determined.

There are other methods of determining the elastic constants of a shale in the laboratory that may be more effective than the 3 core method from the same sample. The methodology used by Chang et al. (1994) to examine a block of phenolite, a TI medium composed of paper and phenol resin, can be easily applied to shale rocks. The measurements are done on a large cylinder of material where the axis of the cylinder is parallel to the bedding or layering. The sources and receivers are rotated on the cylinder such that the cylinder is fixed and the polarization of the transmitted shear waves is varied. As well, many different wave paths through the cylinder can be determined. This allows 4 of the 5 elastic constants to be readily determined while the C_{13} constant is determined through curve fitting. Chang & Chang (2001) examined phenolite using a method similar to Chang et al. (1994) but used both small and large sources on a variety of samples to determine all 5 elastic constants as well as looked for differences in group and phase velocities. Another method test on the same material is that employed by Okoye et al. (1996) which could be applied to a shale sample. The observed travel times are fitted with an analytical function in order to reduce numerical problems. The anisotropic inversion technique uses a least squares iterative optimization method which first inverts the P-wave first arrival traveltimes to estimate two elastic parameters and reduces the problems with determining the C_{13} elastic constant. Cheadle et al. (1991) measured the ultrasonic velocities of phenolic in differing directions on a specially cut block. Vestrum (1996) repeated this and also took a sphere of phenolic and measured the differing velocities in differing directions before determining the elastic constants. Karayaka & Kurath (1994) directly measured the strain of phenolic versus the stress applied. These methods may be applied to shale rocks but shales may not easily be machined into the special shapes required or the measurements may not be accurate to allow the determination of elastic constants.

There are other methods already applied to shale for the determination of the elastic constants that do not involve measuring the velocities just parallel, perpendicular, and at 45° to bedding in the laboratory. One method is that employed by Berge et al. (1991) who used ocean bottom sources and 3 component geophones to measure the *in situ* elastic constants of shallow-water marine sediments. The elastic stiffnesses in the model were changed until the synthetic seismograms matched all 3 components of the observed data. Using the P-wave and Stoneley waves to first constrain C_{11}, C_{13}, C_{33}, and C_{44} elastic constants, all 5 elastic constants were determined. However, substantial errors could arise due to lack of knowledge about the density as suggested by measurements from a nearby drill hole. They also mentioned the problem of determining C_{13} in general but in their methodology they were able to constrain it quite well through the shear waves and their relative energies between the shear waves and the Stoneley waves.

Arts et al. (1991) used a specially shaped cube with bevelled sides and corners to measure velocities. The elastic constants were determined but the problem of determining the phase velocities at off axis angles may still have been present. Byun & Corrigan (1990) and Byun et al. (1989) used both P and SH-wave measurements from a multiple-offset VSP and a density log in the borehole to determine the 5 elastic constants to describe the horizontally layered, transversely isotropic (TI) medium. They used a model based iterative inversion of the VSP data in order to determine the 5 elastic constants for each layer from the top down. However, with increasing depth they found that there was an increasing amount of error in the elastic constants. As well, if there is not enough moveout in the SH-wave data, they found they could not determine the C_{66} coefficient. Miller et al. (1994) used the direct arrival times from a walk-away VSP. Since a density log was not available, only the density normalized elastic constants could be determined for the compacted shale sequence. Of these only 4 of the 5 independent elastic constants could be determined due to constraints in the experimental method. White et al. (1983) determined the elastic constants of a shale formation using two closely spaced vertical seismic profiles (VSP). By fitting the velocities gathered, the 5 elastic constants of the shale were determined. Winterstein & Paulsson (1990) used crosshole and VSP data to determine the velocity anisotropy of the shale formation. From the arrival times or velocities, the 5 elastic constants were determined for the shale formation.

The most popular method of determining the elastic constants of a shale in the laboratory, by assuming a transversely isotropic symmetry of known orientation and taking velocity measurements in only 3 directions, yields problems with determining the C_{13} elastic constant. Other laboratory methods and field methods try to compensate by taking more measurements at off-axis angles and employing more complex inversion routines in order to determine the elastic constants. Even these methods assume the material has transversely isotropic symmetry and that the symmetry orientation is known. However, this assumption, despite being well founded, may not be sufficiently complete to adequately describe the anisotropy of such materials.

2.7 The $\tau - p$ method

The method I used in my research was the $\tau - p$ method as first described by Kebaili & Schmitt (1996). The method basically entails performing a walk-away VSP using multiple receiver depths (see Figure 2.7). Once the waveforms from

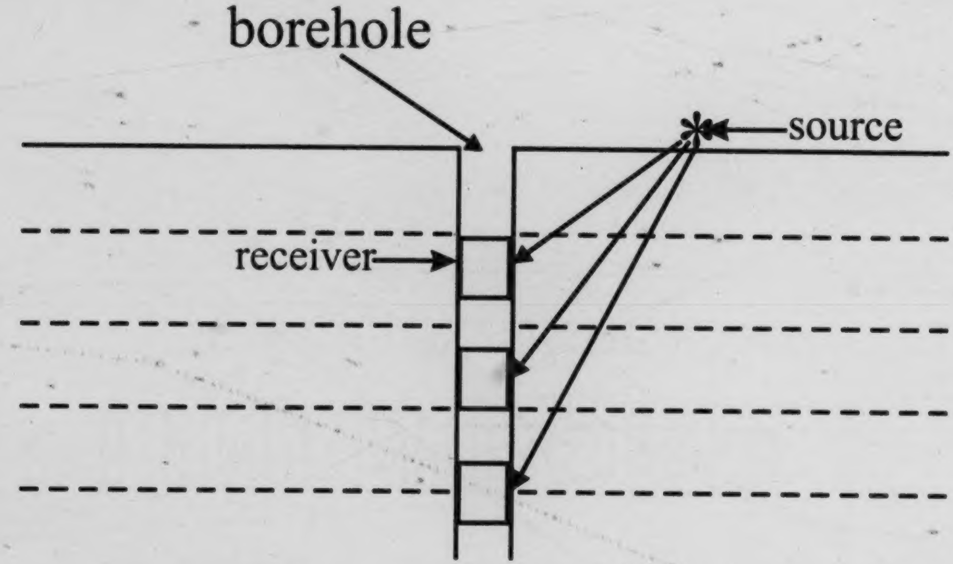

Figure 2.7: A walk-away VSP with multiple geophones in the borehole.

the 3-component receivers are recorded, a $\tau - p$ transform is performed on the data. The $\tau - p$ transform, also known as the slant-stack (Radon) transform, is defined by Tatham (1984) as:

$$F(\tau, p) = \int_{-\infty}^{\infty} f(x, \tau + px)\, dx \tag{2.11}$$

where τ is the intercept time and p is the horizontal slowness.

From the data in the $\tau - p$ domain, the phase velocities can be calculated as functions of the phase angle. This allows us to accurately determine the phase velocities at off-axis angles that previous methods have had problems with. This method was extended to the laboratory on a block of phenolic (Kebaili & Schmitt, 1997). Phenolic is composed of layers of canvas held together by a phenol resin of orthorhombic symmetry. However, the elastic constants could not be determined with P-wave velocities only. In order to determine the elastic constants of any material both P-wave and S-wave velocities must be measured. This methodology allows us to determine the phase velocities accurately at off-axis angles.

The methodology of Mah & Schmitt (2001a) and Mah & Schmitt (2001b) entails the use of one type of P-wave and two types of S-wave transducers that are prepared from piezoelectric ceramics for use as both sources and receivers. The P-wave transducers are 2.0 mm squares that are cut from larger lead zirconate sheets by means of a computer-controlled diamond saw used in electronic chip manufacturing. The S-wave transducers are prepared in a similar manner but are 2.0 mm by 3.0 mm rectangles that are cut in two perpendicular directions such that they are sensitive to the 2 different quasi-S-wave polarizations. The P-wave and S-wave transducers have nominal resonant frequencies of 1.0 MHz and 0.65 MHz, respectively. These transducers are arranged such that there are two sources at a known depth on one side of the block and an array of equally spaced transducers on a perpendicular side. The P-wave transducers vibrate predominantly in the direction perpendicular to the surface of the block. The SH-wave transducers vibrate in a direction perpendicular to the sagittal plane as inferred from the source-receiver array while the SV-wave transducers vibrate in a direction parallel to the sagittal plane. The use of these three different types of transducers allows the propagation of all three wave types to be observed. As mentioned previously, once the waveforms from all 3 types of source-receiver combinations are recorded, a $\tau - p$ transform is performed on the data and the phase velocities are calculated. This method was tested on a block of soda-lime glass (Mah & Schmitt, 2001b) which is an isotropic and almost non-attenuating material that provides an excellent reference (see Chapter 3). Using specially constructed ultrasonic sources and receivers, the P-wave and S-wave velocities were determined for a variety of angles in the isotropic soda-lime glass. It was found that the velocities determined using this method match the velocities as determined by a direct transmission experiment to better than 1.0 %. The phase velocities were then inverted in order to determine the elastic constants of the soda-lime glass. This methodology was further extended to an anisotropic sample (Mah & Schmitt, 2001a) using a block of sample similar but not the same as the one used in Kebaili & Schmitt (1997). Both the P-wave and S-wave phase velocities were determined in various directions. Assuming an orthorhombic symmetry with the symmetry axes parallel to the observed texture in the sample, the elastic constants of the composite were determined. However, more data were obtained (Mah & Schmitt, 2003; see Chapter 4) on the same block of phenolic as used in Mah & Schmitt (2001a). It was shown that sufficient phase velocities were taken in enough directions so that no assumptions were required about the symmetry of the material. The elastic constants of phenolic were determined assuming triclinic symmetry. This also means that no assumptions had to be made about the symmetry axes present in the data. The three papers referred to above detail a new methodology for the determination of the elastic constants on hand sized samples.

2.8 Oil shale characterization

One remaining goal of this thesis was to determine the elastic constants of a real earth material. Shale is very important in seismological studies of sedimentary basins, as it comprises the bulk of the volume. An oil shale was chosen since it was competent, well-layered, and most likely anisotropic. The seismic and ultrasonic properties of the oil shale were determined by its structure and composition. The density, porosity, mineralogical composition, and mineralogical distribution were characterized through the use of thin sections, whole-rock analysis, pyrolysis, X-ray diffraction, scanning electron microscopy, and electron microprobing. The relative proportions of these minerals were determined as well as any differences in the distribution of these minerals such as layering or preferred distribution. Void spaces were also examined. Once this was done, a comprehensive picture of the oil shale mineralogy was established.

Even though the $\tau - p$ methodology yielded good results on the isotropic glass sample and anisotropic synthetic sample, it did not yield good results on the oil shale. The conventional pulse-transmission methodology was used on a specially cut multi-faceted cube of oil shale. The P-wave and S-wave measurements were recorded at pressures up to 200 bar (20 MPa) in a pressure vessel and P-wave and S-wave velocities determined as functions of pressure. The velocity hysteresis was observed and the calculated elastic constants were also determined. Thomsen/Tsvankin parameters were calculated and showed that the anisotropy of the oil shale changes with pressure. Some unexpected values were found for the anisotropy of the oil shale. Chapters 5 and 6 described the characterization of the mineralogical composition and anisotropy of an oil shale. Chapter 7 summarized the results of this work and mentioned possible future work.

References

Arts, R. J., Rasolofosaon, P. N. J., and Zinszner, B. E., 1991, Complete inversion of the anisotropic elastic tensor in rocks: Experiment versus Theory: 61st Ann. Internat. Mtg., Soc. Expl. Geophys., Expanded Abstracts, 1538-1541.

Ajalloeian, R., and Lashkaripour, G. R., 2000, Strength anisotropies in mudrocks: Bulletin of Engineering Geology and the Environment, **59**, 195-199.

Backus, G. E., 1962, Long-wave elastic anisotropy produced by horizontal layering: Journal of Geophysical Research, **67**, 4427-4440.

Banik, N. C., 1984, Velocity anisotropy of shales and depth estimation in the North Sea basin: Geophysics, **49**, 1411-1419.

Beckham, W. E., 1996, Seismic anisotropy and natural fractures from VSP and borehole sonic tools-A field study: Geophysics, **61**, 456-466.

Berge, P. A., Subhashis, M., Fryer, G. J., Barstow, N., Carter, J. A., Sutton, G. H., and Ewing, J. I., 1991, In situ measurement of transverse isotropy in shallow-water marine sediments: Geophysics Journal International, **104**, 241-254.

Bishop, R. S., 1979, Calculated compaction states of thick abnormally pressured shales: American Association of Petroleum Geologists Bulletin, **63**, 918-933.

Brindley, G. W., 1953, An X-ray method for studying orientation of micaceous minerals in shales, clays, and similar materials: Mineralogical Magazine, **30**, 71-78.

Brittan, J., Warner, M., and Pratt, G., 1995, Anisotropic parameters of layered media in terms of composite elastic properties: Geophysics, **60**, 1243-1248.

Brodov, L. Y., Evstifeyev, V. I., Karus, E. V., and Kulichikhina, T. N., 1984, Some results of the experimental study of seismic anisotropy of sedimentary rocks using different types of waves: Geophysical Journal of the Royal astronomical Society, **76**, 191-200.

Buessem, W. R., and Nagy, B., 1953, The mechanics of the deformation of clay:

in Swineford, A., and Plummer, N., Eds., Clays and clay minerals: Proceedings of the second national conference on clays and clay minerals, 480-491.

Byun, B. S., and Corrigan, D., 1990, Seismic traveltime inversion for transverse isotropy: Geophysics, **55**, 192-200.

Byun, B. S., Corrigan, D., Gaiser, J. E., 1989, Anisotropic velocity analysis for lithology discrimination: Geophysics, **54**, 1564-1574.

Carcione, J. M., 2000, A model for seismic velocity and attenuation in petroleum source rocks: Geophysics, **65**, 1080-1092.

Carlson, R. L., Schaftenaar, C. H., and Moore, R. P., 1984, Causes of compressional-wave anisotropy in carbonate-bearing, deep-sea sediments: Geophysics, **49**, 525-532.

Chang, Y., and Chang, C., 2001, Laboratory results for the features of body-wave propagation in a transversely isotropic media: Geophysics, **66**, 1921-1924.

Chang, C., Gardner, G. H. F., and McDonald, J. A., 1994, A physical model of shear-wave propagation in a transversely isotropic solid: Geophysics, **59**, 484-487.

Cheadle, S. P., Brown, R. J., and Lawton, D.C., 1991, Orthorhombic anisotropy: A physical seismic modeling study, Geophysics, **56**, 1603-1613.

Cholach, P., 1994, The elasticity of intrinsically anisotropic rocks, Ph. D. thesis, Univ. of Alberta, Edmonton, Alberta.

Cholet, J., and Richard, H., 1954, A test on elastic anisotropy measurement at Berriane (North Sahara): Geophysical Prospecting, **2**, 232-246.

Christensen, N. I., 1971, Shear wave propagation in rocks: Nature, **229**, 549-550.

Crampin, S., 1985, Evaluation of anisotropy by shear-wave splitting: Geophysics, **50**, 142-152.

Dellinger, J., and Vernik, L., 1994, Do traveltimes in pulse-transmission experiments yield group or phase velocities?: Geophysics, **59**, 1774-1779.

Dey-Barsukov, S., Durrast, H., Rabbel, W., Siegesmund, S., and Wende, S., 2000, Aligned fractures in carbonate rocks: laboratory and in situ measurements of seismic anisotropy: International Journal of Earth Sciences, **88**, 829-839.

Domnesteanu, P. R., Domnesteanu, R., and McCann, C., 2001, The anisotrop[illegible] response of shale elastic coefficients to overpressure: 71st Ann. Interna[illegible], Soc. Expl. Geophys., Expanded Abstracts, 1744-1747.

Dunoyer De Segonzac, G., 1970, The transformation [illegible] minerals during diagenesis and low-grade metamorphism: A revie[illegible]tology, **15**, 281-346.

Dunoyer De Segonzac, G., and Laherr[illegible]59, Application of the continuous velocity log to anisotropy me[illegible]nts in Northern Sahara; Results and consequences: Geophysical P[illegible]ng, **7**, 202-217.

Freund, D., 1992, Ultrasonic compressional and shear velocities in dry clastic rocks as a function of porosity, clay content, and confining pressure: Geophysical Journal International, **108**, 126-135.

Gipson, M. Jr., 1966, A study of the relations of depth, porosity and clay mineral orientation in Pennsylvanian shales: Journal of Sedimentary Petrology, **36**, 888-903.

Harris, J. B., 1996, Shear-wave splitting in Quaternary sediments: Neotectonic implications in the central New Madrid seismic zone: Geophysics, **61**, 1871-1882.

Hornby, B. E., 1995, Experimental determination of the anisotropic elastic properties of shales, in Fjaer, E., Holt, R. M., and Rathore, J. S., Eds., Seismic anisotropy, Society of Exploration Geophysicists, 238-296.

Hornby, B. E., 1998, Experimental laboratory determinations of the dynamic elastic properties of wet, drained shales: Journal of Geophysical Research, **103**, No. B12, 29945-29964.

Hornby, B. E., Schwartz, L. M., and Hudson, J. A., 1994, Anisotropic effective-medium modeling of the elastic properties of shales: Geophysics, **59**, 1570-1583.

Hunt, J. M., 1996, Petroleum geochemistry and geology, 2nd edition: W. H. Freeman and Company, New York.

Isaac, J. H. and Lawton, D. C., 1999, Image mispositioning due to dipping TI media: a physical seismic modeling study: Geophysics, **64**, 1230-1238.

Johnston, D. H., 1987, Physical properties of shale at temperature and pressure: Geophysics, **52**, 1391-1401.

Johnston, J. E., and Christensen, J. E., 1995, Seismic anisotropy of shales: Journal of Geophysical Research, **100**, No. B4, 5991-6003.

Johnston, D. H., and Toksoz, M. N., 1980, Ultrasonic P and S wave attenuation in dry and saturated rocks under pressure, Journal of Geophysical Research, **85**, No. B2, 925-936.

Jones, L. E. A., and Wang, H. F., 1981, Ultrasonic velocities in Cretaceous shales from the Williston basin: Geophysics, **46**, 288-297.

Kaarsberg, E. A., 1959, Introductory studies of natural and artificial argillaceous aggregates by sound propagation and X-ray diffraction methods: Journal of Geology, **67**, 447-472.

Kaarsberg, E. A., 1968, Elasticity studies of isotropic and anisotropic rock samples: American Institute of Mining and Metallurgical Engineers Transactions, **241**, 470-475.

Karayaka, M., and Kurath, P., 1994, Deformation and failure behaviour of woven composite laminates, J. Eng. Mat. and Technol., **116**, 222-232.

Katahara, K., 1996, Clay mineral elastic properties: 66th Ann. Internat. Mtg., Soc. Expl. Geophys., Expanded Abstracts, 1691-1694.

Katsube, T. J., Mudford, B. S., and Best, M. E., 1991, Petrophysical characteristics of shales from the Scotian shelf: Geophysics, **56**, 1681-1689.

Kebaili, A., and Schmitt, D. R., 1996, Velocity anisotropy observed in wellbore seismic arrivals: Combined effects of intrinsic properties and layering: Geophysics, **61**, 12-20.

Kebaili, A., and Schmitt, D. R., 1997, Ultrasonic anisotropic phase velocity determination with the Radon transformation, Journal of the Acoustical Society of America, **101**, 3278-3286.

Kim, J. W., Bryant, W. R., Watkins, J. S., and Tieh, T. T., 1999, Electron microscopic observations of shale diagenesis, offshore Louisiana, USA, Gulf of Mexico: Geo-Marine Letters, **18**, 234-240.

Levin, F., 1992, P-wave anisotropy of the Pierre Shale: Geophysics, **57**, 1346-1347.

Lo, T., Coyner, K. B., and Toksoz, M. N., 1986, Experimental determination of elastic anisotropy of Berea sandstone, Chicopee shale, and Chelmsford granite: Geophysics, **51**, 164-171.

Mah, M., and Schmitt, D.R., 2001a, Experimental determination of the elastic coefficients of an orthorhombic material, Geophysics, **66**, 1217-1225.

Mah, M., and Schmitt, D. R., 2001b, Near point-source longitudinal and transverse mode ultrasonic arrays for material characterization, IEEE Transactions on Ultrasonics, Ferroelectrics, and Frequency Control, **48**, 691-698.

Mah, M., and Schmitt, D. R., 2003, Determination of the complete elastic stiffnesses from ultrasonic phase velocity measurements: Journal of Geophysical Research - Solid Earth,**108(B1)**, art. no. 2016.

Mavko, G., Mukerji, T., and Godfrey, N., 1995, Predicting stress-induced velocity anisotropy in rocks: Geophysics, **60**, 1081-1087.

McDonal, F. J., Angona, F. A., Mills, R. L., Sengbush, R. L., Van Nostrand, R. G., and White, J. E., 1958, Attenuation of shear and compressional waves in Pierre shale: Geophysics, **23**, 421-439.

Melia, P. J., and Carlson, R. L., 1984, An experimental test of P-wave anisotropy in stratified media: Geophysics, **49**, 374-378.

Miller, D. E., Leaney, S., Borland, W. H., 1994, An in situ estimation of anisotropic elastic moduli for a submarine shale: Journal of Geophysical Research, **99**, B11, 21659-21665.

Musgrave, M. J. P., 1970, Crystal acoustics, Holden-Day, San Francisco.

Nichols Jr., T. C., and Collins, D. S., 1986, In situ and laboratory geotechnical tests of the Pierre Shale near Hayes, South Dakota - A characterization of engineering behaviour: Canadian Geotechnical Journal, **23**, 181-194.

Nur, A., and Simmons, G., 1969, Stress-induced velocity anisotropy in rock: An experimental study: Journal of Geophysical Research, **74**, 6667-6674.

Okoye, P. N., Zhao, P., and Uren, N. F., 1996, Inversion technique for recovering the elastic constants of transversely isotropic materials: Geophysics, **61**, 1247-1257.

Podio, A. L., Gregory, A. R., and Gray, K. E., 1968, Dynamic properties of dry and water-saturated Green River shale under stress: Society of Petroleum Engineers Journal, **8**, 389-404.

Potter, P. E., Maynard, J. B., and Pryor, W. A., 1980, Sedimentology of shale, Springer-Verlag, New York.

Pros, Z. and Babuska, V., 1967, A method for investigating the elastic anisotropy on spherical rock samples, Z. Geophys., **33**, 289-291.

Rundle, J. B., and Schuler, K. W., 1981, A composite model for the anisotropic elastic moduli of lean oil shale: Geophysics, **46**, 163-171.

Sargand, S. M., Hazen, G. A., and Miller, K. M., 1987, Multiaxial testing of compacted shales: in Joshi, R. C., and Griffiths, F. J., Eds., Proceedings of the international symposium on prediction and performance in geotechnical engineering, 377-383.

Sayers, C. M., 1994, The elastic anisotropy of shales: Journal of Geophysical

Research, **99**, 767-774.

Smith, J. E., 1971, The dynamics of shale compaction and evolution of pore-fluid pressures: Mathematical Geology, **3**, 239-263.

Snarskiy, A. N., 1961, Relationship between primary migration and compaction of rocks: Petroleum Geology, **5**, 362-365.

Sondergeld, C. H., and Rai, C. S., 1986, Laboratory observations of shear-wave propagation in anisotropic media: The Leading Edge, **11**, No. 2, 38-43.

Sondergeld, C. H., and Rai, C. S., 2000, Ultrasonic measurement of anisotropy on the Kimmeridge shale: 70th Ann. Internat. Mtg., Soc. Expl. Geophys., Expanded Abstracts, 1858-1861.

Tatham, R. H., 1984, Multidimensional filtering of seismic data: Proceedings of the IEEE, **72**, 1357-1369.

Thomsen, L., 1986, Weak elastic anisotropy: Geophysics, **51**, 1954-1966.

Tosaya, C., and Nur, A., 1982, Effects of diagenesis and clays on compressional velocities in rocks: Geophysical Research Letters, **9**, 5-8.

Vernik, L., 1993, Microcrack-induced versus intrinsic elastic anistotropy in mature HC-source shales: Geophysics, **58**, 1703-1706.

Vernik, L., 1994, Hydrocarbon-generation-induced microcracking of source rocks:

Geophysics, **59**, 555-563.

Vernik, L., and Landis, C., 1996, Elastic anisotropy of source rocks: Implications for hydrocarbon generation and primary migration: American Association of Petroleum Geologists Bulletin, **80**, 531-544.

Vernik, L., and Liu, X., 1997, Velocity anisotropy in shale: A petrophysical study: Geophysics, **62**, 521-532.

Vernik, L., and Nur, A., 1992, Ultrasonic velocity and anisotropy of hydrocarbon source rocks: Geophysics, **57**, 727-735.

Vestrum, R.W., 1994, Group and phase-velocity inversions for the general anisotropic stiffness tensor, M.Sc. thesis, Univ. of Calgary, Calgary, Alberta, Canada.

Vestrum, R. and Lawton, D., 1999, Anisotropic depth migration: Reducing lateral-position uncertainty of subsurface structures in thrust-belt environments, 69th Ann. Internat. Mtg, Soc. of Expl. Geophys., Expanded Abstracts, 1107-1109.

Vestrum, R. W., Lawton, D. and Schmid, R., 1999, Imaging structures below dipping TI media: Geophysics, **64**, 1239-1246.

Wang, Z., Wang, H., and Cates, M. E., 2001, Effective elastic properties of solid clays: Geophysics, **66**, 428-440.

White, J. E., Martineau-Nicoletis, L., and Monash, C., 1983, Measured anisotropy in Pierre shale: Geophysical Prospecting, 31, 709-725.

Wild, P., and Crampin, S., 1991, The range of effects of azimuthal isotropy and EDA anisotropy in sedimentary basins: Geophysical Journal International, **107**, 513-529.

Williamson, P. R., Sams, M. S., and Worthington, M. H., 1993, Crosshole imaging in anisotropic media: The Leading Edge, **12**, No. 1, 19-23.

Winterstein, D. F., and Paulsson, B. N. P., 1990, Velocity anisotropy in shale determined from crosshole seismic and vertical seismic profile data: Geophysics, **55**, 470-479.

Chapter 3

$\tau - p$ methodology

3.1 Abstract

Specially constructed near point-source ultrasonic transducers (0.75 MHz) were designed to preferentially stimulate and receive the one longitudinal (P) and two transverse (S) propagation modes. Arrays of these transducers were placed on a rectangular prism of common soda-lime glass that served as an ideal homogeneous, isotropic medium, in order to evaluate the uncertainty of a newly developed phase velocity measurement method. Through the use of the Radon transform, the data are transformed from the offset-time ($x - t$) domain to the intercept time - horizontal slowness ($\tau - p$) domain.

From the shape of the curves in the $\tau - p$ domain the phase velocity of the propagating waves may be determined for a range of directions. The phase velocities determined using this method were accurate for incidence angles up to 76°, 64°, and 77° for the P, SV, and SH wave modes, respectively. Phase velocities of 5724 ± 64 m/s, 3411 ± 30 m/s, and 3467 ± 15 m/s were determined for the P-wave, SV-wave, and SH-wave modes, respectively. This agrees with the direct transmission P-wave and S-wave velocities of 5690 ± 60 m/s and 3440 ± 26 m/s to better than 1 %.

3.2 Introduction

A more complete elastic description of composite materials is needed in various disciplines. In geophysics, understanding the intrinsic anisotropy of the materials through which seismic waves pass is necessary to provide better values of the elastic parameters of rocks for purposes of modelling. Artificial composites are becoming increasingly popular in materials engineering because of their structural advantages. The elastic wave anisotropy of these materials provides important diagnostic information on strong and weak directions and for detecting incipient fractures. In both rocks and composite materials, the loss of structural symmetry when preferentially oriented cracks are introduced can result in complex sets of elastic coefficients. However, experimentally determining such elastic coefficients, even for relatively simple cubic and transversely isotropic materials, remains challenging and room remains for new methodologies.

In this chapter, the further development of an experimental method for measuring longitudinal and shear phase velocities with propagation angle in laboratory test pieces is described. Near point-source longitudinal wave transducers have previously been described but the present contribution focussed on the shear (transverse) wave mode transducers (Kebaili & Schmitt, 1997). The test employs arrays of small, specially constructed ultrasonic transducers that impart and receive the longitudinal (P) and two transverse (S) elastic wave modes. Common source gathers of the traces so obtained in the offset (x) - time (t) domain are transformed to the vertical incidence time (τ) - horizontal slowness (p) domain. This conversion is effected by a special Radon transformation, referred to as a slant-stack, which has the quality of decomposing observed sets of direct ray arrivals into the equivalent set of plane waves. The advantage of this procedure is that the phase (plane wave) velocities, which are sometimes difficult to measure experimentally in anisotropic media but which are necessary to characterize a material's elasticity, are obtained directly. Newly developed shear mode transducers are described. The method of determining phase velocities is evaluated on a well-behaved isotropic glass for all three modes of propagation. This test provides estimates of the experimental errors and the range of propagation angles reasonably covered in the test.

3.3 Background

3.3.1 Plane-wave Decomposition

An ultimate goal for use of the present methodology is in the determination of phase (i.e., plane wave) velocities in anisotropic media. Not being able to measure phase velocities directly substantially complicates the determination of the elastic coefficients in pulse transmission measurements (Musgrave, 1970; Auld, 1973). These problems may be reduced by implementing a plane-wave decomposition via a form of the Radon transform called the $\tau - p$ transform in the geophysical literature (Gardner & Lu, 1991). Consider the sample of Figure 3.1(a) which is instrumented with a series of coplanar detectors on the top surface and transmitters at distances z_1 and z_2 from the top surface. Since the sample is homogeneous, elastic wave energy propagates along straight ray paths from the transmitter to the receivers. The receivers detect energy in the far field since the minimum source depth is 2.0 cm (Gooberman, 1969). The corresponding plots of the arrival time to the receivers as a function of offset distance from the edge of the sample (Figure 3.1(b)) have hyperbolic-like shape. Consider only the topmost arrival curve for source 1. In the absence of additional information, this arrival curve could just as easily be created by plane waves arriving at the surface, which had passed through source 1 at the time it had been activated. The observed travel-time curve can be constructed from the envelope of a continuum of such plane waves all propagating in different directions.

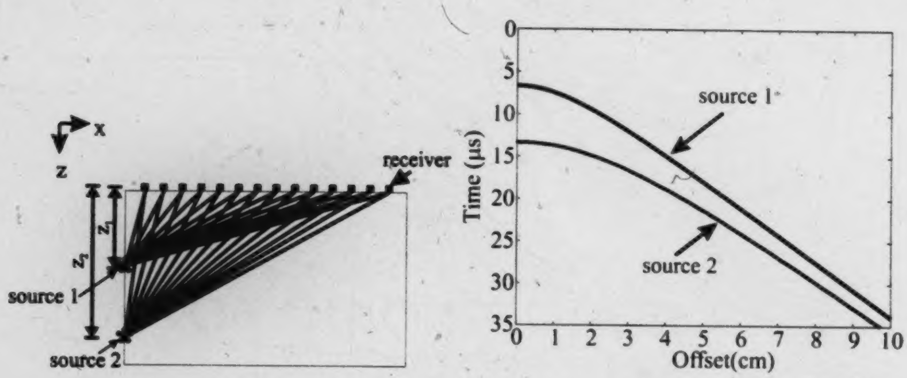

(a) Plan view of the plane containing sources and receivers with ray paths for a homogeneous anisotropic medium where the offset is measured in the x-direction.

(b) Composite travel-time versus offset (x) curves obtained for the two different source positions in a).

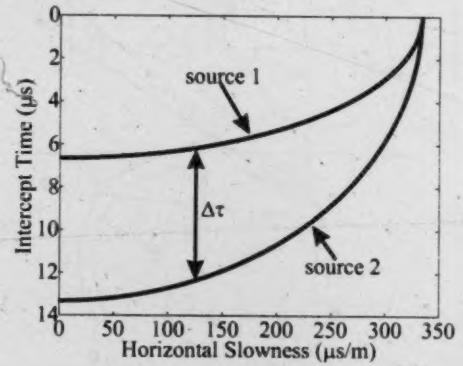

(c) Composite of the $\tau - p$ transform of the travel-time curves in b) with the determination of τ at a given constant horizontal slowness p illustrated.

Figure 3.1: Illustration of $\tau - p$ methodology using sources of a known distance apart.

Each of the constituent plane waves may be described by the phase propagation angle θ as measured from the normal to the surface at which it propagates or, equivalently, by the horizontal slowness $p = \sin\theta/\nu$ where ν is the phase velocity. The transit time for this hypothetical plane wave from the source at depth z to the observation position at receiver offset x is

$$t(x) = px + qz \tag{3.1}$$

where $q(p) = \cos\theta/\nu$ is the vertical slowness. This last formula is often written by Kebaili & Schmitt (1997) as

$$t(x) = px + \tau(p) \tag{3.2}$$

where $\tau(p)$ is called the intercept time. Consequently, each plane wave constituting the travel time envelope may be described in terms of its horizontal slowness (p), which implicitly contains the phase propagation angle θ, and the dependent intercept time τ.

The $x - t$ domain arrival time curve 1 of Figure 3.1(b) is converted to its corresponding representation in the $\tau - p$ domain by plane-wave decomposition (Figure 3.1(c)). This is effected by the Radon, or $\tau - p$, transformation (Robinson, 1982). Tatham (1984) defines the slant-stack (Radon) transform in a more formal sense as

$$F(\tau, p) = \int_{-\infty}^{\infty} f(x, \tau + px)\, dx \tag{3.3}$$

where F is the integration of the amplitudes $f(x,t)$ along the straight line $t = \tau + px$ with intercept time τ and slope p. This basically means the data are decomposed into different plane wave components where for each τ value on a given horizontal slowness p, the amplitudes of all the samples along the line given by the line $t = \tau + px$ are summed together. For example, a simple line with intercept time τ at $x = 0$ and with slope p in the $x - t$ domain maps to the point (τ, p) in the $\tau - p$ domain or a hyperbola in the $x - t$ domain is transformed into an ellipse in the $\tau - p$ domain. It is the shape of this ellipse that contains information on the variation of phase velocity with direction.

The essential components of the $\tau - p$ phase velocity determination method were previously described (Kebaili & Schmitt, 1997) and are only outlined here. In the technique, the pulsed elastic wave energy produced from a minimum of two source transducers are detected by a coplanar array of receiving transducers mounted on the adjacent side of the test piece (Figure 3.1(a)). The sets of arrival times from each of the two transducers yield hyperbolic-like offset versus travel-time curves in the $x - t$ domain (Figure 3.1(b)) which transform to ellipse-like curves in the $\tau - p$ domain (Figure 3.1(c)).

If the block of material is homogenous, then at constant horizontal slowness (p) the vertical slowness (q) according to Kebaili & Schmitt (1997) is

$$q(p) = \frac{\tau_2(p) - \tau_1(p)}{z_2 - z_1} \tag{3.4}$$

where τ_1 and τ_2 are the intercept times at constant p corresponding to the $\tau - p$ curves for the sources at offsets z_1 and z_2, respectively (Figure 3.1(c)). In an isotropic medium, q remains a constant but it is worth noting that both p and q in an anisotropic material depend on the propagation angle θ within the plane. The phase velocity ν is then

$$\nu(\theta) = \left(q^2(\theta) + p^2(\theta)\right)^{-1/2} \tag{3.5}$$

at the phase propagation angle:

$$\theta = \arctan\left(\frac{p}{q}\right). \tag{3.6}$$

3.3.2 Experimental Method

Experiments were carried out on blocks of soda-lime glass with a bulk density of 2600 ± 100 kg/m^3. Silicate glasses are essentially frozen fluids with no preferred textural direction and provide an isotropic and homogeneous mechanical medium. The 20 cm × 20 cm × 8 cm block employed was prepared from materials used in wall construction. Two adjacent perpendicular surfaces were prepared

Mode	Pulse transmission velocity (m/s)	$\tau - p$ velocity (m/s)
P	5690 ± 60	5724 ± 64
SV	3440 ± 26	3411 ± 30
SH	3440 ± 26	3467 ± 30

Table 3.1: Comparison of standard pulse transmission and $\tau - p$ phase velocities.

using a surface grinder, the flatness of the surfaces were measured to be better than 100 μm. P-wave and S-wave velocities were measured in a number of different orientations using conventional pulse transmission methods and the average results are given in Table 3.1.

3.3.3 Point-source transducers

Longitudinal and two transverse wave transducers that acted as both sources and receivers were prepared from piezo-electric ceramics. The transducers were made as small as possible in order to reduce transducer dimensional effects. However, reducing the size of the transducers introduced complications due to directionality constraints.

The longitudinal or P-wave transducers were prepared from commonly available PZT-5 (lead zirconate) sheets by cutting them into 2.0 mm squares using a computer-controlled diamond saw like that in electronic chip manufacturing. These transducers predominantly expand essentially as a point-source in the direction perpendicular to the block (Figure 3.2(a)). The transverse or S-wave piezo-electric ceramics (EBL #3 - Stavely Sensors) were cut into 2 mm × 3 mm rectangles in two perpendicular directions to make transducers preferentially sensitive to the two different quasi-S wave polarizations. The two cuts ideally produce displacements parallel to the surface of the test piece, referred to hereafter as SV and SH, that are parallel (Figure 3.2(b)) and perpendicular

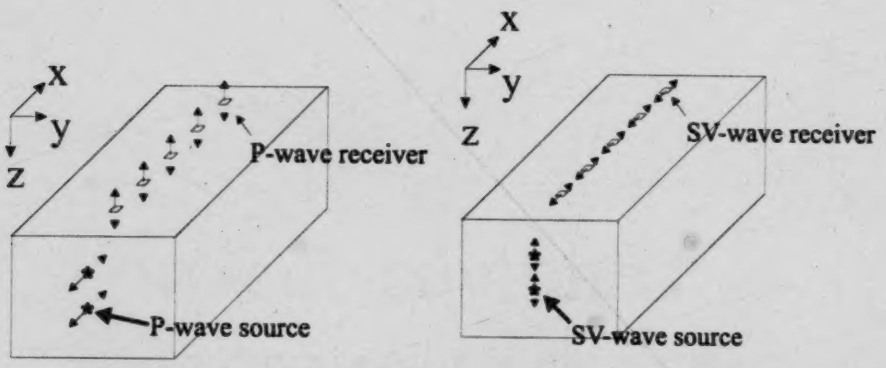
x
y
z
P-wave receiver
P-wave source
x
y
z
SV-wave receiver
SV-wave source

(a) Ideal particle motion imparted and received by the P-wave mode transducer.

(b) Ideal particle motion imparted and received by the SV-wave mode transducer.

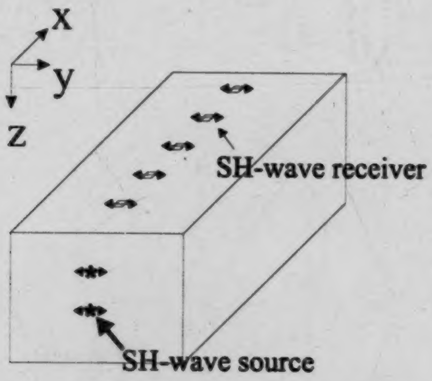
x
y
z
SH-wave receiver
SH-wave source

(c) Ideal particle motion imparted and received by the SH-wave mode transducer.

Figure 3.2: Ideal particle motion imparted and received by the piezoelectric transducers.

(Figure 3.2(c)) to the source-receiver array plane, respectively.

The slant-stack method relies on the ability to illuminate a variety of source-detection paths through the material. However in the far field, such simple point-source displacements have considerable directionality (White, 1983; Gooberman, 1969). The P-wave transducers radiated energy at nearly all angles and successfully provided strong amplitude at all detecting receivers. The hypothetical directionality of the P-wave transducers is shown in Figure 3.3(a). In contrast, the SV-wave transducers radiated energy mostly at small angles and very little at larger angles as required for proper reception (Figure 3.3(b)). The use of SV-wave transducers were experimentally confirmed as being a poor SV-wave source. Instead, the longitudinal (P-wave) transducers generated better SV-like polarizations and were consequently used for transmitting in both the P and SV arrays as confirmed experimentally. This was expected as the P-wave transducers acted as vertical point-sources that also generated an SV-wave radiation pattern with substantial energy at oblique angles (Figure 3.3(c)). The SH-waves were generated by a source with particle displacement perpendicular to the surface and sufficient energy was radiated outward in the proper directions to be received (Figure 3.3(d)).

According to Gooberman (1969), in the near field, there are huge fluctuations in the amplitude and shape of the wavelet as measured by the receiver transducers. However, the methodology requires measurements from the far field. The distances considered to be near field and far field are determined by the size and shape of the source transducer. The near field limit for the experimental set up in this work was calculated to be 5 times the width of the source transducer. For example, the P-wave transducers were 2 mm in width which translates into a near field limit of 1 cm. However, the nearest receiver has a minimum distance of 2 cm from the source, which indicates the far field is being measured.

All the transducers were mechanically damped to increase their bandwidth by potting in a urethane-metal powder mixture. The P-wave transducers were mounted on a conductive, malleable, removable substrate that was clamped to

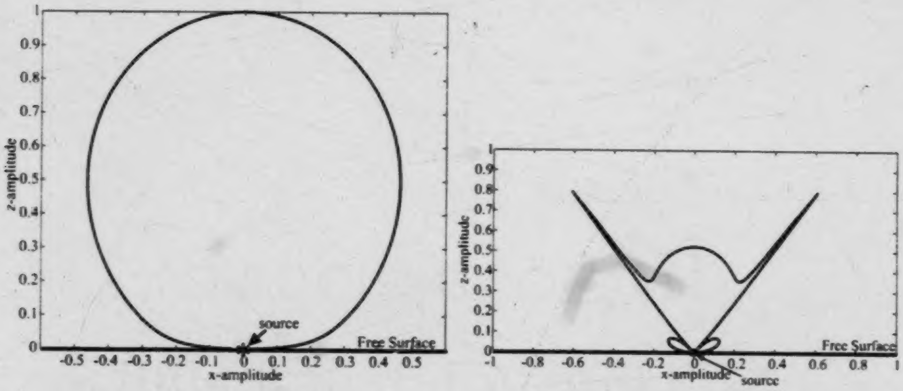

(a) The theoretical radiation pattern for the P-wave generated by source vibrating normal to the surface.

(b) The theoretical radiation pattern for the SV-wave generated by source vibrating parallel to the surface.

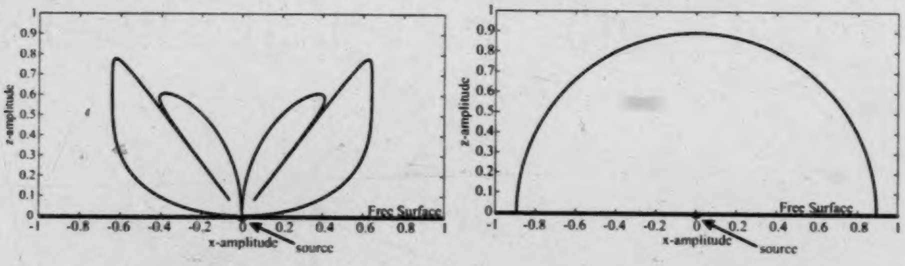

(c) The theoretical radiation pattern for the SV-wave generated by source vibrating normal to the surface.

(d) The theoretical radiation pattern for the SH-wave generated by source vibrating parallel to the surface

Figure 3.3: Theoretical radiation pattern for the 3 modes of propagation for source normal and parallel to the surface.

the block. The same, however, can not be done with the shear wave transducers due to poor coupling achieved by mere clamping. Both SV and SH transducers were directly glued to the samples using conductive silver paint. After mechanical damping and attachment, the resonant frequency of the P and S wave transducers were both near 0.75 MHz (Figure 3.4) with effective bandwidths from 0.15 MHz

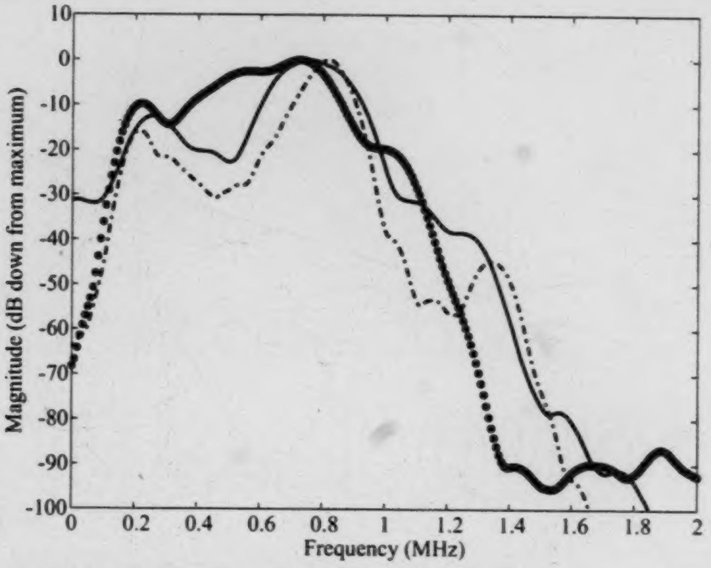

Figure 3.4: Frequency spectrum of the P-wave, SV-wave, and the SH-wave data represented by the solid, dot-dash, and dotted lines, respectively.

to 1.20 MHz.

The transducers were placed on the sample in a coplanar array as shown in Figure 3.2(a) with two transmitters on one side at a spacing of 2.0 ± 0.1 cm. The receiving transducers were mounted in a linear array on the adjacent perpendicular surface at a spacing of 0.5 ± 0.1 cm. The source transducers were activated with a 300 V, 10 ns rise time spike. The response of the receiver transducers to the resulting elastic waves were digitally acquired by a high speed sampling oscilloscope at a rate of 8 ns/sample for 120 μs with the waveforms transferred via a GPIB bus to a computer for archiving and analysis. Random noise was a significant problem due to the small sizes of the transducers. Approximately 2000 individual pulses were stacked on the oscilloscope to improve the data quality. The sample was shielded in a grounded steel box and high frequency line filters were included on all electrical equipment to reduce this noise.

Only simple processing of the waveforms was carried out to reduce the effects of trigger noise and spurious reflected and other mode arrivals. The high amplitude trigger noise was simply muted as were portions of the trace before and after the desired arrivals by modulation with a simple tapered window (Figures 3.5, 3.7, and 3.9). These data were then bandpass filtered to remove any of the remaining high frequency noise above 1.70 MHz and so that frequencies between 0.15 MHz and 1.20 MHz are kept.

3.4 Results and discussion

3.4.1 Determination of Phase Velocities

Examples of the processed waveforms acquired on the glass block are shown in Figure 3.6(a). These generally show that in the isotropic, low-attenuation glass the waveforms retain much of the same character with offset and indicate that consistent signals are generated and received. The $\tau - p$ transform was accomplished by a conventional $x - t$ domain slant-stack (Mah, 1999). The Radon transform (hereafter referred to as slant-stack) of the P-wave $x - t$ traces obtained on the glass block at the depth of 2.0 cm is shown in Figure 3.6(b). The $\tau(p)$ values at the first amplitude peak, used in $\Delta(p) = \tau_1(p) - \tau_2(p)$ in Equation 3.4, were picked semi-automatically.

The raw unprocessed SV-wave modes are shown in Figure 3.8(a). The first set of arrivals is that of the P-wave mode unavoidably generated by the source with the SV-wave mode following soon after. After muting out of non-SV-wave energy, the SV-wave arrival can be seen in Figure 3.8(b). The arrivals are not as clean or consistent as the other waveform modes but the corresponding $\tau - p$ transform yields a smooth continuous curve (Figure 3.8(c)). The Radon transform methodology contains a degree of averaging which is an additional benefit especially if traces are lost. The $\tau - p$ curve (Figure 3.8c) deviates from the

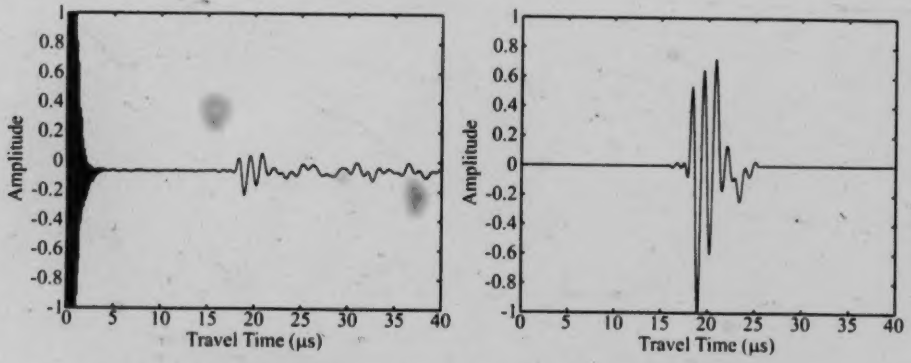

(a) Raw waveform recorded by a receiver at 10.0 cm offset on the glass block with a P wave source transducer at 2.0 cm depth.

(b) The waveform of (a) after muting, windowing, and bandpass filtering to remove noise.

Figure 3.5: Observed P-wave trace at 10.0 cm offset on the glass block.

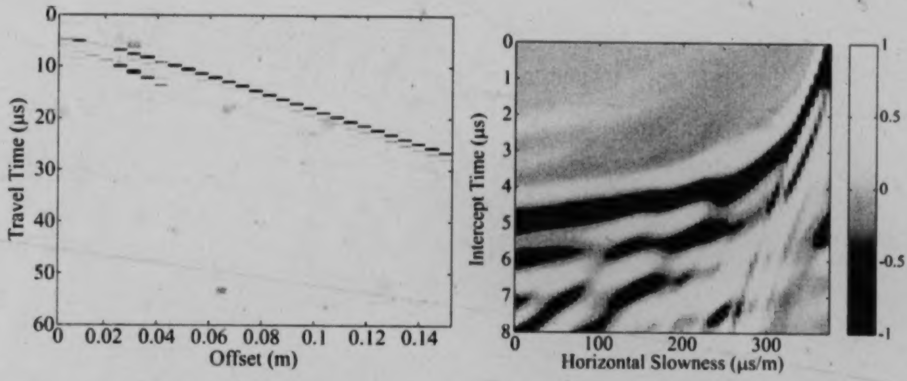

(a) Observed amplitude versus time traces with offset on the glass block for the P wave source transducer at 2.0 cm depth.

(b) The $\tau - p$ transform obtained by slant-stacking of (a) with an intercept time (τ) increment of 8 ns and horizontal slowness (p) increment of 2.5 μs/m.

Figure 3.6: Observed P-wave traces on the glass block and corresponding $\tau - p$ transform.

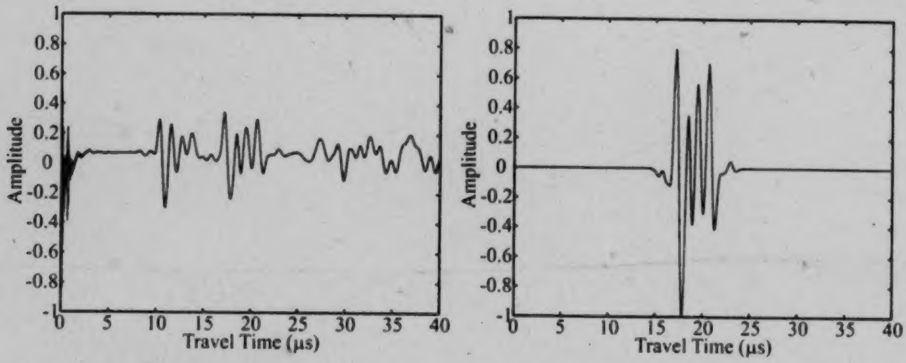

(a) Raw waveform recorded by a receiver at 4.0 cm offset on the glass block with a SV wave source transducer at 4.0 cm depth.

(b) The waveform of (a) after muting, windowing, and bandpass filtering to remove noise.

Figure 3.7: Observed SV wave trace at 4.0 cm offset on the glass block.

ideal shape (Figure 3.1(c)) at both the beginning and end. The end of the curve at 300 μs/m is straight instead of being ideally curved. Also the $\tau - p$ curve (Figure 3.8c) deviates at the beginning (i.e., 0 μs/m) from having a zero slope. The cleanest, most consistent waveforms acquired are those of the SH-wave mode (Figure 3.10(a)). The waveforms show no noticeable dispersion. The corresponding $\tau - p$ curve yields a smooth, continuous curve (Figure 3.10(b)). The $\tau - p$ curves for all three modes of propagation show events other than the main arrival. These are aliasing effects caused by having discrete receiver locations instead of a continuous array.

Analysis of the shape of the $\tau - p$ curves for all 3 propagation modes using Equation 3.4 yielded the vertical slowness (q) as a function of the horizontal slowness (p) (Figure 3.11). If the material is truly isotropic, the velocity does not change with direction of propagation and hence the $p - q$ curves will be circular. In Figure 3.11, for the higher horizontal slowness values, the $p - q$

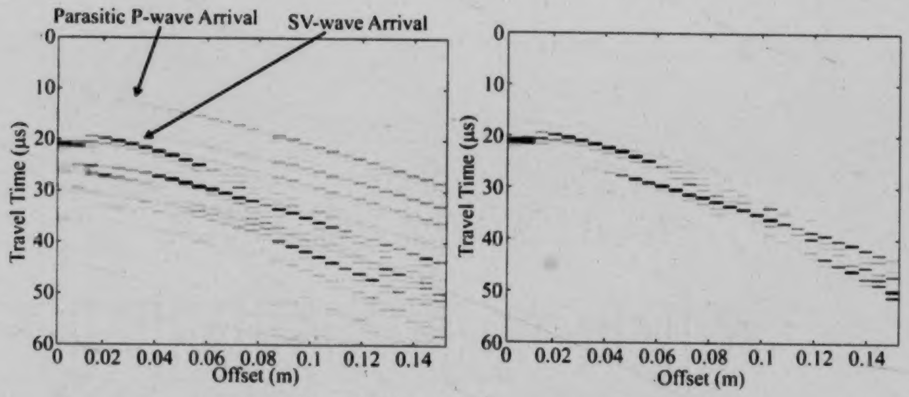

(a) Unmodified SV mode records for the 6.0 cm deep source displaying strong P mode arrivals and transducer directionality effect.

(b) Isolated SV mode arrivals after muting of P mode arrivals followed by peak amplitude normalization.

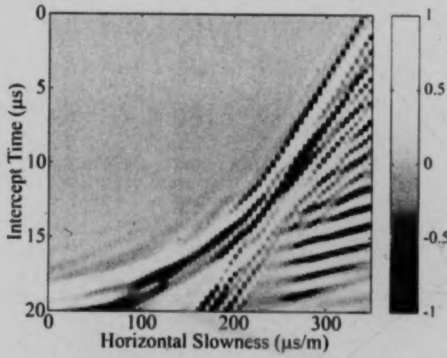

(c) Peak amplitude normalization of the $\tau - p$ transform via slant-stack of b) with an intercept time (τ) increment of 8 ns and a horizontal slowness (p) increment of 5 μs/m.

Figure 3.8: Analysis of the SV mode arrivals.

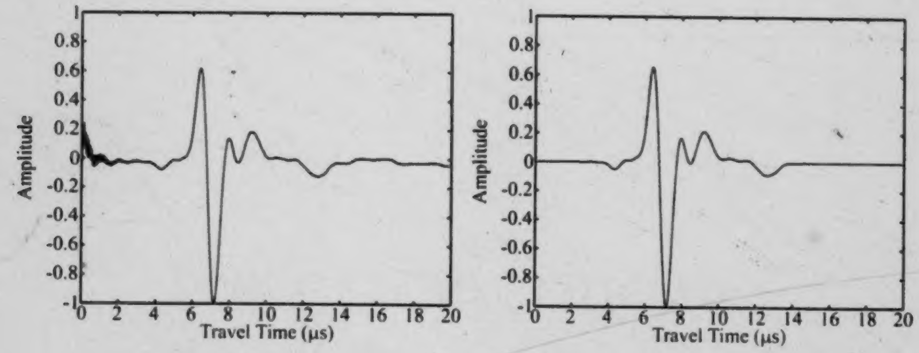

(a) Raw waveform recorded by a receiver at 0.5 cm offset on the glass block with a SH wave source transducer at 2.0 cm depth.

(b) The waveform of (a) after muting, windowing, and bandpass filtering to remove noise.

Figure 3.9: Observed SH wave trace at 0.5 cm offset on the glass block.

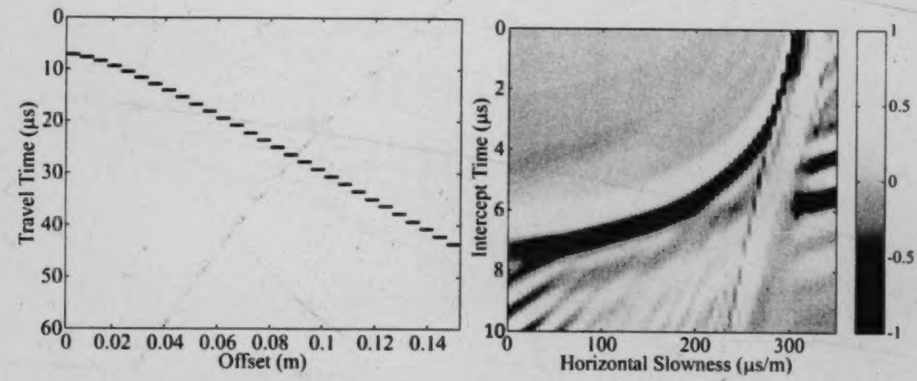

(a) Observed amplitude versus time traces with offset on the glass block for the SH wave source transducer at 2.0 cm depth

(b) The $\tau - p$ transform obtained by slant-stacking of (a) with an intercept time (τ) increment of 8 ns and a horizontal slowness (p) increment of 5 μs/m.

Figure 3.10: Analysis of the SH mode arrivals.

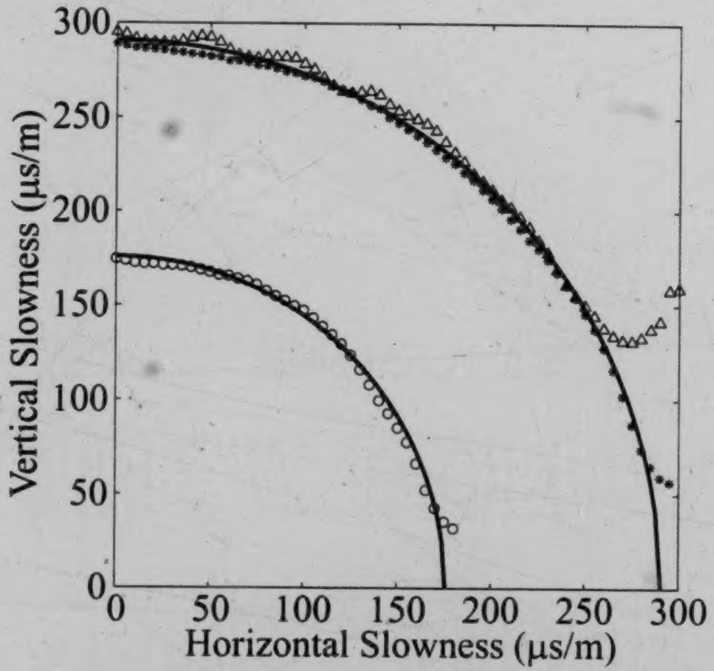

Figure 3.11: The vertical slowness (q) as a function of the horizontal slowness (p) for all 3 modes of propagation. The solid lines represent the ideal P-wave and S-wave slowness as calculated from the average phase velocities derived from the data. Symbols represent the P-wave (o), the SV-wave (triangles), and the SH-wave (*) slownesses.

curves deviate from the ideal circular shape. These higher horizontal slowness values correspond to higher angles in the plane of investigation. These deviations correspond to angles greater than 76°, 64°, and 77° for the P, SV, and SH modes, respectively. This implies that the $\tau - p$ transform is being employed to determine values for where there is insufficient coverage. As well there were deviations for angles less than 5° for all 3 modes of propagation which were most likely caused by inadequate data coverage at near offsets as can be seen in Figure 3.8(c). Since there was only a limited amount of space and the transducers were of a finite size, this problem may never be completely resolved.

Using Equations 3.5 and 3.6, the $\tau - p$ curves yielded phase velocities for the P-wave, SV-wave, and SH-wave polarizations (Table 3.1). These phase velocities were calculated by averaging the velocities over valid angles of propagation and the error cited is that of the standard deviation of the velocities. The phase velocities as functions of the phase propagation angles for all 3 modes of propagation are shown in Figure 3.12. There was some waver in the phase velocities which was most likely due to errors in receiver placement. The P-wave, SH-wave, and SV-wave velocities agree to better than 1 % with P-wave and S-wave velocities measured directly through the block as noted earlier. This suggests that uncertainties of better than 1 % may be expected using the $\tau - p$ technique under well controlled conditions for a homogeneous material. For practical purposes the glass may be considered essentially lossless (i.e., nondispersive) and waveform spreading was not a problem.

Although the phase velocities were readily determined, some experimental problems remain. Even though dispersion is not readily observable, it may still be present. This dispersion must have some influence on the accuracy of the $\tau - p$ method of phase velocity determination since it changes the shape of the waveform with distance and needs to be considered in future (see Martinez and McMechan, 1984). Other potential problems reside with the difficulties of cleanly separating different arrivals and the unavoidable P-SV mode coupling. This is due to the complexities in polarization of the different modes (e.g., Crampin, 1978) and the related imperfections of the transmitting and receiving transducers. A final problem is that only a limited range of angles may be covered with the transducer arrays and for equal spacing of transducers this will introduce a sampling bias towards the far offset transducers.

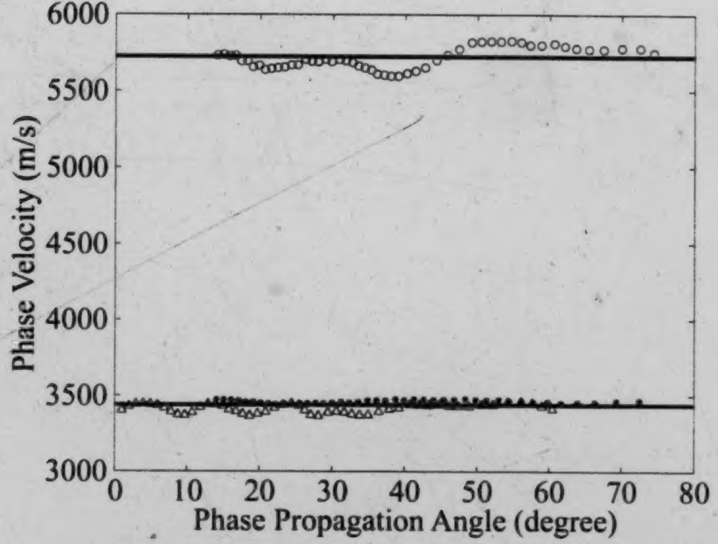

Figure 3.12: Summary of the phase velocities versus phase propagation angle θ obtained from the $\tau - p$ analysis of the arrivals. Symbols represent the P-wave (o), the SV-wave (triangles), and the SH-wave (*) particle motion polarizations. The solid lines represent the phase velocities calculated from the elastic constants as derived from the inversion.

3.5 Conclusions

Phase velocities were determined directly as functions of phase propagation angles on an isotropic glass. Special, near-point transducers were developed to impart and receive different elastic wave energies. These transducers were designated as P, SV, and SH to indicate the primary mode of particle motion to which each different transducer was sensitive. Clean P and SH modes could be generated and received in isotropic glass. However, the SV mode was complicated by the coupled nature of P and SV waves and by difficulties related to the directionality of SV mode receivers in terms of imparting the desired wave energy into the medium. Six arrays of these transducers were constructed on the glass block allowing 144 individual P, SV, and SH mode phase velocities to be obtained. The P-wave and S-wave velocities were recovered using the slant-stack (Radon) transform to better than 1 % relative to conventional pulse transmission tests. It is important to note that in the glass it was difficult to detect any dispersion by spreading of the observed waveforms with increasing propagation distance. It was also discovered that there is a physical limit as to the directions in which the phase velocities can be calculated which is determined by the data coverage present.

This technique is currently being used to determine the phase velocities with propagation angle in an anisotropic material. These phase velocities are then inverted in order to determine the elastic constants of the material. One great advantage of the present methodology is that it can be applied to samples of simple shape such as rectangular prisms and even cylinders. The latter will be particularly useful in the context of determining anisotropy in earth materials, which are often assumed to be transversely isotropic, using existing core samples with a minimum of additional preparation.

References

Auld, B. A., 1973, Acoustic fields and waves in solids, John Wiley and Sons, Inc., New York, NY.

Crampin, S., 1978, Seismic-wave propagation through a cracked solid: polarization as a possible dilatancy diagnostic: Geophys. J. R. Astr. Soc., **53**, 467-496.

Gardner, G. H. F., and Lu, L., 1991, Slant-stack processing, Society of Exploration Geophysicists, Tulsa, OK.

Gooberman, G. L., 1968, Ultrasonics: Theory and Application, English University Press Ltd., London, England.

Kebaili, A., and Schmitt, D. R., 1997, Ultrasonic anisotropic phase velocity determination with the Radon transformation: J. Acoust. Soc. Am., **101**, 3278-3286.

Mah, M., 1999, Experimental determination of the elastic coefficients of anisotropic materials with the slant-stack method, M.Sc. thesis, Univ. of Alberta.

Martinez, R. D., and McMechen, G. A., 1984, Analysis of absorption and dispersion effects in tau-p synthetic seismograms, 54th Ann. Internat. Mtg., Soc. Expl. Geophys., Expanded Abstracts, Session: S24.2.

Musgrave, M. J. P., 1970, Crystal acoustics, Holden-Day, San Francisco, CA.

Robinson, E. A., 1982, Spectral approach to geophysical inversion by Lorentz, Fourier, and Radon transforms: Proc. IEEE, **70**, 1039-1054.

Tatham, R. H., 1984, Multidimensional filtering of seismic data: Proc. IEEE, **72**, 1357-1369.

White, J. E., 1983, Underground Sound, Elsevier Science Publishing Company Inc., New York, NY.

Chapter 4

Determination of the complete elastic stiffnesses from ultrasonic phase velocity measurements

4.1 Abstract

The complete set of 21 elastic stiffnesses of a composite material are found from ultrasonic measurements of the phase velocity anisotropy. Quasi-P and quasi-S wave phase-speeds at a variety of incident angles within a number of differing planes through the material are obtained using the $\tau - p$ plane wave decomposition technique. The 779 individual phase velocities were inverted, under no *a priori* presumptions about the symmetry or orientation of the material, to provide all the stiffnesses. These show that the material has nearly orthorhombic symmetry as is expected from its texture. This orthorhombic character was further apparent in a number of bootstrap tests of the inversion that assumed differing levels of symmetry from triclinic to orthorhombic and using various subsets of the measured phase velocities. However, the present analysis does not account for the effects of wave-speed dispersion evident in the observed waveforms. This dispersion is particularly severe for the in-plane q-S polarization and is possibly a consequence of the fine layered structure of the material.

4.2 Introduction

Most rocks are intrinsically anisotropic and the need to include this anisotropy in seismological studies of the crust is increasingly recognized. For example, in overthrust regions where sedimentary layers are tilted, ignoring anisotropy leads to seriously erroneous geologic interpretation of seismic profiles. At larger scales, the shear wave birefringence produced by metamorphic texture is still not completely understood. The intrinsic elastic rock properties are one important piece of information needed to properly interpret and model such seismic responses. However, there are surprisingly few measurements of velocity anisotropy on candidate rocks. Experimental determinations are not necessarily easy to make, and many have often relied on numerous simplifying assumptions about the material's texture and orientation to simplify the measurements.

Velocity anisotropy is tied more fundamentally to the material's elastic properties and an important goal of experimental anisotropy determination is to estimate the complex elastic behavior. Such values are useful in seismic modelling of complex wavefields through earth models. However, at this writing there exist even fewer complete determinations of the elastic coefficients of rock.

A method for determining the complete set of all 21 independent elastic coefficients from ultrasonic compressional and shear wave measurements is described here. This builds on earlier but less general results that inverted an earlier and smaller set of phase velocity observations under the assumption of orthorhombic symmetry and prior knowledge of principal directions (Chapter 3; Mah & Schmitt, 2001a). The general method inverts phase velocities that are provided experimentally by a well known plane wave decomposition technique. The method was tested on a composite material to obtain elastic coefficients up to triclinic symmetry. Bootstrap testing used various subsets of the data to evaluate the accuracy of the inversion methodology. The set of elastic stiffnesses obtained largely confirms the expectation that this material has orthotropic symmetry but nontrivial values of the non-orthorhombic stiffness coefficients may provide an indication of the level of error due to sample heterogeneity and dispersion.

4.3 Background

4.3.1 Phase Velocities and Elasticity

Twenty-one independent coefficients C_{IJ} define a material's elasticity in the most general case (e.g., Musgrave, 1970). Finding all of these coefficients is difficult to achieve experimentally. To make the problem tractable most studies on rock proceed on the basis of texture either isotropy, transversely isotropy (TI), or orthotropy with 2, 5, or 9 independent elastic constants, respectively, and also assume the axes of symmetry of the materials are known (see Appendix A).

The symmetries that might be expected in rocks, the number of independent elastic coefficients necessary to describe such materials, their arrangement within a principally aligned Voigt notation elastic stiffness tensor representation (Nye, 1985), and the formulas used to obtain the coefficients from measured velocities (e.g., Cheadle et al., 1991; Neighbours & Schacher, 1967) are summarized in Table 4.1. This is by no means the complete set of equations that may be used to determine the elastic coefficients directly from phase velocities. The value of 0 in a given cell means that stiffness is trivial. The use of the C_{IJ} only means that the stiffness must be determined by an inversion procedure or that the formula required is complicated. They are only the most convenient and compact equations.

The decision to use a given set of formulas is based primarily on the texture of the rock. For example, shales consist of fine horizontal layers with a preferential alignment of platelike clay minerals. Such a structure is symmetric with respect to rotations around an axis normal to the layering. This produces a TI medium requiring a minimum of 5 well-chosen phase velocity measurements (Thomsen, 1986; Johnston & Christensen, 1995). Metamorphic rocks, such as gneiss, have preferred mineralogic orientations induced by ductile straining that produces a well-defined foliation and lineation. The symmetry of this texture is represented by three orthogonal mirror-planes describing orthotropy. Such symmetry might be further reduced, however, by the inclusion of cracks that need not be preferentially aligned with the mineralogic texture of the material (Sayers, 1998). Since neither the degree of symmetry nor its orientation in any given sample is necessarily known, it is best to make no prior assumptions about the nature of the symmetry and to treat the material initially as triclinic with 21 independent elastic constants (e.g., Neighbours & Schacher, 1967; Arts et al., 1991; Vestrum, 1994).

4.3.2 Theoretical Relations

A brief review of the theory linking velocity with moduli is necessary to illustrate the linkage between elastic properties and P and S phase velocities and as background to the inversion technique described later. A homogeneous anisotropic medium obeys the general Hooke's law (in Einstein indicial notation),

$$\sigma_{ij} = c_{ijkl}\epsilon_{kl} \tag{4.1}$$

where σ_{ij}, ϵ_{kl}, and c_{ijkl} are the stresses, strains, and elastic stiffnesses, respectively. Note that through the bulk of this paper the reduced Voigt notation C_{IJ} (e.g., Bass, 1995) is employed instead to represent these elastic stiffnesses. The full tensor c_{ijkl} notation more naturally assists description of the mathematics. After some mathematical manipulations (see Appendix A) and if one assumes a plane wave solution of the following form,

$$U_i = A_i e^{i\frac{2\pi}{\lambda}(n_r x_r - \nu t)} \tag{4.2}$$

where U_i is the displacement in the i^{th} direction, A_i is the amplitude of the particle motions of the propagating wave, λ is the wavelength of the propagating wave, $\mathbf{n} = n_1\mathbf{i} + n_2\mathbf{j} + n_3\mathbf{k}$, $\mathbf{n}$ is of unit length, $\mathbf{i}$, $\mathbf{j}$, and $\mathbf{k}$ are the unit vectors parallel to the x-axis, y-axis, and z-axis, respectively, x_r is the position vector, ν is the phase velocity, and t is the time travelled. There are 3 distinct plane waves travelling with orthogonal particle motions, one quasi-P wave and two quasi-S plane-waves propagate in any direction. For these plane waves, the phase velocities and polarization directions are the eigenvalues and eigenvectors of the Christoffel equation:

$$\Gamma_{il}A_l = \rho\nu^2 A_i \ , \tag{4.3}$$

where ν is the phase velocity, A_i is the amplitude of the particle motions of the propagating wave, and Γ_{il} are the Christoffel symbols that depend on the elastic constants via:

$$\Gamma_{il} = c_{ijkl}n_j n_k \ , \tag{4.4}$$

where n_j and n_k are the direction cosines defining the direction of the plane wave propagation (see Appendices A and B for more details).

When the elastic stiffnesses c_{ijkl} are known, the wave speeds in any direction are determined by solving Equation 4.3 (e.g., Musgrave, 1970; Auld, 1973). This is an eigenfunction problem in which for any given propagation direction $\mathbf{n}$, three eigenvalues relating to the one quasi-P and two quasi-S speeds with corresponding polarizations of these waves provided by the eigenvectors result. These wave speeds refer to the monofrequency phase, or plane wave, velocities which generally differ from the corresponding group, or ray, velocity that is detected in normal time-of-flight pulse transmission tests. The experimental velocity measurement technique employed here is unique in that it provides phase velocities to the inversion.

Equation 4.3 above and Appendix A indicate that the elastic coefficients may be determined by measuring wave speeds in a sufficient number of appropriately directions. The use of elastic wave velocities to determine elastic coefficients has long been popular (Markham, 1957; Neighbours & Schacher, 1967; Pros & Babuska, 1967; van Buskirk et al., 1986; Arts et al., 1991; Cheadle et al., 1991; Vestrum, 1994; Okoye et al., 1996). In early studies of anisotropy, many of the metallic elements investigated had simple structures (e.g., cubic or hexagonal) requiring only a few strategically oriented measurements (e.g., Neighbours & Schacher, 1967), as summarized in Tables 4.1, 4.2, 4.3, and 4.4 (Derivations of these equations can be seen in Appendix A). The lower the symmetry of the material, the greater the number of velocity measurements required (Neighbours & Schacher, 1967). An isotropic medium needs only 1 compressional and 1 shear wave velocity determination (see Appendix A.3) whereas in principal triclinic materials can be characterized by 21 strategically placed velocity measurements (Arts et al., 1991). However, use of direct approaches as described in Tables 4.1, 4.2, 4.3, and 4.4 are further problematic in that it may be difficult to know *a priori* the axes and planes of symmetry of the test sample. This is particularly true in rocks where preferentially aligned cracks and minerals may coexist (e.g., Sayers, 1998). As a consequence there are almost no determinations of elastic constants for symmetries on rocks below orthotropic and even these usually presume some knowledge of the sample symmetry prior to measurement.

Elastic Stiffness	Isotropic	Cubic
C_{11}	$\rho\nu_P^2$ along any $\overrightarrow{n}$	$\rho\nu_P^2$ along any symmetry axis
C_{22}	same as C_{11}	same as C_{11}
C_{33}	same as C_{11}	same as C_{11}
C_{44}	$\rho\nu_S^2$ along any $\overrightarrow{n}$	$\rho\nu_S^2$ along any symmetry axis
C_{55}	same as C_{44}	same as C_{44}
C_{66}	same as C_{44}	same as C_{44}
C_{12}	$\rho\left(\nu_P^2 - \nu_S^2\right)$ along any $\overrightarrow{n}$	$2\rho\nu_P^2 - 2C_{44} - C_{11}$ along $\overrightarrow{n} =$ $[0, \pm1/\sqrt{2}, \pm1/\sqrt{2}]$, $[\pm1/\sqrt{2}, 0, \pm1/\sqrt{2}]$, or $[\pm1/\sqrt{2}, \pm1/\sqrt{2}, 0]$
C_{13}	same as C_{12}	same as C_{12}
C_{23}	same as C_{12}	same as C_{12}
C_{14}	0	0
C_{15}	0	0
C_{16}	0	0
C_{24}	0	0
C_{25}	0	0
C_{26}	0	0
C_{34}	0	0
C_{35}	0	0
C_{36}	0	0
C_{45}	0	0
C_{46}	0	0
C_{56}	0	0

Table 4.1: General summary of how various elastic constants are directly determined from phase velocity measurements for isotropic and cubic media.

Elastic Stiffness	Hexagonal
C_{11}	$\rho\nu_P^2$ along any $\vec{n}$ within $x-y$ plane
C_{22}	same as C_{11}
C_{33}	$\rho\nu_P^2$ along $\vec{n} = [0, 0, \pm 1]$
C_{44}	$\rho\nu_S^2$ with polarization $[0, 0, \pm 1]$ along any $\vec{n}$ within $x-y$ plane
C_{55}	same as C_{44}
C_{66}	$\rho\nu_S^2$ with polarization $[0, \pm 1, 0]$ along $\vec{n} = [\pm 1, 0, 0]$ or with polarization $[\pm 1, 0, 0]$ along $\vec{n} = [0, \pm 1, 0]$
C_{12}	C_{11}-$2C_{66}$
C_{13}	$-C_{44} - \sqrt{(C_{11}+C_{44}-2\rho\nu_P^2)(C_{33}+C_{44}-2\rho\nu_P^2)}$ along $\vec{n} = [0, \pm/\sqrt{2}, \pm/\sqrt{2}]$ or $[\pm/\sqrt{2}, 0, \pm/\sqrt{2}]$
C_{23}	same as C_{13}
C_{14}	0
C_{15}	0
C_{16}	0
C_{24}	0
C_{25}	0
C_{26}	0
C_{34}	0
C_{35}	0
C_{36}	0
C_{45}	0
C_{46}	0
C_{56}	0

Table 4.2: General summary of how various elastic constants are directly determined from phase velocity measurements for a hexagonal media.

Elastic Stiffness	Orthorhombic
C_{11}	ρv_P^2 along $\overrightarrow{n}$ = [± 1, 0, 0]
C_{22}	ρv_P^2 along $\overrightarrow{n}$ = [0, ± 1, 0]
C_{33}	ρv_P^2 along $\overrightarrow{n}$ = [0, 0, ± 1]
C_{44}	ρv_S^2 with polarization [0, 0, ± 1] along $\overrightarrow{n}$ = [0, ±, 0] or with polarization [0, ± 1, 0] along $\overrightarrow{n}$ = [0, 0, ± 1]
C_{55}	ρv_S^2 with polarization [0, 0, ± 1] along $\overrightarrow{n}$ = [± 1, 0, 0] or with polarization [± 1, 0, 0] along $\overrightarrow{n}$ = [0, 0, ± 1]
C_{66}	ρv_S^2 with polarization [± 1, 0, 0] along $\overrightarrow{n}$ = [0, ± 1, 0] or with polarization [0, ± 1, 0] along $\overrightarrow{n}$ = [± 1, 0, 0]
C_{12}	$-C_{66} - \sqrt{(C_{11} + C_{66} - 2\rho v_P^2)(C_{22} + C_{66} - 2\rho v_P^2)}$ along $\overrightarrow{n} = [\pm/\sqrt{2}, \pm/\sqrt{2}, 0]$
C_{13}	$-C_{55} - \sqrt{(C_{11} + C_{55} - 2\rho v_P^2)(C_{33} + C_{55} - 2\rho v_P^2)}$ along $\overrightarrow{n} = [\pm/\sqrt{2}, 0, \pm/\sqrt{2}]$
C_{23}	$-C_{44} - \sqrt{(C_{22} + C_{44} - 2\rho v_P^2)(C_{33} + C_{44} - 2\rho v_P^2)}$ along $\overrightarrow{n} = [0, \pm/\sqrt{2}, \pm/\sqrt{2}]$
C_{14}	0
C_{15}	0
C_{16}	0
C_{24}	0
C_{25}	0
C_{26}	0
C_{34}	0
C_{35}	0
C_{36}	0
C_{45}	0
C_{46}	0
C_{56}	0

Table 4.3: General summary of how various elastic constants are directly determined from phase velocity measurements in an orthorhombic medium.

Elastic Stiffness	Monoclinic	Triclinic
C_{11}	C_{11}	C_{11}
C_{22}	ρv_P^2 along $\overrightarrow{n} = [0, \pm 1, 0]$	C_{22}
C_{33}	C_{33}	C_{33}
C_{44}	ρv_S^2 with polarization $[0, \pm 1, 0]$ along $\overrightarrow{n} = [0, 0, \pm 1]$	C_{44}
C_{55}	C_{55}	C_{55}
C_{66}	ρv_S^2 with polarization $[0, \pm 1, 0]$ along $\overrightarrow{n} = [\pm 1, 0, 0]$	C_{66}
C_{12}	C_{12}	C_{12}
C_{13}	C_{13}	C_{13}
C_{23}	C_{23}	C_{23}
C_{14}	0	C_{14}
C_{15}	C_{15}	C_{15}
C_{16}	0	C_{16}
C_{24}	0	C_{24}
C_{25}	C_{25}	C_{25}
C_{26}	0	C_{26}
C_{34}	0	C_{34}
C_{35}	C_{35}	C_{35}
C_{36}	0	C_{36}
C_{45}	0	C_{45}
C_{46}	$\rho v_S^2 - 1/2\,(C_{66} - C_{44})$ with polarization $[0, \pm 1, 0]$ along $\overrightarrow{n} = [1/\sqrt{2}, 0, 1/\sqrt{2}]$	C_{46}
C_{56}	0	C_{56}

Table 4.4: General summary of how various elastic constants are directly determined from phase velocity measurements in monoclinic and triclinic media.

A lack of knowledge of any principal directions can also be problematic as the form of the elastic stiffness matrix will change depending upon the orientation of the co-ordinate system. When the axes of symmetry are not known, the stiffness matrix that is determined may appear to be rotated. For example, the illustrative but physically realizable stiffness matrix for a hypothetical orthorhombic material viewed from a co-ordinate frame rotated only 10° from the material's symmetry axes (Table 4.6) is more complicated than when viewed from the symmetry axes co-ordinate frame (Table 4.5). In fact, a face value examination of Table 4.6 might suggest the material has monoclinic symmetry.

C_{IJ}	J = 1	J = 2	J = 3	J = 4	J = 5	J = 6
I = 1	9	3	2	0	0	0
I = 2	3	8	1	0	0	0
I = 3	2	1	7	0	0	0
I = 4	0	0	0	6	0	0
I = 5	0	0	0	0	5	0
I = 6	0	0	0	0	0	4

Table 4.5: Elastic constants of an imaginary orthorhombic material before rotation as represented in a principal x-y-z frame.

It is important to ask what minimal set of phase velocity observations is necessary to adequately determine the full set of elastic constants. According to Ditri (1994) phase velocities must be obtained in a minimum of 3 orthogonal planes to obtain sufficient information so that all 21 elastic constants may be determined. These 3 planes need not be oriented along any principal axis directions, but must be orthogonal. To effectively recover the elastic constants in each of these planes of investigation, all 3 modes of propagation should be employed in 3 well-chosen directions of propagation, even though there may be

C_{IJ}	J = 1	J = 2	J = 3	J = 4	J = 5	J = 6
I = 1	9.1736	2.9397	1.7660	0	-0.4718	0
I = 2	2.9397	8.0000	1.0603	0	0.3420	0
I = 3	1.7660	1.0603	7.2943	0	0.8138	0
I = 4	0	0	0	5.9397	0	-0.3420
I = 5	-0.4718	0.3420	0.8138	0	4.7660	0
I = 6	0	0	0	-0.3420	0	4.0603

Table 4.6: Elastic constants of an imaginary orthorhombic material after 10° rotation about the $y-axis$.

some redundancy in the measurements when all 3 planes are considered. Ditri (1994) assumes that the particle motion polarization is known perfectly and that there is adequate data coverage. These assumptions may not be valid in our experimental set up. Ditri's method recovers 15 elastic constants from measurements within any given single plane and leaves 6 elastic constants undiscovered. All 21 elastic constants can be obtained from measurements of P and S phase velocities in 3 mutually orthogonal planes through the sample.

4.4 Experimental Phase-Velocity Measurements

4.4.1 Plane-wave Decomposition

Before continuing further, it is important to reiterate that the phase velocities referred to above are plane-wave velocities. Although these will be close to the group, or ray, velocity as would usually be determined by picking of travel time between a point source and a receiver in anisotropic materials, the group and phase velocities do not in general have the same magnitude. Measuring plane waves in a laboratory or field setting is not straightforward or even physically possible. To overcome this difficulty we employed plane wave decomposition ($\tau - p$ transform) to obtain phase velocities from a series of observed traces. The essential components of the phase velocity determination method are previously described (Kebaili and Schmitt, 1997). The method is most easily employed on a rectangular prism of the material. Essentially, a closely spaced linear array of specially constructed P, SV, or SH mode transducers detect the elastic wave pulses from at least two coplanar source transducers on the side of the block. (Figure 4.1). P and SV refer to those polarizations that lie nearly parallel to this sagittal plane while SH indicate shear polarization nearly perpendicular to the sagittal plane. The sets of arrival times from each of the two transducers yield hyperbolic-like offset versus travel-time curves in the $x - t$ domain which transform to ellipse-like curves in the $\tau - p$ domain after plane wave decomposition. If the block of material is homogenous but anisotropic, then at known horizontal slowness $p\,(= \sin(\theta)/\nu)$ the vertical slowness q (Kebaili & Schmitt, 1997) is

$$q(p) = \frac{\tau_2(p) - \tau_1(p)}{z_2 - z_1}, \tag{4.5}$$

where τ_1 and τ_1 are the intercept times at constant p corresponding to the $\tau - p$ curves for the sources at depths z_1 and z_2, respectively. In an anisotropic material, the vertical slowness q also depends on the phase propagation angle θ within the plane. The phase velocity ν is then

$$\nu(\theta) = \left(q^2(\theta) + p^2(\theta)\right)^{-1/2}, \tag{4.6}$$

propagating at the phase propagation angle within the sagittal plane:

$$\theta = \arctan\left(\frac{p}{q}\right). \tag{4.7}$$

Details on the transducer construction and characterization and the level of experimental error may be found in Chapter 3 and Mah & Schmitt (2001b) where the methodology was evaluated on isotropic soda-lime glass. Three types of transducers have been developed. Each provide enhanced detection and reception of P, SV, or SH mode polarizations. Tests of the $\tau - p$ method on homogeneous glass blocks indicate that phase velocities are determined to better than 1 % uncertainty in such an isotropic homogeneous, high quality factor medium.

It must be noted that there are limitations to the $\tau - p$ methodology. It has been stated already that group and phase velocities do not necessarily coincide. Modelling of the wave surfaces (i.e., representing group velocities) in various strongly anisotropic media shows that these surfaces may contain cusps or caustics (e.g., Carcione, 1990; White, 1982). These cusps are manifest as a triplication in the SV waveforms profile (Musgrave, 1970). Testing of the $\tau - p$ methodology on synthetic travel time data containing severe cusps shows that

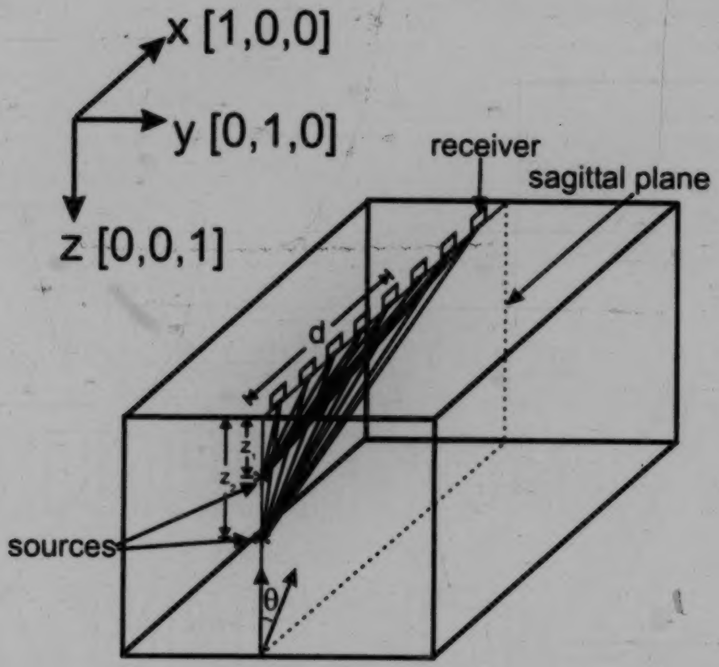

Figure 4.1: View of the $x-z$ sagittal plane containing sources and receivers with ray paths for a homogeneous anisotropic medium. The angle of phase velocity propagation direction θ within this plane is shown. The offset, d, of the receivers is shown as well. The depth of sources 1 and 2 is shown as z_1 and z_2, respectively.

the methodology does not yield valid phase velocity along directions where these cusps are present. However, from direct observations of the travel times and modelling results, there are no readily apparent cusps present in the trace profiles.

4.4.2 Sample Characterization

The composite material used in these experiments was a large block 66 cm × 27 cm × 17 cm of Grade CE Phenolic with a mass density of 1395 kg/m^3 milled to provide flat and perpendicular surfaces paralleling the layering ($x-y$ plane or $z-$

$axis$), the warp ($x - axis$), and the weave ($y - axis$) (Chapter 3; Mah & Schmitt (2001a)). This material is basically composed of layers of canvas held together by a phenol resin. Since each layer of canvas has definite texture as defined by the directions of the straight and woven fibers termed warp and weft, respectively, this gives two mirror planes of symmetry (Figure 4.2). Approximately 20 fiber mats per cm are stacked together within the material (Figure 4.2) giving a third mirror plane of symmetry. This layering, warp, and weave reduce the symmetry to orthorhombic (Karayaka & Kurath, 1994) with a substantial anisotropy in planes parallel to the $z - axis$ (Figure 4.2) but with a much weaker anisotropy within the $x - y$ plane (Chapter 3; Mah & Schmitt, 2001a). If phenolic is indeed orthorhombic, it will have a set of natural symmetry axes. These axes will be orthogonal to each other and will be perpendicular to the mirror planes of symmetry present in the material.

4.4.3 Experimental Configuration

The transducers were placed on the sample in a coplanar array as shown in Figure 4.1 with two transmitters on one side at a spacing of 2.0 ± 0.1 cm and 4.0 ± 0.1 cm, respectively. The receiving transducers are mounted in a linear array on the adjacent perpendicular surface at a spacing of 0.5 ± 0.1 cm. The source transducers were activated with a 300 Volt, 10 ns rise time spike and the corresponding response of the receiver transducers was digitally acquired by a high speed sampling oscilloscope at a rate of 8 ns/sample. Random noise was a significant problem due to the small sizes of the transducers. Approximately 2000 individual pulses were stacked on the oscilloscope and the sample was magnetically shielded to improve the data quality.

Only simple processing of the waveforms was carried out to reduce the effects of trigger noise, spurious reflections and other mode arrivals. The high amplitude

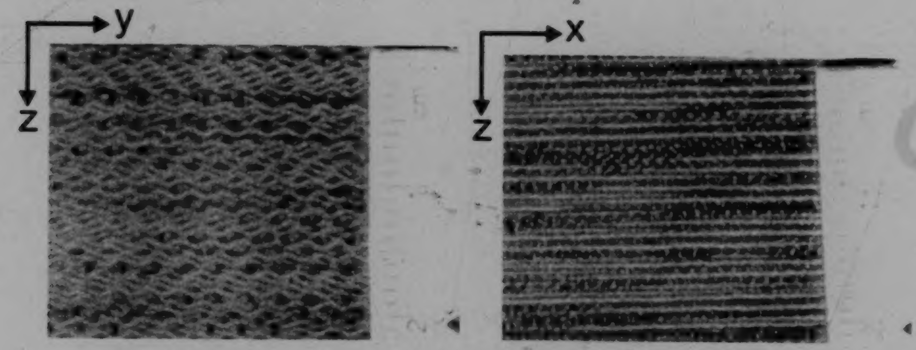

(a) Cross-section in the $y - z$ plane with scale bar in cm.

(b) Cross-section in the $x - z$ plane with scale bar in cm.

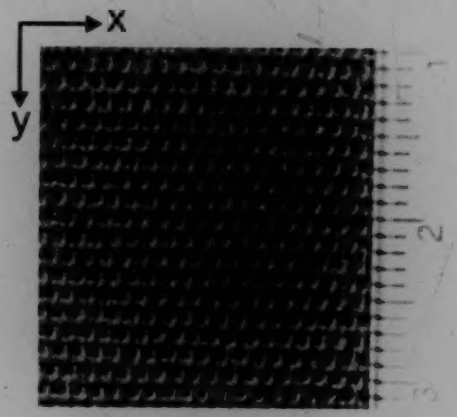

(c) Cross-section in the $x - y$ plane with scale bar in cm.

Figure 4.2: Cross-section of the phenolic sample.

trigger noise was simply muted as were portions of the trace before and after the desired arrivals by modulation with a simple tapered window. These traces were then bandpass filtered (bandpass = 0 MHz - 0.15 MHz - 1.20 MHz - 1.70 MHz) to remove any of the remaining high frequency noise since the peak frequency of the signal is about 0.8 MHz.

4.5 Results and Discussion

4.5.1 Phase Velocities

Special arrays of near-point source piezoelectric transducers were employed within 5 different planes on the composite material oriented with respect to the texture in the $x-z$, the $y-z$, the $x-y$, the $xy-z$ (a diagonal plane containing the z axis rotated 45° from the $x-axis$), and the $xz-y$ plane (a diagonal plane containing the $y-axis$ rotated 46° from the $x-axis$) (Figure 4.3). The three different P, SV, and SH polarizations at two different source depths were employed in each of these planes resulting in a total of 30 individual sets of data composed of 1004 source-receiver combinations. 779 high-quality measurements of the phase velocity were determined from analysis of the resulting $\tau-p$ curves.

In the $x-z$ array, the P-wave transducers were arranged with the sources at 2 cm and 4 cm depth on the $y-z$ surface parallel to the $z-axis$ and the receivers mounted on the $x-y$ surface parallel to the $x-axis$ (Figure 4.1). The processed waveforms (Figure 4.4(a)) for the $xz-y$ array (plane 5) have a hyperbolic-like moveout with increasing offset and show only a modest degree of waveform spreading. The $\tau-p$ transform (Figure 4.4(b)) has an ellipse-like shape as expected. The vertical slowness q is obtained as a function of the horizontal slowness p from the $\tau-p$ transform using data from another array at a differing source depth and Equation 4.5.

From the complete set of $\tau-p$ transformations, the P, SV, and SH phase velocities were obtained (Figures 4.8 and 4.9) in the 5 planes studied. However, there were limitations to the experimental setup. It could not fully interrogate small incident angles (Chapter 3; Mah & Schmitt, 2001a). When tested on an isotropic material, valid phase velocities were obtained between phase angles θ from 5° to 70° (Chapter 3; Mah & Schmitt, 2001b). When the $q-p$ plot from the data in plane 5 was converted to $\nu-\theta$ using Equations 4.6 and 4.7, the phase

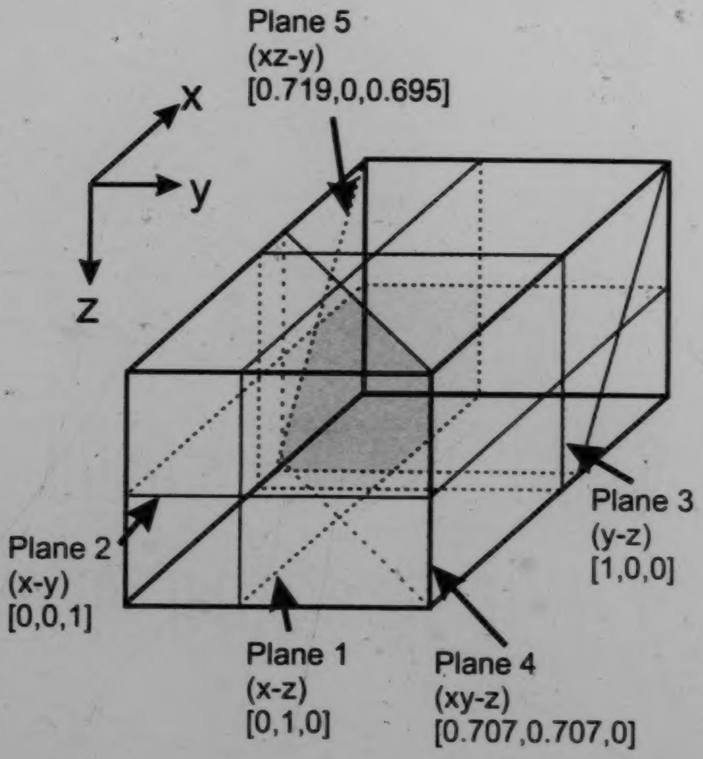

Figure 4.3: The five planes on the composite block in which arrays were prepared and designated as x-z, x-y, y-z, xy-z (i.e., diagonal plane 4), and xz-y (i.e., diagonal plane 5).

velocity increased from 2843 ± 80 m/s to 3451 ± 80 m/s as the propagation direction varies from near vertical to subhorizontal (Figure 4.9).

Due to strong coupling, both the P and SV modes were generated at the same time, thus complicating analysis of the SV mode results. By increasing the depth of the sources on the side of the block to 4 cm and 6 cm (Figure 4.1), the P and SV wave separate sufficiently to be observed separately (Figure 4.5). After the P-wave arrivals and the trigger noise were muted and after application of bandpass filtering, the SV-wave arrival could be clearly seen (Figure 4.6(a)). At these

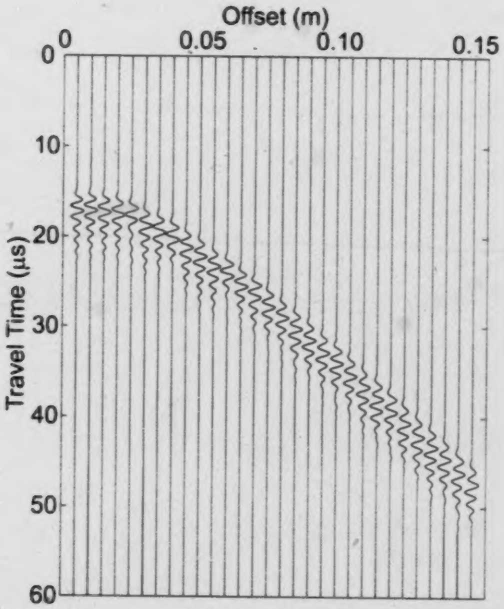

(a) Amplitude versus time traces with offset for the 4.0 cm deep P-wave source.

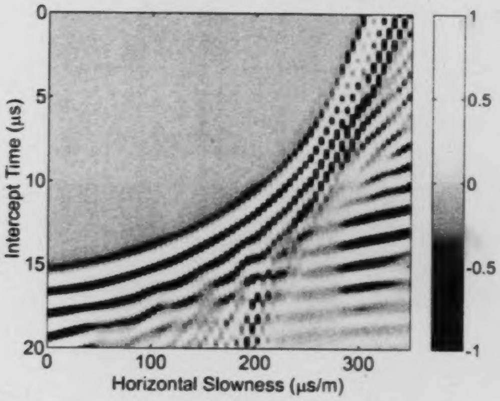

(b) $\tau - p$ transform of (a) from which the series of τ_1 (p) is obtained with an intercept time (τ) increment of 8 ns and horizontal slowness (p) increment of 2.5 μs/m.

Figure 4.4: The P-wave results from the $xz - y$ plane.

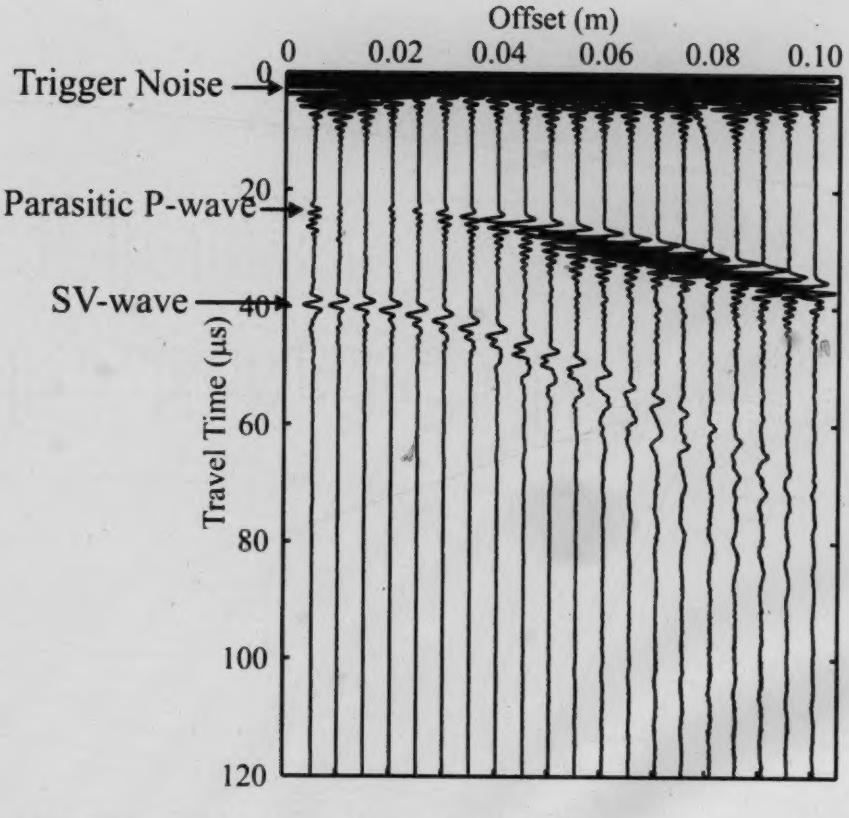

Figure 4.5: Unprocessed SV mode arrivals before muting, windowing, and band-pass filtering.

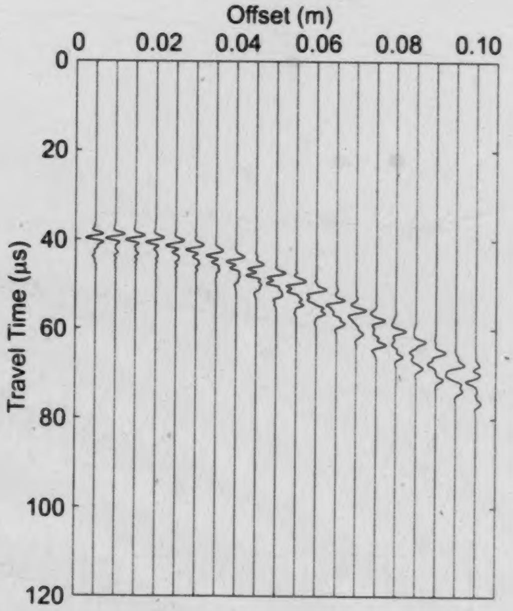

(a) Isolated SV mode arrivals after muting of P mode arrivals followed by peak amplitude normalization.

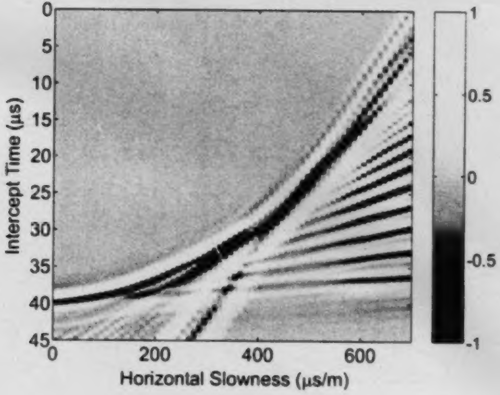

(b) Peak amplitude normalization of the $\tau - p$ transform via slant-stack of (a) with an intercept time (τ) increment of 8 ns and horizontal slowness (p) increment of 5 μs/m.

Figure 4.6: The SV-wave results from the $xz - y$ plane.

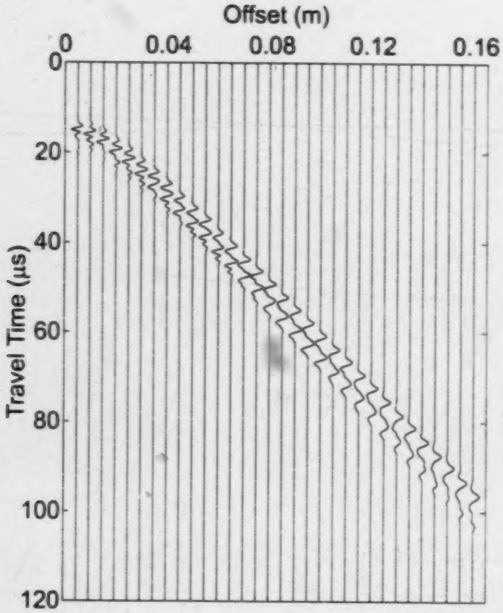

(a) The SH mode records for the 2.0 cm deep source.

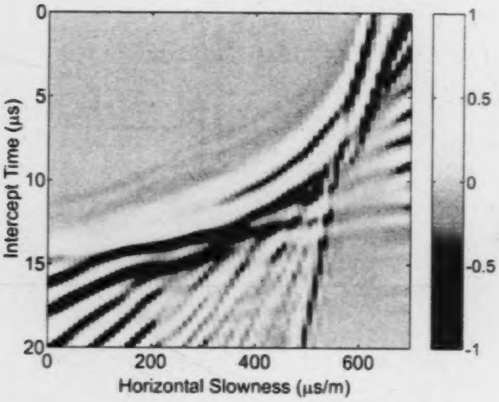

(b) The corresponding $\tau - p$ transformation of (a) with an intercept time (τ) increment of 8 ns and horizontal slowness (p) increment of 5 μs/m.

Figure 4.7: The SH-wave results from the $xz - y$ plane.

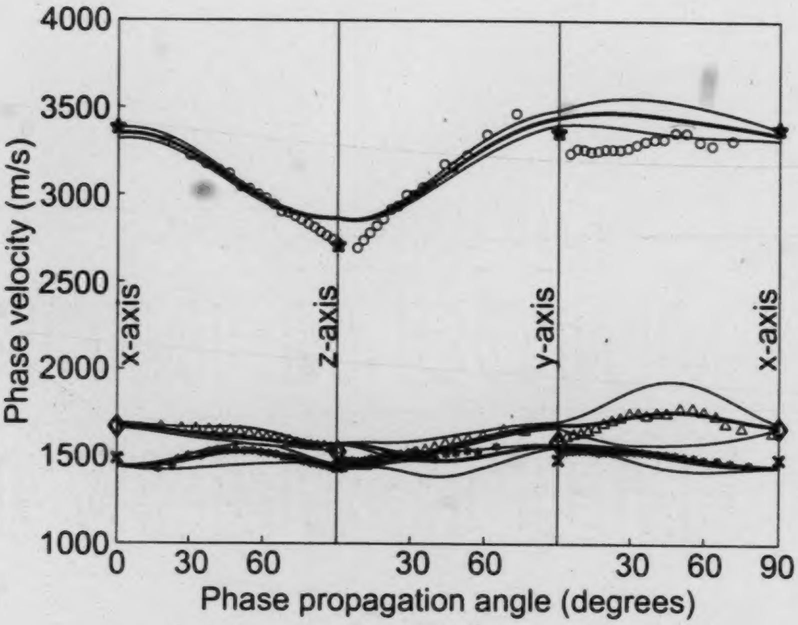

Figure 4.8: A composite of phase velocities in the x-z, y-z, and x-y planes where the direction of the x-z plane phase velocities has been reversed in order to put them in the proper orientation. Summary of the phase velocities versus propagation angle θ obtained from the $\tau - p$ analysis of the arrivals. Only every third data point has been plotted due to the high density of the data. Symbols denote the velocities of the P-wave (circles), the S1-wave (triangles), and the S2-wave (stars) polarizations. The S1-wave is the fast shear wave and is equivalent to the SV-wave while the S2-wave is the slow shear wave and corresponds to the SH-wave. Pentagrams, diamonds, and Xs denote the phase velocities as determined by large transducers for the P-wave, S1-wave, and S2-wave polarizations, respectively. The thick solid lines are the corresponding theoretical phase velocities as calculated from the inversion results. The shaded bands are the uncertainties in the phase velocities propagated through from the uncertainties in the elastic constants.

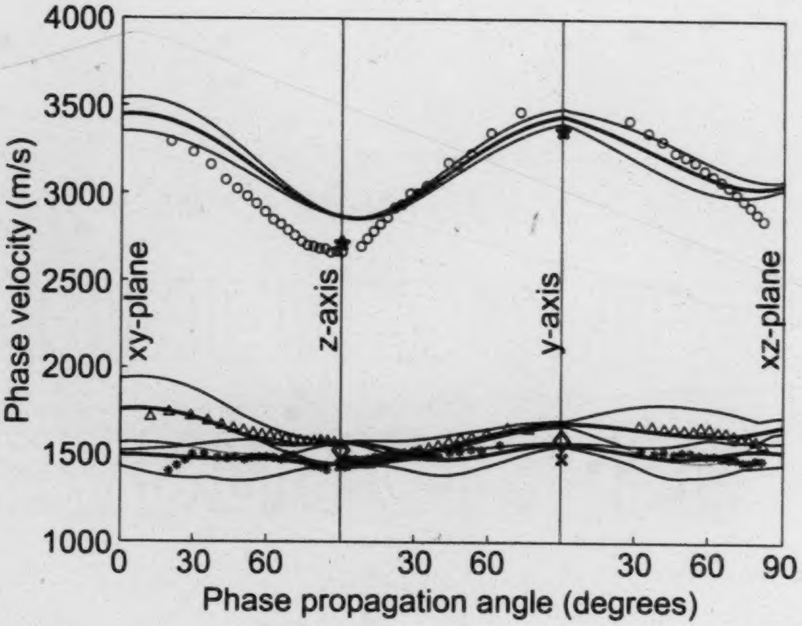

Figure 4.9: A composite of phase velocities in the xy-z, y-z, and xz-y planes where the direction of the xy-z and xz-y planes phase velocities has been reversed in order to put them in the proper orientation. Summary of the phase velocities versus propagation angle θ obtained from the $\tau - p$ analysis of the arrivals. Only every third data point has been plotted due to the high density of the data. Symbols denote the velocities of the P-wave (circles), the S1-wave (triangles), and the S2-wave (stars) polarizations. The S1-wave is the fast shear wave and is equivalent to the SV-wave while the S2-wave is the slow shear wave and corresponds to the SH-wave. Pentagrams, diamonds, and Xs denote the phase velocities as determined by large transducers for the P-wave, S1-wave, and S2-wave polarizations, respectively. The thick solid lines are the corresponding theoretical phase velocities as calculated from the inversion results. The shaded bands are the uncertainties in the phase velocities propagated through from the uncertainties in the elastic constants.

greater source depths, the limitations of the methodology at steep angles became more apparent such as the $\tau - p$ curve having a straight tail (Figure 4.6(b)) instead of being theoretically elliptic-like or curved. Though the SH mode traces were cleaner (Figure 4.7(a)) and the corresponding $\tau - p$ transform was more elliptical (Figure 4.7(b)), there were still more problems. There was more noticeable spreading of the pulse with propagation distance (Figure 4.7 (a) and (b)).

4.5.2 Inversion for Elastic Coefficients

An inversion method was developed to obtain the elastic coefficients from the observed phase velocities and propagation angles. The iterative inversion employs both the nearest neighbour and the secant methods (Kincaid and Cheney, 1996). The inversion started with the calculation of the phase velocities using both Equations 4.3 and 4.4 from an initial guess of the elastic coefficients. The differences between the calculated phase velocities and the observed phase velocities were then determined. Using a simulated annealing type approach, the elastic coefficients were perturbed and the differences between the calculated phase velocities and observed phase velocities were redetermined and solutions that reduced this difference were accepted. Gradually, the differences between the calculated phase velocities with those observed were then minimized. Testing of the algorithm on forward modelled hypothetical phase velocities suggests the method is accurate and stable. The inversion for a set of noise free phase velocities reproduces the original elastic coefficients to within 0.01 % while the inversion of a set of phase velocities with random errors of up to 10 % reproduce the elastic coefficients to within 3 %. The robustness of this inversion was previously tested in Chapter 3 and Mah & Schmitt (2001a) by calculating the phase velocities from the inverted elastic coefficients and plotting these theoretical phase velocities against the original input phase velocities. This has also been done for the phase velocities in this work assuming a triclinic symmetry (Figures 4.8 and 4.9). Using the Monte Carlo method, the errors in the theoretical phase velocities were calculated from the uncertainties in the elastic constants and are displayed in Figures 4.8 and 4.9.

The ability of this inversion algorithm to find the global minimum in the differences between the phase velocities was tested by comparing the results as found by a simulated annealing algorithm similar to the ones outlined by Kirkpatrick et al. (1983) and Szu & Hartley (1987). Comparisons of the results from both inversion methods show no significant differences indicating that a global minimum was indeed reached by the non-linear inversion.

There are some limitations to the inversion methodology. If there are extremely complex polarizations present in the material, the observer may have some difficulty in determining which of the two shear wave polarizations is the SH-wave polarization and which is the SV-wave polarization especially if the wave surfaces of the two shear polarizations intersect or "kiss". This may lead to erroneous elastic stiffness determination. On the basis of the present results and that of others (Vestrum, 1994), the shear polarizations in phenolic are not overly complex. If the material has a more complex anisotropy, this methodology may fail. However, the composite material studied here is likely more anisotropic than most natural rocks and earth materials.

In this inversion, no assumptions were made about the symmetry of the material and the inversion may solve for all 21 independent elastic stiffnesses. In other words, no a priori information is known about the symmetry or position of the coordinate axes. Initially the inversion was applied to all 779 values of phase velocity versus phase angle as summarized in Figures 4.8 and 4.9. Two greatly different seed values were used: one in which all the elastic coefficients were initially zero and a second which used those provided by Vestrum (1994) on a similar material. The iterations ceased once 500 iterations of the inversion were performed. The calculation typically required only 520 seconds on a 266 MHz (ca. 1998) machine using a high level programming language.

The inverted results are shown in Table 4.10 in Voigt notation (Case 4, Triclinic) and statistical analysis shows the elastic constants are accurate to within 3.8 %. The statistical analysis consisted mainly of introducing random errors in the phase velocities and observing the corresponding changes in the elastic constants. As can be seen in Table 4.10 (Case 4, Triclinic), the values of the non-orthorhombic elastic stiffnesses are quite small relative to those that fill the non-zero positions for perfectly orthorhombic elastic stiffnesses. This may be due in part to the coordinate axes being very closely aligned with the symmetry axes of the material. This implies the material phenolic is quite close to being orthorhombic in nature as is expected given its textural symmetry (Figure 4.2). Even if the coordinate axes chosen were not aligned with the symmetry axes, a simple series of rotations could be performed that would align the coordinate axes of the elastic stiffness tensor with the symmetry axes. The choice of the seeds was not important as both initial guesses approached the solution within 300 iterations and the final difference between the solutions differed by only 5 MPa or less than 0.2 %.

Orthorhombic

$$\begin{bmatrix} 15.9 & 7 & 6.8 & 0 & 0 & 0 \\ 7 & 15.5 & 6.9 & 0 & 0 & 0 \\ 6.8 & 6.9 & 11.1 & 0 & 0 & 0 \\ 0 & 0 & 0 & 3.4 & 0 & 0 \\ 0 & 0 & 0 & 0 & 3 & 0 \\ 0 & 0 & 0 & 0 & 0 & 3.8 \end{bmatrix}$$

error = 32.5 m/s

Monoclinic

$$\begin{bmatrix} 15.5 & 7 & 6.4 & 0 & 0.3 & 0 \\ 7 & 15.6 & 6.8 & 0 & 0.3 & 0 \\ 6.4 & 6.8 & 10.9 & 0 & 0.3 & 0 \\ 0 & 0 & 0 & 3.4 & 0.1 & 0 \\ 0.3 & 0.3 & 0.3 & 0.1 & 3 & 0 \\ 0 & 0 & 0 & 0 & 0 & 3.8 \end{bmatrix}$$

error = 30.6 m/s

Triclinic

$$\begin{bmatrix} 14.9 & 6.3 & 5.2 & 0.7 & 0.9 & -0.5 \\ 6.3 & 14.9 & 5.7 & 0.8 & 1.5 & -0.4 \\ 5.2 & 5.7 & 10 & 0.7 & 0.8 & 0.1 \\ 0.7 & 0.8 & 0.7 & 3.3 & -0.1 & 0.1 \\ 0.9 & 1.5 & 0.8 & -0.1 & 3 & 0.2 \\ -0.5 & -0.4 & 0.1 & 0.1 & 0.2 & 3.7 \end{bmatrix}$$

error = 22.9 m/s

Table 4.7: Elastic stiffnesses in GPa as calculated in Case 1 using velocities only from the 3 orthogonal planes (planes 1, 2, and 3) of the observed phase velocities and assuming different types of symmetry for the inversion. The error associated with each set of elastic constants is the rms error between the experimental phase velocities and the theoretical phase velocities as calculated from that set of elastic constants.

Orthorhombic

$$\begin{bmatrix} 16.4 & 7.1 & 6.6 & 0 & 0 & 0 \\ 7.1 & 15.4 & 6.6 & 0 & 0 & 0 \\ 6.6 & 6.6 & 10.6 & 0 & 0 & 0 \\ 0 & 0 & 0 & 3.4 & 0 & 0 \\ 0 & 0 & 0 & 0 & 3 & 0 \\ 0 & 0 & 0 & 0 & 0 & 3.8 \end{bmatrix}$$

error = 37.6 m/s

Monoclinic

$$\begin{bmatrix} 16.1 & 7.1 & 6.4 & 0 & -0.2 & 0 \\ 7.1 & 15.5 & 6.6 & 0 & 0 & 0 \\ 6.4 & 6.6 & 10.5 & 0 & -0.1 & 0 \\ 0 & 0 & 0 & 3.4 & -0.1 & 0 \\ -0.2 & 0 & -0.1 & -0.1 & 3 & 0 \\ 0 & 0 & 0 & 0 & 0 & 3.8 \end{bmatrix}$$

error = 36.8 m/s

Triclinic

$$\begin{bmatrix} 16.6 & 7.4 & 6.5 & -0.1 & -0.1 & -0.3 \\ 7.4 & 15.5 & 6.4 & -0.4 & 0.1 & -0.3 \\ 6.5 & 6.4 & 10.3 & -0.2 & -0.2 & -0.5 \\ -0.1 & -0.4 & -0.2 & 3.3 & 0 & -0.1 \\ -0.1 & 0.1 & -0.2 & 0 & 3 & 0 \\ -0.3 & -0.3 & -0.5 & -0.1 & 0 & 3.9 \end{bmatrix}$$

error = 32.9 m/s

Table 4.8: Elastic stiffnesses in GPa as calculated in Case 2 using velocities from the 3 orthogonal planes and one diagonal plane (planes 1, 2, 3, and 4) and assuming different types of symmetry for the inversion. The error associated with each set of elastic constants is the rms error between the experimental phase velocities and the theoretical phase velocities as calculated from that set of elastic constants.

Orthorhombic

$$\begin{bmatrix} 15.3 & 7.1 & 6.5 & 0 & 0 & 0 \\ 7.1 & 15.8 & 6.9 & 0 & 0 & 0 \\ 6.5 & 6.9 & 11 & 0 & 0 & 0 \\ 0 & 0 & 0 & 3.4 & 0 & 0 \\ 0 & 0 & 0 & 0 & 2.9 & 0 \\ 0 & 0 & 0 & 0 & 0 & 3.8 \end{bmatrix}$$

error = 42.8 m/s

Monoclinic

$$\begin{bmatrix} 15.3 & 7.1 & 6.4 & 0 & 0.4 & 0 \\ 7.1 & 16 & 6.9 & 0 & 0.2 & 0 \\ 6.4 & 6.9 & 10.8 & 0 & 0.3 & 0 \\ 0 & 0 & 0 & 3.4 & 0 & 0 \\ 0.4 & 0.2 & 0.3 & 0 & 2.9 & 0 \\ 0 & 0 & 0 & 0 & 0 & 3.9 \end{bmatrix}$$

error = 35.8 m/s

Triclinic

$$\begin{bmatrix} 14.8 & 6.2 & 5.4 & 1.2 & 0.9 & -0.5 \\ 6.2 & 14.7 & 5.5 & 1 & 0.9 & -0.6 \\ 5.4 & 5.5 & 9.9 & 0.8 & 0.7 & -0.7 \\ 1.2 & 1 & 0.8 & 3.3 & 0 & 0.1 \\ 0.9 & 0.9 & 0.7 & 0 & 3 & 0 \\ -0.5 & -0.6 & -0.7 & 0.1 & 0 & 3.8 \end{bmatrix}$$

error = 24.3 m/s

Table 4.9: Elastic stiffnesses in GPa as calculated in Case 3 using velocities from the 3 orthogonal planes and one diagonal plane (planes 1, 2, 3, and 5) and assuming different types of symmetry for the inversion. The error associated with each set of elastic constants is the rms error between the experimental phase velocities and the theoretical phase velocities as calculated from that set of elastic constants.

Orthorhombic

$$\begin{bmatrix} 15.3 & 7.1 & 6.8 & 0 & 0 & 0 \\ 7.1 & 15.8 & 7.3 & 0 & 0 & 0 \\ 6.8 & 7.3 & 11.5 & 0 & 0 & 0 \\ 0 & 0 & 0 & 3.4 & 0 & 0 \\ 0 & 0 & 0 & 0 & 2.9 & 0 \\ 0 & 0 & 0 & 0 & 0 & 3.9 \end{bmatrix}$$

$\text{error} = 54.4$ m/s

Monoclinic

$$\begin{bmatrix} 15.3 & 7 & 6.8 & 0 & 0.2 & 0 \\ 7 & 15.8 & 7.3 & 0 & -0.2 & 0 \\ 6.8 & 7.3 & 11.5 & 0 & -0.1 & 0 \\ 0 & 0 & 0 & 3.4 & -0.1 & 0 \\ 0.2 & -0.2 & -0.1 & -0.1 & 2.9 & 0 \\ 0 & 0 & 0 & 0 & 0 & 3.9 \end{bmatrix}$$

$\text{error} = 52.9$ m/s

Triclinic

$$\begin{bmatrix} 15.6 & 7.5 & 6.7 & 0.1 & 0.2 & 0.4 \\ 7.5 & 16.5 & 7.6 & -0.4 & -0.1 & 0.4 \\ 6.7 & 7.6 & 11.4 & -0.3 & 0 & 0.4 \\ 0.1 & -0.4 & -0.3 & 3.4 & 0 & -0.1 \\ 0.2 & -0.1 & 0 & 0 & 2.9 & -0.1 \\ 0.4 & 0.4 & 0.4 & -0.1 & -0.1 & 3.9 \end{bmatrix}$$

$\text{error} = 43.7$ m/s

Table 4.10: Elastic stiffnesses in GPa as calculated in Case 4 using velocities from all 5 planes (planes 1, 2, 3, 4, and 5) and assuming different types of symmetry for the inversion. The error associated with each set of elastic constants is the rms error between the experimental phase velocities and the theoretical phase velocities as calculated from that set of elastic constants.

Other workers have inverted observed velocities for elastic stiffnesses but the inversion here differs significantly from their earlier attempts. Arts et al. (1991) assumed the material was triclinic and solved for all 21 elastic parameters using the measurements of the phase velocities and the corresponding polarizations for various directions of propagation. In order to achieve this, their experiment required a specialized machining of a sample into a multifaceted polyhedron with 18 parallel faces. Okoye et al. (1996) studied the material phenolite that shares some similarities with phenolic but is transversely isotropic. Their inversion assumes the material is transversely isotropic and applies a smooth polynomial fitting to the velocities before iteratively applying the least-squares method. Vestrum (1994) tested a machined sphere of phenolic that is similar to the material used in this work. The inversion used an iterative application of Newton's method on group velocities obtained from the sphere. The present inversion requires the phase velocities with the corresponding polarizations for differing directions of propagation as obtained using the $\tau - p$ methodology. The present inversion is applied without the application of a smooth polynomial fitting unlike Okoye et al. (1996). The inversion does use the application of an iterative least-squares inversion similar to Arts et al. (1991) and Okoye et al. (1996) as well as the use of the secant method that is similar to Newton's method used by Vestrum (1994). However, pseudo-random jumps are included to prevent entrapment in localized minima in the residuals, and so differ from the use of damping factors by Vestrum (1994).

In this study, P, SV, and SH phase velocities were obtained in five distinct sagittal planes (Figure 4.3). As noted earlier, velocities need to be obtained in a minimum of three orthogonal planes to determine the 21 elastic stiffnesses (Ditri, 1994). Two additional diagonal planes of measurements were taken to further test the stability of the inversion. Although the general inversion makes no assumptions with respect to the degree of symmetry, additional tests of the inversion did restrict the symmetry to orthorhombic and monoclinic. In orthorhombic symmetry, one assumes that coordinate axes are aligned with the natural symmetry axes present in the material before determining all 9 elastic constants. While in monoclinic symmetry, one assumes that only 1 of the coordinate axes is aligned with the natural symmetry axes present in the material.

Comparison of the elastic constants as determined assuming the different symmetry classes (Tables 4.7, 4.8, 4.9, and 4.10) shows that values for the "non-orthorhombic" elastic stiffnesses are substantially smaller (10 %) than the orthorhombic stiffness. Further, the orthorhombic elastic constants for all 3 symmetry assumptions agree within error. This strongly suggests that the material is orthorhombic in nature and that the inversion method developed does not depend on the level of symmetry assumed. So long as the symmetry used in the inversion is not higher than that for the material, the present analysis suggests that the elastic stiffnesses are adequately sampled.

Bootstrap type tests were run using only subsets of the observed velocities to test the statistical stability of the solution. The inversions were performed again for 4 different subsets of the data (Tables 4.7, 4.8, 4.9, and 4.10). In Case 1, only the 3 mutually orthogonal planes of data were used (i.e., plane 1, plane 2 and plane 3 in Figure 4.3). In Case 2, the 3 mutually orthogonal planes and one of the diagonal planes of data were used. Similarly in Case 3, the 3 mutually orthogonal planes and the remaining diagonal plane of data were used. While in Case 4, all 5 planes of data were used. An rms error between the theoretical and experimental phase velocities was calculated for each set of elastic constants in Tables 4.7, 4.8, 4.9, and 4.10. The better the fit of the elastic constants to the anisotropy present in the data, the lower the rms error. In general, as the amount of data used in the inversion increases, the rms error increases. This unexpected result is due to the inversion attempting to fit the error in the phase velocities and being unable to. When the number of elastic constants or complexity of the anisotropy is increased, the rms error between the theoretical and experimental phase velocities decreases due to the inversion fitting the more complex symmetry present in the data.

In order to test whether this reduction in the rms error is statistically significant, F-tests were performed assuming a 95 % confidence level and a null hypothesis that there was no difference in the results assuming the differing levels of symmetry (Mendenhall (1975)). It was found that this hypothesis was false for all of the comparisons of the differing levels of symmetry except for the comparison of orthorhombic symmetry to monoclinic symmetry in Cases 1, 2, and 4. This means that, for the majority of the results, there was a significant statistical difference in the inversion results when a more complex symmetry was assumed. The elastic constants as determined for different subsets of the data agree within error to the elastic constants as determined with all the data available. While there was adequate data coverage, the orientation of the planes that were investigated did not bias the inversion.

Instead of assuming different levels of symmetry and different subsets of the data, the best solution may be to perform the inversion using all the data available while generally assuming triclinic symmetry. This results in a set of elastic constants that could be progressively transformed by rotation of coordinate axes until the principal directions of a more symmetric material, if they exist, are found. For example, using a brute force search the elastic constants as determined assuming triclinic symmetry using all data available (Case 4) was rotated in order to minimize the "non-orthorhombic" elastic constants. It was found that the elastic constants were essentially in the optimum coordinate system already. This was confirmed by performing the rotations using software provided by an independent source. The elastic constants were already in the optimum coordinate system due to the sample being initially aligned with the visually observable planes of symmetry.

The theoretical phase velocities are forward modelled using the elastic stiffnesses obtained by the triclinic inversion (Tables 4.7, 4.8, 4.9, and 4.10) using all the available data (Case 4) and plotted against the original input phase velocities (Figures 4.8 and 4.9). As can be seen in these plots there are discrepancies between the calculated and input values.

Interestingly, even though the theoretical P-wave phase velocities do not match the experimental P-wave phase velocities near the coordinate axes, the experimental P-wave phase velocities seem to approach the same value at the coordinate axes and especially as they approach the $z - axis$. In order to investigate these discrepancies more thoroughly, large transducers were mounted on a sample of the material in order to simulate the generation of plane waves propagating in the material. Pulse transmission measurements where taken and the indirect measurements of the phase velocities were plotted in Figures 4.8 and 4.9 as Xs, diamonds and pentagrams. The plane wave velocities as determined by the $\tau - p$ method closely matched the plane velocities as determined by the large transducers along the $z - axis$ and $x - axis$. However, there are large discrepancies in the phase velocities along the $y - axis$.

Some of the discrepancies may be due to transducer aperture effect or P-SV coupling. Since the P mode generally has a higher velocity and consequently a larger wavelength, one concern was that near-field effects might influence the receivers. To test whether this was the case, the P-mode polarization experiments were redone in planes 1 and 3 using source depths of 4 cm, 6 cm, and 8 cm. The phase velocities obtained agreed well with the phase velocity data previously obtained using sources at 2 cm and 4 cm depth. This implies that the wavefield is being sampled in the far-field and not in the near field.

Most likely these discrepancies are due to increased dispersion in the y-direction as compared to the other directions since there are discrepancies in the phase velocities for all 3 modes of propagation. Anisotropic dispersion as noted by Carcione & Cavallini (1995) may be an explanation for the increased dispersion in the y-direction. This added level of complexity has not been accounted for in the inversion and may cause the inversion to try and fit data that it possibly cannot. This may lead to the large discrepancies between the theoretical and experimental phase velocities not only in the y direction but in other directions as well.

Although, the elastic coefficients were readily determined from a number of phase velocities in the above inversion assuming differing symmetries and using different subsets of the data, some experimental problems remain. The most important is the observation of substantial dispersion as previously noted in Chapter 3 and Mah & Schmitt (2001a). This dispersion must have some influence on the accuracy of the $\tau - p$ method and consequently must affect the determination of the elastic coefficients. Although components of the dispersion may be due to intrinsic attenuation, it is also likely that part of the effect may be a consequence of wave propagation through the layered structure of the composite. Although difficult to quantify, there appears to be less dispersion in the $x - y$ plane waveforms suggesting that the observed dispersion is symptomatic of the layering. Indeed, such layering induced dispersion is not unexpected especially once the dimensions of the layers approach the wavelength of the illuminating elastic wave energy (e.g., Helbig, 1984). This may be the case in the present material as the wavelength of the shear waves approach 2 mm which is only a factor of 4 greater than the nominal 0.5 mm scale of the layering.

Other potential problems reside with the difficulties of cleanly separating different arrivals and the unavoidable P-SV mode coupling. This is due to the complexities in polarization of the different modes in an anisotropic medium (e.g., Crampin, 1978) and the related imperfections of the transmitting and receiving transducers. A final problem is that only a limited range of angles may be covered with the transducer arrays and for equal spacing of transducers this will introduce a sampling bias towards the far offset transducers that could be accounted for in future tests of the method.

4.6 Conclusions

Phase velocities were determined directly as a function of phase propagation angle on an anisotropic composite material. Special, near-point source transducers were developed to impart and receive different elastic wave energies. These transducers were designated as P, SV, and SH to indicate the primary mode of particle motion that each different transducer was sensitive to. However, it must be noted that such pure modes do not generally propagate in anisotropic media where more complex polarizations exist and the designations should only be considered as descriptive. Clean P and SH modes could be generated and received in both glass and the test anisotropic composite. However, the SV mode is complicated by the coupled nature of P and SV waves and by difficulties experienced by the directionality of SV mode receivers to impart the desired wave energy into the medium. Thirty arrays of these transducers were constructed along 5 strategic planes of the composite material allowing 779 individual P, SV, and SH mode phase velocities to be obtained.

Making no assumption about the symmetry of the phenolic block, twenty-one independent elastic stiffnesses were obtained by a nonlinear inversion procedure. The inversion technique and experimental configuration are not symmetry dependent so long as the symmetry assumed and data collected adequately describe the material. Despite the paucity of constricting assumptions used in the inversion, the twenty-one independent elastic stiffnesses suggest the composite is predominantly orthorhombic. Phase velocities then calculated in a forward manner using the obtained elastic constants are in generally good agreement with those observed. However, some discrepancies remain and these may be due in part to the fact that there is very noticeable dispersion in all the waveform modes (i.e., pulse spreading with increasing propagation distance) particularly for the SV mode. This dispersion is not accounted for in the present $\tau - p$ velocity determination method and may contribute in part to the discrepancies.

Future technical work will focus on development of the technique in order to make it less cumbersome and so that it can be employed under pressure. One great advantage of the present methodology is that it can be applied to samples of simple shape such as rectangular prisms and even cylinders. The latter will be particularly useful in the context of determining anisotropy in shales which may often be assumed to be transversely isotropic using core samples with a minimum of additional preparation. Of more fundamental concern, however, is the potential for experimental tests of the trade-off between wave velocity anisotropy, dispersion, and scale in layered anisotropic media; this has implications beyond laboratory determination of elastic properties. The $\tau - p$ method will aid in such fundamental experimental studies of layered media.

References

Arts, R. J., Rasolofosaon, P. N. J., and Zinszner, B. E., 1991, Complete inversion of the anisotropic elastic tensor in rocks: Experiment versus Theory, 61st Ann. Internat. Mtg., Soc. Expl. Geophys., Expanded Abstracts, 1538-1541.

Auld, B. A., 1973, Acoustic fields and waves in solids, 2 volumes, John Wiley and Sons, Inc., New York, NY.

Backus, G. E., 1962, Long-wave anisotropy produced by horizontal layering: Journal of Geophysical Research, **67**, 4427-4440.

Bass, J. D., 1995, Elasticity of minerals, glasses, and melts, in Mineral physics and crystallography: A handbook of physical constants, pp. 45-63, edited by Thomas J. Ahrens, American Geophysical Union, Washington D. C.

Carcione, J. M., 1990, Wave propagation in anisotropic linear viscoelastic media: theory and simulated wavefields: Geophys. J. Int., **101**, 739-750.

Carcione, J. M., and Cavallini, F., 1995, The generalized SH-wave equation: Geophysics, **60**, 549-555.

Cheadle, S. P., Brown, R. J., and Lawton, D.C., 1991, Orthorhombic anisotropy: A physical seismic modeling study: Geophysics, **56**, 1603-1613.

Crampin, S., 1978, Seismic-wave propagation through a cracked solid: polarization as a possible dilatancy diagnostic: Geophys. J. R. astr. Soc., **53**, 467-496.

Ditri, J., 1994, On the determination of the elastic moduli of anisotropic media from limited acoustical data: J. Acoust. Soc. Am., **95**, 1761-1767.

Helbig, K., 1984, Anisotropy and dispersion in periodically layered media: Geophysics, **49**, 364-373.

Johnston, J. E., and Christensen, N. I., 1995, Seismic anisotropy of shales: J. Geophys. Res., **100**, no. B4, 5991-6003.

Karayaka, M., and Kurath, P., 1994, Deformation and failure behaviour of woven composite laminates: J. Eng. Mat. and Technol., **116**, 222-232.

Kebaili, A., and Schmitt, D. R., 1997, Ultrasonic anisotropic phase velocity determination with the Radon transformation: J. Acoust. Soc. Am., **101**, 3278-3286.

Kincaid D., and Cheney W., 1996, Numerical Analysis, 816 pp., Brooks/Cole Publishing Company, Pacific Grove, Calif.

Kirkpatrick, S., Gelatt, Jr., C. D., and Vecchi, M. P., 1983, Optimization by simulated annealing: Science, **220**, 671-680.

Mah, M., 1999, Experimental determination of the elastic coefficients of anisotropic materials with the slant-stack method, M.Sc. thesis, Univ. of Alberta, Edmonton, Alberta, Canada.

Mah, M., and Schmitt, D. R., 2001a, Experimental determination of the elastic coefficients of an orthorhombic material: Geophysics, **66**, 1217-1225.

Mah, M., and Schmitt, D. R., 2001b, Near point-source longitudinal and transverse mode ultrasonic arrays for material characterization: IEEE Trans. Ultrason., Ferroelect., Freq. Contr., **48**, 691-698.

Marion, D., Mukerji, T., and Mavko, G., 1994, Scale effects on velocity dispersion: From ray to effective medium theories in stratified media: Geophysics, **59**, 1613-1619.

Markham, M.F., 1957, Measurement of elastic constants by the ultrasonic pulse method: British J. Appl. Phys., **6**, 56-63.

Martinez, R. D., and McMechen, G. A., 1984, Analysis of absorption and dispersion effects in tau-p synthetic seismograms, 54th Ann. Internat. Mtg., Soc. Expl. Geophys., Expanded Abstracts, Session: S24.2.

Melia, P. J., and Carlson, R. L., 1984, An experimental test of P-wave anisotropy in stratified media: Geophysics, **49**, 374-378.

Mendenhall, W., 1975, Introduction to probability and statistics, 4th edition, 460 pp., Wadsworth Publishing Company Inc., Belmont, Calif.

Musgrave, M. J. P., 1970, Crystal acoustics, 288 pp., Holden-Day, San Francisco, Calif.

Neighbours, J. R., and Schacher, G. E., 1967, Determination of elastic constants from sound-velocity measurements in crystals of general symmetry: J. Appl. Phys., **38**, 5366-5375.

Nye, J. F., 1985, Physical properties of crystals, 322 pp., Oxford Science Publications, London, England.

Okoye, P.N., Zhao, P. and Uren, N.F., 1996, Inversion technique for recovering the elastic constants of transversely isotropic materials: Geophysics, **61**, 1247-1257.

Pros, Z. and Babuska, V., 1967, A method for investigating the elastic anisotropy on spherical rock samples: Z. Geophys., **33**, 289-291.

Rasolofosaon, P. N. J., Rabbel, W., Siegesmund, S., and Vollbrecht, A., 2000, Characterization of crack distribution: fabric analysis versus ultrasonic inversion: Geophys. J. Int., **141**, 413-424.

Rio, P., Mukerji, T., Mavko, G., and Marion, D., 1996, Velocity dispersion and upscaling in a laboratory-simulated VSP, Geophysics, **61**, 584-593.

Sayers, C. M., 1998, Misalignment of the orientation of fractures and the principle axes for P and S waves in rocks containing multiple non-orthogonal fracture sets: Geophys. J. Int, **133**, 459-466.

Szu, H., and Hartley, R., 1987, Fast simulated annealing: Physics Letters A., **122**, 157-162.

Thomsen, L., 1986, Weak elastic anisotropy: Geophysics, **51**, 1954-1966.

van Buskirk, W. C., Cowin, S. C., and Carter Jr., R., 1986, A theory of acoustic measurement of the elastic constants of a general anisotropic solid: J. Mat. Sci., **21**, 2759-2762.

Vestrum, R.W., 1994, Group and phase-velocity inversions for the general anisotropic stiffness tensor, M.Sc. thesis, Univ. of Calgary, Calgary, Alberta, Canada.

White, J. E., 1982, Computed waveforms in transversely isotropic media: Geophysics, **47**, 771-783.

White, J. E., 1983, Underground Sound, 253 pp., Elsevier Science Publishing Company Inc., New York, NY.

Chapter 5

Rock Sample Characterization

5.1 Abstract

A layered oil shale is examined in detail using a variety of different techniques. Visual observations of the oil shale show that it is highly layered with thin section work confirming this. X-ray diffraction showed that albite, calcite, dolomite, pyrite, and quartz were present in the sample. Pyrolysis and whole-rock analysis showed that the sample is about 49.20 weight % kerogen as well as helped determine weight percentages of various minerals present. Scanning electron microscopy and electron microprobing shed further light on the layering present in the sample and what minerals compose these layers. The nature of the layering present in the oil shale was determined as well as the composition of these layers.

5.2 Introduction

A layered oil shale was acquired from the oil shale facility located in Parachute Creek, Colorado (Figure 5.1). The oil shale facility is located at 39° 34' 48" latitude and 108° 06' 24" longitude. An oil shale was chosen as the sample to be tested because these shales tend to be homogeneous at the laboratory-sized sample and to be well consolidated. Further, their layered appearance suggests they are likely to be transversely isotropic.

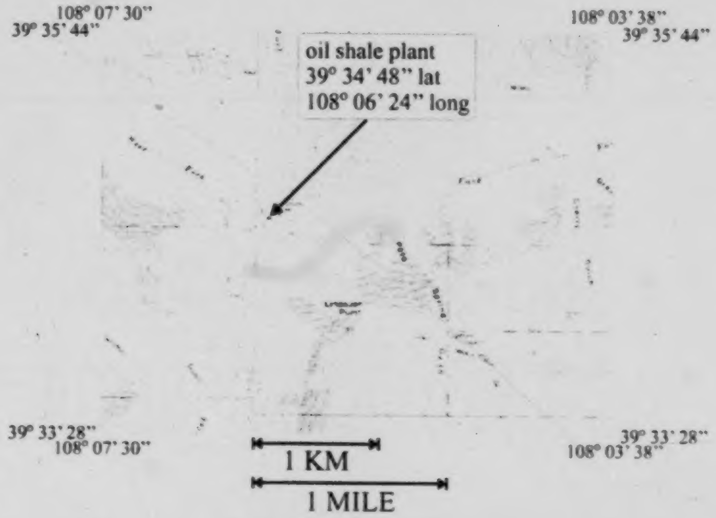

Figure 5.1: Map of the oil shale facility as located in Parachute Creek, Garfield County, Colorado as modified from USGS map Forked Gulch, Colorado.

The Parachute Creek Oil shale facility is located in the southern portion of the Piceance Creek Basin the lithology of which was produced in a lacustrine depositional environment. The Piceance Creek Basin was connected to the Uinta Basin to the west in Utah during Eocene times when the Green River Formation was first being deposited. The more well known Green River Basin is just to the north in Wyoming. These lake basins are thought to have had similar depositional environments (Tuttle, 1991). In order to understand the conditions under which these sediments were deposited, one must first look to modern lake depositional environments before discussing ancient lake depositional environments (Bradley, 1966).

A lake is defined by Webster (1997) as 'a body of fresh or salt water of considerable size, surrounded by land'. However, lakes are much more complex than this. For example, lakes can be classified as being a fresh water lake, brackish lake, or salt lake depending on the ion concentration of the water (Einsele, 1992).

As well, the pH of the lake may vary from alkaline (Stollhofen, et al. 2000; Kelts, 1988) to acidic (Einsele, 1992; Kelts, 1988;).

Lakes can be perennial (constantly wet) or ephemeral (intermittently dry) which is related to how much water is input to a lake compared to how much is lost. Of course, this depends on numerous factors such as river inflow, precipitation, evaporation, infiltration, and river outflow (Kelts, 1988; Bohacs et al., 2000). In the case of ephemeral lakes, the amount of water lost by a lake clearly exceeds that input into a lake. For perennial lakes, the amount of water input is equal to or greater than the amount lost.

The amount of water input and lost by a lake partially depends on the climate the in which the lake exists. In general, precipitation and evaporation rates tend to be higher in tropical areas near the equator than in other areas (Barron, 1990). However, the overall precipitation to evaporation ratio tends to be positive in tropical areas. Another interesting phenomenon is the smaller temperature difference between summer and winter in the tropical areas than in non-tropical areas. The seasonal temperature differences in tropical areas tends to be less than 20°C while in temperate areas it tends to exceed differences of 40°C (Barron, 1990).

In tropical environments where there are no large seasonal changes in temperature, a stratified lake can form because a large temperature change will cause cool water at the surface of the lake to sink and warm water to rise which in turn causes circulation (Einsele, 1992). A stratified lake is divided into 2 parts referred to as the epilimnion and the hypolimnion. The epilimnion is the upper layer of warm and circulating water while the hypolimnion is the deeper, cooler, and non-circulating water in a thermally stratified lake. If the lake is permanently stratified, it is considered meromictic and the water in the hypolimnion does not circulate. This causes the water of the hypolimnion to become deficient in oxygen that is consumed by the decay of deposited organic matter; the oxygen cannot be replenished because there is no mixing of the water with the atmosphere nor any photosynthesis. This oxygen deficient water leads to conditions that may readily preserve organic matter (Einsele, 1992; Kelts, 1988).

There are various theories as to what type of deposition environment was present during the formation of the mudstone in the Piceance Creek Basin. All the most recent theories support the idea that it was a lacustrine deposition environment; but there is disagreement as to the specific type of lacustrine depositional environment. Two different possible models for the deposition of oil shales in the Piceance Creek Basin are reported (1) Green River model, and (2) the deep anoxic lake or stratified lake model.

The former Green River model essentially describes a playa lake in which the lake is shallow but anoxic (i.e., devoid of oxygen). In such a lake, the water levels rise and fall due to periodic evaporation and inflow of runoff and precipitation. When the lake is flooded by runoff from nearby elevated areas, the inflow mixes the deeper oxygen deficient water with the shallow oxygen rich water disrupting the stratification. As well, the dolomitic particles would be flushed into the basin. In this case, the lake is only stratified for a portion of the year (Eugster & Surdam, 1973; Lundell & Surdam, 1975; Surdam & Wolfbauer, 1975).

In the deep anoxic or stratified model, the lake is both deeper and anoxic; the organic-rich sediments accumulate in the deep, permanently stratified lake waters. The dolomites present in the sediments are thought to be caused by alteration of calcite (Bradley, 1966; Bradley and Eugster, 1969; Cole, 1984; Desborough, 1978; Johnson, 1981; Smith, 1983; Smith & Lee, 1982; Tuttle & Goldhaber, 1991).

Whether the Piceance Creek Basin formed according to the Green River Basin or the deep anoxic lake, both have conditions that are consistent with a tropical climate and depositional environment leading to the formation of organic-rich oil shales.

5.2.1 Background

The velocity anisotropy and the corresponding elastic constants of a rock are determined not only by the bulk mineralogic composition but also according to the organization of these constituent minerals within the rock. It is well known that a sample composed of many thin and isotropic layers will, overall, be effectively anisotropic (e.g., Backus, 1967). Most sedimentary rocks, such as shales and oil shales, consist of many fine layers. This layering in itself will cause the rock to be anisotropic in nature. Here, the sample of oil shale obtained from the Piceance Creek basin, Colorado was analyzed using a variety of methods in order to determine its composition and structure. While there are many papers that try to determine the elastic constants of various rocks, few papers relate the anisotropy of the rock to its composition. Carlson et al. (1984) examined in detail 40 cores taken from the Deep Sea Drilling Project (DSDP) where the density, porosity and carbonate content were examined in addition to the compressional wave velocities perpendicular and parallel to bedding allowing the percent anisotropy to be calculated. Hornby (1995) determined the elastic constants as a function of pressure and examined the mineralogy and layering of the shale sample. Johnston & Christensen (1995) determined the elastic constants for a variety of pressures as well as examined the samples using oriented X-ray diffraction, scanning electron microscopy, and whole-rock analysis. Kaarsberg (1959) examined the velocity anisotropy and found that the oriented X-ray diffraction results confirmed that there is anisotropy present. Sayers (1994 & 1999) related the velocity anisotropy of shales back to clay distribution functions while Vernik & Nur (1992) examined the relationship between velocity anisotropy and total organic content, kerogen content, and maturity of shales.

5.2.2 Sample Analysis

The sample chosen for this study is commonly referred to as an *oil shale* although this name may be a misnomer. The oil shale was originally deposited approximately 44 to 53 million years ago in the Parachute Creek Member of the Green River Formation (Daub et al., 1985; Dyni, 1987). The sample had a low bulk density of only 1.57 g/cm^3 as determined by measuring the volume and mass of the sample. The sample had a measured rock fabric density of 1.74 g/cm^3 as determined by a multipycnometre. If one assumes there are no isolated pore spaces, a porosity of 9.8 % was calculated for the oil shale. The material was well laminated and predominantly medium to dark greyish brown with white-cream coloured layers (Figure 5.2(a)) matched descriptions of similar samples by Hail (1992) and Brobst & Tucker (1973). The layering was more or less planar with each layer being quite thin (Figure 5.2(b)). The sample had a Mohs hardness between 3.5 and 4. On a scratch plate, it streaked a medium brown.

In order to perform further tests with respect to the layering, a set of coördinate axes was chosen with the $x - axis$ and $y - axis$ parallel and $z - axis$ perpendicular to the layering plane (Figure 5.3).

The colour and laminations present in the sample gave some indication of the type of the depositional environment in which the sample was formed. The deposits have been extensively studied. Cole & Picard (1978) described 4 separate environments in the Piceance Creek Basin:

- deltaic/interdeltaic mudflat - small to medium scale cross-stratification
- carbonate flat - algal growth structures with minor ripple marks and small-scale cross-stratification

- proximal open lacustrine - horizontal continuous and discontinuous laminations
- distal open lacustrine - disruptive horizontal laminations with nodular growth structures of saline minerals

Since the sample had horizontal continuous laminations, it was likely deposited in a proximal open lacustrine environment. The fact that the sample closely resembled materials described by Cole (1984), Brobst & Tucker (1973), Grabowski & Pevear (1985), and Picard & High (1972) supports this contention.

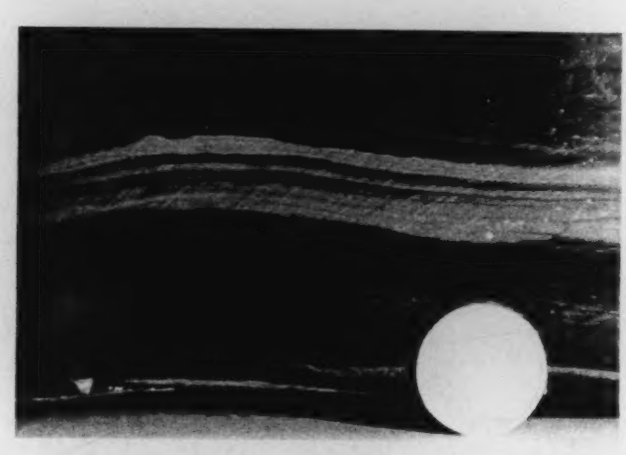

(a) Close up of oil shale sample with cross-section perpendicular to layering.

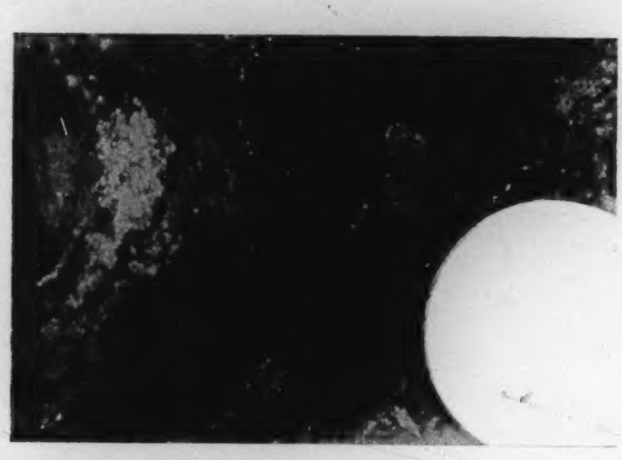

(b) Close up of oil shale sample with cross-section parallel to layering.

Figure 5.2: Close up of oil shale sample (Penny diameter = 19.08 mm).

5.3 Thin section

Thin sections of a sample of the oil shale were made in the 3 mutually perpendicularly directions. One thin section was taken parallel to bedding (i.e., normal to

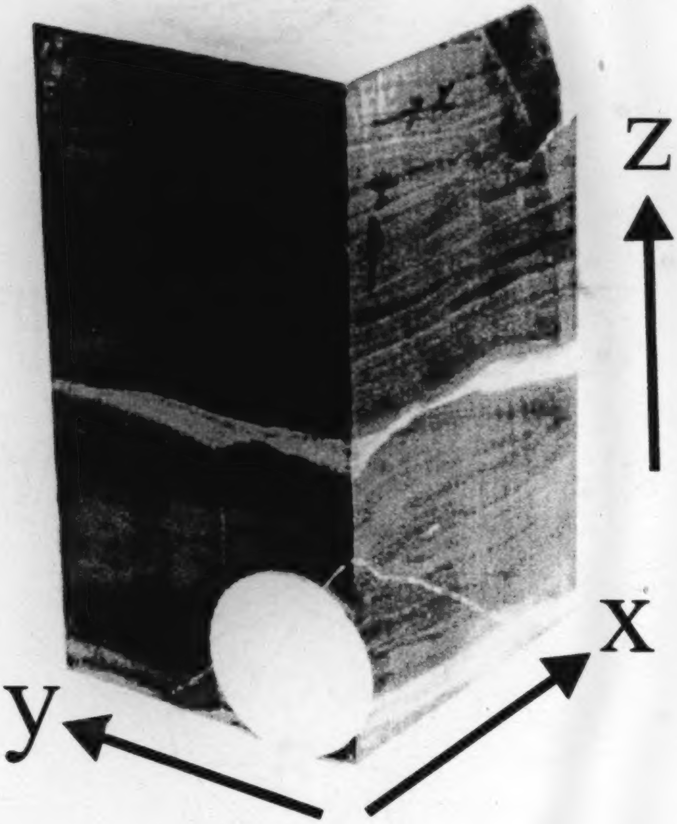

Figure 5.3: Layering of oil shale sample with respect to coordinate axes (2 dollar coin diameter = 28 mm).

the $z - axis$) (Figure 5.4(c)). The other 2 were taken perpendicularly to bedding and normal to the $x - axis$ (Figure 5.4(a)) and $y - axis$ (Figure 5.4(b)).

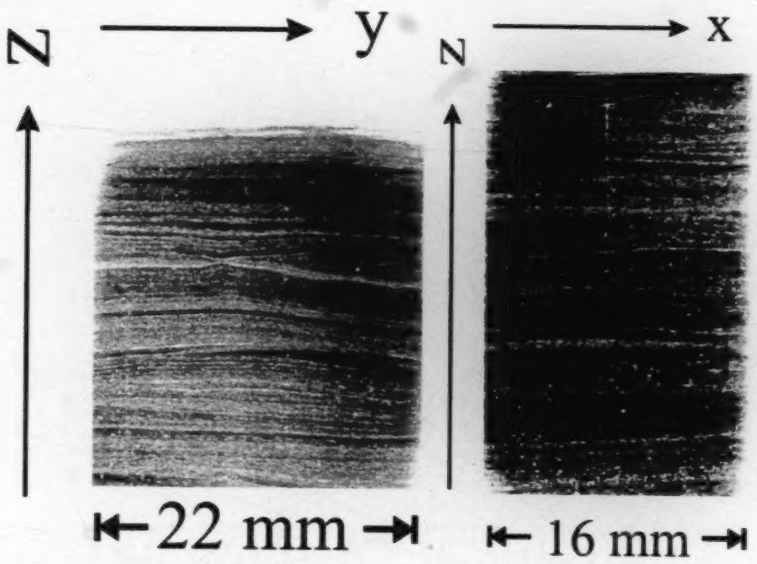

(a) Perpendicular to bedding where normal to surface is parallel to $x-axis$.

(b) Perpendicular to bedding where normal to surface is parallel to $y-axis$.

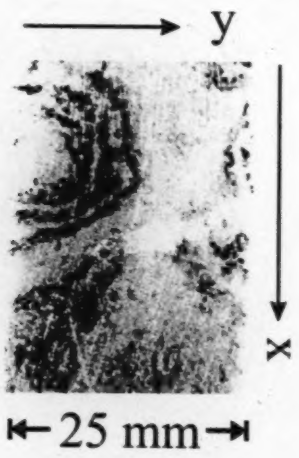

(c) Parallel to bedding where normal to surface is parallel to $z-axis$.

Figure 5.4: Thin section of oil shale taken in 3 perpendicular directions.

From the thin sections in Figures 5.4(a) and 5.4(b), 3 different types of extremely finely grained layers were present in the sample that were distinguishable based on colour. The lightest coloured layers are almost white and make up about 10 % by volume of the oil shale; medium brown and dark brownish-black layers make up 55 % and 33 % of the sample respectively as determined by microscope observation. The remaining 2 % by volume of the sample was composed of small whitish grains. Under cross-polarized light and using a magnification of 440 xs, the sample appeared predominantly brown and dim with the occasional brightly lit grain. This indicated the presence of birefringent minerals in both the layers and the small grains since only anisotropic minerals will transmit light when viewed under cross-polaroids (Moorhouse, 1959).

Rotation of the thin sections under polarized light in Figures 5.4(a) and 5.4(b) showed brightening and extinctions of the off-white layers indicating the presence of birefringent minerals (Phillips, 1971). In contrast, the dark brown and black layers displayed no changes in appearance when rotated. The medium brown layers showed a very modest change in intensity with angle. Coupled with the results of the X-ray diffraction, electron microprobe, and whole-rock analysis (to be discussed later), the lighter layers most likely contain calcite and/or dolomite (Winchell, 1933) while the dark layers are primarily kerogen or some other form of carbon. The medium brown layers might contain a mixture of birefringent and non-birefringent minerals. The small brightly lit grains also experienced brightening and extinction. This indicated that the minerals were birefringent and while they could not be positively identified, they are most likely composed of either calcite or quartz. It is useful to note that each individual birefringent layer and grain brightened and extinguished as a whole but at a different angles that seemed random compared to the overall layering and that of the other layers and grains. This possibly indicates there was some preferential orientation within that layer or grain but that this was not preferentially oriented with respect to the other layers or grains. Most of the grains are likely either calcite or dolomite since no 'wandering' extinctions were observed which means the grains are not composed of quartz (Moorhouse, 1959). This indicates that the crystallographic axes are randomly oriented in nature. Rotation of the thin section in Figure 5.4(c) showed no obvious brightening or extinctions in the 'layer' while the off-white grains present showed brightening and extinctions. If there was an overall preferential alignment of calcite or dolomite one would see an overall brightening or extinction of the thin sample as it is rotated. This was not observed which indicates there was most likely no overall preferential alignment of the calcite or dolomite present in the thin sections.

The examination of the thin sections showed the oil shale is composed of 3 differing extremely finely grained layers with the occasional small grain present. One type of layer is off-white in colour and composed of birefringent minerals with each layer having its predominant crystallographic axes in a random direction. This random orientation of the crystallographic axes may imply that there is no overall preferential orientation of the acoustic anisotropy within a layer. The off-white grains also seemed to have their crystallographic axes in random directions. In order to help define what minerals composed our sample, other tests such as X-ray diffraction were needed.

5.4 X-ray diffraction

5.4.1 What is X-ray diffraction?

Briefly, X-rays are electromagnetic waves that have a wavelength on the order of Å (10^{-10} m) and were discovered by W. C. Roëntgen in 1895 (Giancoli, 1985). These X-rays are used to probe the crystal structure of minerals. Minerals are composed of various atoms ordered in a regular fashion. The atoms form layers with an interatomic spacing (d) as shown in Figure 5.5. X-rays are electromagnetic waves and therefore can interact with each other and produce constructive interference. As the X-rays are reflected by the various layers of the crystal, the difference in the paths travelled by the X-rays is determined by the following:

$$2\Delta x = 2d \sin(\theta) \tag{5.1}$$

where $2\Delta x$ is the path difference of the X-rays and d is the interatomic spacing. If this path difference is equal to some multiple of the wavelength (λ):

$$n\lambda = 2\Delta x \tag{5.2}$$

constructive interference of the X-rays will occur according to the following:

$$n\lambda = 2d \sin(\theta) \ . \tag{5.3}$$

This is also known as Bragg diffraction.

Bragg diffraction is usually measured in an X-ray diffractometer (Figure 5.6). The X-rays were generated by the X-ray tube and the resulting intensities of the reflected/diffracted X-rays were detected by the detector. The diffraction angle (2θ) was measured by the goniometer. The intensities of the X-rays were measured as a function of the diffraction angle (2θ). The sample can be either in powder form or a specially prepared thin section. For mineral identification usually the powdered form was used. However, there have been instances (e.g., Kaarsberg (1959) and Johnston & Christensen (1995)) in which thin sections were used in order to semi-quantitatively provide some information about the orientation of the minerals in a sample.

For X-ray diffraction, wavelengths (λ) of 0.5 to 2.5Å were used (Guinier, 1963). For the powder and oriented X-ray diffraction here, a Rigaku geigerflex power diffractometer with a Co X-ray tube (λ = 1.78897Å) was used. The intensities of the diffracted X-rays as functions of angle as measured for each

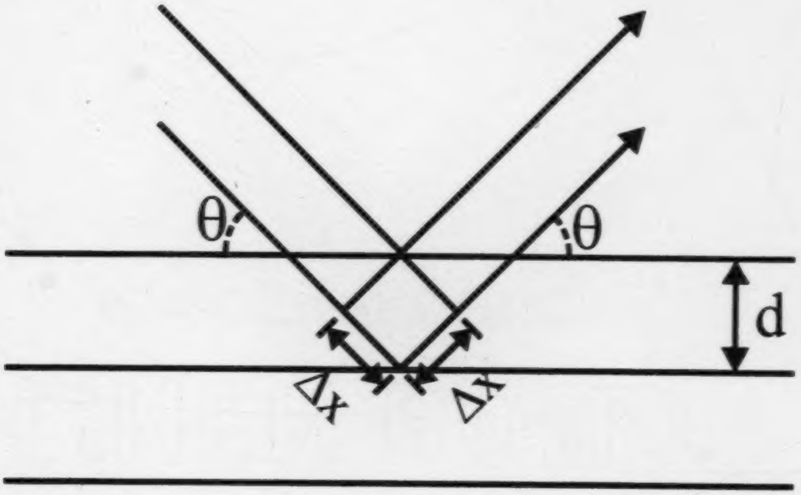

Figure 5.5: Example of Bragg diffraction occurring in a crystal where d is the interatomic distance between the layers. θ is the angle at which the X-rays hit the crystal at and $2\Delta x$ is the path difference of the X-rays.

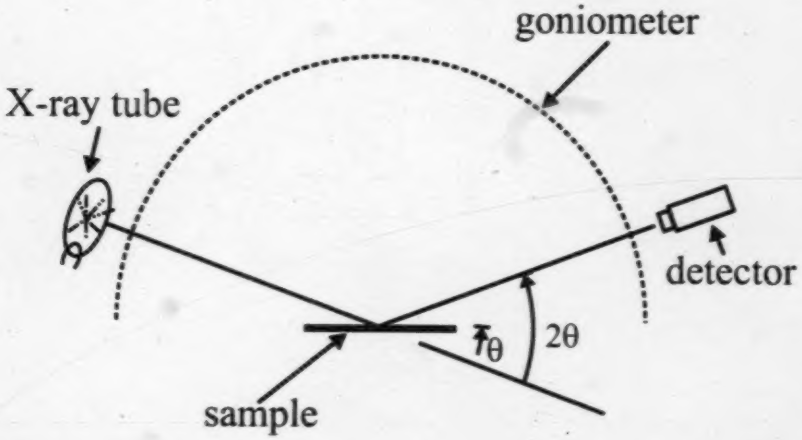

Figure 5.6: Schematic of X-ray diffractometer with sample being examined, X-ray tube as source of X-rays, and X-ray detector to detect intensity of reflected X-rays. The diffraction angle (2θ) is measured by the goniometer.

mineral were unique and allowed the mineralogical composition of each sample to be identified. For example, calcite ($CaCO_3$) and dolomite ($CaMg(CO_3)_2$) were somewhat chemically similar, but their powder X-ray diffraction patterns are quite different where (Figure 5.7). In essence, both the powder and oriented X-ray diffractions gave some idea of the minerals were contained in the sample. However, determination of relative quantities was much less certain. Ideally, a perfectly oriented large single crystal that is free of lattice defects would be measured. In oriented X-ray diffraction, the mineral grains are not necessarily properly oriented, of large enough size, or free of lattice defects. This can lead to the results being heavily biased by the distribution of sizes and orientations of the mineral grains; in particular the small grained clays may not give strong diffraction peaks and could easily not be recognized (Kaarsberg, 1959). A distribution of grain sizes as opposed to a single uniform size of mineral grains causes the width of a peak to broaden as observed in clays (Langford et al., 2000). Not only does the distribution of grain sizes affect the peaks observed in X-ray diffractions but the smaller the grain size is the broader the peaks are as well as the peaks are of lower intensity as can be observed in clays and dawsonite (Ungar et al., 2001; Warr & Rice, 1994; Zen & Hammarstrom, 1975).

5.4.2 Powder X-ray diffraction results

As mentioned previously, for powder X-ray diffraction to be performed on a sample, the sample must be ground down to a fine powder. For optimal powder X-ray diffraction results, the sample should be ground down to a powder less than 45 μm in size which is equivalent to passing a 325-mesh screen (Klug & Alexander, 1974). Our sample was ground down to a powder with particle sizes around 10 μm. This large number of randomly oriented crystals in the powder allows the X-rays from the source to be diffracted and generate continuous uni-

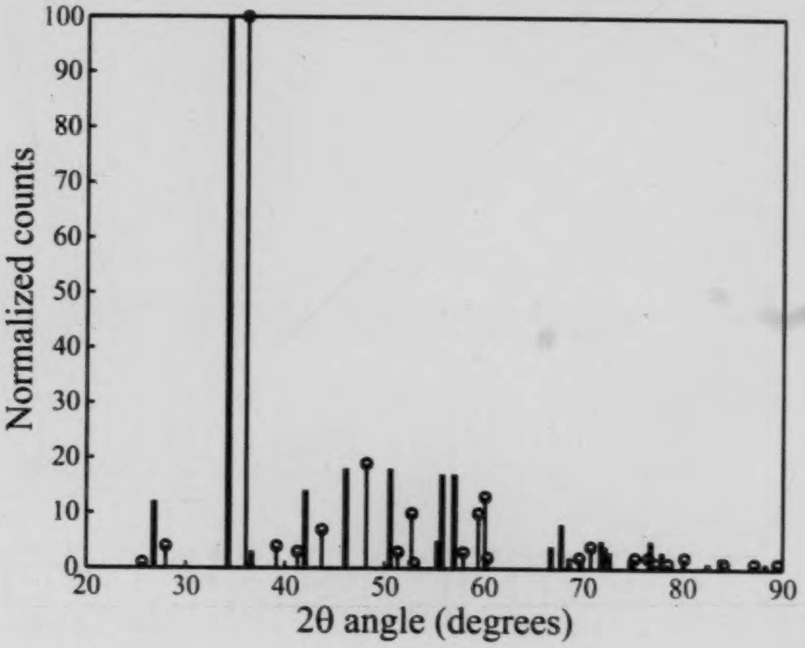

Figure 5.7: Comparison of the powder X-ray diffraction of calcite and dolomite. Calcite is represented by the solid bars (Swanson & Fuyat, 1953) and dolomite by the stems with the circles on the top (Howie & Broadhurst, 1958). *2θ* angle is that measured in Figure 5.6.

form diffraction rings that can be picked up by the detector. The grinding down of the sample may reduce the size of the crystallites (single mineral crystals) and cause lattice deformations that in turn may cause broadening of the peak lines (Klug & Alexander, 1974). However, the smaller the distribution of crystallite sizes, the smaller the width of the powder X-ray diffraction line profiles (Langford et al., 2000). The resulting profile is then examined to see what minerals may be present. In our work, the minerals were identified by comparison with minerals as catalogued by the Joint Committee on Powder Diffraction Standards (JCPDS) database. A sample of the oil shale was examined at the University of Alberta in the Earth and Atmospheric Sciences Department. The powder X-

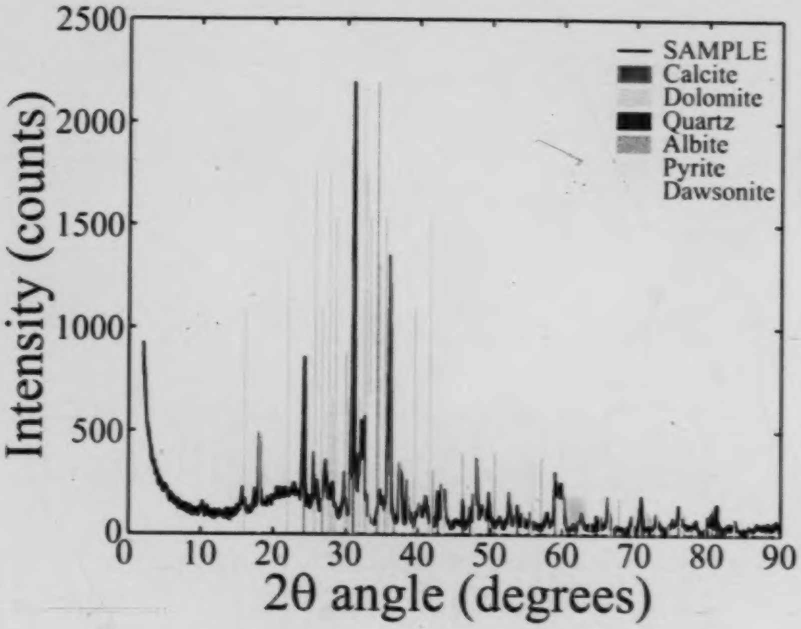

Figure 5.8: Powder X-ray diffraction of results of oil shale sample.

ray diffraction profile (Figure 5.8) indicated that the oil shale contained calcite ($CaCO_3$), dolomite ($CaMg(CO_3)_2$), quartz (SiO_2), albite ($NaAlSi_3O_8$), pyrite (FeS_2), and dawsonite ($NaAlCO_3(OH)_2$). There was also the possibility that it contained some anorthoclase ($(Na,K)AlSi_3O_8$). Usually the profile is relatively flat with distinct peaks. However, this powder X-ray diffraction pattern has a large "hump" or bulge from 13 to 31 degrees 2θ. This is likely indicative of the presence of some amorphous material (e.g., kerogen) or of incipient clay (i.e., the constituents of the clay are present but are still disordered and have not yet formed a "crystalline" structure). Interestingly enough, illite has its largest peak at about 23 degrees 2θ (Figure 5.9) which coincides with the "hump" present in the powder X-ray diffraction pattern.

When a material is amorphous or non-crystalline in nature, it generates dif-

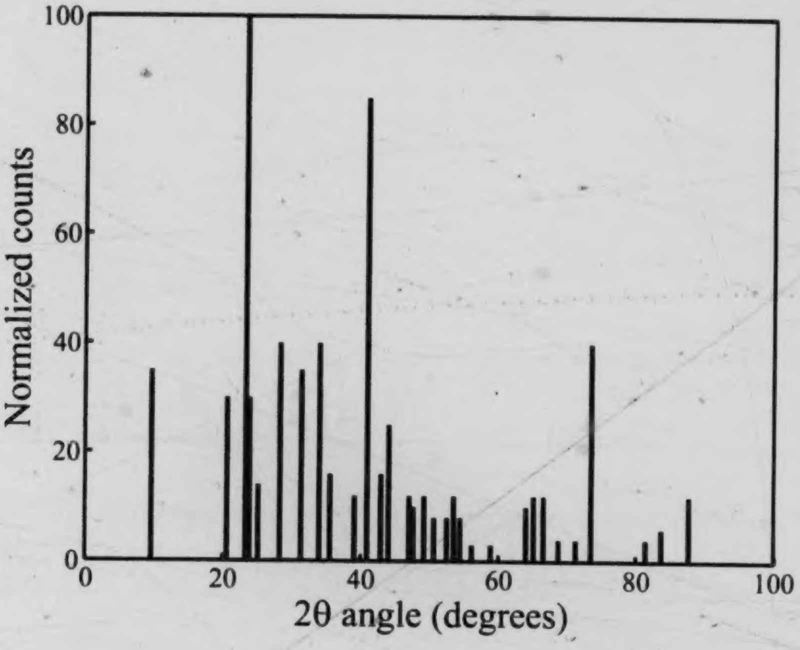

Figure 5.9: Powder X-ray diffraction signature of illite (Brindley, 1977).

fuse diffraction patterns, i.e., instead of distinct peaks, broad peaks are seen (Klug & Alexander, 1974; Scardi & Leoni, 1999; Warr & Rice, 1994; Robinson & Bevins, 1986). However, the broadening of the peaks tends to be less than one degree in the 2θ angle domain (Warr & Rice, 1994; Robinson & Bevins, 1986). Another possibility is the presence of mixed-layer or interstratified clay minerals where different types of clay minerals are interstratified. It has been postulated that the majority of clays are actually composed of mixed-layer clay minerals (Weaver & Pollard, 1973). This means instead of the layers within the clays being composed of a single clay mineral type, different types of clay minerals form the various layers in the clay with each clay layer being on the order of 1-10 μm thick. Since the composition of these interstratified clays is highly variable, it may not be recognized in the JCPDS database for X-ray diffraction patterns. The presence of interstratified clays will still not produce the large "hump" from 13 to 31 degrees 2θ since these interstratified clays if present would still produce very distinct X-ray diffraction patterns, e.g., illite-montmorillonite clay (Figure 5.10). Since this sample is an oil shale, it is more likely that this is the kerogen or carbon present in the sample since kerogen is naturally amorphous but other oil shales have at least some clay.

The dominant clay mineral in the study area is illite $(K_{1-1.5}Al_4\ (Si_{7-6.5}.Al_{1-1.5}.O_{20})\ (OH)_4)$ according to Smith & Lee (1982) and is present everywhere in the Piceance Creek basin but no quantitative estimate of the amount of illite is given. A study of drill core samples in the Piceance Creek basin yielded illite values of 0 to 18 % by weight that varied with depth with the majority being less than 10 % by weight (Meddaugh & Salotti, 1983). While the presence of illite has widely varying values, the amount of kerogen or organic carbon present in samples of the Piceance Creek basin was consistent with ranges of any where from as little as 5 % to 27 % by weight with the majority being in the 10 % to 20 % by weight range (Meddaugh et al., 1984). Studies of other oil shales in the nearby area yielded ranges from 8 % to over 30 % by weight (Horsefield et al., 1993; and Katz, 1988;). Therefore, it would not be usual to have a sample containing no illite yet a high amount of organic carbon or kerogen.

5.4.3 Oriented X-ray diffraction results

Specially prepared thin sections of the sample are used in oriented X-ray diffraction. The thin section is mounted and prepared in a similar manner as a regular thin section except that it is not as thin since one is not concerned with transmission of or transparency to light. What is of concern is how parallel the surface of the sample is to the surface of the glass slide on which it is mounted. If the surfaces are not parallel, this may bias the results. Unlike powder X-ray

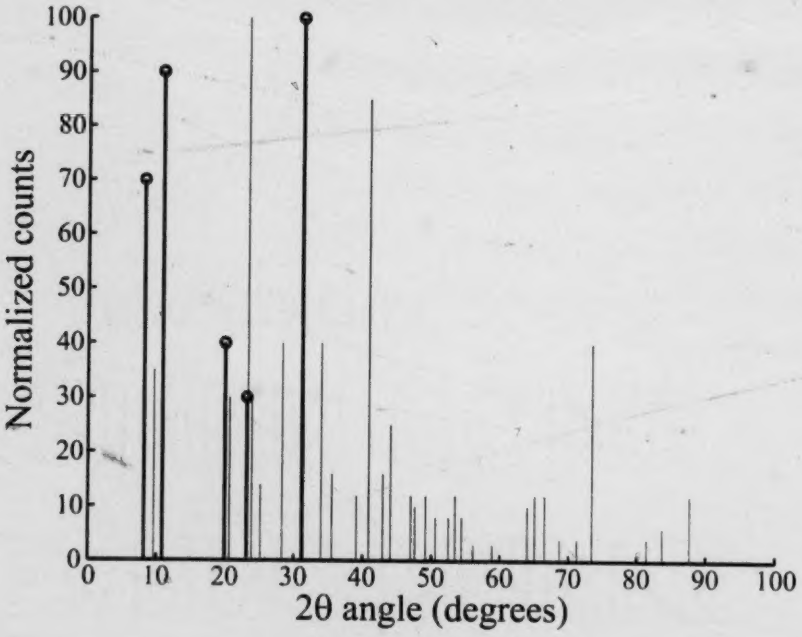

Figure 5.10: Powder X-ray diffraction signature of illite and illite-montmorillonite clay minerals. Illite is represented by the solid bars (Brindley, 1977) and illite-montmorillonite by the stems with the circles on the top (Bayliss, 1989).

diffraction where the sample is ground, in oriented X-ray diffraction the polished sample is used. Instead of exposing the incident X-rays to a large number of crystals at random orientations, the X-rays are exposed to crystal orientations that may be quite oriented if there is a strong texture to the material. This means that the diffracted X-rays no longer form uniform continuous rings as they would in powder diffraction. Instead, the amplitudes will be highly dependent on the angle between the crystal face as it lies within the thin section and the X-ray source. As such, a sample is rotated with respect to the X-ray beam, the strengths of the peaks will change if the minerals have a preferential alignment. Three different thin sections were chosen with the normal to the surface of each thin section being parallel to one the 3 coordinate axes similar to those of

Figures 5.4(a), 5.4(b), and 5.4(c). The corresponding X-ray diffraction results are shown in Figures 5.11(a), 5.11(b), and 5.11(c), respectively where the same minerals as those found in the powder X-ray diffraction were identified. However, the powder X-ray diffraction profiles in Figures 5.11(a) and 5.11(b) are almost identical to those of the powder X-ray diffraction results (Figure 5.8). However, the spectrum of the thin section taken parallel to the layering (Figure 5.4(c)) shown in Figure 5.11(a) is quite different from the previous 2. The oriented X-ray diffraction results indicate the presence of the same minerals as the powder X-ray diffraction results such as calcite, dolomite, quartz, albite, pyrite, and dolomite. The possible amorphous "hump" located at 23 degrees 2θ is reduced in the profile indicating that perhaps there is less amorphous material present in the thin section. There is also a major change in the relative heights of the various diffraction peaks associated with the various minerals. Either this may indicate a possible change in the relative abundances of the minerals or that the mineral orientations are not random but have some texture.

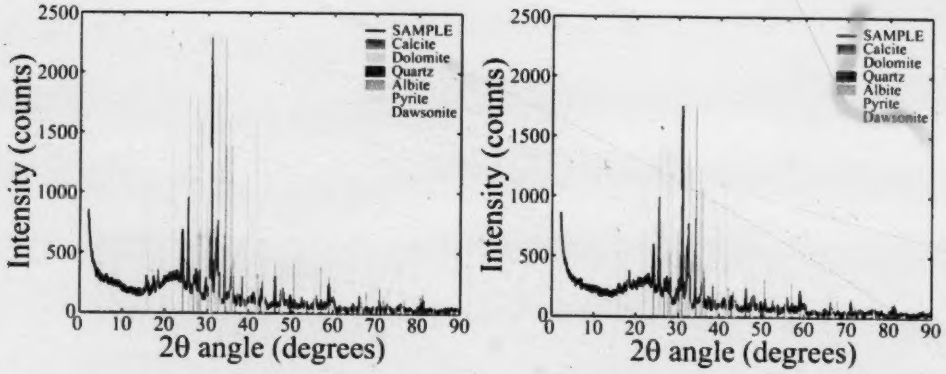

(a) X-ray diffraction of oil shale sample in the $y - z$ plane.

(b) X-ray diffraction of oil shale sample in the $x - z$ plane.

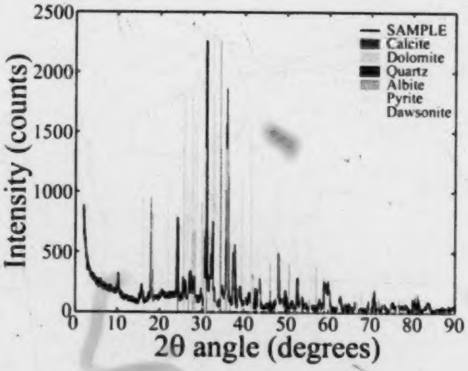

(c) X-ray diffraction of oil shale sample in the $x - y$ plane.

Figure 5.11: X-ray diffraction of oil shale sample

X-ray diffraction shows us the presence of certain minerals in the sample but does not give an exact measure of the amount of these minerals present in the sample or an exact measure of the preferential orientation of these minerals. Other methods such as pyrolysis and whole-rock analysis may give more information about the composition of the sample.

5.5 Pyrolysis and whole-rock analysis

5.5.1 What is pyrolysis and whole-rock analysis?

Pyrolysis and whole-rock analysis are two quite commonly used quantitative methods of determining the compositions of rocks. In pyrolysis, the sample is burned under controlled conditions and the resulting gases are analyzed in order to determine the amount of carbon, hydrogen, nitrogen, and sulfur present in the sample. Typically this is done by burning the finely ground sample in free flowing oxygen. The CO_2, H_2O, and SO_2 given off by combustion is measured by selective infrared detectors. Once the amounts of these gases are determined, the amount of nitrogen present may then be determined by thermal conductivity detection.

Whole-rock analysis is based on X-ray fluorescence spectroscopy. In X-ray fluorescence spectrometry (XRF), an X-ray beam excites secondary X-rays (X-ray fluorescence). These secondary X-rays are analyzed for both wavelength (frequency) and intensity. The wavelengths of the X-rays depend on the elements present in the sample. The intensities of the X-rays are determined by the composition of the sample (Lachance, 1989). There are two methods of preparing the sample for whole-rock analysis. In the first, the crushed or ground rock is pressed into a powder disc (Leake et al., 1969). In the second, glass beads are made from the powder sample after being fused with borax (anhydrous sodium tetraborate) then reformed into a pellet which is then burned or oxidized (Claise, 1989). In the method described by Claise (1989), about 1/4 gram of finely ground rock is heated in a furnace at 1000°C with 7 to 9 grams of lithium tetraborate or lithium metaborate in a platinum alloy crucible. The mixture is stirred occasionally and when completely mixed and bubble free, is poured into a mould and cooled at a specific rate in order to control the crystallization of the sample. In the method described by Leake et al. (1969), the powdered rock sample is combined with a thermo-setting phenol formaldehyde binding compound before being pressed and heated at 110°C for 30 minutes.

5.5.2 Pyrolysis and whole-rock analysis results

Pyrolysis tests of the sample were performed in the Microanalytical Service Laboratory at the University of Alberta. The results of pyrolysis are shown in Table(5.1). Interestingly, the sample is about 36 % carbon by weight since carbon has a low density compared to other elements present in the sample. The carbon present in the oil shale is associated with either the kerogen or the carbonate minerals (i.e., calcite and dolomite) present. The nitrogen present in the sample must be associated with the kerogen since it is not contained in any other mineral identified by powdered X-ray diffraction. The hydrogen present in the sample is associated with the kerogen or dawsonite. Similarly, the sulfur in the sample must be associated with the kerogen or pyrite present in the sample. This test by itself does not give us enough information to determine the exact composition of the oil shale sample.

This analysis is in agreement with a soxhlet analysis that was performed in the Earth and Atmospheric Sciences Building by Dean Rokosh. In soxhlet analysis, the organic material is removed by repeat washings with an organic solvent. The remaining undissolved material was analyzed using X-ray diffraction for clay minerals but none was found. The sample was analyzed again using a sedigraph

element	weight %
C	35.9117
H	4.6313
N	1.0862
S	1.420

Table 5.1: Pyrolysis of oil shale sample.

in which the sample was burned at 500°C to remove the organic carbon material only. The sample weighed 5.3 g and 3.1 g before and after burning, respectively, leading to an estimate of 42 wt. % organic matter in relative agreement with previous tests. The remaining unburned material was then analyzed with a sedigraph in order to determine the amount of sand/silt/clay ratio. The majority of the unburned material (76 wt. %) falls between 8-16 μm (fine silt). No sand was found, however 3-5 wt. % could be classified as being clay-sized particles. X-ray analysis of the unburned materials revealed quartz, feldspars, dolomite, dawsonite, pyrite, and muscovite but still did not reveal the existence of any clay minerals. This was somewhat unexpected as we had thought because the material was called an "oil shale" that it would contain abundant clays.

Whole-rock analysis of the sample was done at a private firm speciali [redacted] in geochemical analysis. The results of the whole-rock analysis ar [redacted] in Table(5.2).

As can be seen in Table 5.2, the oil shale contains a larg [redacted] potassium (K). The only mineral that was found to contain pota [redacted] previous tests was anorthoclase ((Na, K)$AlSi_3O_8$). The whole-roc [redacted] leads to a molar ratio of Si : 0.284 Al : 0.2191 Na + K while feld [redacted] as albite ($NaAlSi_3O_8$) and anorthoclase ((Na,K)$AlSi_3O_8$) have a [redacted] 3 Si : Al : Na + K. This means by comparison there is an excess [redacted] Al and a deficit of Na and K to Al. It is impossible to balance the [redacted] of Si, Al, Na, and K using albite, anortho-

Oxide	weight %
SiO_2	29.67±0.01
Al_2O_3	7.15±0.01
CaO	2.63±0.01
MgO	1.51±0.01
Na_2O	1.90±0.01
K_2O	2.57±0.01
Fe_2O_3	4.74±0.01
MnO	0.02±0.01
TiO_2	0.39±0.01
P_2O_5	0.13±0.01
Cr_2O_3	0.01±0.01
Loss on ignition	49.20±0.01
Sum	99.92±0.01
C(org)	35.90±0.05
C (total)	37.00±0.01

Table 5.2: Whole-rock analysis oil shale sample.

clase and dawsonite ($NaAlCO_3(OH)_2$) alone. Small amounts of clay present in the analysis may explain the discrepancies in the ratio. According to Smith & Lee (1982), illite is the clay most likely to be present in the area. Clays such as illite ($K_{1-1.5}Al_4$ $(Si_{7-6.5}.Al_{1-1.5}.O_{20})$ $(OH)_4$) having a elemental molar ratio of 7-6.5 Si : 5 - 5.5 Al : 1 - 1.5 K. As well, there is a high amount of silicon (Si) present in the sample. So quartz ($Si0_2$) which has been identified previously by X-ray diffraction methods is included in the analysis. There are other possible errors that may affect the results of the whole-rock analysis. According to Claise (1989), if the pH of the sample is unknown a mixture of lithium metaborate and lithium tetraborate is used in forming the sample. However, if the pH of the sample is quite high only lithium tetraborate should be used in preparing the sample, otherwise crystallization may occur which would interfere with the whole-rock analysis. Cooling problems may also cause the incipient crystallization that would affect the analysis. The literature supports the presence of illite so the following analysis was performed with illite having the chemical composition $K_{1.25}Al_4(Si_{6.75}.Al_{1.25}.O_{20})\ (OH)_4$. The following analysis yielded the best results when anorthoclase was assumed to have the chemical composition $Na_{0.116}K_{0.884}AlSi_3O_8$. One unexpected result was the presence of titanium (Ti) in the results. In order to account for this, ilmenite ($FeTiO_3$) was included in the analysis. Ilmenite was chosen since electron microprobing (to be discussed later) showed all the titanium was associated with iron (Fe) and ilmenite is one possible mineral that contains both iron and titanium.

By assuming the non-kerogen minerals in the sample are albite, anorthoclase, calcite, dawsonite, dolomite, illite, ilmenite, pyrite, and quartz the relative amounts of non-kerogen mineral are determined in Table 5.3 from Table 5.2 using a simple least-squares stoichiometry computer program written by myself in Matlab. If one assumes that the loss on ignition of 49.20 wt. % in Table 5.2 is equivalent to the amount of kerogen present in the sample then the overall composition can be described in Table 5.4. As one can see from pyrolysis and whole-rock analysis, the composition of the rock can be determined but this does not tell us much about how these minerals are distributed or how they are oriented. In order to shed more light on this, scanning electron microscopy and electron microprobing were employed.

Mineral	molar %	weight %
Albite	20.8	29.5
Anorthoclase	18.3	27.3
Calcite	3.2	1.7
Dawsonite	2.4	1.9
Dolomite	11.8	11.7
Illite	2.1	7.9
Ilmenite	1.4	1.2
Pyrite	17.5	11.4
Quartz	22.6	7.3
Total	100.1	99.9

Table 5.3: Relative amounts of non-kerogenous minerals as deduced by whole-rock analysis.

Mineral	weight %
Albite	15.0
Anorthoclase	13.9
Calcite	0.9
Dawsonite	1.0
Dolomite	5.9
Illite	4.0
Ilmenite	0.6
Pyrite	5.8
Quartz	3.7
Kerogen	49.2
Total	100.0

Table 5.4: Overall composition of oil shale sample as deduced by whole-rock analysis.

5.6 Scanning electron microscope

5.6.1 What is scanning electron microscopy?

The electron microscope was first built by M. Knoll in 1935 while the first true scanning electron microscope was built by M. von Ardenne in 1938 (Wischnitzer, 1970; Woolfson & Ziman, 1972). Its primary use is to image the surface of a sample not unlike an optical microscope would. The electron microscope is similar to an optical microscope in the sense that both use lenses in order to focus either a beam of electrons or light to gain information about the surface of the sample. However, the magnification or resolution of an electron microscope is much higher than that of an optical microscope. Unlike an optical microscope, the "lenses" that are used for focusing are not composed of transparent materials with a high index of refraction but are magnetic in nature. A magnetic field is used to focus the electrons. In a scanning electron microscope (SEM) as shown in Figure 5.12, an electron gun is the source of electrons which are focused by the condenser lens and the objective lens. Since this is a scanning electron microscope, the electron beam is diverted by the scanning coils in order to systematically scan the surface of the sample with the electrons. The scanning beam of electrons has energy that ranges from tens to hundreds of electron Volts (eV). The majority of the electrons have elastic collisions with the atoms in the sample. However, some electrons will have inelastic collisions and will cause some secondary electrons to be ejected from the atoms in all directions (Woolfson & Ziman, 1972). Some of these secondary electrons will be registered by the detector. As the surface of the sample is scanned, a 2-D picture of this surface is produced. In order to accelerate the electrons towards the sample, an electric potential in the kilovolts is used. In order to achieve this, the sample is usually covered with some conductive coating such as silver or gold. As well in order to reduce the scattering of the electrons, scanning is done under a vacuum.

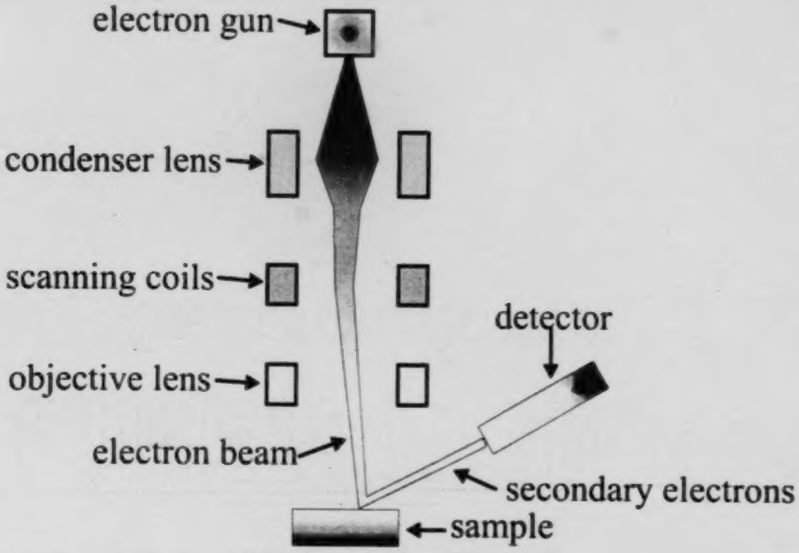
electron gun
condenser lens
scanning coils
detector
objective lens
electron beam
secondary electrons
sample

Figure 5.12: Schematic of scanning electron microscope.

5.6.2 SEM results on the oil shale samples

In the following work, a scanning electron microscope (JEOL6301F-(Field Emission Scanning Electron Microscope)) in the Earth and Atmospheric Sciences Department at the University of Alberta was used. The two samples of the oil shale, each about 0.7 cm^3 in volume, were covered in gold and placed in the scanning electron microscope in a vacuum of about 10^{-7} torr. As well, there was an attached energy dispersive system (EDS) analyzer made by PGT for simple elemental analysis. The EDS analyzer works by measuring the fluorescence or light (in our case X-rays) given off by the sample. When electrons strike the atoms of a sample, most of the transferred energy is in the form of heat but can be given off in the form of light or X-rays. The wavelengths of the X-rays given off by the atoms that were struck by the electrons are governed by the Moseley Law:

$$\frac{1}{\lambda} = A\,(Z - b)^2 \tag{5.4}$$

where λ is the wavelength of light emitted, A is a constant, Z is the atomic number of the atom, and b is a constant (Glashow, 1994). Therefore, by analyzing the X-ray spectrum given off at a particular location on the sample, a rough measure of the elements present is given.

Three orthogonal sides of the sample were analyzed, each side was approximately perpendicular to one of the coordinate axes previously chosen (Figure 5.3). Low-resolution pictures of the layering in the $y - z$ plane and $x - z$ plane are shown in Figures 5.13 and 5.14, respectively. The surface of the sample indicates that there is layering approximately normal to the $z - axis$. Higher resolution views of the layering show that many of the layers are composed of fine, amorphous material as shown in the center of Figure 5.15. In Figure 5.15, the thickness of one of these layers is about 20 μm. There are also areas composed of large numbers of disordered semi-tabular grains (Figure 5.16). As well one can see that the average size of the grains is on the order of 1 μm. Occasionally, voids that are oval shaped with their long axes usually parallel to the layering (Figure 5.17) are seen. A look at the $x - y$ plane parallel to layering shows semi-tabular particles parallel to layering (Figure 5.18) but also the presence of very small needle-shaped particles (Figure 5.19). These very small needle-shaped particles are also seen in scanning electron microscope (SEM) pictures in both the $y - z$ plane and the $x - z$ plane but they are too small to be identified using energy dispersive system (EDS) analysis.

Energy dispersive system (EDS) analysis of various areas on the oil shale sample showed calcium and magnesium which indicates the presence of dolomite ($CaMg(CO_2)_2$), areas containing sodium and aluminium indicating albite ($NaAlSi_3O_8$), areas containing sodium, potassium, and aluminium indicating anorthoclase

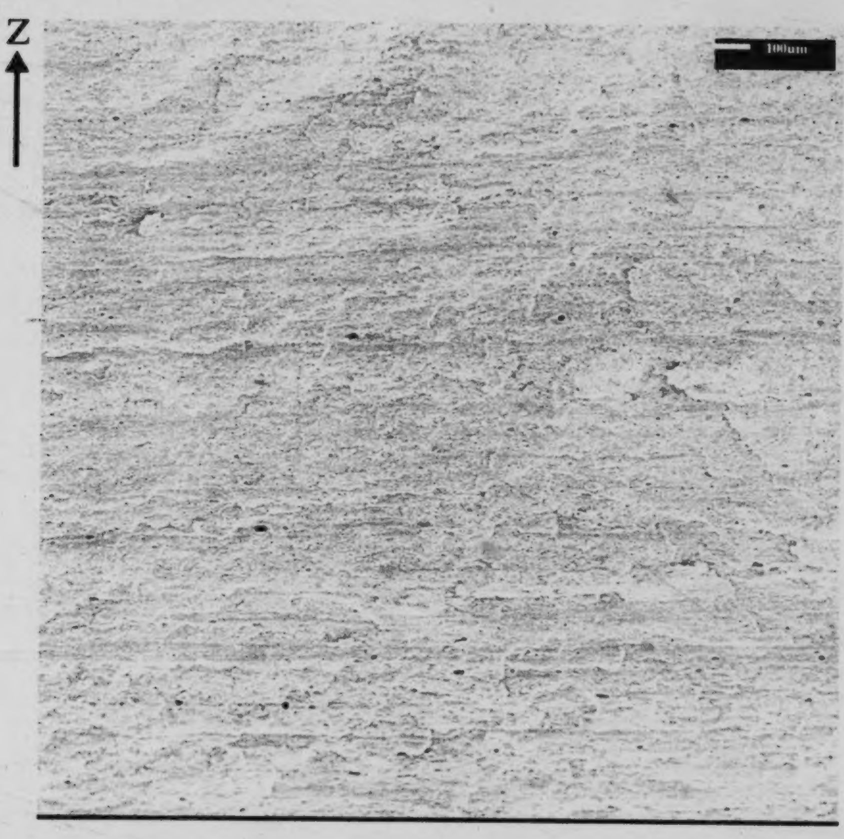

Figure 5.13: Low resolution SEM view of layering in the $y - z$ plane. Viewable area = 4.97 mm^2.

((Na,K) ($Si_3Al)O_8$), as well as areas that contain titanium indicating some titanium rich mineral.

This oil shale sample also had a few interesting features such as the presence of a large jagged particle as can be seen on the lower left edge of Figure 5.15. A close up of this particle showed that it was approximately 7 μm in diameter and is quite jagged and angular (Figure 5.20). The shape indicated that the mineral grain was formed in solution and not transported very far. The energy dispersive system (EDS) analysis showed that it contained calcium and magnesium which

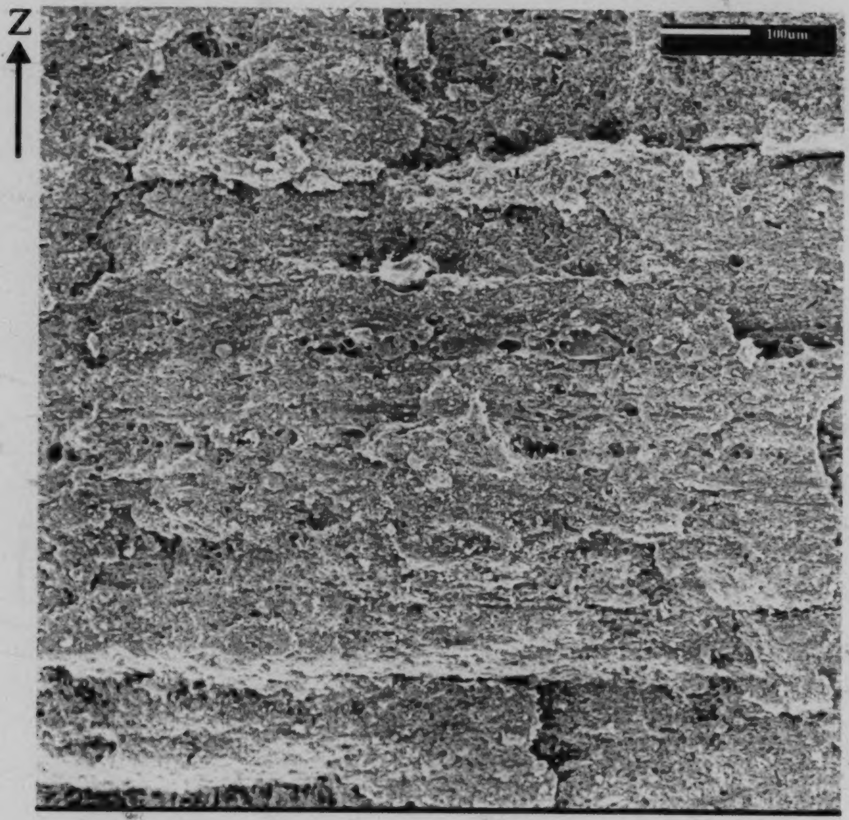

Figure 5.14: Low resolution SEM view of layering in the $x - z$ plane. Viewable area = 0.818 mm^2.

indicated that it was most likely a small piece of dolomite ($CaMg(CO_2)_2$). As well the jaggedness of the dolomite particle seems to indicate that it was deposited by direct precipitation from solution and not by replacement of calcite. The oil shale sample also contained the occasional quartz grain as confirmed by the EDS analysis (Figure 5.21). The quartz grain in Figure 5.21 was approximately 71 μm in length and was angular to subangular in shape indicating that it was not been transported very far from its source.

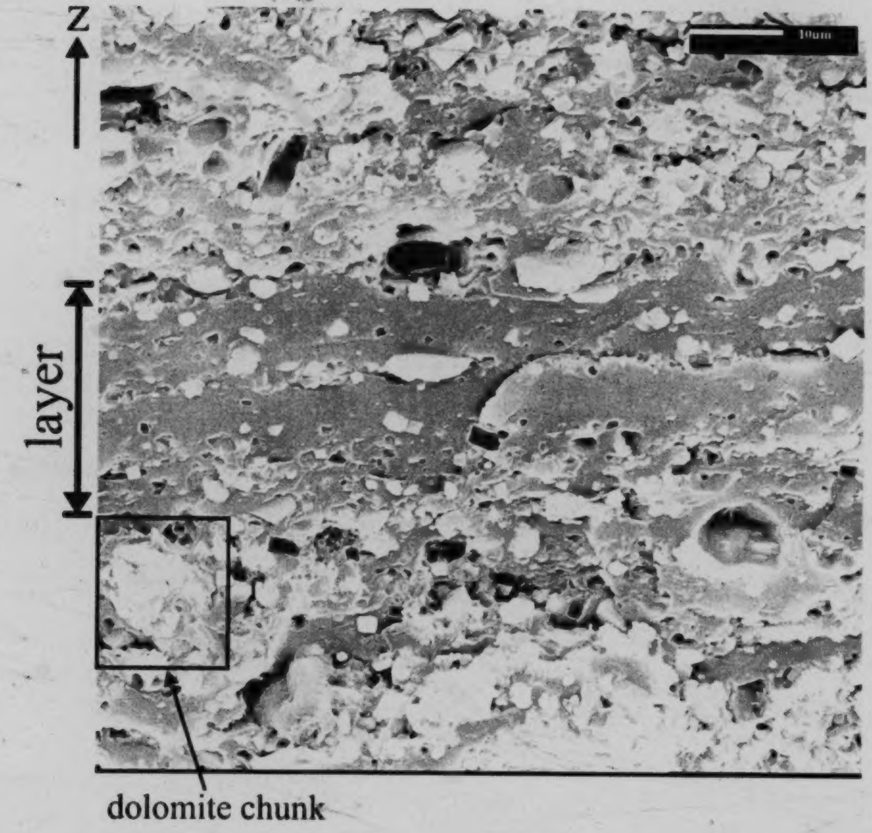
z
10um
layer
dolomite chunk

Figure 5.15: High resolution SEM view of layering in the $y - z$ plane showing a band of structureless material. Viewable area = 6.71×10^{-3} mm^2.

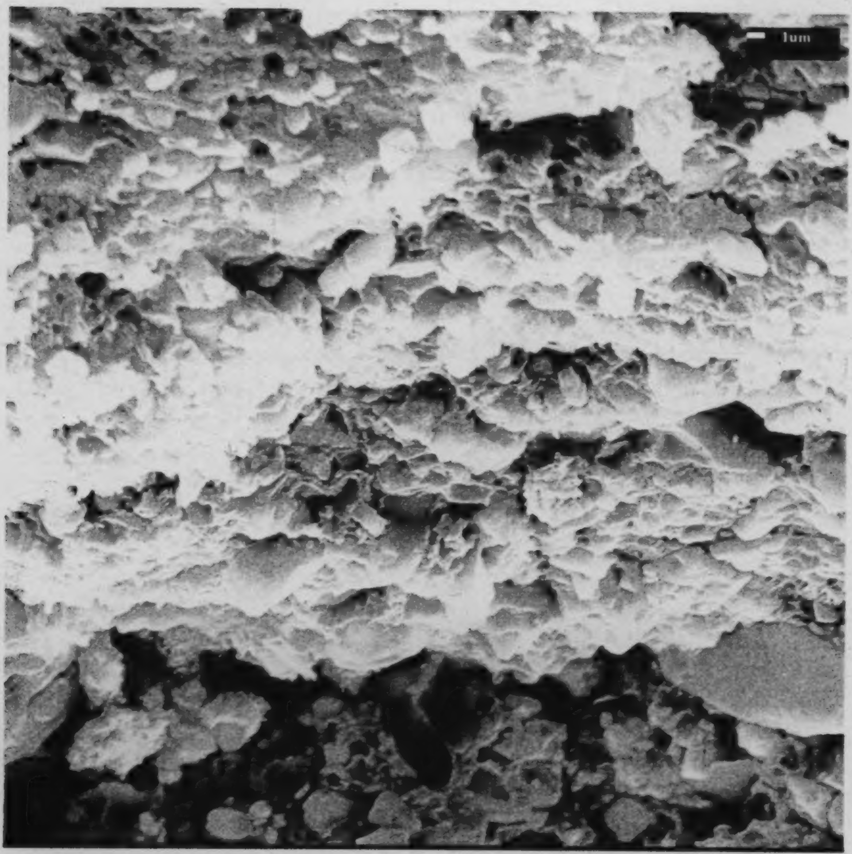

Figure 5.16: High resolution SEM view of layering in the $x - z$ plane showing an area composed of disordered semi-tabular grains.

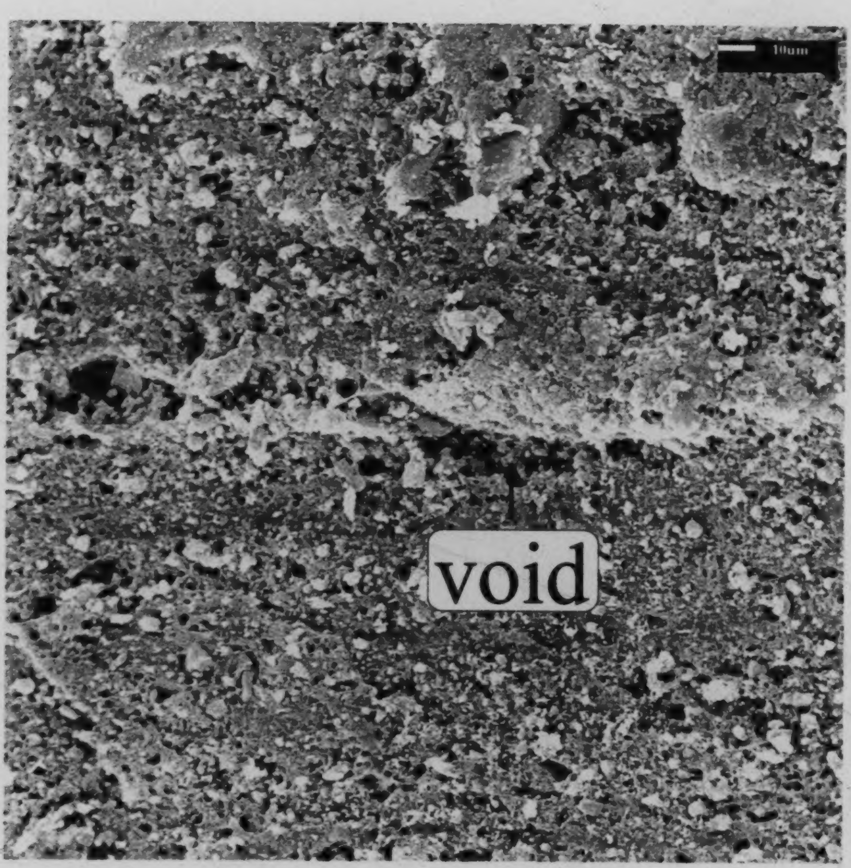

Figure 5.17: High resolution SEM of a void in the $y - z$ plane.

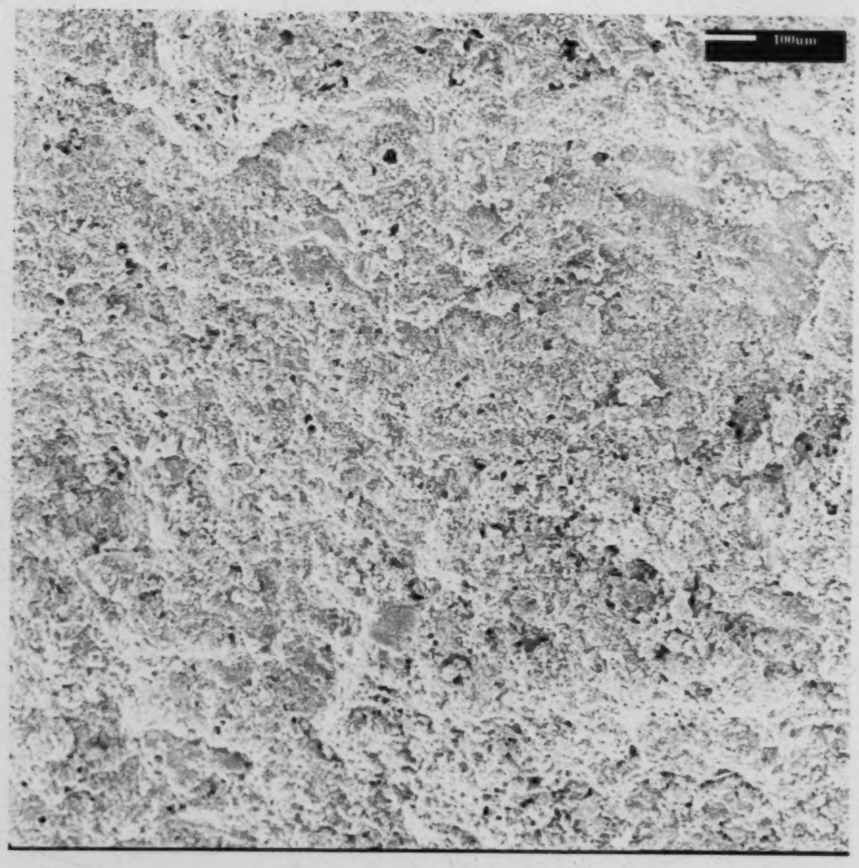

Figure 5.18: Low resolution SEM view of layering in the $x - y$ plane.

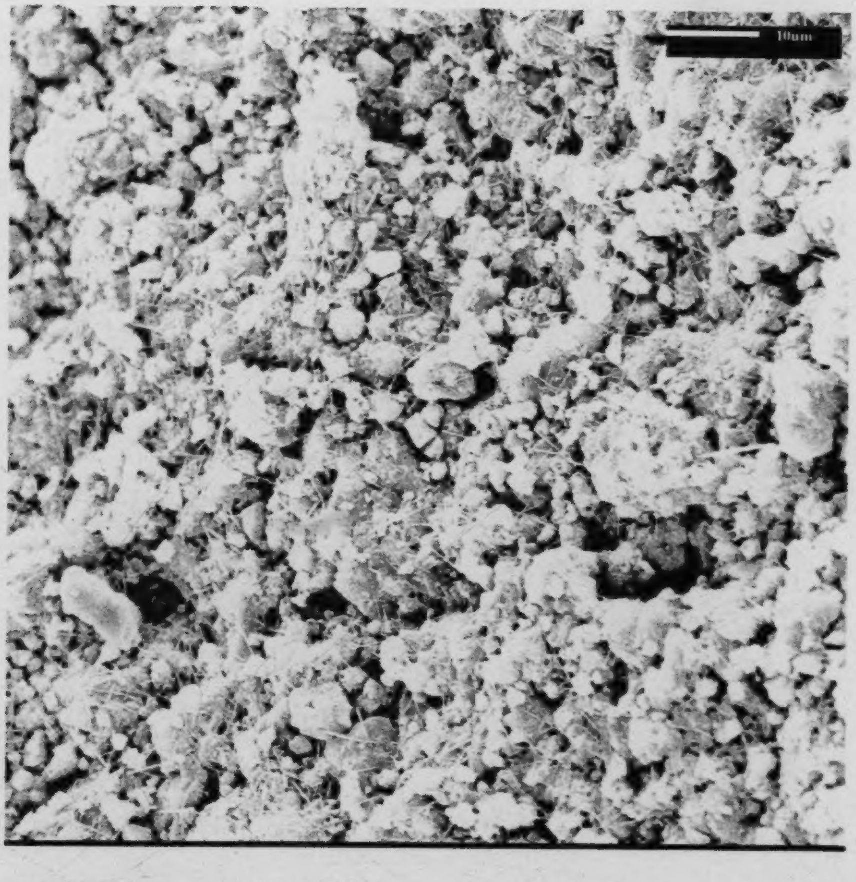

Figure 5.19: High resolution SEM view of layering in the $x - y$ plane showing unidentifiable needle-shaped particles.

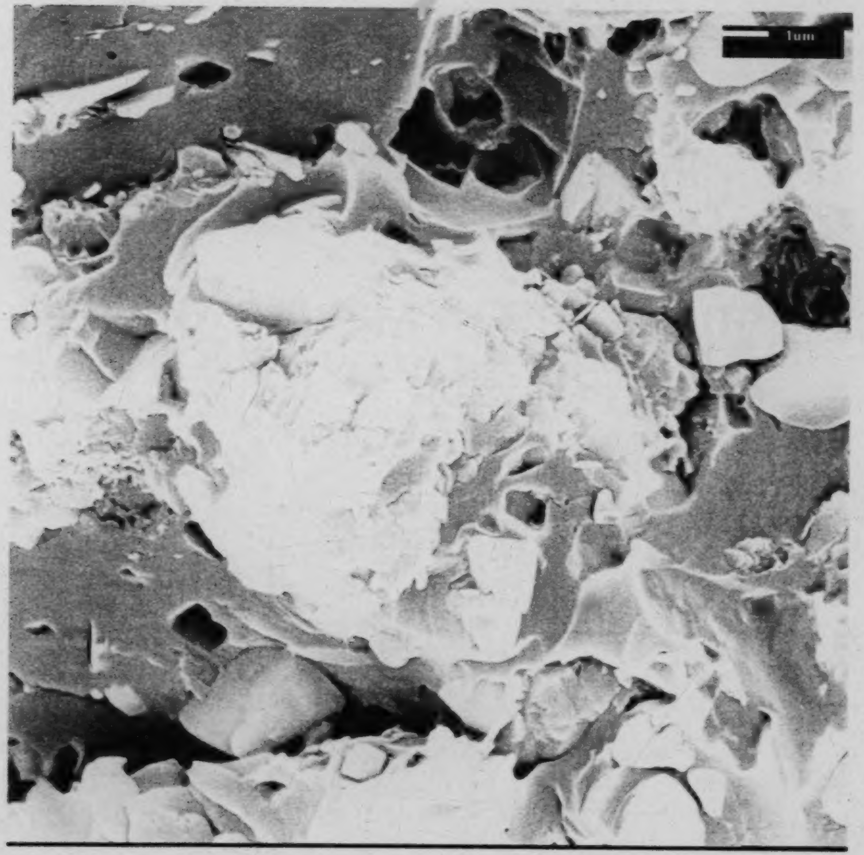

Figure 5.20: High resolution SEM view of the dolomite chunk in the $y-z$ plane.

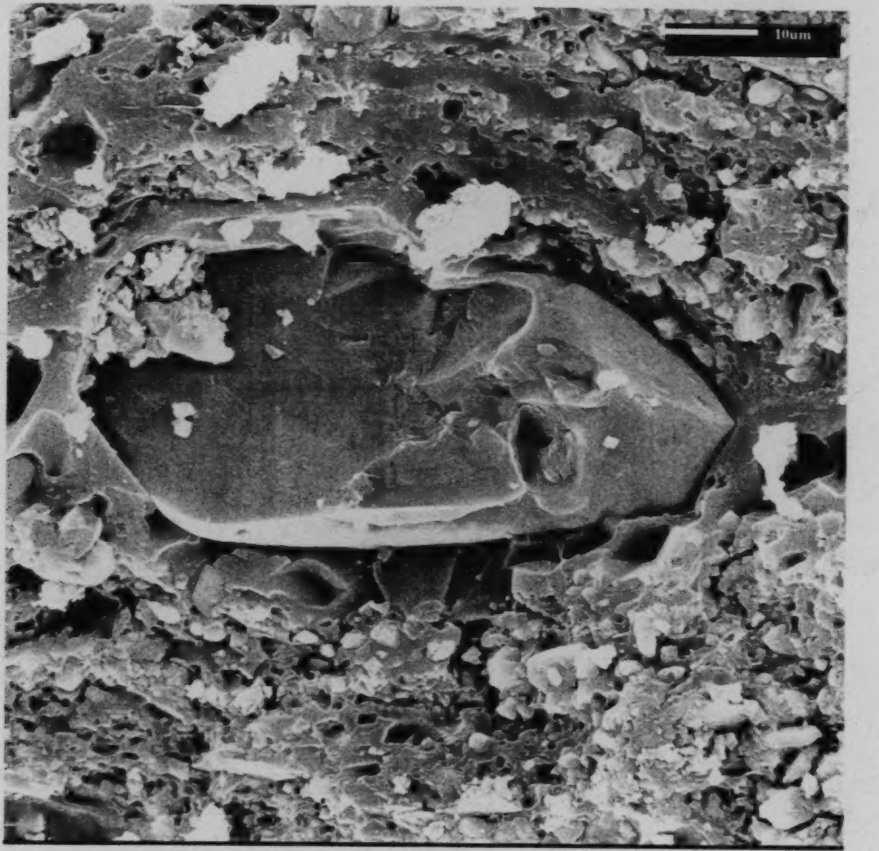

Figure 5.21: High resolution SEM view of quartz grain in the $x - z$ plane.

Overall, scanning electron microscopy allowed us to determine that the oil shale sample contained dolomite, albite, anorthoclase, and some other titanium rich mineral and that the average grain size was on the order of 1 μm except for dolomite that had the occasional grain with a diameter of about 7 μm. This did not preclude the presence of other minerals. It showed us that the sample was composed of minerals in layers that were approximately perpendicular to the $z - axis$ and that the layer thickness was on the order of tens of μm. Angular grains of dolomite were found that indicated they might have been formed in solution by direct precipitation. Angular to subangular grains of quartz were found that indicated this quartz was not transported far from its source.

5.7 Electron microprobe

5.7.1 What is electron microprobing?

Electron microprobing was conceived by R. Castaing and A. Guinier in 1949 in a report presented to the Electron Microscope Conference in Delft, Netherlands (Beaman & Isasi, 1972; Birk, 1963; Theisen, 1965). The report described a method of using an electron microscope to focus a beam of electrons on a sample coupled with an attached x-ray spectrometer to measure the X-rays given off from the sample. The wavelengths of the X-rays (λ) can be measured and the atomic numbers and/or elements present at that point can be determined using Equation 5.4. The use of precise motors that allow detailed controlled movements of the sample allows the determination of the elements that are present at a given spot throughout the sample that in turn allows us to perform detail spectrochemical analysis of the whole sample.

As described previously, electron microprobing is an extension of the scanning electron microscope (See Figure 5.12). So similarly it has a filament and anode (electron gun) as well as a condenser lens and objective lens in addition to gun alignment coils and deflection coils (Figure 5.22). The electron beam is generated by heating the tungsten filament to about 2800 K and putting a potential of 1-50 kV across the filament and anode. The gun alignment coils are used to ensure that the electron beam is centered along the optical axis of the electron microprobe. The condenser and objective lenses focus the electron beam while the condenser lens and objective aperture control the beam current and beam diameter. The beam current is monitored by the probe current detector (PCD). The deflection coils control the scanning of the electron beams.

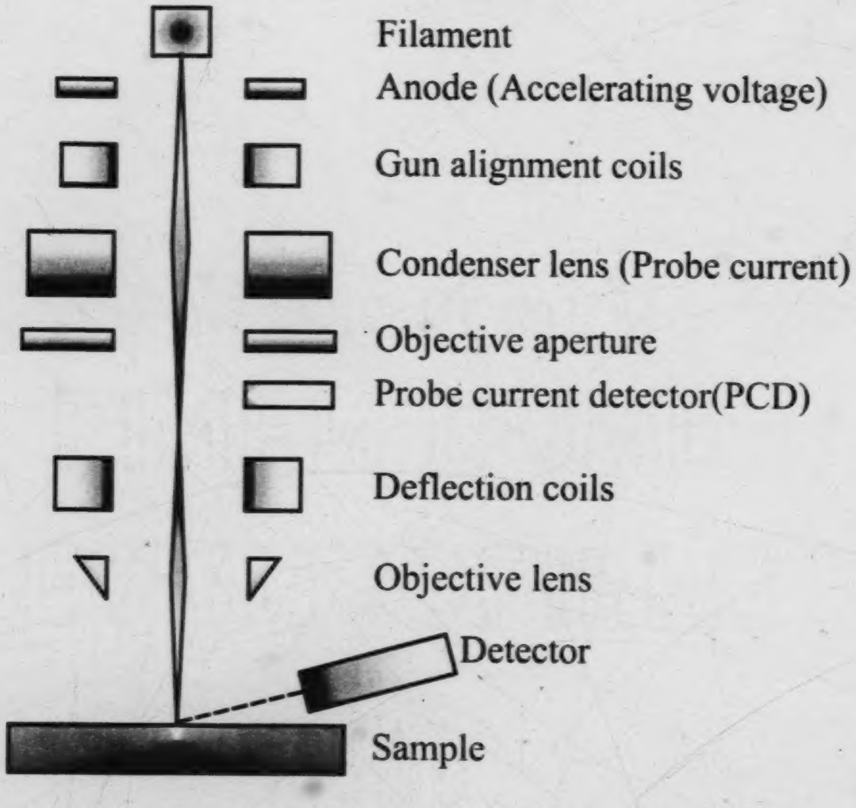
Filament
Anode (Accelerating voltage)
Gun alignment coils
Condenser lens (Probe current)
Objective aperture
Probe current detector(PCD)
Deflection coils
Objective lens
Detector
Sample

Figure 5.22: Diagram of electron microprobe.

When the electron beam hits the sample, Bremsstrahlung, Auger electrons, backscattered electrons, secondary electrons, visible light, X-rays, and heat are given off (Figure 5.23). Bremsstrahlung is radiation that is given off by a charged particle (i.e., an electron) when it undergoes deceleration such as when it hits the nucleus of an atom. Backscattered electrons are electrons that have struck atoms within the sample and have re-emerged from it. Backscattered electrons generally have much higher energies (>> 50 eV) than secondary electrons (<< 50 eV) (Reed, 1975). Secondary electrons are electrons that were initially part of the sample but have received enough energy from collisions with the incident electron beam to be released from the sample. Just like secondary electrons, auger electrons are emitted due to collisions with the incident electron beam but are formed without the generation of X-rays. According to Heinrich (1981) when an electron is removed from the inner shell of an atom, an electron drops from an outer shell to fill this vacancy. However, stored potential energy is freed which may either be spent generating an X-ray photon or be spent freeing an outer electron (Auger electron) from orbit. As mentioned previously, sometimes an X-ray photon is generated (Heinrich, 1981). These X-rays have a characteristic energy that can be detected by either an energy dispersive spectrometer (EDS) or wavelength dispersive spectrometer (Beaman & Isasi, 1972) which in turn can indicate which element from which the X-ray was generated. The energy of the X-ray is related to the atomic number by Moseley's Law:

$$E = K\,(Z - 1)^2 \tag{5.5}$$

where E is the energy of the X-ray in keV, Z is the atomic number (i.e., 1 for hydrogen, 2 for helium, etc ...), and $K = 1.042 \times 10^{-2}$ keV for electron displacement from the inner most electron shell.

Not only can the element be determined by the energy of the X-ray but also the relative concentrations of the elements can be determined by the rate at which the X-rays are detected. As well, visible light and heat are given off by the collision of the electron beam with the sample. The source of this visible light is cathodoluminescence that is caused by the primary electron beam (Heinrich, 1981).

Not all of the interactions are measured. Only the backscattered electrons, secondary electrons, X-rays and visible light are measured over the surface of the sample giving us maps of the element concentrations, surface topography, and luminescent minerals. The topography of the sample can be determined by

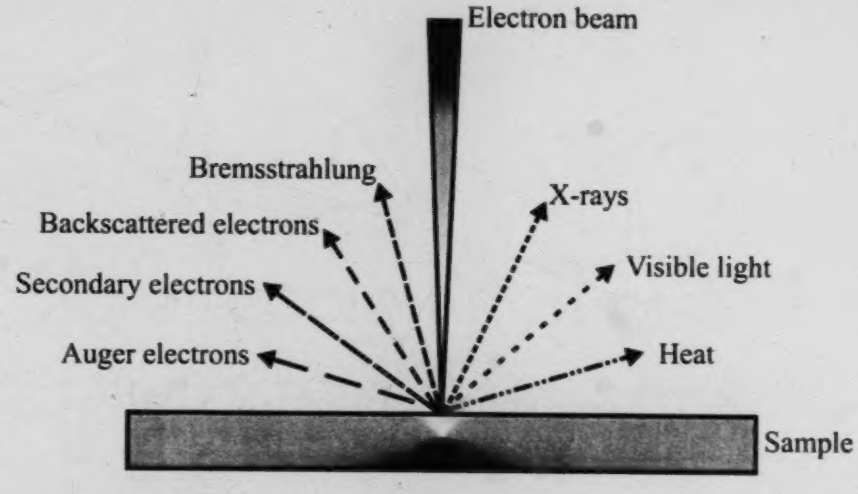

Figure 5.23: The electron beam striking the sample causes the production of backscattered electrons, secondary electrons, Auger electrons, Bremsstrahlung, X-rays, heat, and light.

analyzing the backscattered electron images.

5.7.2 Electron microprobe results

The electron microprobe work was performed at the University of Alberta in the Electron Microprobe Laboratory located in the Earth and Atmospheric Sciences building. The facility employs a JEOL 8900 microprobe that employs both a wavelength dispersive spectrometer (WDS) and an energy dispersive spectrometer (EDS). For analysis of the sample, only the energy dispersive spectrometer was used. Sample preparation consisted of specially prepared thin sections coated with carbon to reduce electrical resistance. Three thin sections were prepared, each mutually perpendicular with their surfaces parallel and perpendicular to the coordinate system previously chosen (See Figure 5.3). The sample was analyzed using an accelerating voltage of 15.0 kV and a probe current of 2.000×10^{-8} A. Typically, elements were scanned for aluminum, calcium, carbon, iron, magnesium, potassium, silicon, sodium, and sulfur. As well, other elements such as titanium were measured.

A sample in the $y - z$ plane was analyzed for aluminum, calcium, carbon, iron, magnesium, potassium, silicon, sodium, and sulfur as shown in Figures 5.24 through 5.32. Further analysis of the concentrations of the elements as determined by electron microprobe images yielded images of the various minerals. Assuming that the minerals as determined by X-ray diffraction are present, the minerals albite, anorthoclase, calcite, dawsonite, dolomite, pyrite, and quartz were determined as shown in Figures 5.33, 5.34, 5.35, 5.36, 5.37, 5.40, and 5.41, respectively. Further analysis of the element concentrations showed areas where relatively high amounts of potassium, aluminum, and silicon were present. Both orthoclase ($KAlSi_3O_8$) and illite ($K_{1-1.5}Al_4$ $(Si_{7-6.5} \cdot Al_{1-1.5} \cdot O_{20})$ $(OH)_4$) contain potassium, aluminum, and silicon. Illite was included in the analysis, orthoclase was not because it is more likely that illite is present in the sample. The illite in the sample seems to be spotty (Figure 5.39). Analysis of the Figures 5.33, 5.34, 5.35, 5.36, 5.37, 5.40, and 5.41 yielded the relative amounts of non-kerogenous minerals (Table 5.5) that are present in this sample. If one assumes that the sample contains 49.20 wt. % kerogen as derived by whole-rock analysis, the relative amounts of all minerals present (Table 5.6) can be determined from the relative amounts of the non-kerogenous minerals (Table 5.5).

Further examination of Figures 5.24 through 5.37, 5.39, 5.40, and 5.41 shows that this layering in the oil shale is quite pervasive and is observable on many different scales right down the microscopic with the average layer thickness of 35 μm. It also showed that kerogen was prevalent throughout the sample with layers of other minerals distributed within the kerogen. In depth analysis of Figures 5.27 and 5.28 showed the presence of a ferromagnesium mineral that was not found in X-ray diffraction test (Figure 5.38). It is possible that this mineral is

Mineral	weight %
Albite	13.85
Anorthoclase	0.25
Calcite	17.60
Dawsonite	0.23
Dolomite	26.76
Illite	9.86
Pyrite	18.02
Quartz	13.41
Total	99.98

Table 5.5: Relative amounts of non-kerogenous minerals in oil shale sample in $y - z$ plane sample.

Mineral	weight %
Albite	7.04
Anorthoclase	0.13
Calcite	8.94
Dawsonite	0.12
Dolomite	13.59
Illite	5.01
Pyrite	9.15
Quartz	6.81
Kerogen	49.20
Total	99.99

Table 5.6: Relative amounts of minerals in oil shale sample in $y - z$ plane sample.

ankerite ((Ca, Mg, Fe) $(CO_3)_2$) that has been observed previously in the area (Cole & Picard, 1978) but without additional testing this cannot be confirmed.

According to Tucker & Wright (1990) there are 5 different scenarios under which dolomite can be formed:

- evaporative dolomitization - dolomite is formed by direct precipitation out of solution in evaporitic environments where water with a high Mg/Ca ratio is concentrated by evaporation until dolomite is precipitated
- seepage-reflux dolomitization - dolomitizing or magnesium rich fluids are generated through evaporation of lagoon water or tidal flat pore waters. These dolomitizing fluids seep into underlying carbonate sediments and alter them to dolomite.
- mixing zone dolomitization - seawater mixes with fresh ground water forming a dilute solution with a high Mg/Ca ratio that seeps into pre-existing limestone. The dilute solution allows dolomite to be formed much easier.
- burial dolomitization - compaction of sediments in a basin dewaters the sediments which in turn produces Mg^{2+} rich fluids that dolomitize the calcite through which the fluids travel
- sea water dolomitization - sea water flows through carbonate sediments directly and alters them to dolomite

All of the 5 previous scenarios require that the Mg/Ca ratio of the fluids be at least greater than 5 which is confirmed by other works (Gaines, 1990; Carpenter, 1990) and may be applicable to the Piceance Creek basin even though it is a lacustrine depositional environment and not a marine depositional environment.

The previous 5 scenarios can be divided into 2 major groups, primary dolomite precipitation and dolomite generation by alteration of carbonates. Primary dolomite precipitation is formed from solution through the following reaction:

$$Ca^{2+} + Mg^{2+} + 2(CO_3^{2-}) = CaMg(CO_3)_2 \ , \qquad (5.6)$$

and dolomitization of carbonates is formed by alteration of carbonates by the following reaction:

$$2CaCO_3 + Mg^{2+} = CaMg(CO_3)_2 + Ca^{2+} \ . \qquad (5.7)$$

According to Tucker & Wright (1990), it is more likely to have dolomite formed by replacement of calcite ($CaCO_3$) even though dolomite has been observed to be deposited by direct precipitation (Friedman, 1980). However, closer examination of Figures 5.35 and 5.37 shows that the calcite and dolomite present tend to be distributed differently. While calcite tends to form thin layers or small grains approximately a few μm in diameter, dolomite forms larger grains which are generally greater than 5 μm in diameter and do not form thin layers. This tends to imply that dolomite was not formed by replacement of calcite. If dolomite was formed by replacement of calcite, the dolomite distribution would be more uniform instead of forming layers as seen in Figure 5.37. Furthermore, if dolomite was formed by direct precipitation it may form the larger grains seen in Figure 5.37. If dolomite was formed by direct precipitation this would imply that the depositional environment of the Piceance Creek Basin was indeed more like the Green River model (Eugster & Surdam, 1973; Lundell & Surdam, 1975; Surdam & Wolfbauer, 1975) than the deep anoxic lake model (Bradley, 1966; Bradley and Eugster, 1969; Cole, 1984; Desborough, 1978; Johnson, 1981; Smith, 1983; Smith & Lee, 1982; Tuttle & Goldhaber, 1991).

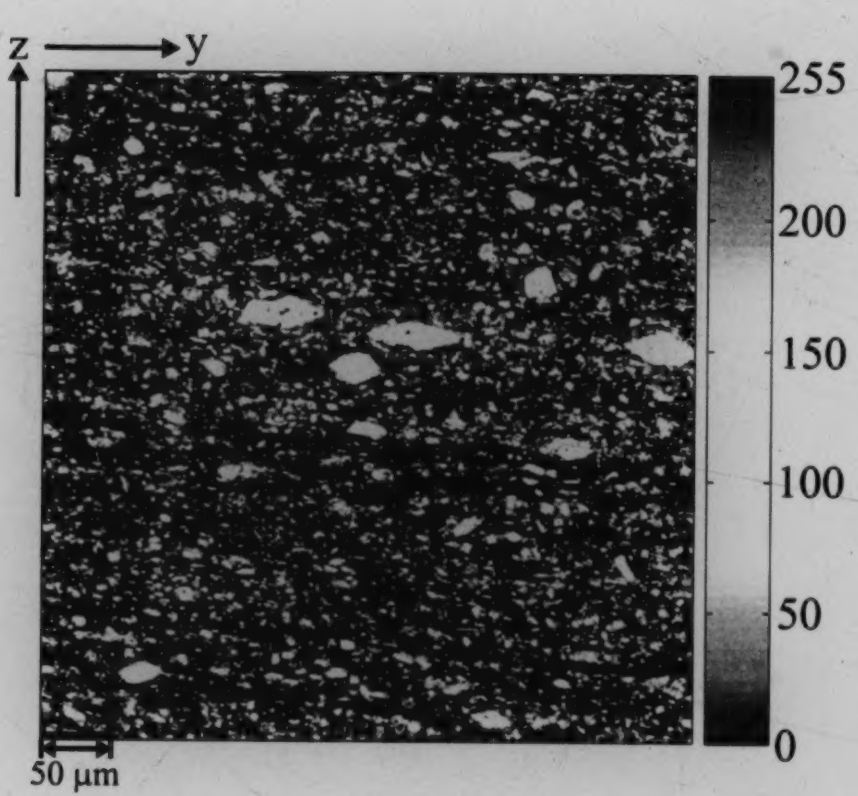
z
y
255
200
150
100
50
0
50 μm

Figure 5.24: Electron microprobe image of aluminium in the $y - z$ plane where scale on right-hand side indicates relative concentration.

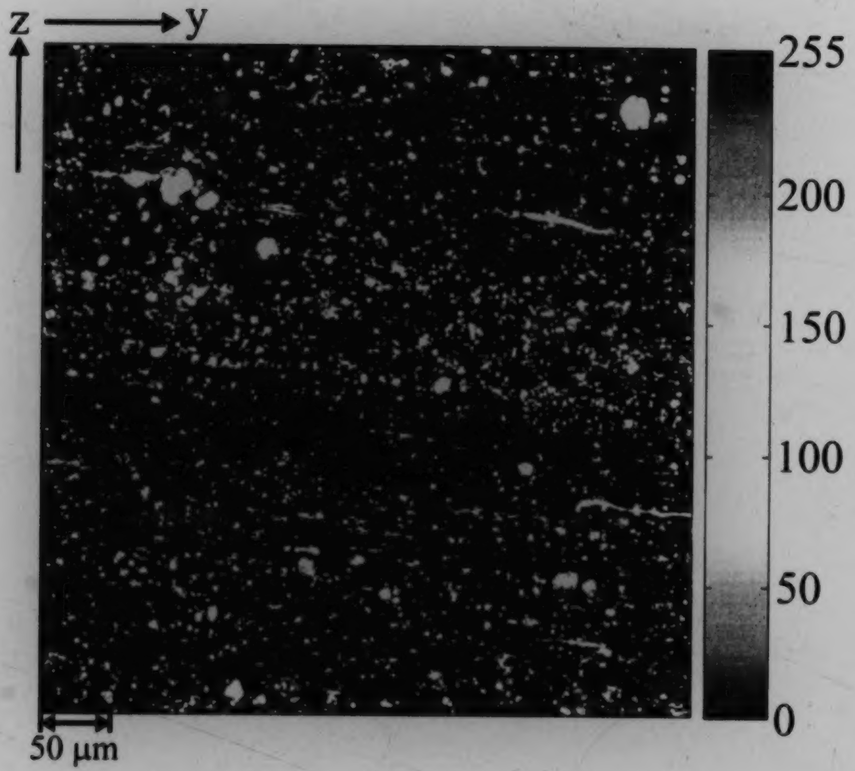
z
y
255
200
150
100
50
0
50 μm

Figure 5.25: Electron microprobe image of calcium in the $y - z$ plane where scale on right-hand side indicates relative concentration.

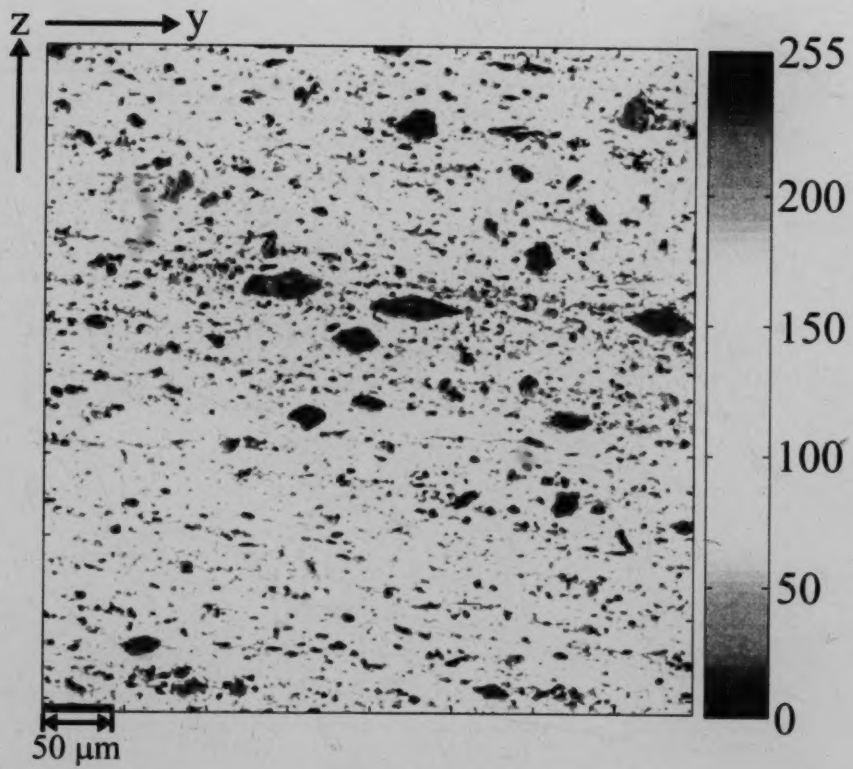
z
y
255
200
150
100
50
0
50 μm

Figure 5.26: Electron microprobe image of carbon in the $y - z$ plane where scale on right-hand side indicates relative concentration.

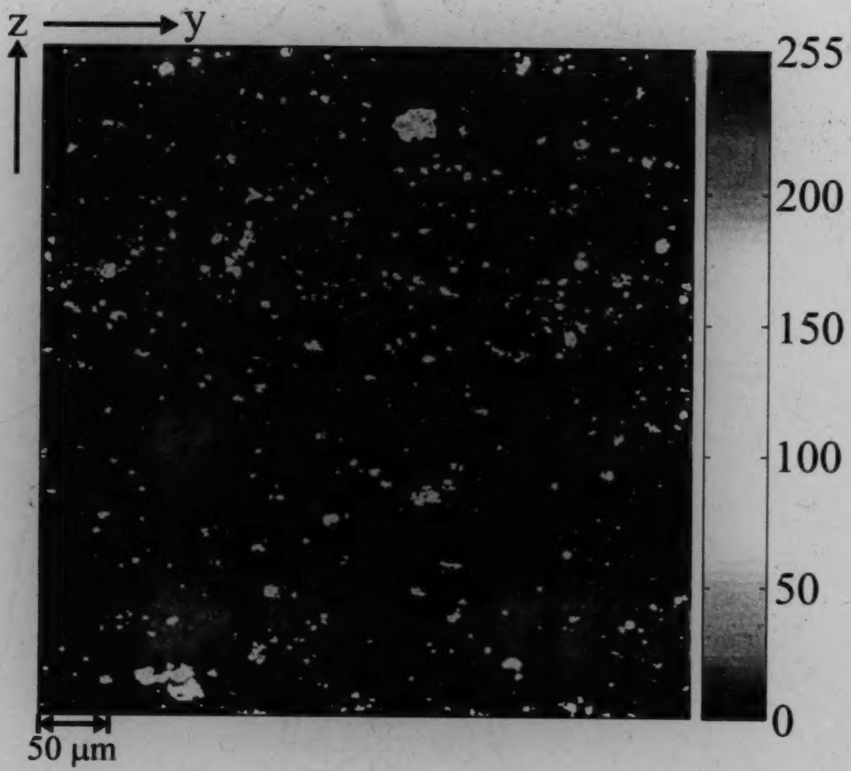
z
y
255
200
150
100
50
0
50 μm

Figure 5.27: Electron microprobe image of iron in the $y - z$ plane where scale on right-hand side indicates relative concentration.

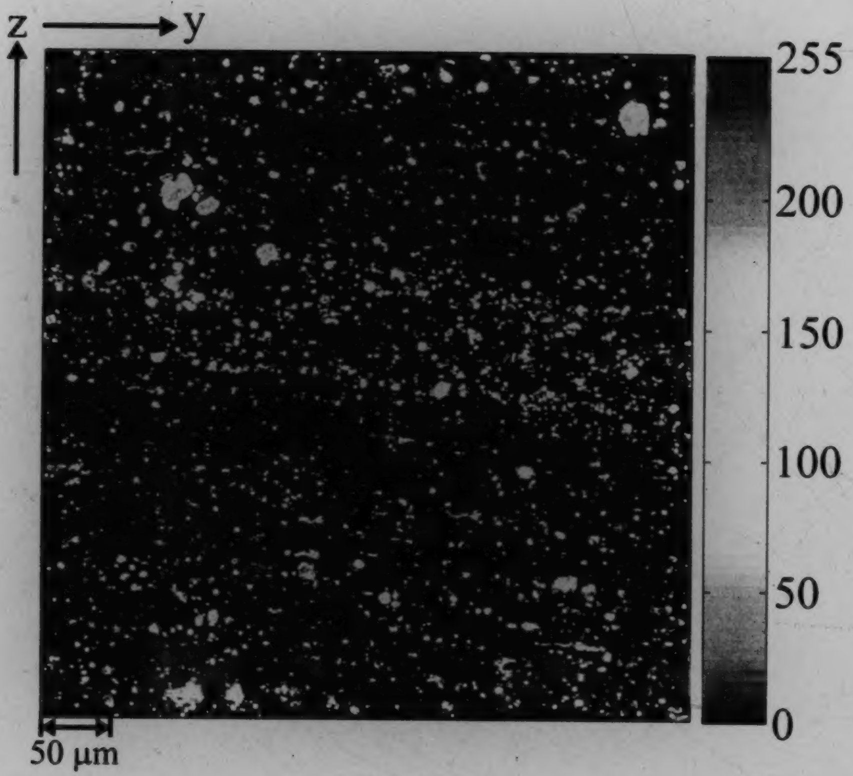
z
y
255
200
150
100
50
0
50 μm

Figure 5.28: Electron microprobe image of magnesium in the $y - z$ plane where scale on right-hand side indicates relative concentration.

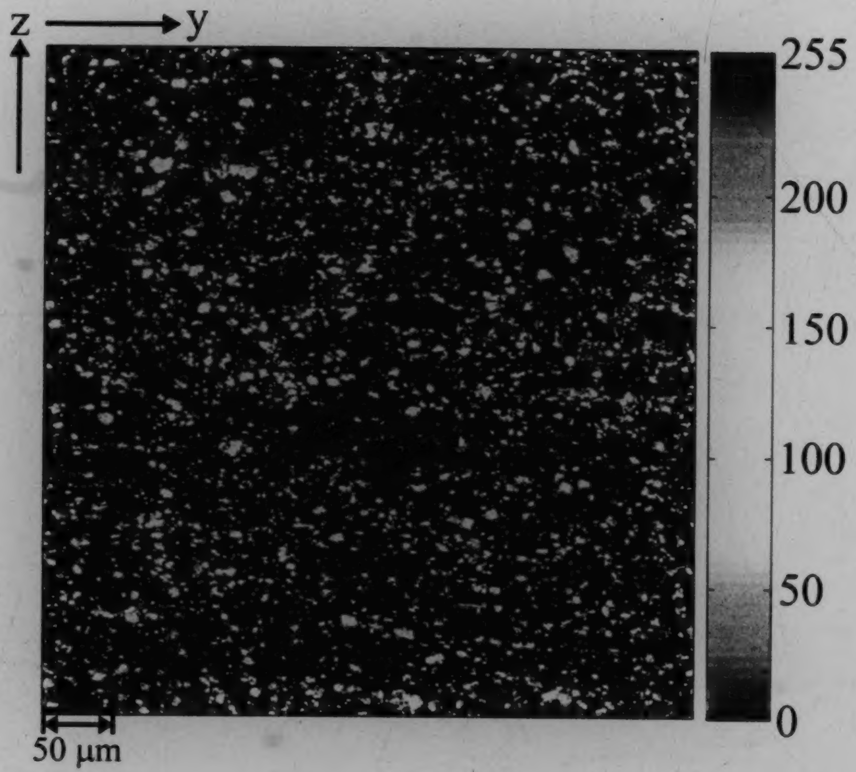
z
y
255
200
150
100
50
0
50 μm

Figure 5.29: Electron microprobe image of potassium in the $y - z$ plane where scale on right-hand side indicates relative concentration.

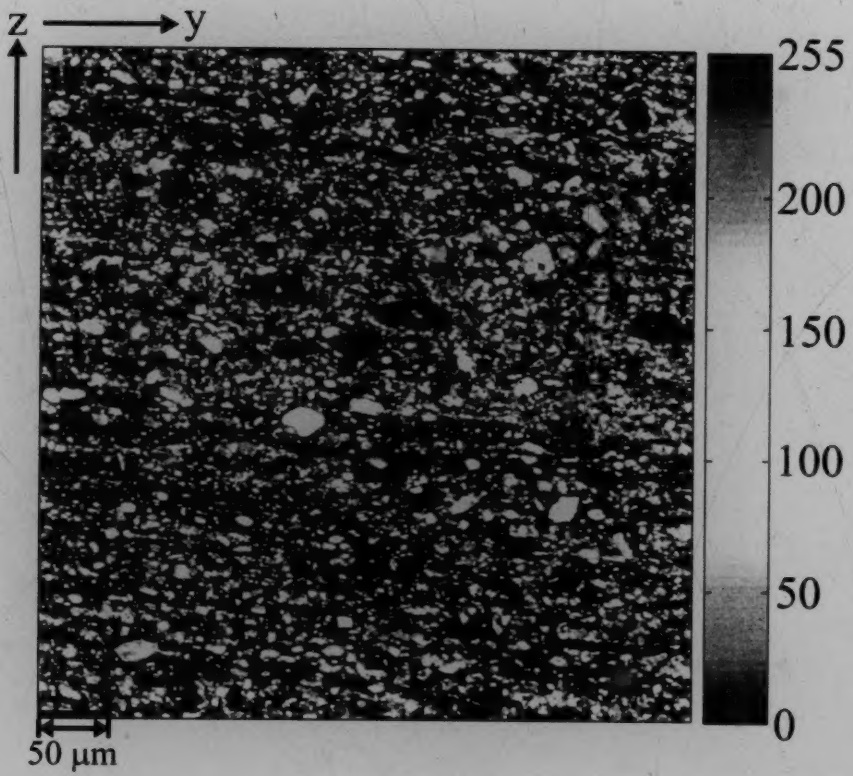
z
y
255
200
150
100
50
0
50 μm

Figure 5.30: Electron microprobe image of silicon in the $y - z$ plane where scale on right-hand side indicates relative concentration.

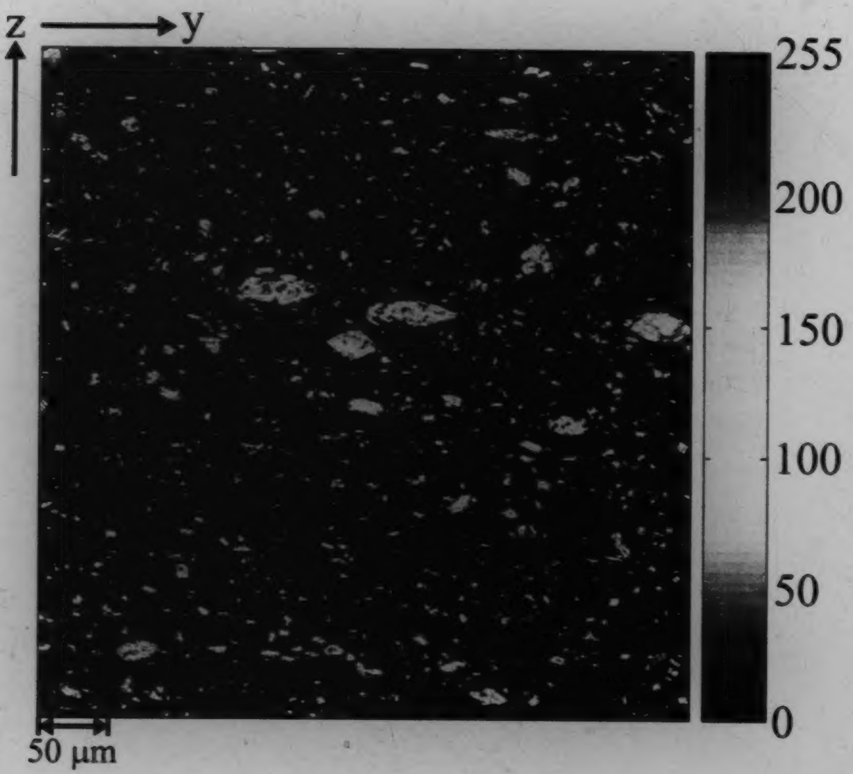
z
y
255
200
150
100
50
0
50 μm

Figure 5.31: Electron microprobe image of sodium in the $y-z$ plane where scale on right-hand side indicates relative concentration.

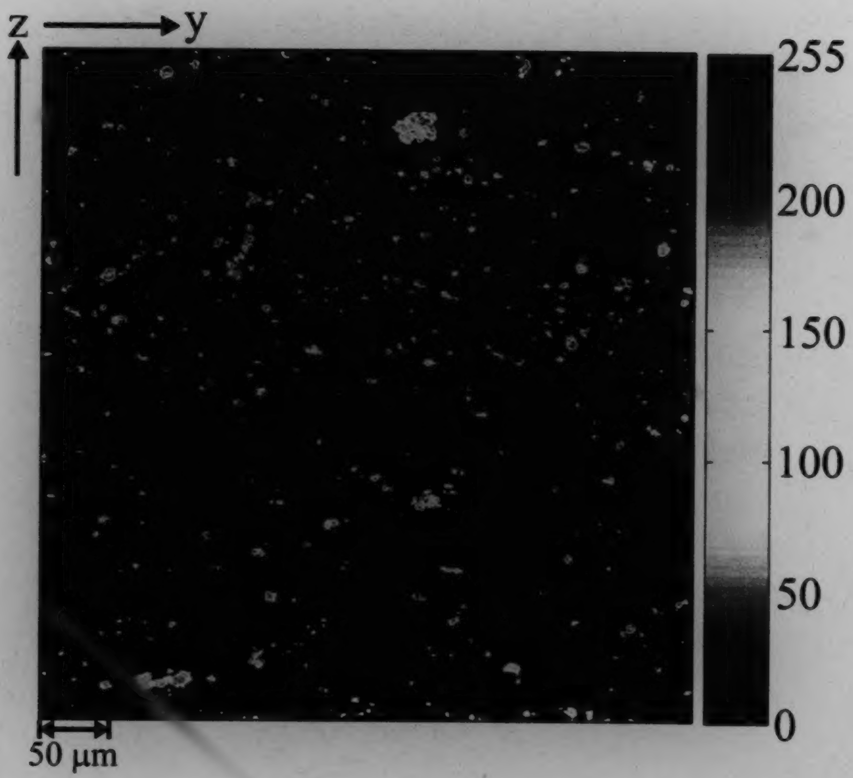
z
y
255
200
150
100
50
0
50 μm

Figure 5.32: Electron microprobe image of sulfur in the $y - z$ plane where scale on right-hand side indicates relative concentration.

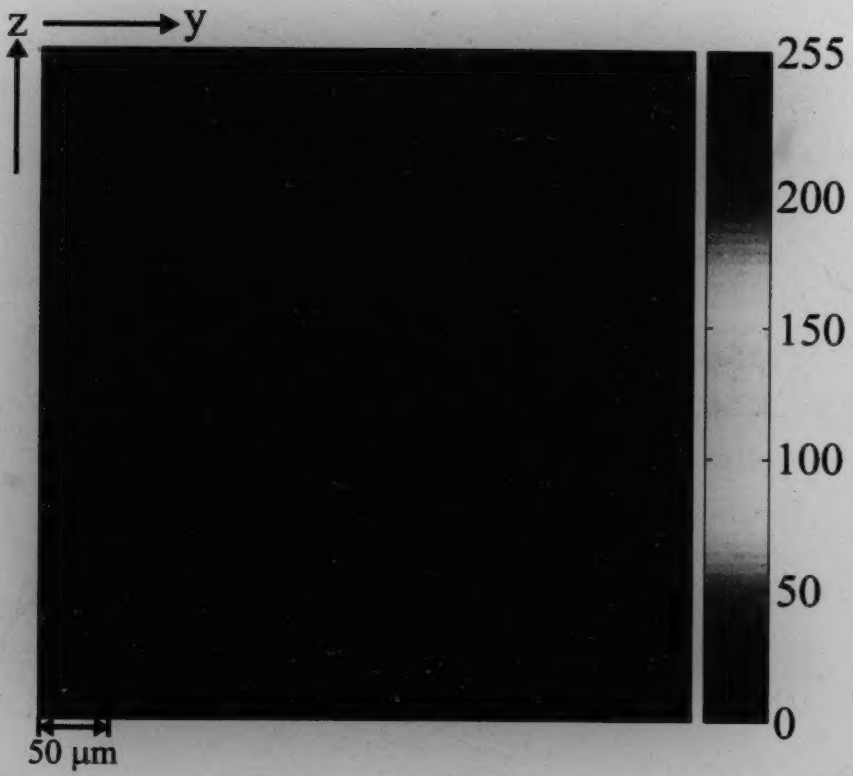
z
y
255
200
150
100
50
0
50 μm

Figure 5.33: Computed electron microprobe image of albite in the $y - z$ plane where scale on right-hand side indicates relative concentration.

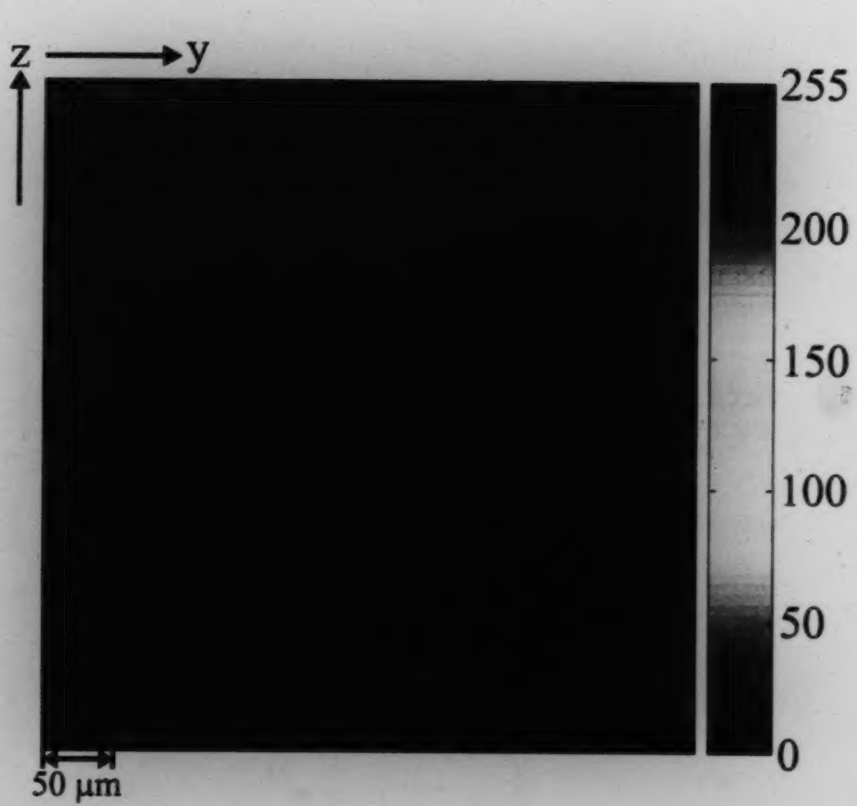
z
y
255
200
150
100
50
0
50 µm

Figure 5.34: Computed electron microprobe image of anorthoclase in the $y-z$ plane where scale on right-hand side indicates relative concentration.

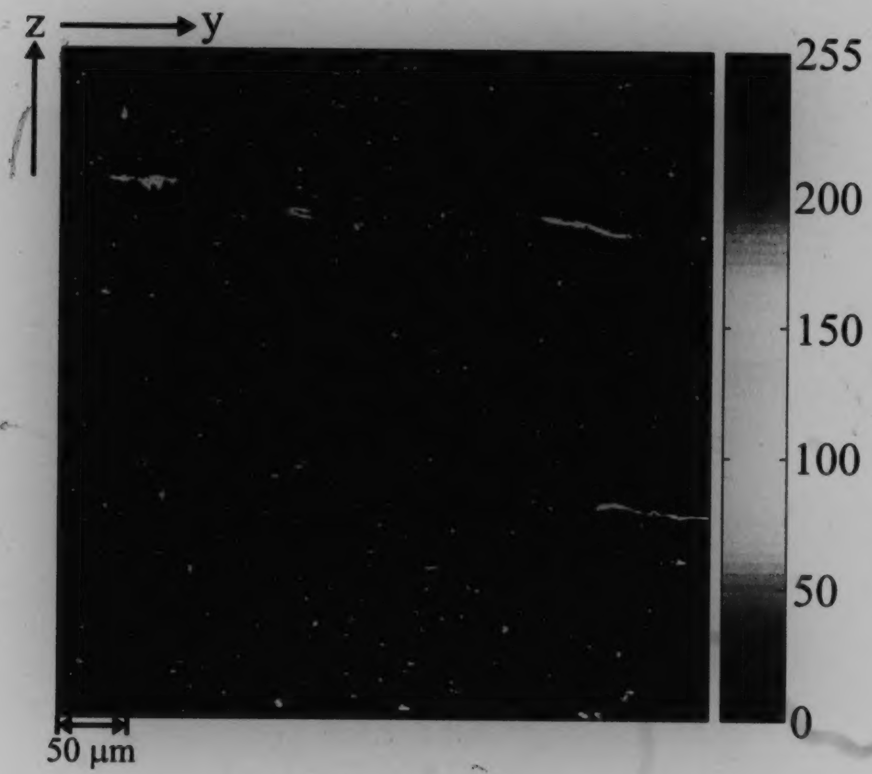
z
y
255
200
150
100
50
0
50 μm

Figure 5.35: Computed electron microprobe image of calcite in the $y - z$ plane where scale on right-hand side indicates relative concentration.

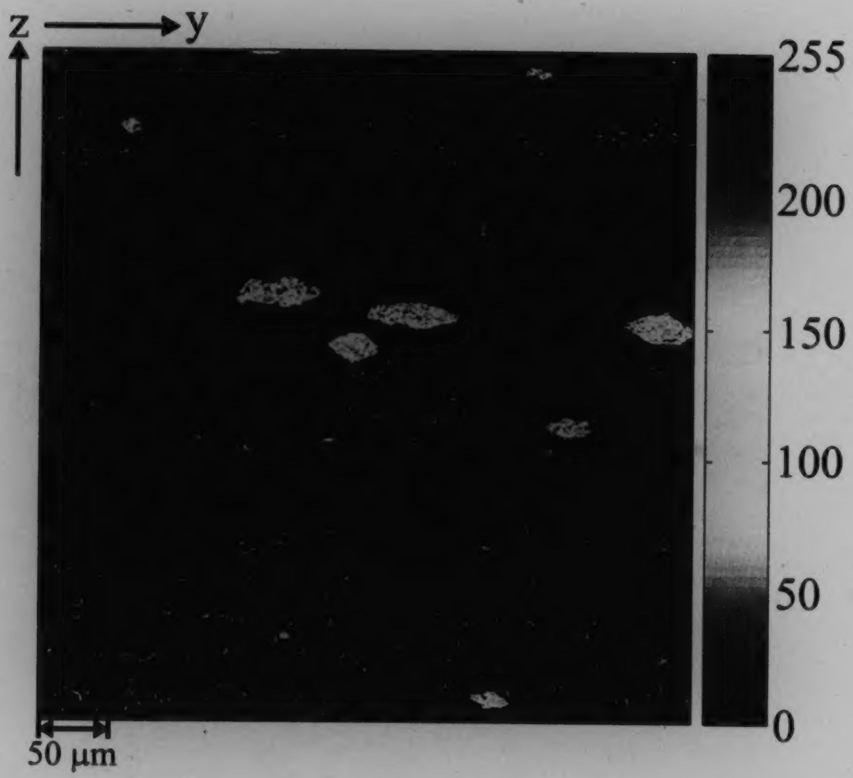
z
y
255
200
150
100
50
0
50 μm

Figure 5.36: Computed electron microprobe image of dawsonite in the $y - z$ plane where scale on right-hand side indicates relative concentration.

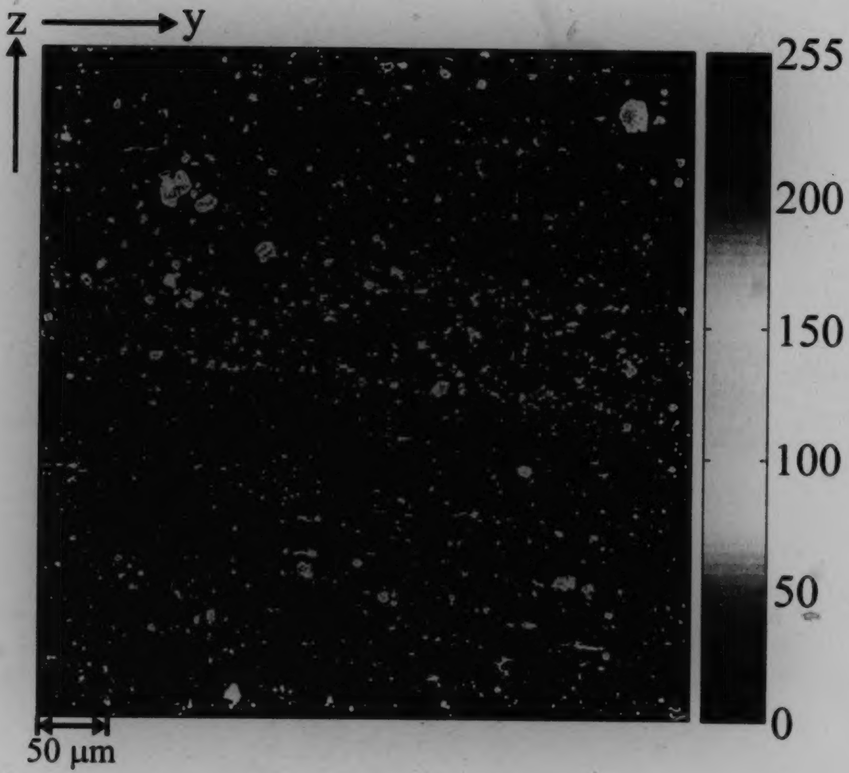
z
y
255
200
150
100
50
0
50 μm

Figure 5.37: Computed electron microprobe image of dolomite in the $y - z$ plane where scale on right-hand side indicates relative concentration.

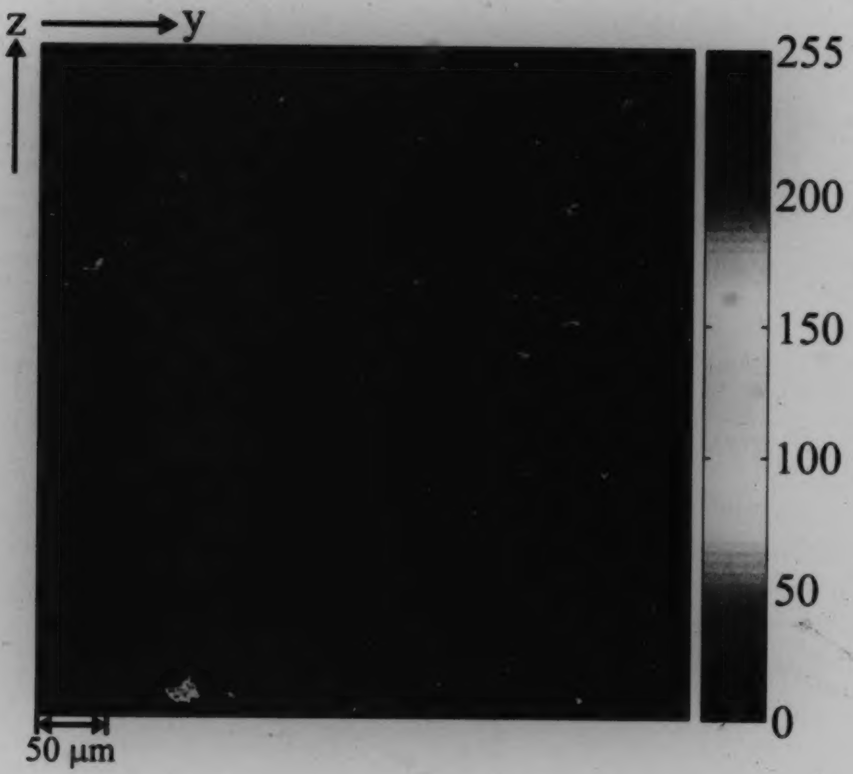
z
y
255
200
150
100
50
0
50 μm

Figure 5.38: Computed electron microprobe image of a ferromagnesium mineral in the $y-z$ plane where scale on right-hand side indicates relative concentration.

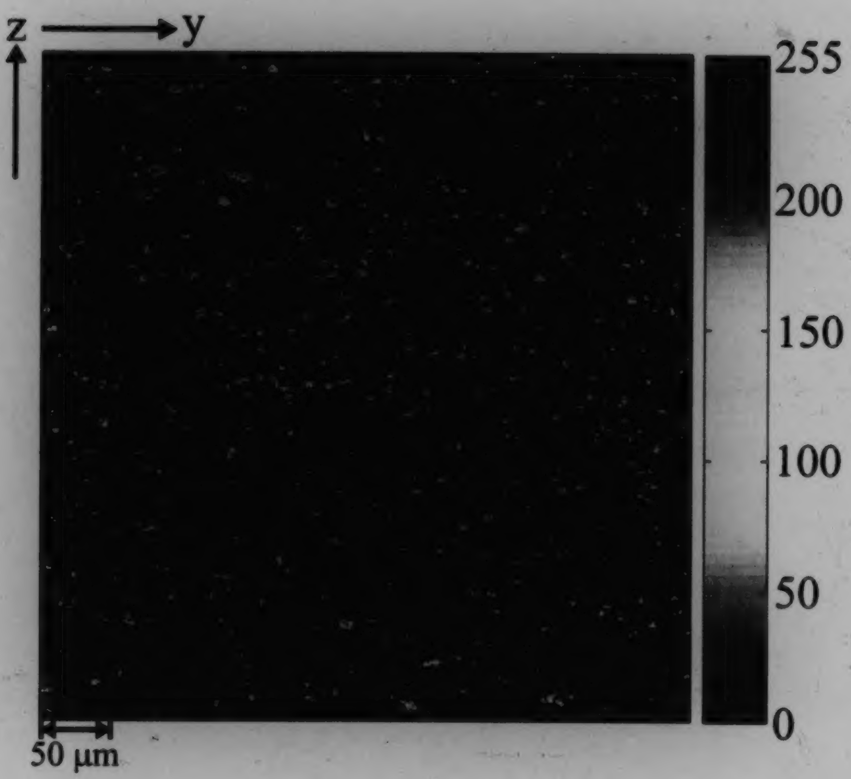
z
y
255
200
150
100
50
0
50 μm

Figure 5.39: Computed electron microprobe image of illite in the $y-z$ plane where scale on right-hand side indicates relative concentration.

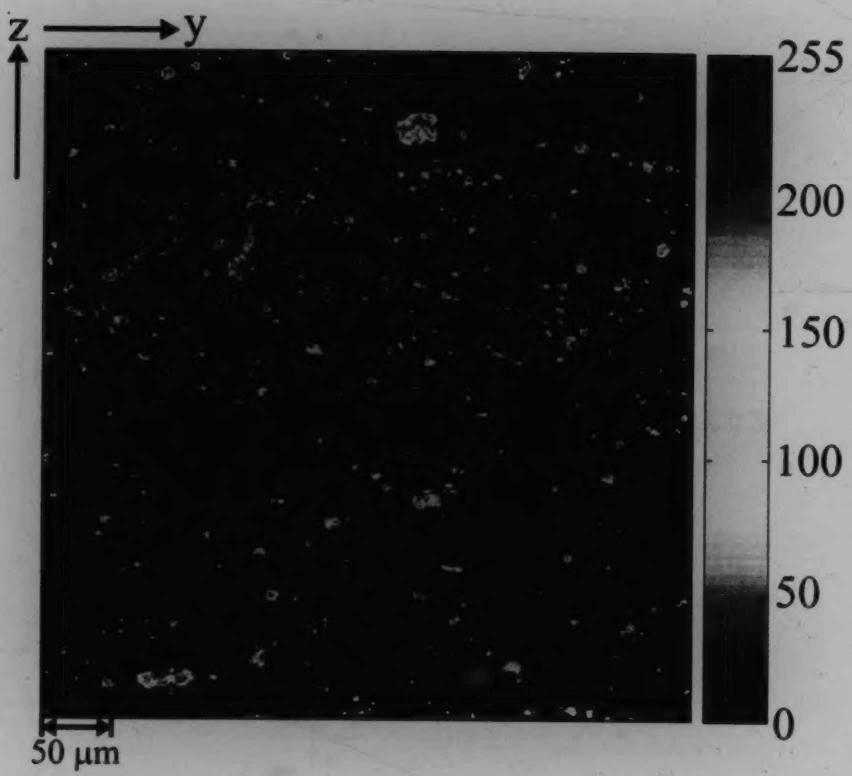
z
y
255
200
150
100
50
0
50 μm

Figure 5.40: Computed electron microprobe image of pyrite in the $y - z$ plane where scale on right-hand side indicates relative concentration.

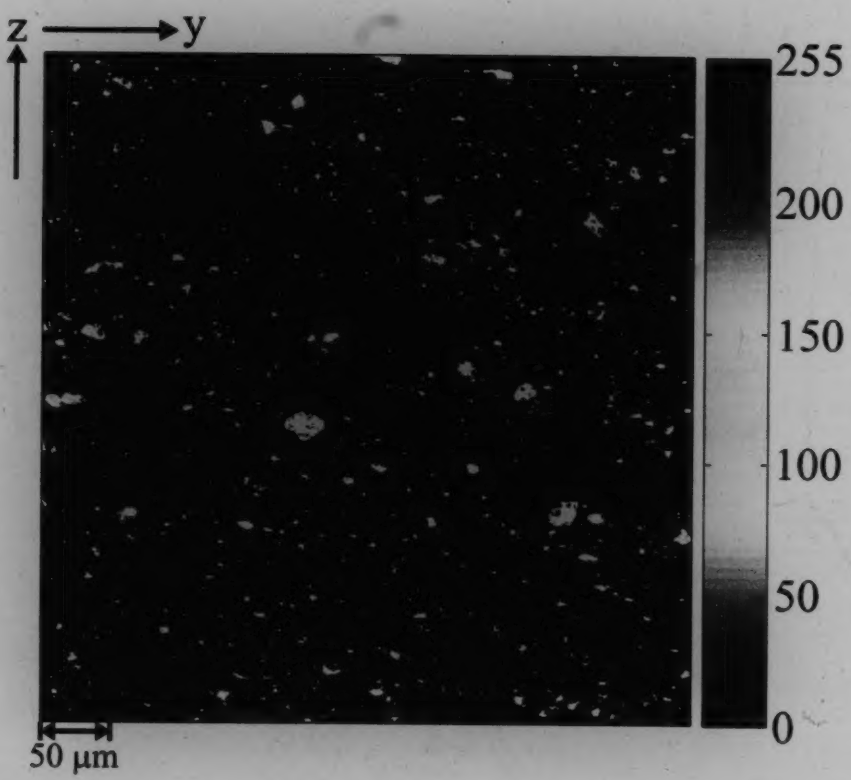
z
y
255
200
150
100
50
0
50 μm

Figure 5.41: Computed electron microprobe image of quartz in the $y - z$ plane where scale on right-hand side indicates relative concentration.

Another sample in the $x - z$ plane was analyzed for calcium, carbon, iron, magnesium, sulfur, and titanium are shown in Figures 5.42, 5.43, 5.44, 5.45, 5.46, and 5.47, respectively. Further analysis of these elemental concentrations yielded images of calcite, dolomite, a ferromagnesium mineral, ilmenite, and pyrite in Figures 5.48, 5.49, 5.50, 5.51, and 5.52, respectively. Closer examination of Figures 5.48 and 5.49 showed the same differences between calcite and dolomite as seen previously in the $y - z$ plane where the calcite grains tend to be smaller than the dolomite particles however the calcite did not form thin layers as previously seen. As well, the presence of trace amounts of a mineral that contains both iron and titanium was found (Figure 5.51) and is thought to be most likely ilmenite ($FeTi0_3$) even though such a mineral was not identified using X-ray diffraction. This may be due to the small quantity of ilmenite present in the sample.

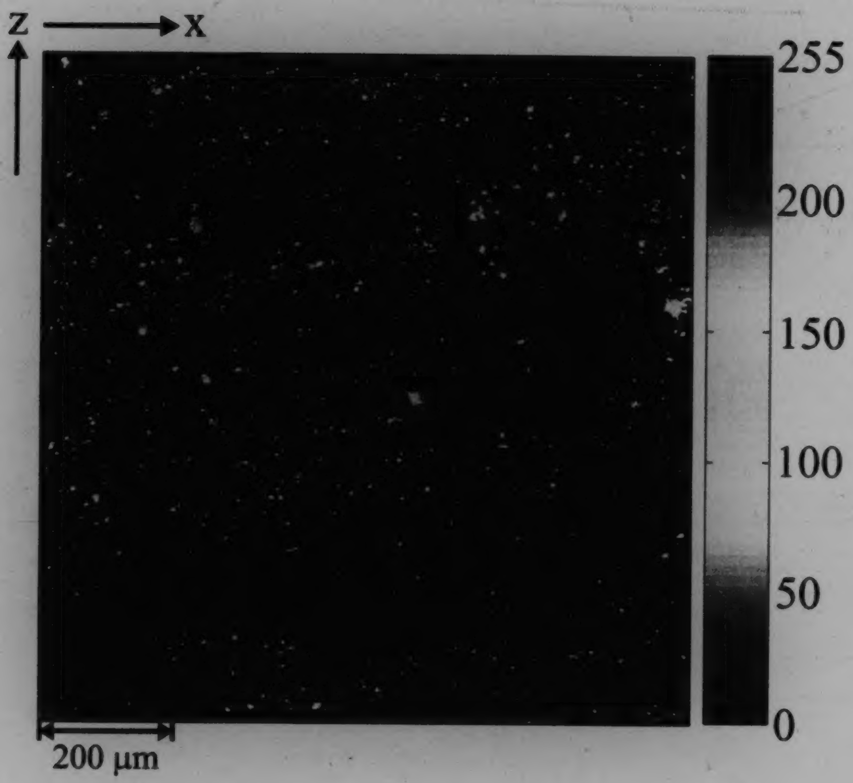
Z
X
255
200
150
100
50
0
200 μm

Figure 5.42: Electron microprobe image of calcium in the $x - z$ plane where scale on right-hand side indicates relative concentration.

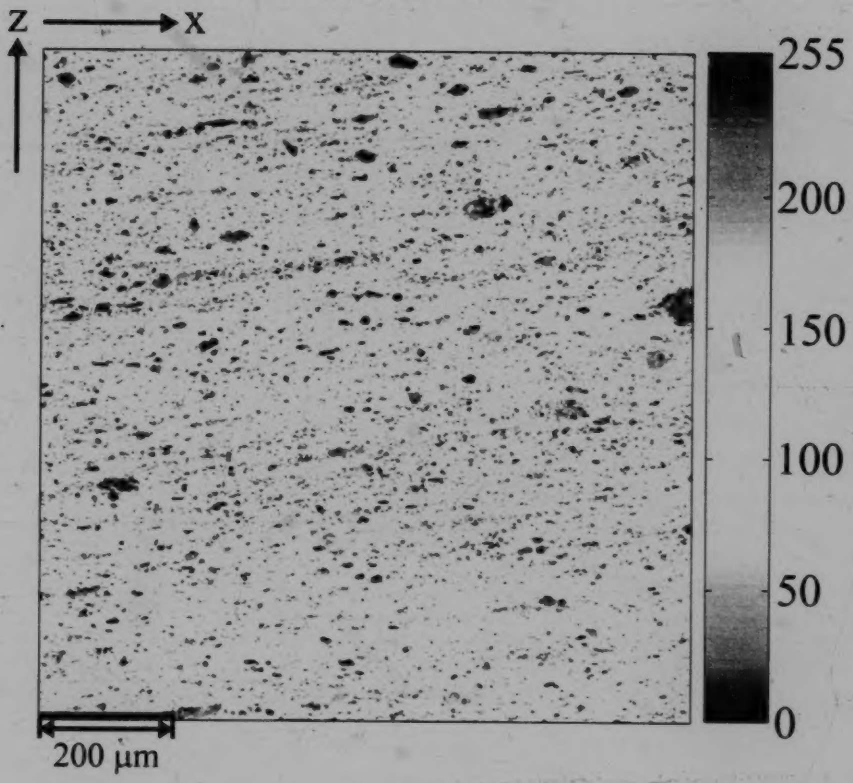
Z
X
255
200
150
100
50
0
200 μm

Figure 5.43: Electron microprobe image of carbon in the $x - z$ plane where scale on right-hand side indicates relative concentration.

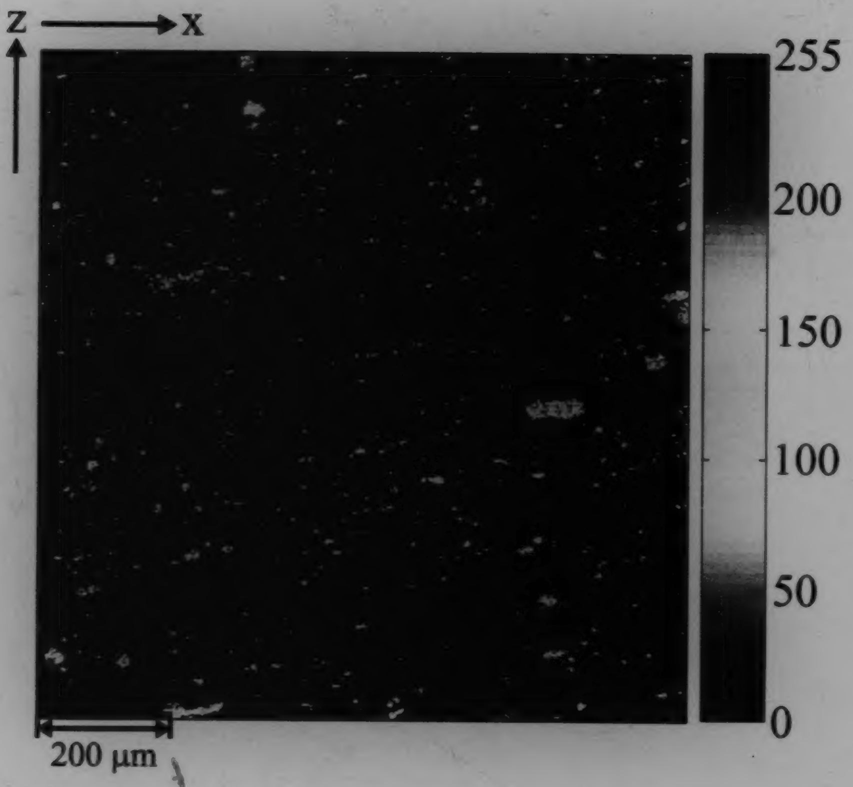
Z
X
255
200
150
100
50
0
200 μm

Figure 5.44: Electron microprobe image of iron in the $x - z$ plane where scale on right-hand side indicates relative concentration.

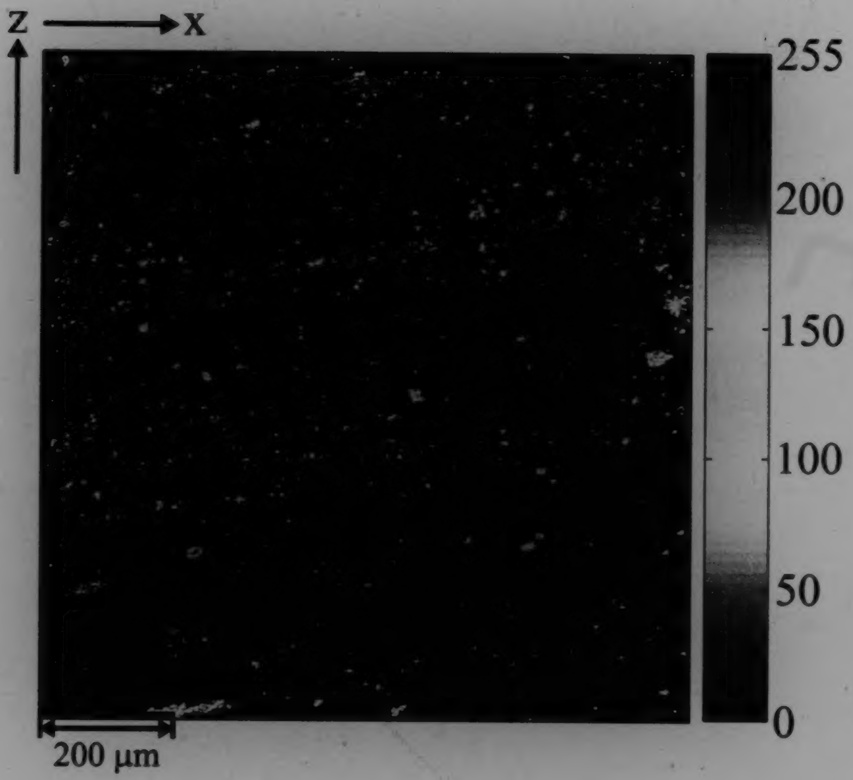
Z
X
255
200
150
100
50
0
200 μm

Figure 5.45: Electron microprobe image of magnesium in the $x - z$ plane where scale on right-hand side indicates relative concentration.

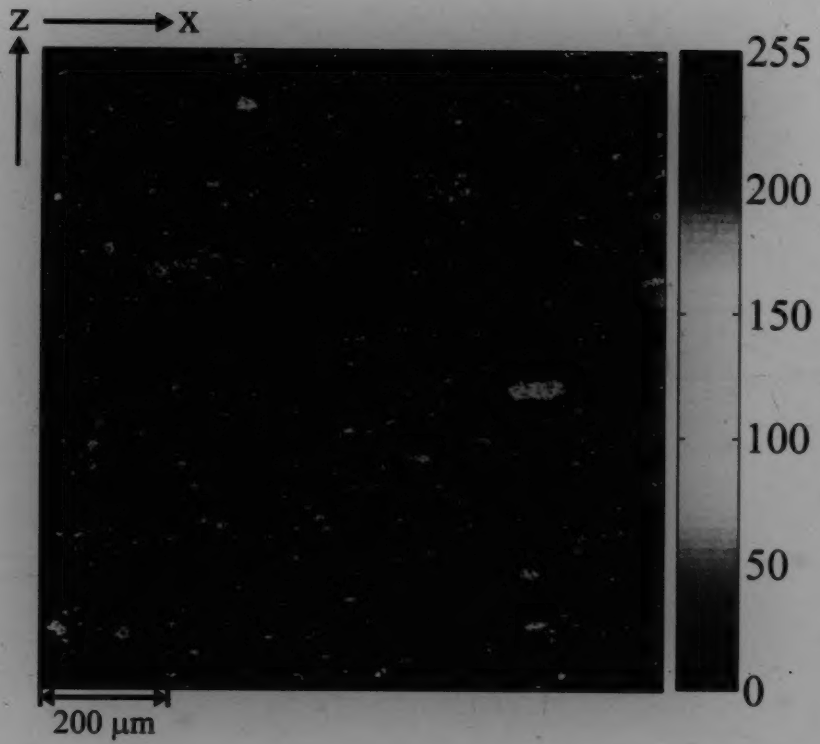
Z
X
255
200
150
100
50
0
200 µm

Figure 5.46: Electron microprobe image of sulfur in the $x-z$ plane where scale on right-hand side indicates relative concentration.

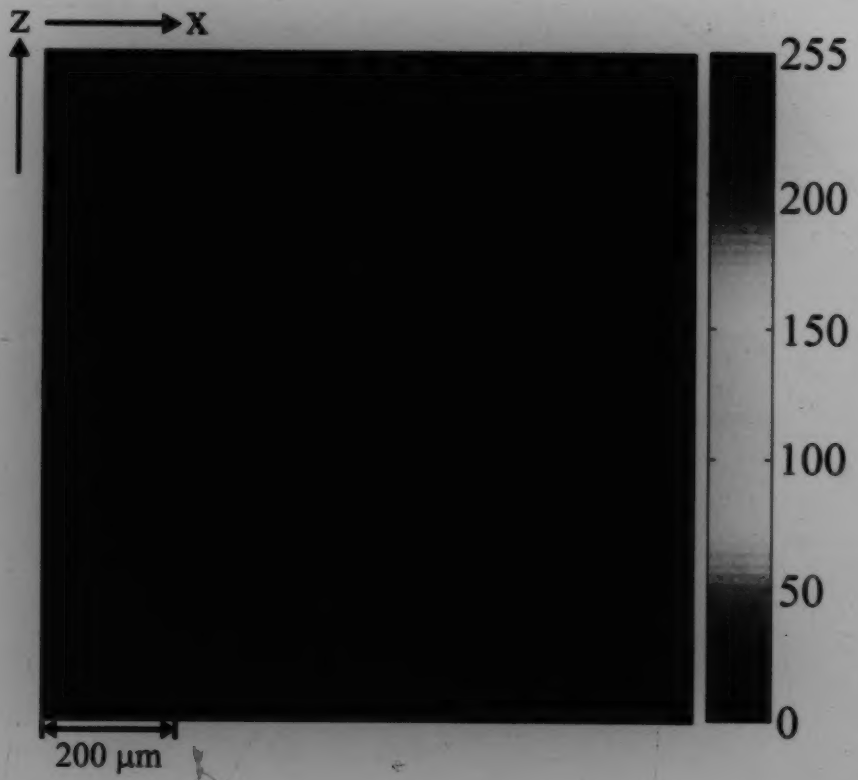
Z
X
255
200
150
100
50
0
200 µm

Figure 5.47: Electron microprobe image of titanium in the $x - z$ plane where scale on right-hand side indicates relative concentration.

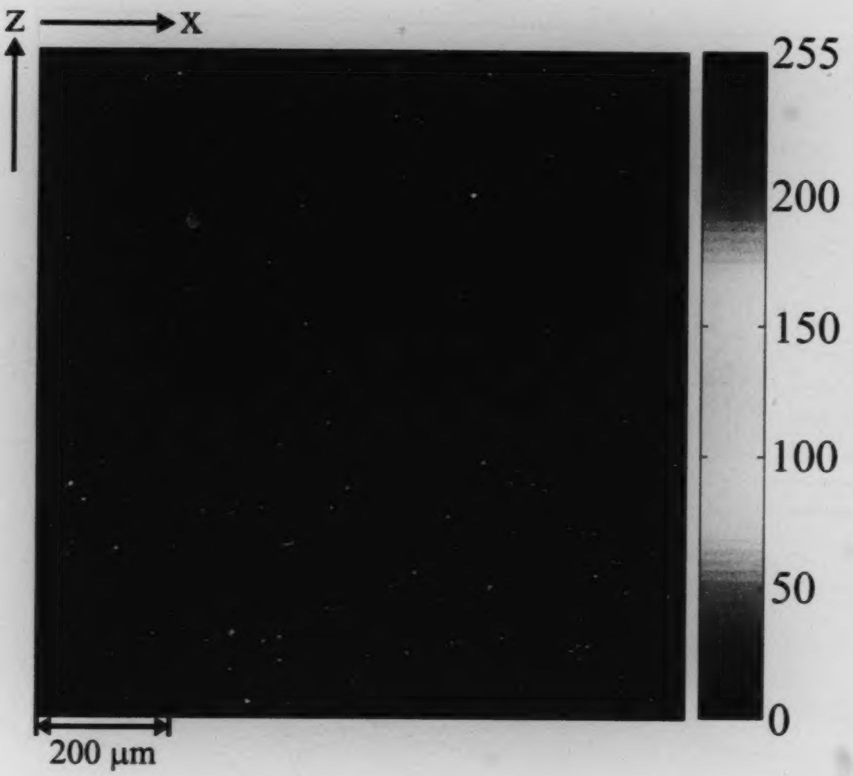
Z
X
255
200
150
100
50
0
200 μm

Figure 5.48: Computed electron microprobe image of calcite in the $x - z$ plane where scale on right-hand side indicates relative concentration.

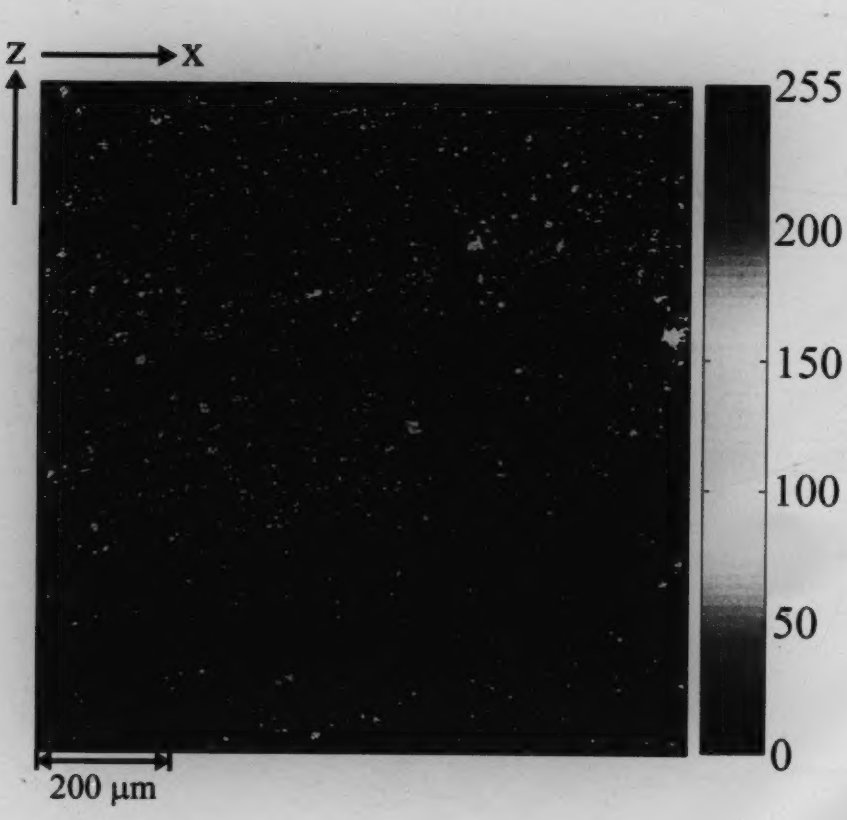
Z
X
255
200
150
100
50
0
200 μm

Figure 5.49: Computed electron microprobe image of dolomite in the $x-z$ plane where scale on right-hand side indicates relative concentration.

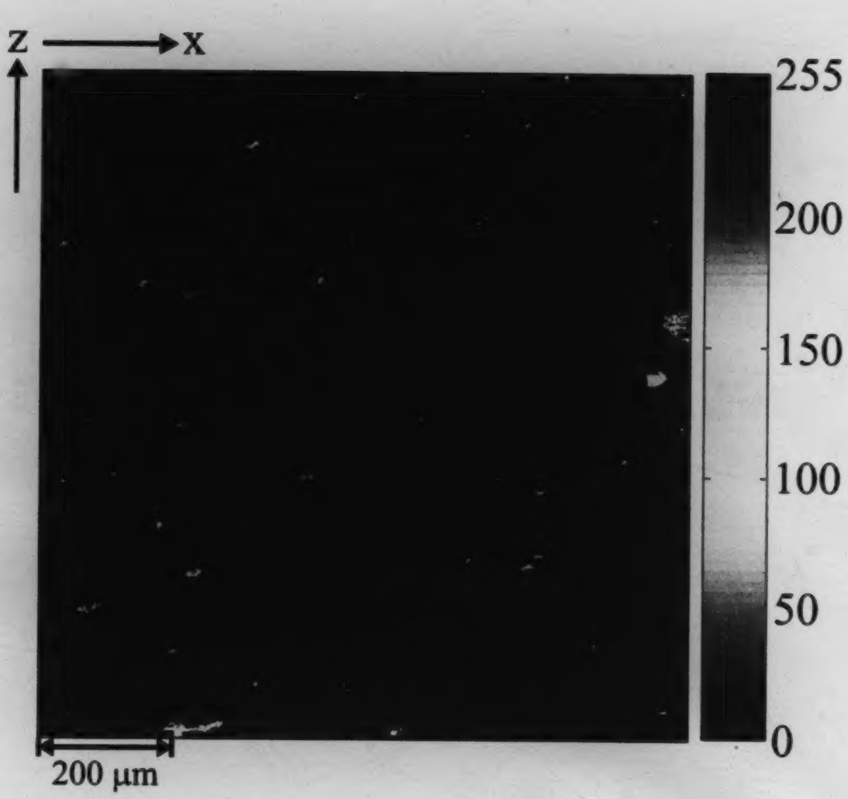
Z
X
255
200
150
100
50
0
200 μm

Figure 5.50: Computed electron microprobe image of a ferromagnesium mineral in the $x - z$ plane where scale on right-hand side indicates relative concentration.

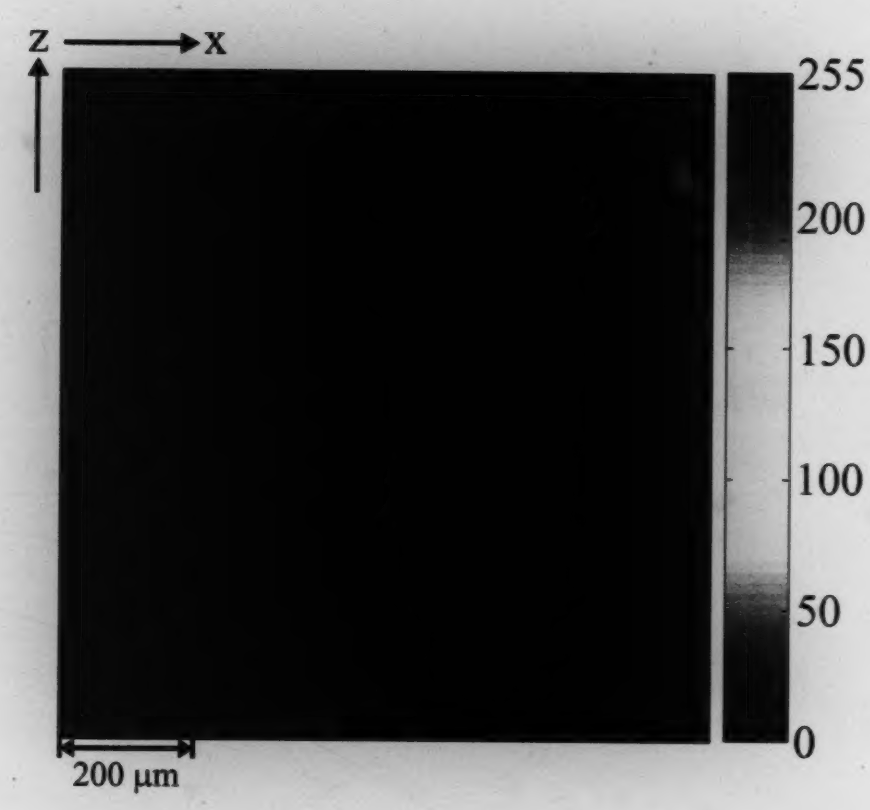

Figure 5.51: Computed electron microprobe image of ilmenite in the $x - z$ plane where scale on right-hand side indicates relative concentration.

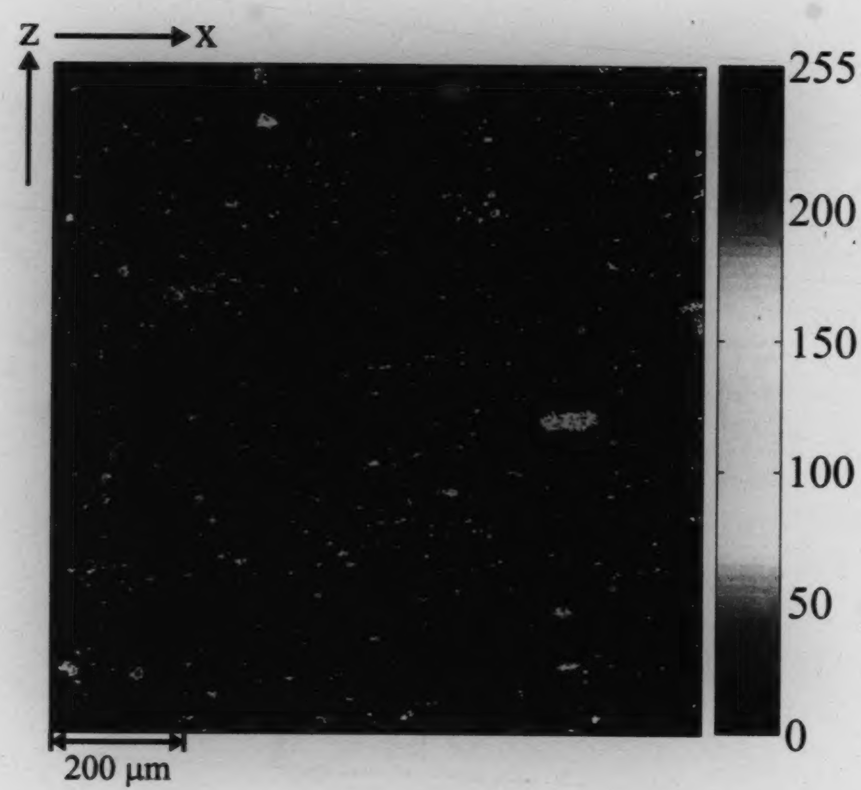
Z
X
255
200
150
100
50
0
200 μm

Figure 5.52: Computed electron microprobe image of pyrite in the $x - z$ plane where scale on right-hand side indicates relative concentration.

In the $x-y$ plane aluminum, calcium, carbon, iron, magnesium, potassium, silicon, sodium, and sulfur was analyzed in the same fashion as previously done as shown in Figures 5.53 through 5.61, respectively. Analysis of these data allowed the mineral concentrations of albite, anorthoclase, calcite, dawsonite, dolomite, pyrite, and quartz to be computed as shown in Figures 5.62 through 5.66, 5.68, 5.69, and 5.70, respectively. Further analysis also yielded the presence of a ferromagnesium mineral (Figure 5.67). The relative amounts of non-kerogeneous minerals in this layer were computed (Table 5.7). Assuming that 49.20 wt % of the sample was kerogen, the relative amounts of minerals present in the sample were calculated (Table 5.8). Not surprisingly, the mineral concentrations shown in Tables 5.7 and 5.8 do not match those in Tables 5.5 and 5.6 since the $x-y$ plane analysis will be heavily biased by which layer in which the sample is taken however there is at least a rough correspondence in the proportion of the minerals. Another possibility for the discrepancy is that matrix correction factors have not been taken into account affecting the concentration of the various minerals. Matrix correction factors are used to account for backscattering of primary electrons, absorption of emitted X-rays, and the generation of secondary X-rays by fluorescence (Beaman & Isasi, 1972; Birk, 1963; Theisen, 1965). In order to apply matrix correction factors, a more detailed study of the sample would have to be performed.

Mineral	weight %
Albite	15.33
Anorthoclase	1.08
Calcite	5.92
Dawsonite	1.01
Dolomite	11.07
Illite	13.02
Pyrite	12.88
Quartz	36.99
Total	100.00

Table 5.7: Relative amounts of non-kerogenous minerals in oil shale sample in $x - y$ plane sample.

Mineral	weight %
Albite	7.79
Anorthoclase	0.55
Calcite	3.01
Dawsonite	0.51
Dolomite	5.62
Illite	6.61
Pyrite	6.54
Quartz	20.16
Kerogen	49.20
Total	99.99

Table 5.8: Relative amounts of minerals in oil shale sample in $x - y$ plane sample.

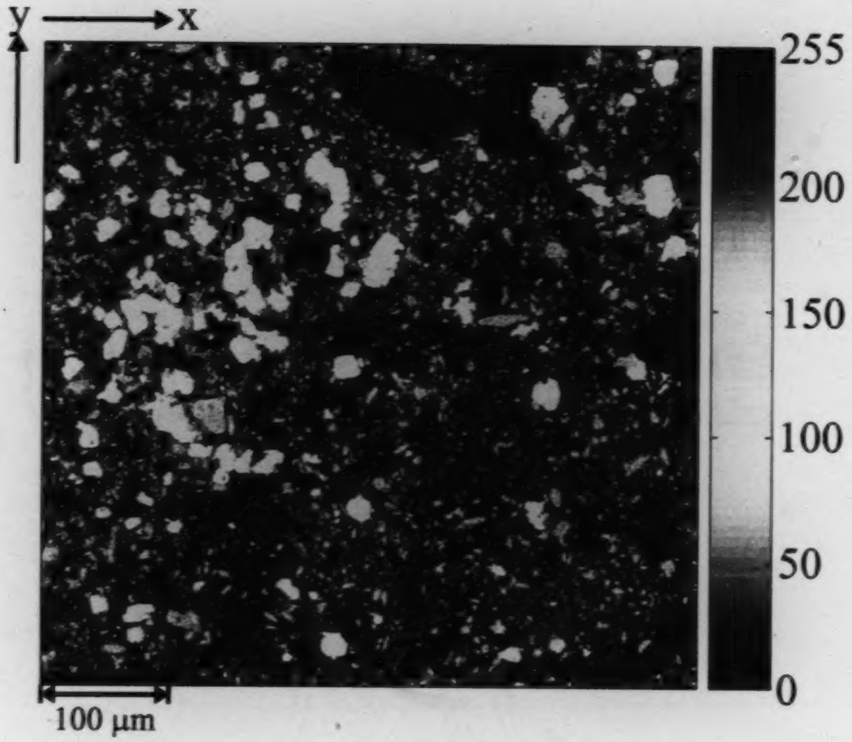
y
x
255
200
150
100
50
0
100 μm

Figure 5.53: Electron microprobe image of aluminium in the $x - y$ plane where scale on right-hand side indicates relative concentration.

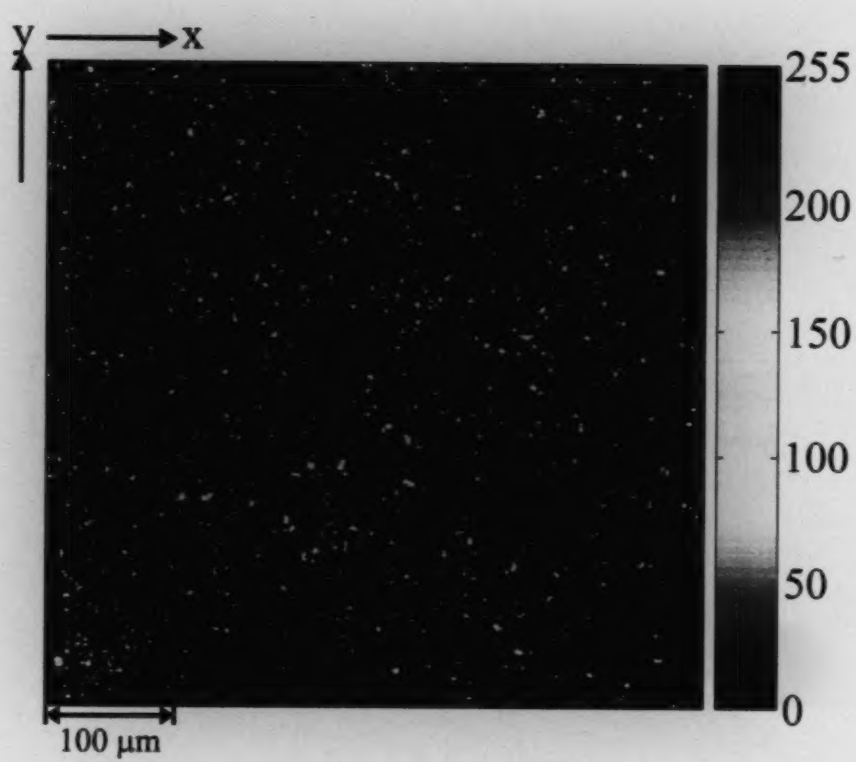
y
x
255
200
150
100
50
0
100 μm

Figure 5.54: Electron microprobe image of calcium in the $x-y$ plane where scale on right-hand side indicates relative concentration.

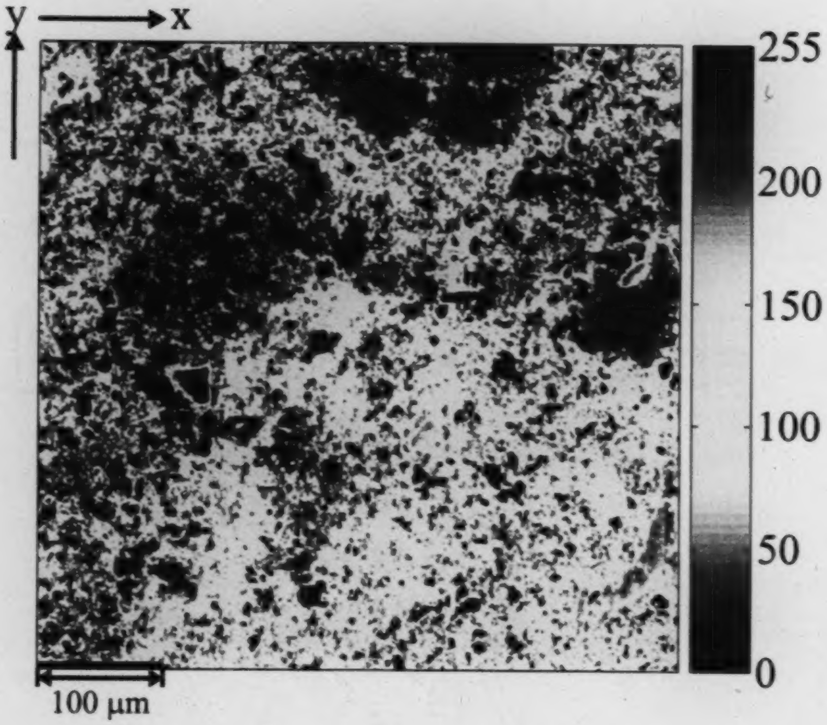
y
x
255
200
150
100
50
0
100 μm

Figure 5.55: Electron microprobe image of carbon in the $x - y$ plane where scale on right-hand side indicates relative concentration.

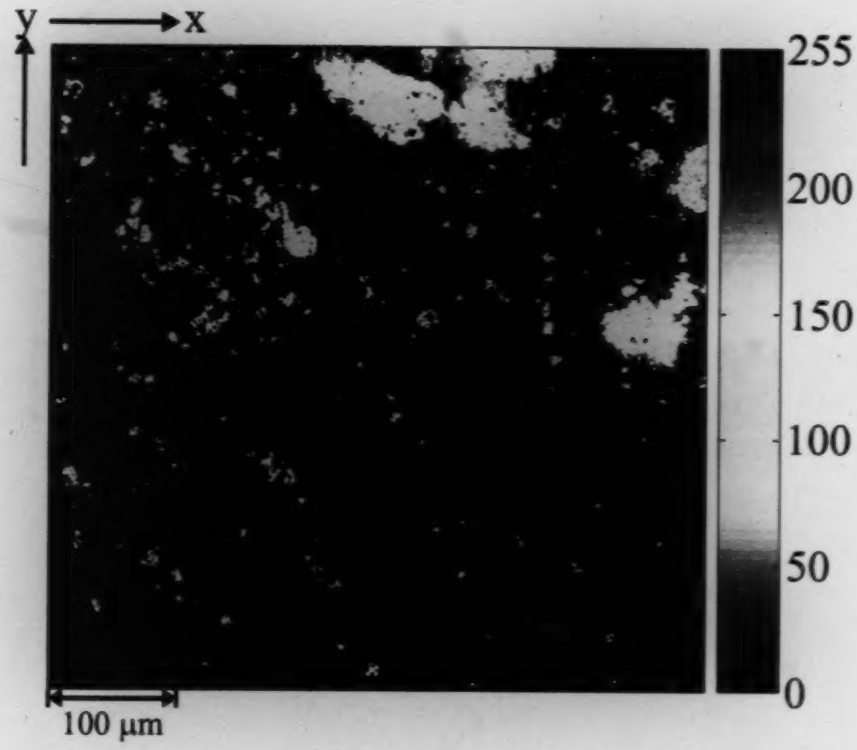
y
x
255
200
150
100
50
0
100 μm

Figure 5.56: Electron microprobe image of iron in the $x - y$ plane where scale on right-hand side indicates relative concentration.

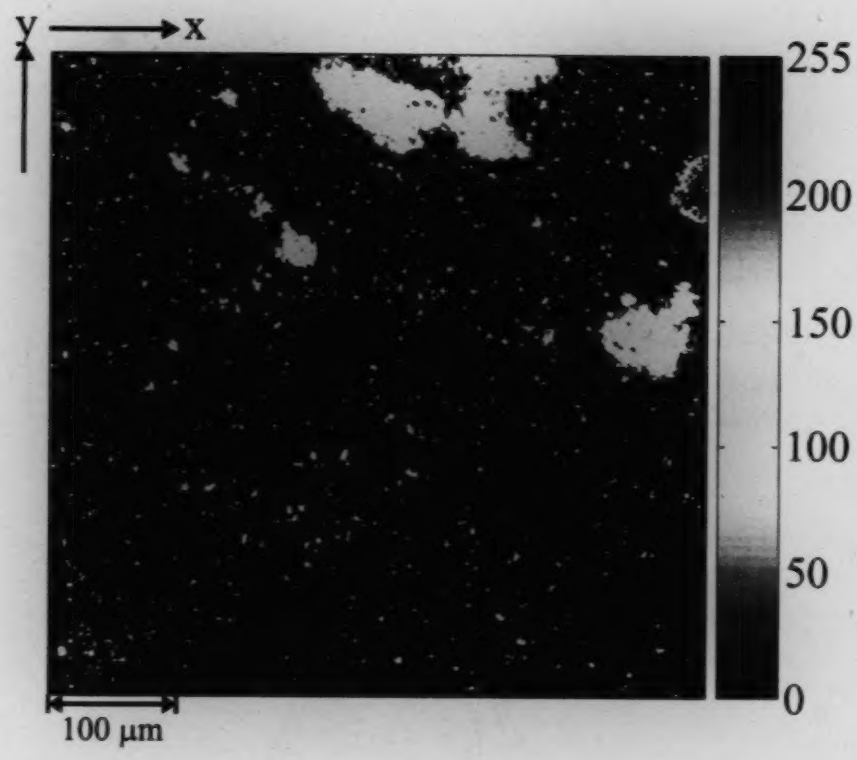
y
x
255
200
150
100
50
0
100 µm

Figure 5.57: Electron microprobe image of magnesium in the $x - y$ plane where scale on right-hand side indicates relative concentration.

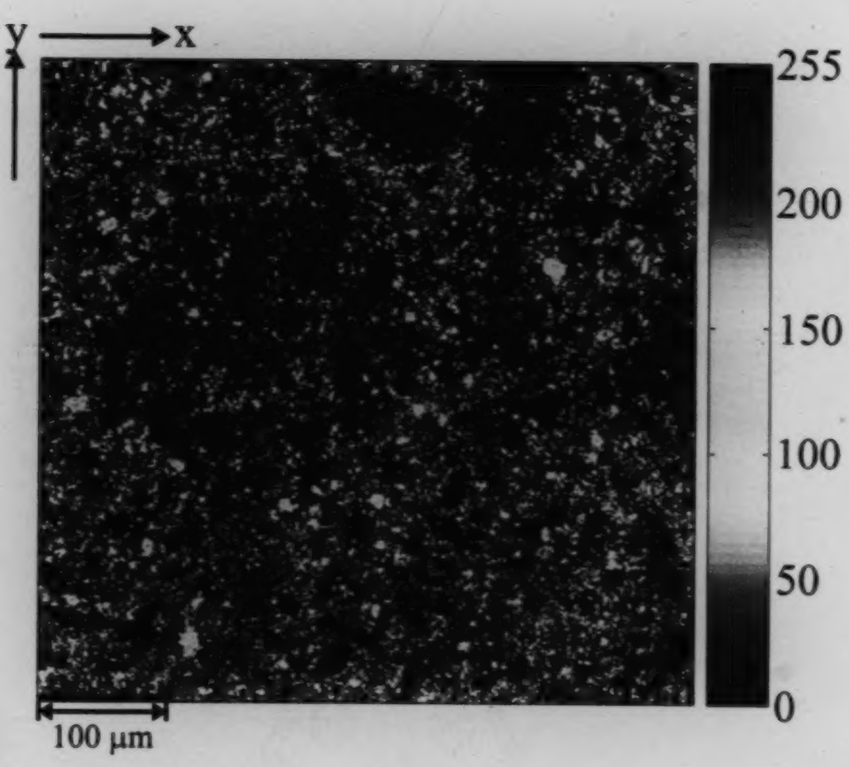
y
x
255
200
150
100
50
0
100 μm

Figure 5.58: Electron microprobe image of potassium in the $x - y$ plane where scale on right-hand side indicates relative concentration.

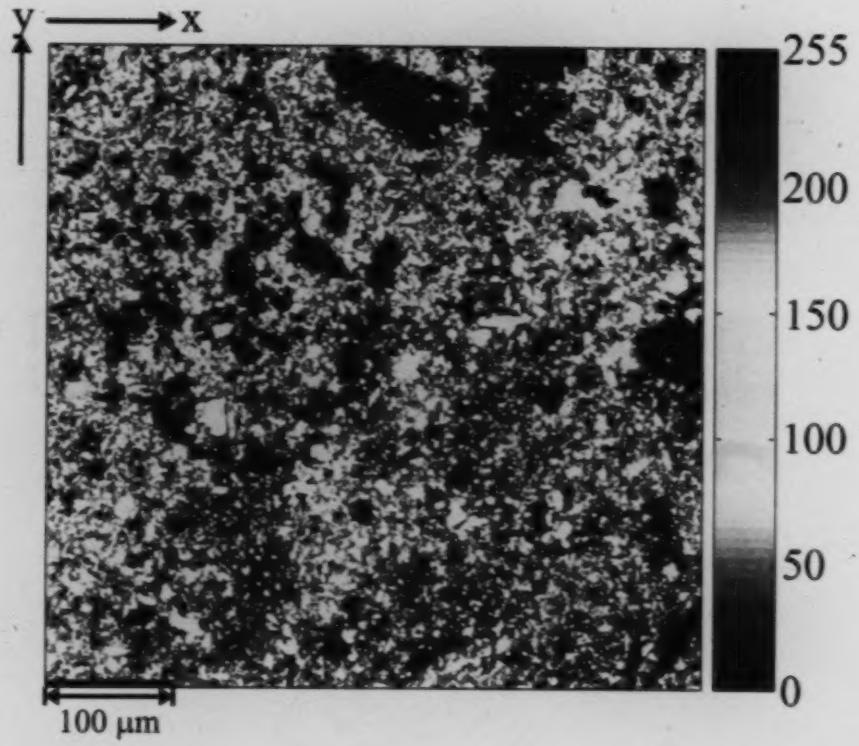
y
x
255
200
150
100
50
0
100 μm

Figure 5.59: Electron microprobe image of silicon in the $x - y$ plane where scale on right-hand side indicates relative concentration.

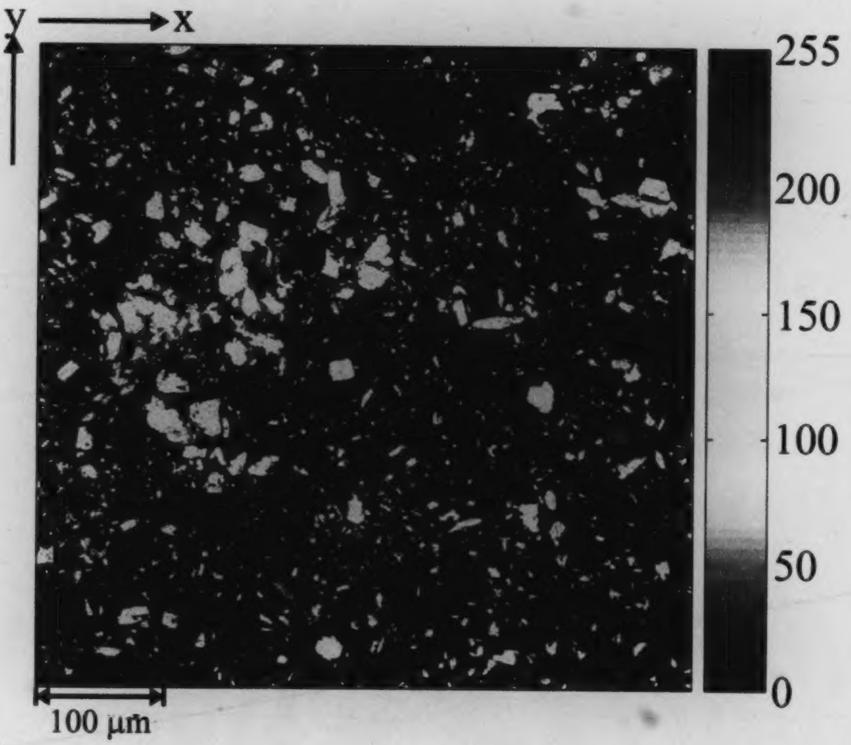
y
x
255
200
150
100
50
0
100 μm

Figure 5.60: Electron microprobe image of sodium in the $x - y$ plane where scale on right-hand side indicates relative concentration.

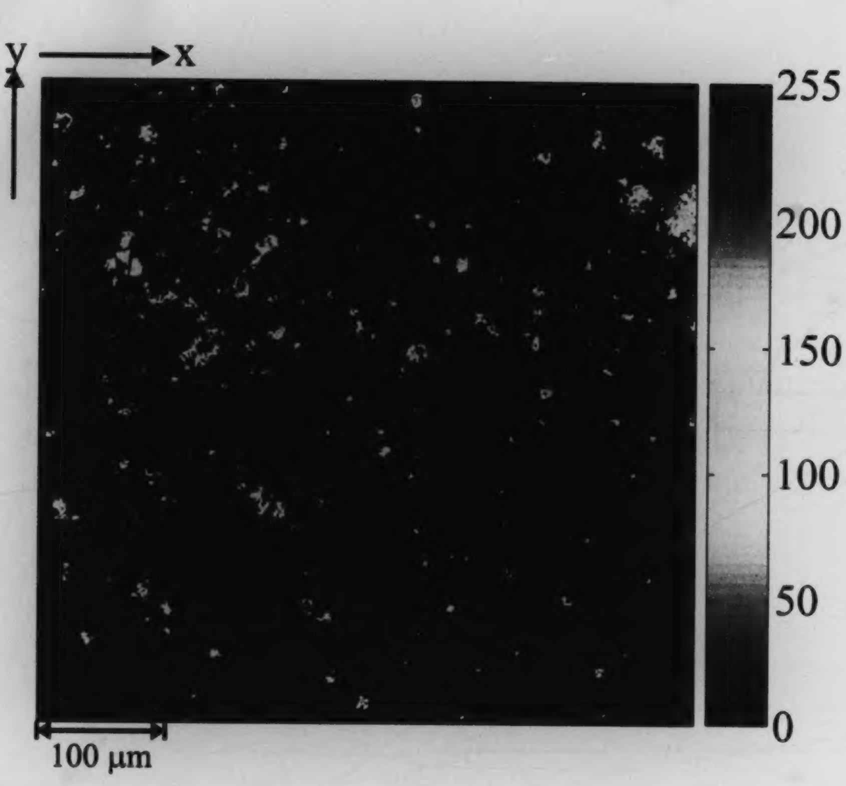
y
x
255
200
150
100
50
0
100 μm

Figure 5.61: Electron microprobe image of sulfur in the $x - y$ plane where scale on right-hand side indicates relative concentration.

2

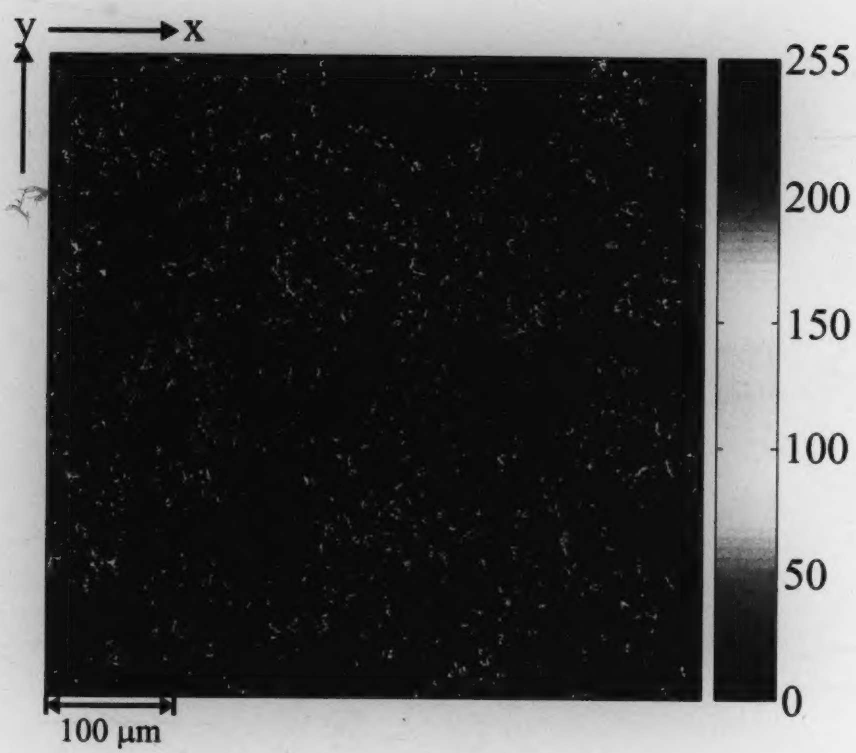
y
x
255
200
150
100
50
0
100 μm

Figure 5.62: Computed electron microprobe image of albite in the $x - y$ plane where scale on right-hand side indicates relative concentration.

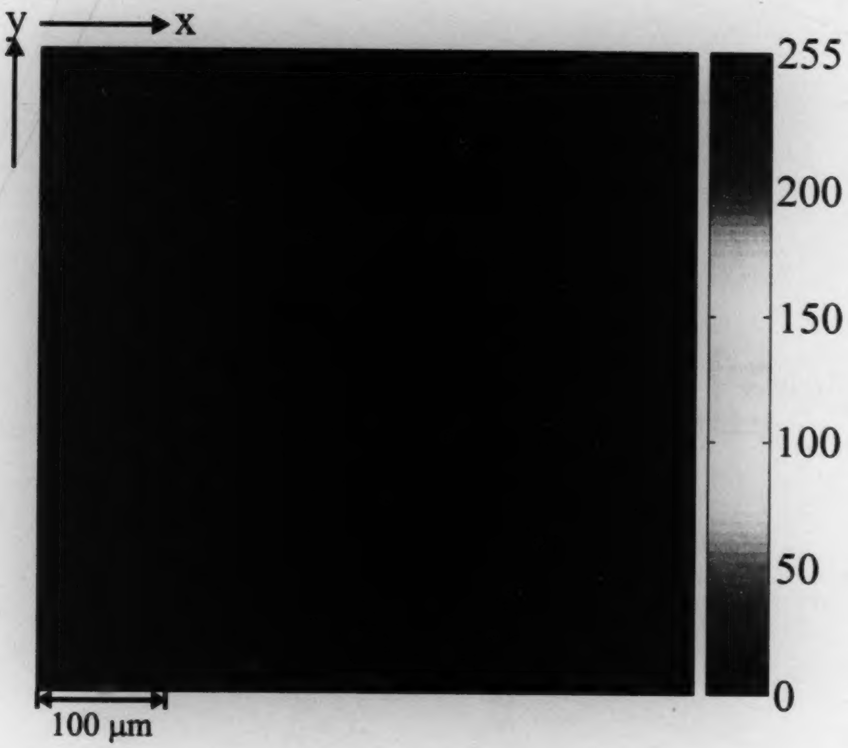
y
x
255
200
150
100
50
0
100 μm

Figure 5.63: Computed electron microprobe image of anorthoclase in the $x - y$ plane where scale on right-hand side indicates relative concentration.

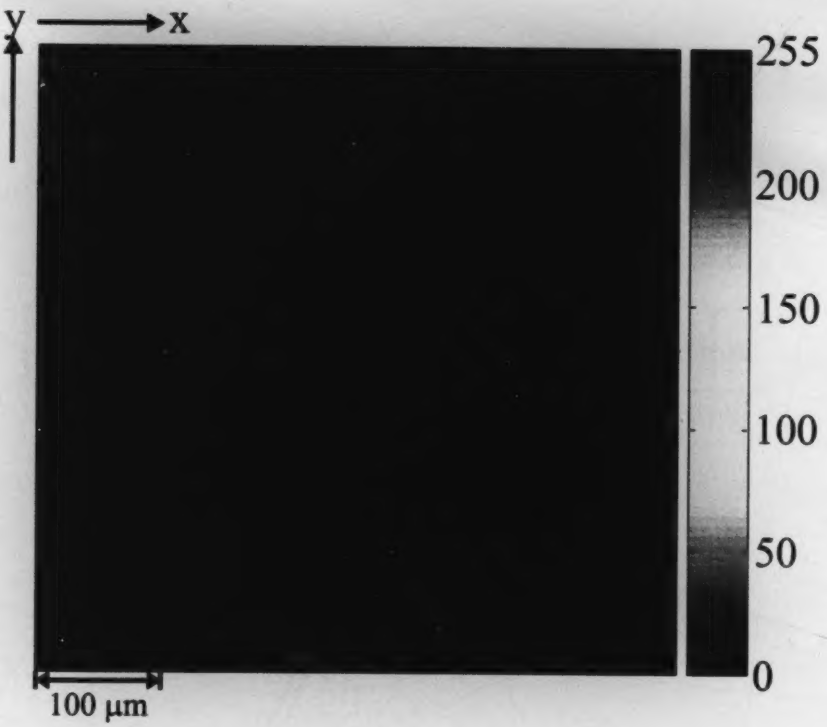
y
x
255
200
150
100
50
0
100 μm

Figure 5.64: Computed electron microprobe image of calcite in the $x - y$ plane where scale on right-hand side indicates relative concentration.

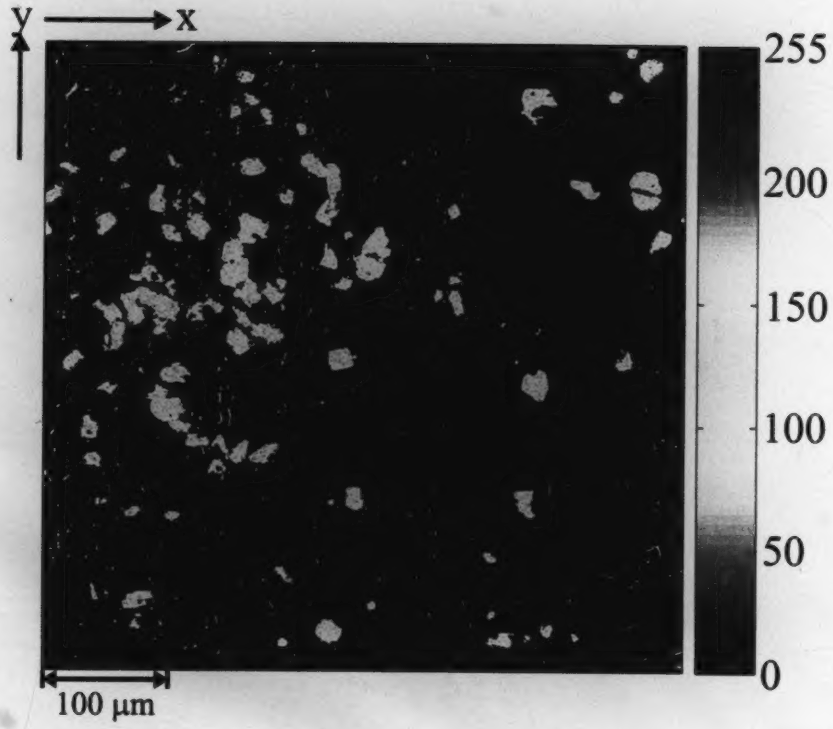
y
x
255
200
150
100
50
0
100 μm

Figure 5.65: Computed electron microprobe image of dawsonite in the $x - y$ plane where scale on right-hand side indicates relative concentration.

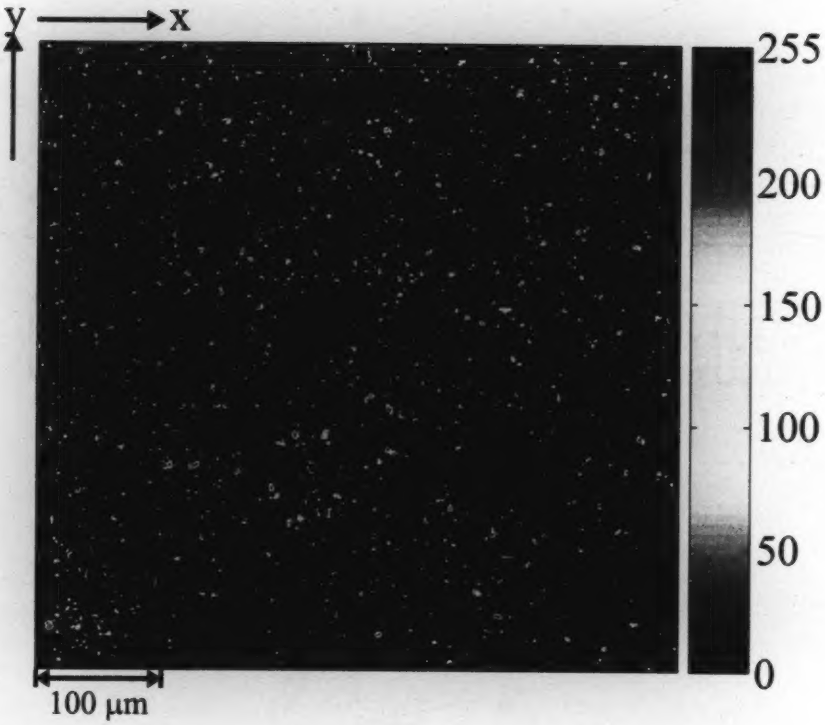
y
x
255
200
150
100
50
0
100 μm

Figure 5.66: Computed electron microprobe image of dolomite in the $x - y$ plane where scale on right-hand side indicates relative concentration.

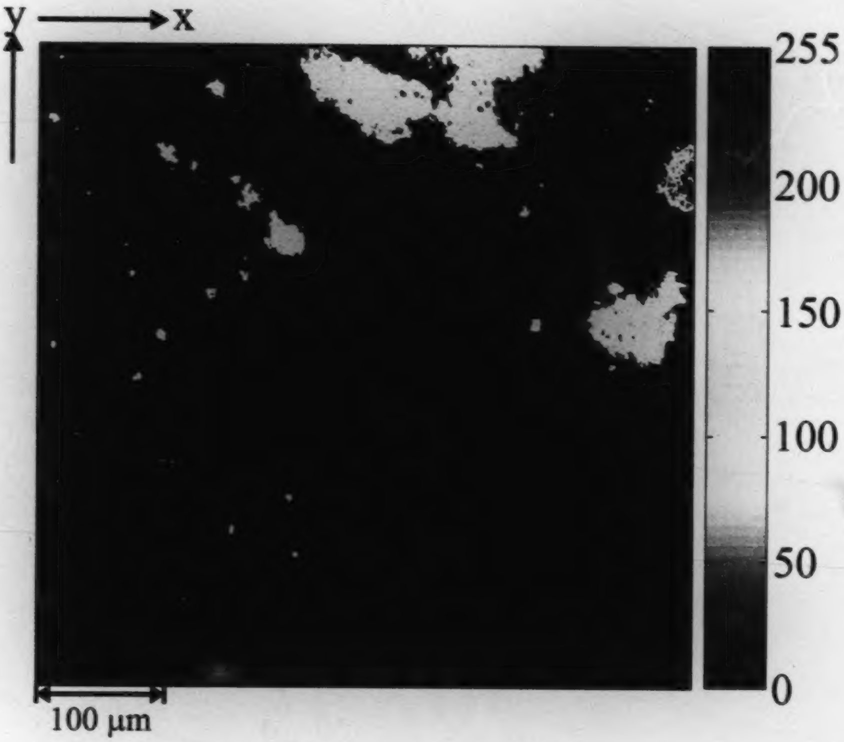
y
x
255
200
150
100
50
0
100 μm

Figure 5.67: Computed electron microprobe image of a ferromagnesium mineral in the $x - y$ plane where scale on right-hand side indicates relative concentration.

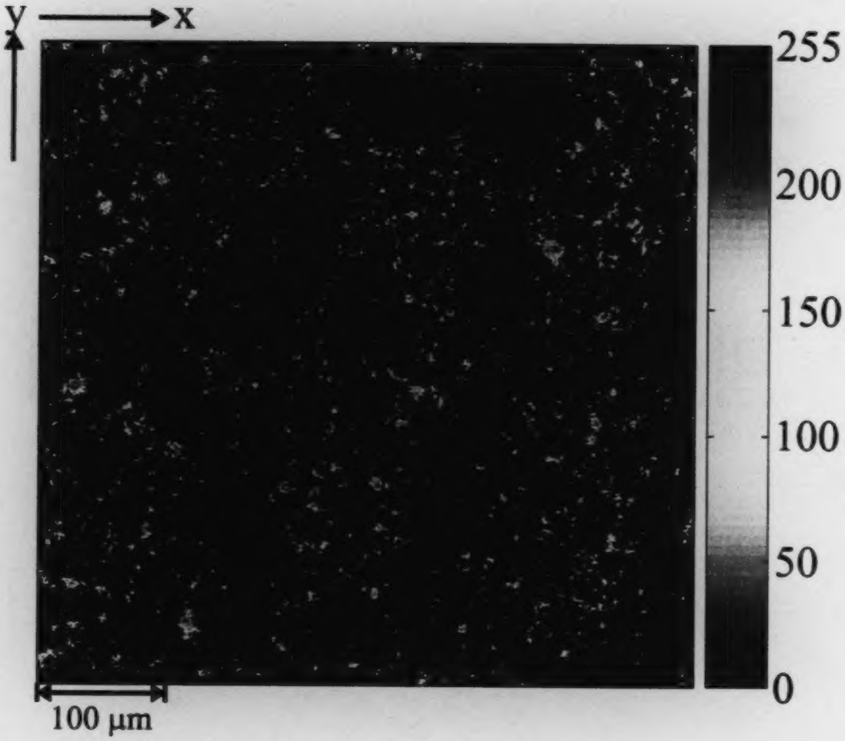
y
x
255
200
150
100
50
0
100 μm

Figure 5.68: Computed electron microprobe image of illite in the $x - y$ plane where scale on right-hand side indicates relative concentration.

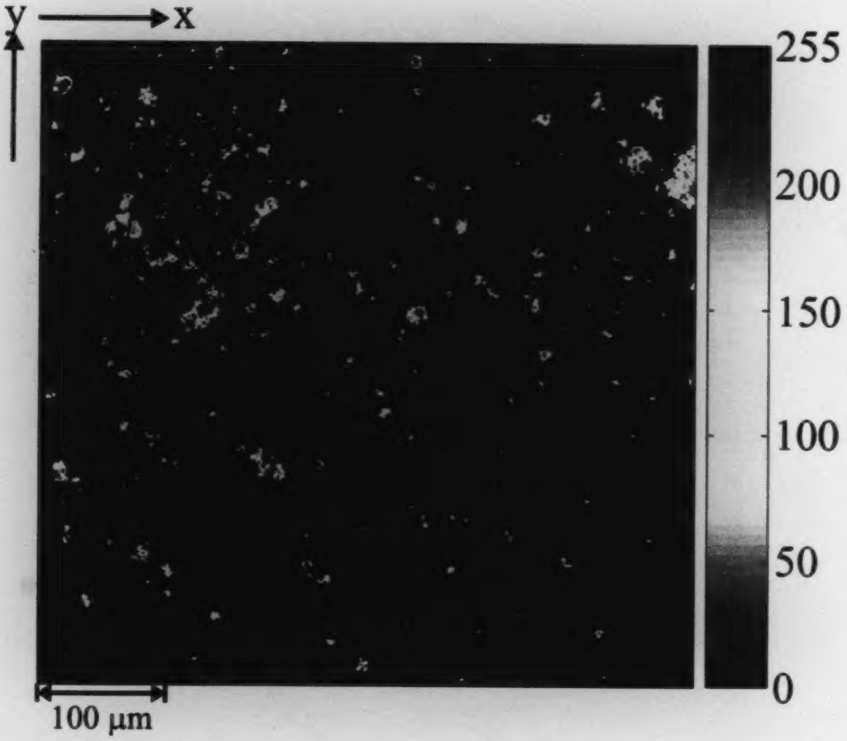
y
x
255
200
150
100
50
0
100 μm

Figure 5.69: Computed electron microprobe image of pyrite in the $x - y$ plane where scale on right-hand side indicates relative concentration.

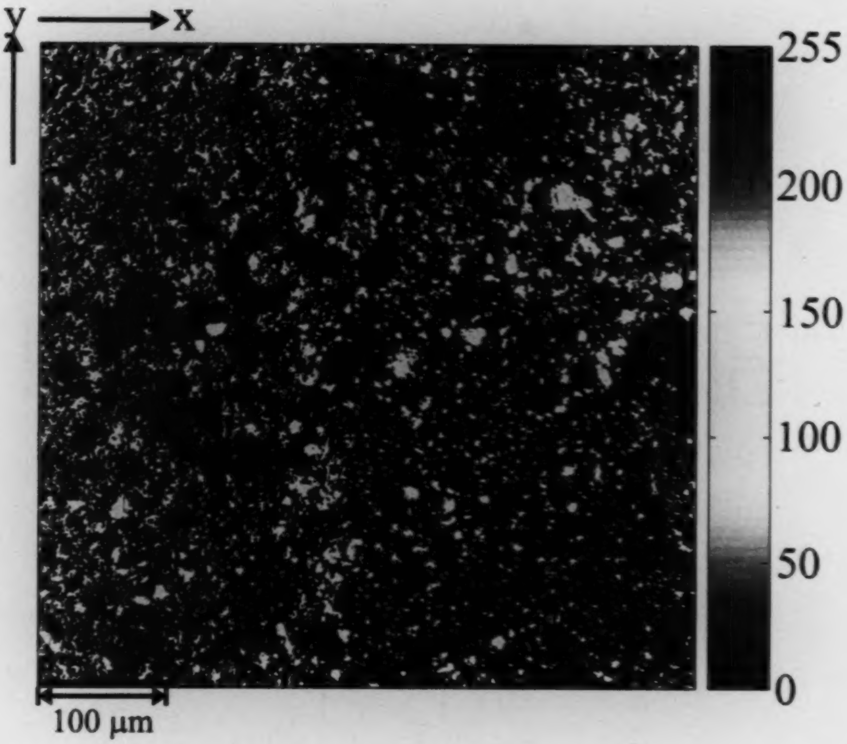
y
x
255
200
150
100
50
0
100 μm

Figure 5.70: Computed electron microprobe image of quartz in the $x - y$ plane where scale on right-hand side indicates relative concentration.

5.8 Summary of density, composition, and structure

The oil shale was deposited in a lacustrine setting with most likely a Green River or playa lake type model. The oil shale has a bulk density of 1.57 g/cm^3, a rock fabric density of 1.74 g/cm^3, and a porosity of 9.8 % with a Mohs hardness between 3.5 and 4 and is composed of fine parallel layers of dark brown and light coloured materials. Thin section analysis has showed the presence of birefringent minerals with powder X-ray diffraction confirming the presence of calcite and dolomite as well as albite, dawsonite, pyrite, and quartz. Oriented X-ray diffraction has shown the presence of these same minerals but analysis of the $x - z$ and $y - z$ planes showed differences from the $y - z$ plane of analysis such as a noticeable "hump" in the oriented X-ray diffraction results centered at 23 degrees 2θ and differences in mineral peak heights. The "hump" may be due to the possible presence of incipient clay minerals the existence of which is weakly confirmed by electron microprobe analysis. The differences in mineral peak heights indicate a possible preferred orientation of the various mineral grains. Pyrolysis and whole rock analysis showed that the sample contains 49.20 wt. % of organic material thought to be kerogen and the relative proportion of various minerals. The scanning electron microscope with EDS analysis showed that the layers have a thickness on the order of tens of μm and a large portion of the mineral grains had a diameter of a μm and some of the grains were albite, anorthoclase, dolomite and a titanium rich mineral not identified by X-ray diffraction. Electron microprobing not only confirmed that a titanium rich mineral was present and thought to be ilmenite but also detected a ferromagnesium mineral that was not identified by X-ray diffraction.

Electron microprobing has shown that the pervasive layering is also observable at small scales and helped refine the average layer thickness to about 35 μm with the layers being composed of mineral grains imbedded in the kerogen matrix. The relative proportion of the minerals was also determined (Table 5.9) in addition to the average layer thickness. The electron microprobe analysis also showed the distributions of calcite and dolomite within the rock mass were different. This may indicate that dolomite may have been formed by direct precipitation and not by alteration of calcite.

Through the use of thin sections, X-ray diffraction techniques, pyrolysis, whole rock analysis, scanning electron microscopy, and electron microprobing the oil shale sample was determined to be composed of parallel "layers". These "layers" are actually bands of minerals where there are higher and lower concentrations of certain minerals; some of which are birefringent and have a preferred orientation or preferred distribution. Though no single technique could fully describe the oil shale, the use of a combination of techniques allows a fairly comprehensive description of the oil shale to be determined including the concentrations of the minerals (Table 5.9). Even though the concentrations of the minerals were calculated stoichiometrically from whole-rock analysis and electron microprobe analysis results, the concentrations of ilmenite and a ferromagnesium mineral were not included in the calculations due to a lack of information.

Mineral	weight %
Albite	7.04
Anorthoclase	0.13
Calcite	8.94
Dawsonite	0.12
Dolomite	13.59
Illite	5.01
Pyrite	9.15
Quartz	6.81
Kerogen	49.20
Ilmenite	Trace amounts
Ferromagnesium mineral	Unknown
Total	99.99

Table 5.9: Relative amounts of minerals in oil shale sample.

References

Backus, G. E., 1962, Long-wave elastic anisotropy produced by horizontal layering: Journal of Geophysical Research, **67**, 4427-4440.

Barron, E. J., 1990, Climate and lacustrine petroleum source prediction, in Katz, B. J., ed., Lacustrine basin exploration: Case studies and modern analogs, American Association of Petroleum Geologists, 1-18.

Bayliss, P., 1989, Unit-cell determinations of two-dimensional clay minerals: Powder Diffraction, **4**, 19-20.

Beaman, D. R., and Isasi, J. A., 1972, Electron beam microanalysis, American Society for Testing and Materials, Philadelphia, Pittsburg, USA.

Birks, L. S., 1963, Electron probe microanalysis, John Wiley & Sons, Inc., New

York, New York, USA.

Bohacs, K. M., Carroll, A. R., Neal, J. E., and Mankiewicz, P. J., 2000, Lake-basin type, source potential, and hydrocarbon character: an integrated sequence-stratigraphic-geochemical framework, in Gierlowski-Kordesch, E. H., and Kelts, K. R., eds., Lake basins through space and time: AAPG Studies in Geology 46, 3-34.

Bradley, W. H., 1966, Paleolimnology, in Frey, D. G., ed., Limnology in North America, University of Wisconsin Press, 621-652.

Bradley, W. H., and Eugster, H. P., 1969, Geochemistry and paleolimnology of the trona deposits and associated authigenic minerals of the Green River Formation of Wyoming: U.S. Geological Survey Professional Paper 496-B, U.S. Geological Survey.

Brindley, G., 1977, Penn State University, University Park, Pennsylvania, USA, ICDD Grant-in-Aid.

Brobst, D. A., and Tucker, J. D., 1973, X-ray mineralogy of the Parachute Creek Member, Green River Formation, in the northern Piceance Creek basin, Colorado: U.S. Geological Survey Professional Paper 803, U.S. Geological Survey.

Carlson, R. L., Schaftenaar, C. H., and Moore, R. P., 1984, Causes of compressional-wave anisotropy in carbonate-bearing, deep-sea sediments: Geophysics, **49**, 525-532.

Carpenter, A. M., 1980, The chemistry of dolomite formation I: the stability of dolomite, in Zenger D. H., Dunham, J. B., and Ethington, R. L., eds., Concepts and models of dolomitization, Society of Economic Paleontologists and Mineralogists Special Publication No. 28 : Society of Economic Paleontologists and Mineralogists, 111-121.

Claisse, F., 1989, Automated sample preparation for analysis of geological materials, in Ahmedali, S. T., ed., X-ray fluorescence analysis in the geological sciences: Advances in methodology, Geological Association of Canada, 39-54.

Cole, R. D., 1984, Sedimentological, mineralogical and geochemical definition of oil-shale facies in the lower parachute creek member of Green River Formation, Colorado, in Gary, J. H., ed., Seventeenth Oil Shale Symposium Proceedings, Colorado School of Mines Press., 143-158.

Cole, R. D., and Picard, M. D., 1978, Comparative mineralogy of nearshore and offshore lacustrine lithofacies, Parachute Creek Member of the Green River Formation, Piceance Creek Basin, Colorado, and eastern Uinta Basin, Utah: Geological Society of America Bulletin, **89**, 1441-1454.

Daub, G. J., Weston, L. K., and Rosar, E. D., 1985, Detailed lithologic, rock quality, and hydrologic data from four drill holes in the central Piceance Creek Basin, Rio Blanco County, Colorado in Gary, J. H., ed., Eighteenth Oil Shale Symposium Proceedings, Colorado School of Mines Press., 21-46.

Desborough, G. A., 1978, A biogenic-chemical stratified lake model for the origin of oil shale of the Green River Formation: An alternative to the playa-lake model: Geological Society of America Bulletin, **89**, 961-971.

Dyni, J. R., 1987, The origin of oil shale and associated minerals, in Taylor, J., ed., Oil shale, water resources, and valuable minerals of the Piceance Basin, Colorado; the challenge and choices of development, U.S. Geological Survey Professional Paper, U.S. Geological Survey, 17-20.

Einsele, G., 1992, Sedimentary basins: Evolution, facies, and sediment budget, Springer-Verlag, New York, New York, USA.

Eugster, H. P., and Surdam, R. C., 1973, Depositional environment of the Green River Formation of Wyoming: A preliminary report: Geological Society of America Bulletin, **84**, 1115-1120.

Friedman, G. M., 1980, Dolomite is an evaporative mineral: Evidence from the rock record and from sea-marginal ponds of the Red Sea, in Zenger D. H., Dunham, J. B., and Ethington, R. L., eds., Concepts and models of dolomitization, Society of Economic Paleontologists and Mineralogists Special Publication No. 28 : Society of Economic Paleontologists and Mineralogists, 81-86.

Gains, A. M., 1980, Dolomitization kinetics: Recent experimental studies, in Zenger D. H., Dunham, J. B., and Ethington, R. L., eds., Concepts and models of dolomitization, Society of Economic Paleontologists and Mineralogists Special Publication No. 28 : Society of Economic Paleontologists and Mineralogists, 81-86.

Giancoli, D. C., 1985, Physics: Principles with applications, Prentice Hall Inc., Englewood Cliffs, New Jersey, USA.

Glashow, S., 1994, From alchemy to quarks: The study of physics as a liberal art, Brooks/Cole Publishing Company, Pacific Grove, California, USA.

Grabowski, G. J., and Pevear, D. R., Sedimentology and petrology of profundal lacustrine sediments, Mahogany zone of the Green River Formation, Piceance Creek Basin, northwest Colorado, in Crevello, P. D., and Harris, P. M., eds., Deep-water carbonates: Buildups, turbidites, debris flows and chalks: Society of Economic Paleontologists and Mineralogists, 386-430.

Guinier, A., 1963, X-ray diffraction in crystals, imperfect crystals, and amorphous bodies, W. H. Freeman and Company, San Francisco, CA.

Hail, W. J., 1992, Geology of the central Roan Plateau: U.S. Geological Survey Bulletin 1787, U.S. Geological Survey.

Heinrich, K. F., 1981, Electron beam X-ray microanalysis, Van Nostrand Reinhold Company, Toronto, Ontario, Canada.

Hornby, B. E., 1995, Experimental determination of the anisotropic elastic properties of shales, in Fjaer, E., Holt, R. M., and Rathore, J. S., eds., Seismic anisotropy: Soc. Expl. Geophysics., 238-296.

Horsfield, B., Curry, D. J., Bohacs, K., Littke, R., Rullkotter, J., Schenk, H. J., Radke, M., Schaefer, R. G., Carroll, A. R., Isaksen, G., and Witte, E. G., 1993, Organic geochemistry of freshwater and alkaline lacustrine sediments in the Green River Formation of the Washakie Basin, Wyoming, U.S.A.: Advances in Organic Geochemistry, **22**, 415-440.

Howie, R. A., and Broadhurst, F. M., 1958, X-ray data from dolomite and ankerite: American Mineralogist, **43**, 1210-1216.

Johnson, R. C., 1981, Stratigraphic evidence for a deep Eocene Lake Uinta, Piceance Creek Basin, Colorado: Geology, **9**, 55-62.

Johnston, J. E., and Christensen, N. I., 1995, Seismic anisotropy of shales: Journal of Geophysical Research, **100**, 5991-6003.

Kaarsberg, E. A., 1959, Introductory studies of natural and artificial argillaceous aggregates by sound propagation and X-ray diffraction,: Journal of Geology, **67**, 447-472.

Katz, B. J., 1988, Clastic and carbonate lacustrine systems: an organic geochemical comparison (Green River Formation and East African lake sediments), in Fleet, A. J., Kelts, K., and Talbot, M. R., eds., Lacustrine petroleum source rocks: Geological Society Special Publication No. 40, 81-90.

Kebaili, A., and Schmitt, D. R., 1997, Ultrasonic anisotropic phase velocity determination with the Radon transformation: J. Acoust. Soc. Am., **101**, 3278-3286.

Kelts, K., 1988, Environments of deposition of lacustrine petroleum source rocks: an introduction, in Fleet, A. J., Kelts, K., and Talbot, M. R., eds., Lacustrine petroleum source rocks: Geological Society Special Publication No. 40, 3-26.

Klug, H. P., and Alexander, L. E., 1974, X-ray diffraction procedures for polycrystalline and amorphous materials, 2nd ed., John Wiley $ Sons, Inc., New York, New York, USA.

Lachance, G. L., 1989, Algorithms for the correction of matrix effects in X-ray fluorescence, in Ahmedali, S. T., ed., X-ray fluorescence analysis in the geological sciences: Advances in methodology, Geological Association of Canada, 55-90.

Langford, J. L., Louër, D., and Scardi, P., 2000, Effect of a crystallite size distribution on X-ray diffraction line profiles and whole-powder-pattern fitting: Journal of Applied Crystallography, **33**, 964-974.

Leake, B. E., Hendry, G. L., Kemp, A., Plant, A. G., Harrey, P. K., Wilson, J. R., Coats, J. S., Aucott, J. W., Lünel, T., and Howarth, R. J., 1969, The chemical analysis of rock powders by automatic X-ray fluorescence: Chem. Geol, **5**, 7-86.

Lundell, L. L., and Surdam, R. C., 1975, Playa-lake deposition: Green River formation, Piceance Creek Basin, Colorado: Geology, **3**, 493-497.

Markham, M. F., 1957, Measurement of elastic constants by the ultrasonic pulse method: Brit. J. Appl. Phys., **6**, 56-63.

Meddaugh, W. S., Imbus, I., Ting, F. T. C., and Salotti, C. A., 1984, Variations in organic geochemistry and petrography with depth of burial, Green River

Formation oil shales Piceance Creek basin, Colorado, in Gary, J. H., ed., Seventeenth Oil Shale Symposium Proceedings, Colorado School of Mines Press., 159-170.

Meddaugh, W. S., and Salotti, C. A., 1983, Mineralogy and geochemistry of Green River Formation oil shale, C-A tract, Colorado, in Gary, J. H., ed., Sixteenth Oil Shale Symposium Proceedings, Colorado School of Mines Press., 113-123.

Moorhouse, W. W., 1959, The study of rocks in thin sections, Harper & Row, Publishers, Inc., New York, New York, USA.

Phillips, W. R., 1971, Mineral optics: Principles and techniques, W. H. Freeman and Company, San Francisco, California, USA.

Picard, M. D., and High, L. E., 1972, Paleoenvironmental reconstructions in an area of rapid facies change, Parachute Creek Member of Green River Formation (Eocene), Uinta basin, Utah: Geological Society of America Bulletin, **83**, 2689-2708.

Potter, P. E., Maynard, J. B., and Pryor, W. A., 1980, Sedimentology of shale: Study guide and reference source, Springer-Verlag New York Inc., New York, New York, USA.

Reed, S. J. B., 1975, Electron microprobe analysis, Cambridge University Press, New York, New York, USA.

Robinson, D., and Bevins, R. E., 1986, Incipient metamorphism in the Lower Palaeozoic marginal basin of Wales: J. metamorphic Geol., **4**, 101-113.

Sayers, C. M., 1994, The elastic anisotropy of shales: Journal of Geophysical Research, **99**, 767-774.

Sayers, C. M., 1999, Stress-dependent seismic anisotropy of shales: Geophysics, **64**, 93-98.

Scardi, P., and Leoni, M., 1999, Fourier modelling of the anisotropic line broadening of X-ray diffraction profiles due to line and plane lattice defects: Journal of Applied Crystallography, **32**, 671-682.

Smith, J. W., 1983, The chemistry that formed Green River formation oil shale, in Miknis, F. P., and McKay, J. F., eds., Geochemistry and Chemistry of oil shales, American Chemical Society, 225-248.

Smith, J. W., and Lee, K. K., 1982, Geochemistry and physical paleolimnology of Piceance Creek Basin oil shales, in Gary, J. H., ed., Fifteenth Oil Shale Symposium Proceedings, Colorado School of Mines Press, 101-114.

Stollhofen, H., Stanistreet, I. G., and Gerschutz, S., 2000, Early Jurassic rift-valley-related alkaline lake deposits interbedded with Karoo flood basalts, southern Namibia, in Gierlowski-Kordesch, E. H., and Kelts, K. R., eds., Lake basins through space and time: AAPG Studies in Geology 46, 167-180.

Surdam, R. C., and Wolfbauer, C. A., 1975, Green River formation, Wyoming:

a playa-lake complex: Geological Society of America Bulletin, **86**, 335-345.

Swanson, H. E., and Fuyat, R. K., 1953, Data for 30 inorganic substances: National Bureau of Standards Circular 539 Volume 2, United States National Bureau of Standards.

Theisen, R., 1965, Quantitative electron microprobe analysis, Springer-Verlag, Berlin, Germany.

Tucker, M. E., and Wright, V. P., 1990, Carbonate sedimentology, Blackwell Scientific Publications, London, England.

Tuttle, M. L., ed., Geochemical, Biogeochemical, and Sedimentological studies of the Green River formation, Wyoming, Utah, and Colorado: U.S. Geological Survey Bulletin 1973-A-G, U.S. Geological Survey.

Tuttle, M. L, and Goldhaber, M. B., 1991, Sulfur geochemistry and isotropy of the Green River formation , Wyoming, Utah, and Colorado, in Tuttle, M. L., ed., Geochemical, Biogeochemical, and Sedimentological studies of the Green River formation, Wyoming, Utah, and Colorado: U.S. Geological Survey Bulletin 1973-A-G, U.S. Geological Survey, B1-B20.

Ungar, T, Gubicza, J., Ribarik, G., and Borbely, A., 2001, Crystallite size distribution and dislocation structure determined by diffraction profile analysis: principles and practical application to cubic and hexagonal crystals: Journal of Applied Crystallography, **34**, 298-310.

Vernik, L., and Nur, A., 1992, Ultrasonic velocity and anisotropy of hydrocarbon source rocks: Geophysics, **57**, 727-735.

Warr, L. N., and Rice., H. N., 1994, Interlaboratory standardization and calibration of clay mineral crystallinity and crystallite size data: J. metamorphic Geol., **12**, 141-152.

Weaver, C. E., and Pollard, L. D., 1973, The chemistry of clay minerals, Elsevier ScientifiWebster, 1997, Webster's Universal College Dictionary, Gramercy Books, New York, New York, USA.

Wischnitzer, S., 1970, Introduction to electron microscopy, 2nd ed., Pergamon Press of Canada Ltd., Toronto, Ontario, Canada.

Winchell, A. N., 1933, Elements of optical mineralogy: An introduction to microscopic petrography, Part II. Description of minerals, John Wiley & Sons, Inc., New York, New York, USA.

Woolfson, M. M., and Ziman, J. M., eds., 1972, The scanning electron microscope, Cambridge University Press, London, England.

Zen, E., and Hammarstrom, J. G., 1975, Quantitative determination of dawsonite in Green River shale by powder-sample X-ray diffraction: Effect of grinding: Journal of Research U.S. Geological Survey, **3**, 21-30.

Chapter 6

Elastic Anisotropy of Oil Shale

6.1 Abstract

A layered oil shale is instrumented with P-wave and S-wave ultrasonic transducers in a variety of well-chosen directions. This oil shale is sealed inside a pressure vessel and the waveforms acquired as functions of pressure. P-wave and S-wave velocities were then calculated as functions of pressure. Elastic constants are then calculated as functions of pressure. Analysis of these elastic constants showed that hysteresis is present and that the anisotropy of the sample changed with pressure.

6.2 Introduction

The previous characterization chapter has shown that the oil shale was composed mostly of kerogen, an isotropic, amorphous material, with layers varying in proportions of other minerals such as albite, calcite, dawsonite, dolomite, pyrite, and quartz as determined by X-ray diffraction, whole-rock analysis, scanning electron microscopy, and electron microprobing. Some of these minerals were birefringent and may have had a preferred orientation distribution or orientation as determined through X-ray diffraction and electron microprobing. As well, oriented void spaces were observed. Perhaps more importantly, layering was observed in this material at scales from 35 μm to 1 mm. In this chapter, ultrasonic measurements were taken in a variety of directions in the oil shale in order to determine if there was any velocity anisotropy. The elastic constants were then determined at a variety of different pressures in order to study the anisotropy of the oil shale and how it changed with pressure.

6.3 Background

Velocity isotropy is the usual assumption in seismic data processing and seismic imaging in the oil and gas industry. Many researchers have studied velocity anisotropy and concluded that it affects seismic imaging. The author in the course of his work as a depth imaging geophysicist in the oil and gas industry has found that when anisotropy is incorporated the quality of the seismic image is improved. When anisotropy is not taken into account, the images of the subsurface reflectors can be laterally mispositioned in the final seismic image due to the sideslip of energy (Isaac & Lawton, 1999; Vestrum & Lawton, 1999). When anisotropy is incorporated into the migration, the positioning of the images of the subsurface reflectors is improved (Claerbout, 1985). This lack of certainty adversely affects the interpretation of the subsurface of the earth and reduces the possibility of finding oil and gas deep beneath the earth's surface.

The velocity at which seismic waves travel is determined by the material's elastic behaviour. When the material is assumed to be homogeneous and isotropic, the longitudinal (P-wave) and shear (S-wave) velocities can be described by 2 independent elastic constants, λ and μ (Musgrave, 1970). As the complexity of the material increases from cubic to hexagonal to orthorhombic to triclinic symmetry, the number of independent elastic constants needed to describe the behaviour of the wave travelling through the material increases to 3, 5, 9, and 21, respectively. See Appendix A for more details. This behaviour has typically been studied in homogenous well-behaved materials.

The anisotropic behaviour of numerous synthetic composites and metallic samples have been studied. Some of the earliest measurements were performed on cubic, hexagonal, and trigonal metals such as aluminium, copper, iron, zinc, antimony, and bismuth (Markham, 1957). Elastic properties of very simple synthetic models made of glass and epoxy or plastic and steel layers were also investigated (Marion et al., 1994; Melia & Carlson, 1984). More complex synthetics such as phenolite and phenolic have been studied by numerous authors (Chang & Chang, 2001; Cheadle et al., 1991; Karayaka & Kurath, 1994; Mah & Schmitt, 2001a; Mah & Schmitt, 2003; Rumpker et al., 1996; Vestrum, 1994).

Some researchers have studied crystals and simple materials. Neighbours and Schacher (1967) examined natural crystals of beryllium, cadmium, cobalt, magnesium, rhenium, ruthenium, yttrium, and zinc in order to determine the elastic constants of their hexagonal symmetry. Bass (1995) cataloged the elasticity of many different minerals, glasses, and melts from the literature.

Some researchers have also studied shales or marine sediments in detail (Carlson et al., 1984; Hornby et al., 1995; Johnston & Christensen, 1995; Katahara, 1996; Sayers, 1994; Schaftenaar & Carlson, 1984; Vernik, 1993; Wang et al., 2001). Some have studied how the elastic properties of the rocks change with pressure or burial depth (Kaarsberg, 1959). However, very few have studied what affects the anisotropy of the rocks. There are 3 major different causes of anisotropy:

- intrinsic anisotropy
- oriented microcracks and pores
- layering

in sedimentary rocks.

6.4 Causes of Anisotropy

6.4.1 Intrinsic Anisotropy

One source of anisotropy derives from the fact that the mineral components are anisotropic. Most minerals are elastically anisotropic even though some, such as NaCl with a cubic structure, are optically isotropic. Minerals such as clay and calcite are thought to play roles in the anisotropy of sedimentary rocks. Clay minerals tend to be platy and are highly anisotropic. When these clay minerals are aligned, they cause a strong anisotropic response (Cholach, 2004; Hornby et al., 1995; Johnston & Christensen, 1995; Katahara, 1996; Sayers, 1994; Vernik, 1993; Wang et al., 2001). The presence of aligned clay minerals have been observed in X-ray diffraction studies (Johnston & Christensen, 1995; Kaarsberg, 1959). Velocity anisotropy produced by calcite has been observed in marine sediments (Carlson et al., 1984; Schaftenaar & Carlson, 1984). Intrinsic anisotropy of constituent minerals causing an overall anisotropic response has also been observed in shallow crustal rocks (Brocher & Christensen, 1990).

The previous chapter shows that the oil shale contains a variety of minerals including calcite and dolomite. As noted previously, clay minerals are not conclusively detected in this oil shale but may contain the clay mineral illite that contributes to the anisotropy of other types of shales (Cholach, 2004; Hornby et al., 1995; Johnston & Christensen, 1995; Katahara, 1996; Sayers, 1994; Vernik, 1993; Wang et al., 2001). Another possible source of intrinsic anisotropy in this oil shale is the presence of calcite and dolomite since both are anisotropic and calcite has been thought of as producing anisotropy (Carlson et al., 1984; Schaftenaar & Carlson, 1984). Anisotropic minerals have been observed in this oil shale and may be a source of anisotropy.

6.4.2 Microcracks and oriented pores

Microcracks and oriented pores are a possible source of anisotropy in rocks. During the compaction and diagenesis of sediments, not only are fluids generated that increase the intra-pore pressure (Bishop, 1979; Smith, 1971; Snarskiy, 1961) enough to exceed the confining pressure causing microcracks or fractures to form but the pores may be deformed by confining pressure in such a way that they become preferentially oriented (Kim et al., 1999; Wild & Crampin, 1991). The presence of the microcracks and oriented pores has been observed in previous laboratory studies of shales (Freund, 1992; Hornby, 1998; Johnston & Christensen, 1995; Jones & Wang, 1981; Tosaya & Nur, 1982; Vernik, 1994). Microcracks have not been observed directly in these studies but oriented pores have been observed in the oil shale and may be a source of anisotropy.

6.4.3 Layering

Layering is another possible source of anisotropy in rocks. Studies of layered glass and epoxy or plastic and steel disks have shown that media composed of isotropic layers can produce an anisotropic medium (Marion et al., 1994; Melia & Carlson, 1984). Theoretical and numerical research has confirmed this effective medium effect (Backus, 1962; Carcione et al., 1991; Liu & Schmitt, 2000). For example, layers of kerogen are thought to be isotropic but laboratory studies have confirmed that changes in these layers of kerogen affect the overall anisotropy observed in the rock (Johnston, 1997; Rundle & Schuler, 1981; Vernik & Landis, 1996; Vernik & Nur, 1992).

From pyrolysis and whole-rock analysis, it was determined that the oil shale sample was about 48 % kerogen by weight. This sample seems to be layers of cleaner kerogen versus layers of kerogen plus other minerals. This layering may be a possible source of anisotropy (Johnston, 1997; Rundle & Schuler, 1981;

Vernik & Landis, 1996; Vernik & Nur, 1992).

6.5 Experimental configuration

The most common method of determining velocities in various directions is to take cores in a variety of symmetry dependent directions. For shales this is typically parallel to layering, perpendicular to layering, and at some off-axis angles (Figure 2.6) (Domnesteanu et al., 2000; Hornby, 1995; Hornby, 1998; Johnston & Christensen, 1995; Jones & Wang, 1981; Kaarsberg, 1968; Lo et al., 1986; Podio et al., 1968; Vernik & Landis, 1996). If the diameter of the transducers used is quite large compared with the distances which the ultrasonic waves travel then plane wave (phase) velocities are measured (Dellinger & Vernik, 1994).

Another technique is to use the $\tau - p$ method as first described by Kebaili & Schmitt (1996). This methodology entails using 2 sources at a known depth and a series of evenly spaced receivers (Figure 2.7). A $\tau - p$ transform (Equation 2.11) is then performed on the data in order to determine the phase velocity as a function of the phase propagation angle. This methodology has been employed successfully on glass and phenolic samples (Mah & Schmitt, 2001a; Mah & Schmitt, 2001b; Mah & Schmitt, 2003). Unfortunately, this methodology when performed on the oil shale yielded highly attenuated and consequently poor quality results that did not allow for accurate determination of the elastic constants (Figure 6.1). Stacking of waveforms and filtering did not improve the data quality to acceptable levels. Instead, a more conventional pulse transmission technique was consequently employed.

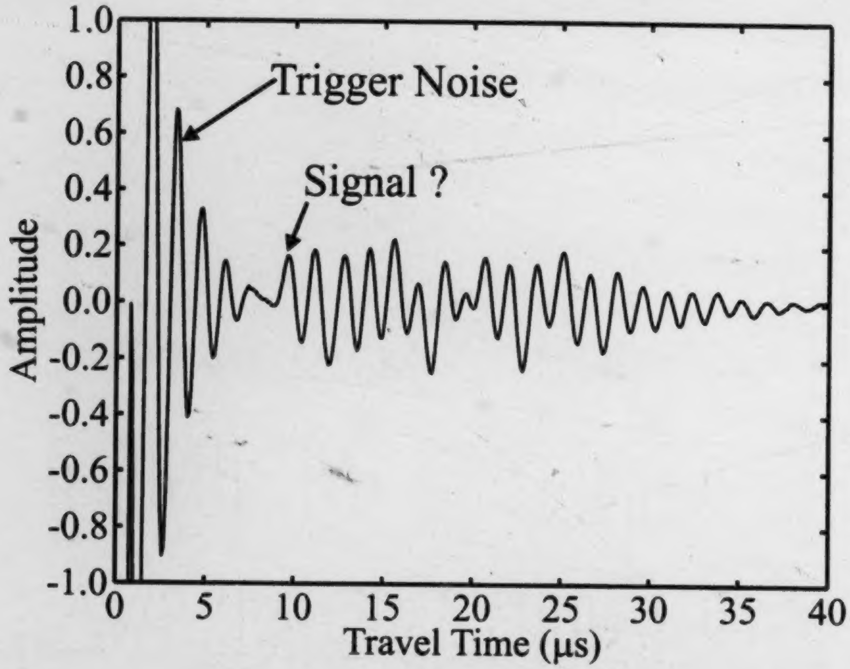

Figure 6.1: P-wave waveform acquired on a oil shale sample using methodology described in Mah & Schmitt (2001a, 2001b, and 2003). Waveform generated by P-wave source at 2.0 cm depth and detected by P-wave receiver at 1.0 cm offset after stacking more than 3000 raw waveforms and preliminary filtering.

6.5.1 Laboratory Set-up

The methodology used in this work employs a specially cut multifaceted prism of the oil shale (Figure 6.2). Velocities in 6 different directions were measured (Figure 6.3). Measurements were made in 3 directions parallel to the axes chosen previously (Figure 5.3). The 3 remaining directions were chosen in the $\vec{n} = \left[0\ \frac{1}{\sqrt{2}}\ \frac{1}{\sqrt{2}}\right]$, $\vec{n} = \left[\frac{1}{\sqrt{2}}\ 0\ \frac{1}{\sqrt{2}}\right]$, and $\vec{n} = \left[\frac{1}{\sqrt{2}}\ \frac{1}{\sqrt{2}}\ 0\right]$ directions (Figure 6.3). Assuming an orthorhombic medium, the measurement of P-wave and S-wave waveforms recorded in these 6 directions allowed all 9 elastic constants to be determined. It has long been known that rock properties change with pressure

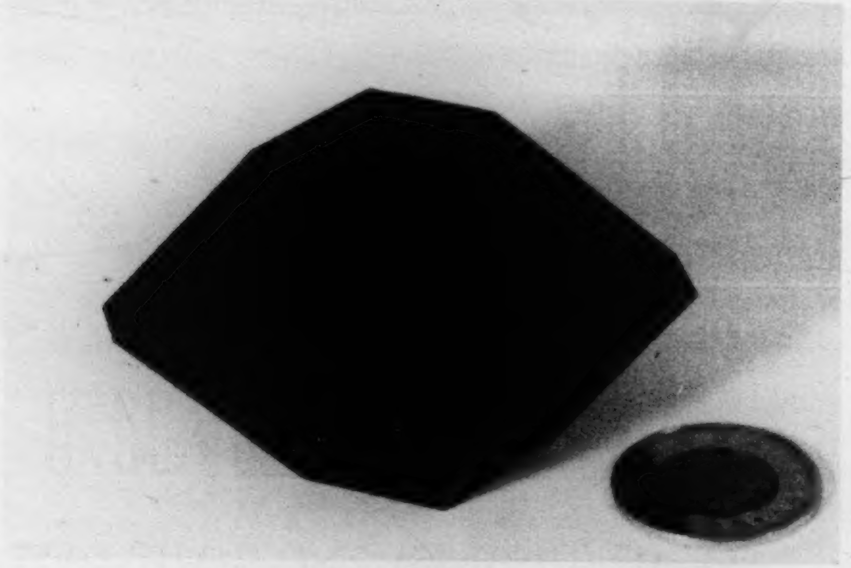

Figure 6.2: Picture of multifaceted cube of oil shale after four sets of cuts (Two dollar coin diameter = 28 mm).

or depth (Banik, 1984; Birch, 1960; Carlson et al., 1984; Faust, 1951; Freund, 1992; Johnston, 1987; Kaarsberg, 1959; Vernik, 1993; Vernik & Liu, 1997) and as such measurements were taken from room pressure (Figure 6.4) to 20 MPa (200 bar) in order to determine how the anisotropy of the oil shale changed with pressure. This maximum pressure corresponds to the lithostatic load at a depth of approximately 1300 m in this formation.

P-wave (longitudinal) and S-wave (transverse) transducers were used to generate and detect the seismic waves travelling through the sample. Piezo-electric ceramics (PZT-5) with a diameter of 25.00 mm ± 0.28 mm and a peak frequency of 1.0 MHz ± 5 % were used in the manufacture of these P-wave transducers. Even though the large diameter limits the placement and number of transducers on the sample, it allows for a wave nearer that of a plane wave to be generated and hence a more accurate phase velocity to be determined (Dellinger & Vernik,

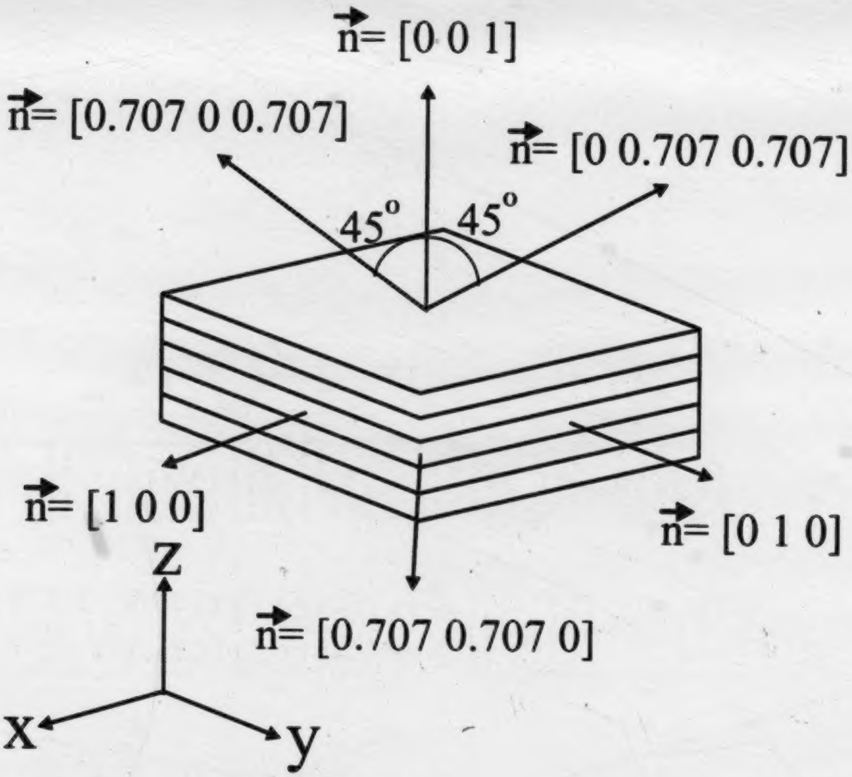

Figure 6.3: Measurements taken at 6 different orientations to layering.

1994). The S-wave transducers also employed piezo-electric ceramics (Navy Type VI - 552) but were 20 mm by 20 mm square with a peak frequency of 1.0 MHz. The transducers were damped with a metallic powder and polyurethane mixture to reduce ringing and improve the quality of the generated waves. A lead foil typically 3/1000 inch thick was used to provide electrical conductivity and a good coupling of the transducer with the sample when mounted. Once the transducers were mounted, the transducers and oil shale were sealed with multiple coats of polyurethane to ensure there was no contamination of the oil shale with the hydraulic fluid used in the pressure vessel.

Measurements of the oil shale were done under pressure inside the pressure vessel. The P-wave and S-wave source transducers were activated with a 300 Volt electrical spike that had a rise time of 10 ns. This caused the source transducers to generate a plane wave that propagated through the sample that in turn was observed by the receiver transducers. The seismic wave generated an electrical response in the receiver transducer that was digitally acquired by a high-speed sampling oscilloscope with a sampling rate of 10 ns/sample for 150 μs. Anywhere from 2000 to 3000 individual waveforms were summed (or stacked) in order to reduce random noise. The waveforms were then transferred via a GPIB bus to a computer for analysis.

As mentioned previously the size of the sample limited the number of transducers that could be applied at any one time. Typically, only 3 sets of transducers could be attached at a given time. The necessary measurements were made on the sample before the sample was recut and resquared (Figure 6.5). Resquaring was necessary in order to ensure that the surfaces were at 45 and 90 degrees to previously chosen coordinate axes (Figure 6.3). Measurements were then taken on these new surfaces in the previously unmeasured directions. This resulted in not only the seismic waves propagating over a different distance for each direction investigated (Table 6.2) but also necessitated multiple runs being performed.

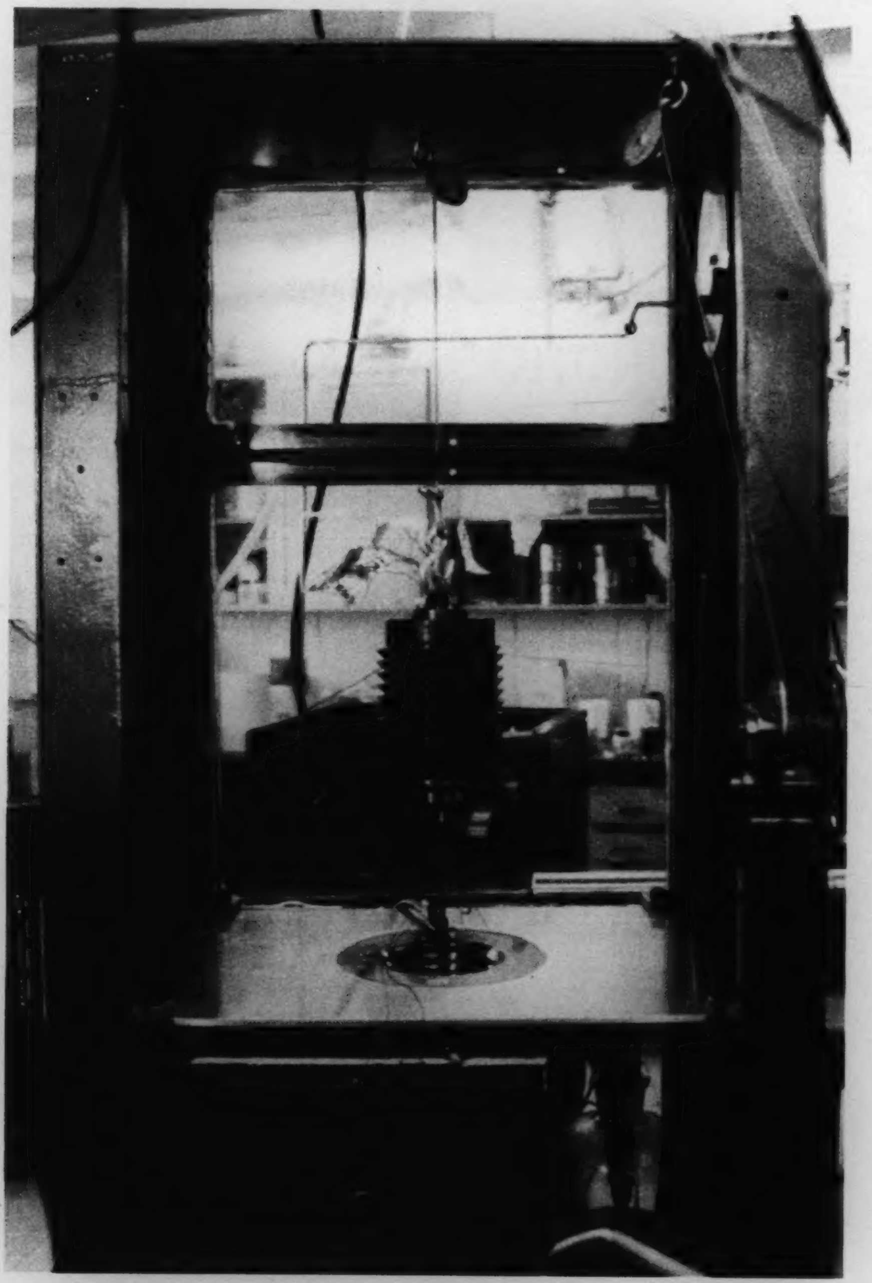

Figure 6.4: Picture of pressure vessel capable of obtaining 200 MPa (2000 bar) confining pressure.

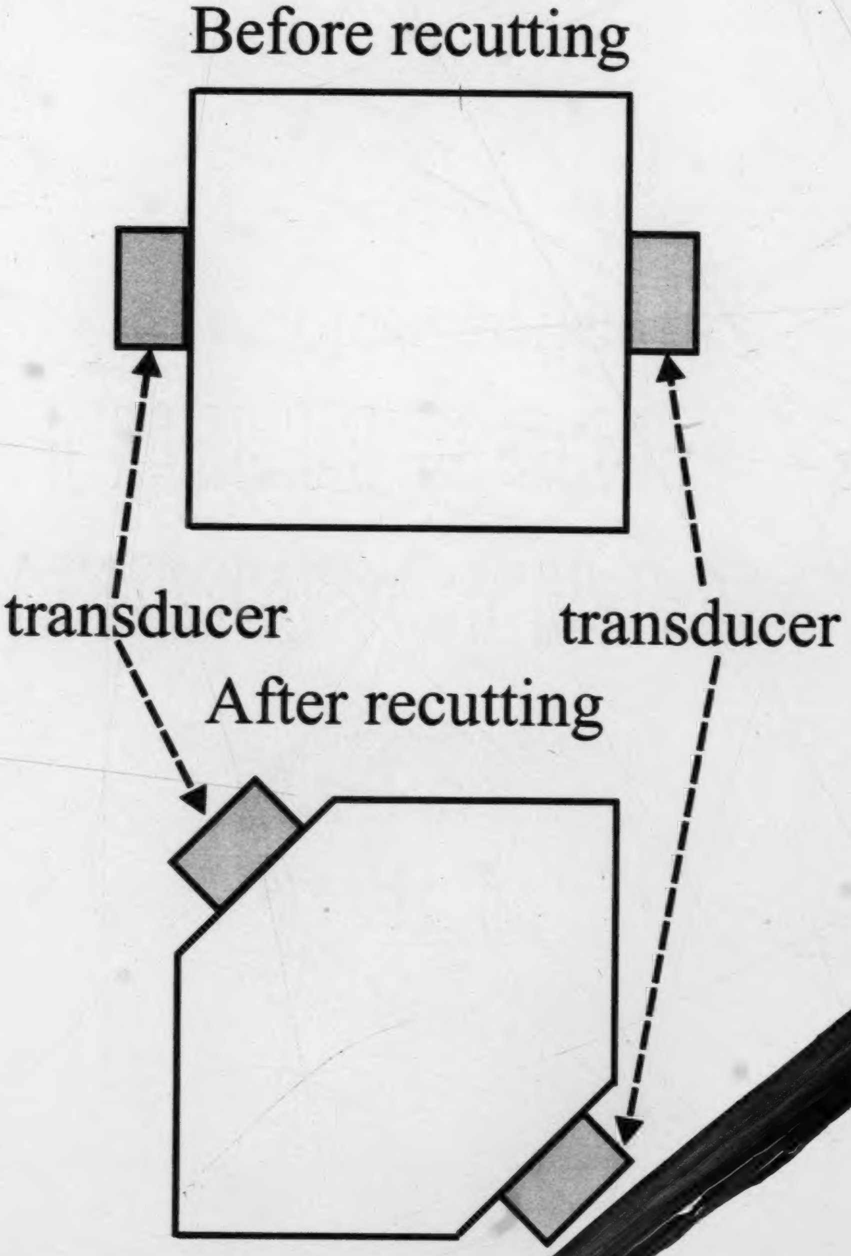
Before recutting
transducer
transducer
After recutting

Figure 6.5: Sample before and after recutting [illegible] transducers mounted.

6.6 Experimental results and analysis

6.6.1 Crush tests and heterogeneity tests

Due to multiple runs being performed in the pressure vessel, crush tests were done to ensure that the properties of the sample were not being permanently changed by the pressure regime the sample under went. If the properties of the sample are changed permanently, the fabric of the rock is said to be damaged or "crushed". In order to determine at what pressures the oil shale could be safely exposed to, it was subjected to an increasing amount of confining pressure and the waveforms recorded until there was a sudden change in the waveform possibly indicating the oil shale was being damaged. The anomalous waveforms were very ringy and of low amplitude. This occurred at approximately between 60 MPa and 70 MPa (600 and 700 bar, respectively) which corresponds to a lithostatic load at a depth between 3900 and 4550 m. Once this threshold is reached, reduction in the confining pressure did not result in reversion to the original waveforms. In contrast, however, repeated pressurization and depressurization of an undamaged oil shale to a maximum pressure of 20 MPa (200 bar) did not yield any noticeable permanent change in the waveforms. It can be reasonably inferred that the properties of the oil shale are not being permanently altered or damaged by repeated pressurization and depressurization to a maximum pressure of 20 MPa (200 bar).

As seen in Figures 5.2 and 5.3, the oil shale has some zones, such as the white-cream coloured layers, that may have different properties from the surrounding dark greyish brown material. In order to evaluate the severity of the heterogeneity, a series of measurements was made at 13 different positions in directions parallel to the x and y-axes (Figure 6.6). Locations E, F, and K are located on a white-cream coloured layer while the other locations are at areas of dark greyish brown rock. P-waves and S-wave waveforms were acquired at all 13

Location	P-wave velocity (m/s)	SH-wave velocity (m/s)	SV-wave velocity (m/s)
A	2423	1255	1016
B	2382	1115	1010
C	2352	1290	982
D	2352	1138	982
E	3146	1925	1729
F	2813	1813	1556
G	2466	1287	1046
H	2392	1228	1036
I	2396	1400	1007
J	2415	1154	984
K	3142	1896	1499
L	2515	1298	1027
M	2434	1250	1025

Table 6.1: P-wave, SH-wave, and SV-wave velocities from the heterogeneity test of location A to M. SV-waves have a polarization of (0 0 1). SH-waves have a polarization perpendicular to direction of travel and the z-axis. Locations A through H were acquired in the $\vec{n}$ = (0 1 0) direction at room pressure while location I through M were acquired in the $\vec{n}$ = (1 0 0) direction at room pressure.

locations. At location E, F, and K the waveforms acquired were quite different from the surrounding areas. This is most noticeable when comparing location C to location E (Figure 6.7). The calculated velocities were also faster at locations E, F, and K (Table 6.1). Therefore, care was taken to choose a multifaceted cube that did not include any noticeable white-cream coloured layers and that was as homogeneous as possible.

6.6.2 Velocity versus pressure

The P-wave and S-wave waveforms were recorded as functions of pressure up to 20 MPa (200 bar) for the 6 well-chosen directions (Figure 6.3). A maximum confining pressure of 20 MPa (200 bar) was chosen since a relatively linear change in velocity with pressure is seen throughout this range and was well under the pressures at which the sample could be damaged. P-wave waveforms travelling in the $\overrightarrow{n} = (1\ 0\ 0)$ direction show a decrease in the arrival time with increasing pressure indicating an increase in velocity (Figure 6.8). S-wave waveforms travelling in the $\overrightarrow{n} = (1\ 0\ 0)$ direction with a polarization of (0 0 1) show a similar change (Figure 6.10). A parasitic P-wave was observed in Figure 6.10 and is most likely caused by a P-wave being generated at the edges of the source or a mode conversion at one of the surfaces. Analysis of the parasitic P-waves did not yield any reliable velocities. Interestingly, the P-wave waveforms had an average peak frequency of 0.975 MHz (Figure 6.9) and the S-wave waveforms had an average peak frequency of 0.090 MHz (Figure 6.11) since the both P-wave and S-wave transducers have an original peak frequency of 1.0 MHz. However, the damping and mounting of the transducers may reduce the peak frequencies.

The arrival times of the first peak or trough were measured and the velocities determined as functions of pressure for the various waveforms recorded. For example, the first trough of a P-wave travelling in the $\overrightarrow{n} = (1\ 0\ 0)$ direction in the oil shale at 20 MPa (200 bar) confining pressure can be measured at 24.63 μs (Figure 6.12). Once the travel time of 0.14 μs through the lead foil used in mounting the transducers is accounted for the P-wave travel time is 24.49 μs. The distance travelled by the P-wave is 59.47 mm allowing a P-wave velocity of 2428 ± 3 m/s to be calculated. The velocities for all 3 polarizations are shown for 0, 10, and 20 MPa in Table 6.2. Please note that the distance used is measured at room pressure and will actually decrease when subjugated to increased pressure. As such, the observed velocities represent lower limits.

P-wave and S-wave velocities travelling in the $\overrightarrow{n} = (1\ 0\ 0)$ direction were determined as functions of pressure (Figure 6.13). It can be seen in Figures 6.14 through 6.20 that the velocity increased with increasing pressure. Not surprisingly, the velocities observed during pressurization are slightly lower than those during depressurization due to hysteresis effects (Gardner et al., 1965; Jones & Wang, 1981; Tutuncu et al., 1998). As well there is a change in the gradient dV_p/dP with the velocities generally increasing faster in the 0 to 4 MPa (40 bar) range as compared with the four MPa (40 bar) to 20 MPa (200 bar) range. This non-linear behaviour is attributed to the progressive closure of the microcracks. The increase in pressure causes closure of these microcracks, which is why there is a more rapid change at low pressure.

Interestingly, the P-wave velocities parallel to the layers in the $\vec{n} = (1\ 0\ 0)$ and $\vec{n} = (0\ 1\ 0)$ directions display more velocity hysteresis than those normal to layering in the $\vec{n} = (0\ 0\ 1)$ direction (Figure 6.14) indicating that there might be some preference to the microcrack orientation. Velocity hysteresis was similarly observed for S-wave velocities (Figures 6.18, 6.19, and 6.20). However, the velocity hysteresis in Figure 6.18 is almost non-existent while it is quite pronounced in Figures 6.19 and 6.20 indicating that there might be a preferentially orientation to the microcracks. During the depressurization of the oil shale, the velocity generally decreases almost linearly down to 1 MPa (10 bar).

Wave Type	Polarization	Direction of Travel	Distance Travelled	Pressure	Phase Velocity
P-wave	[1 0 0]	[1 0 0]	59.47 mm	0 MPa	2301±3 m/s
P-wave	[1 0 0]	[1 0 0]	59.47 mm	10 MPa	2396±3 m/s
P-wave	[1 0 0]	[1 0 0]	59.47 mm	20 MPa	2428±3 m/s
P-wave	$[\frac{1}{\sqrt{2}}\ \frac{1}{\sqrt{2}}\ 0]$	$[\frac{1}{\sqrt{2}}\ \frac{1}{\sqrt{2}}\ 0]$	47.99 mm	0 MPa	2296±3 m/s
P-wave	$[\frac{1}{\sqrt{2}}\ \frac{1}{\sqrt{2}}\ 0]$	$[\frac{1}{\sqrt{2}}\ \frac{1}{\sqrt{2}}\ 0]$	47.99 mm	10 MPa	2362±3 m/s
P-wave	$[\frac{1}{\sqrt{2}}\ \frac{1}{\sqrt{2}}\ 0]$	$[\frac{1}{\sqrt{2}}\ \frac{1}{\sqrt{2}}\ 0]$	47.99 mm	20 MPa	2394±3 m/s
P-wave	$[\frac{1}{\sqrt{2}}\ 0\ \frac{1}{\sqrt{2}}]$	$[\frac{1}{\sqrt{2}}\ 0\ \frac{1}{\sqrt{2}}]$	45.90 mm	0 MPa	2162±3 m/s
P-wave	$[\frac{1}{\sqrt{2}}\ 0\ \frac{1}{\sqrt{2}}]$	$[\frac{1}{\sqrt{2}}\ 0\ \frac{1}{\sqrt{2}}]$	45.90 mm	10 MPa	2200±3 m/s
P-wave	$[\frac{1}{\sqrt{2}}\ 0\ \frac{1}{\sqrt{2}}]$	$[\frac{1}{\sqrt{2}}\ 0\ \frac{1}{\sqrt{2}}]$	45.90 mm	20 MPa	2233±3 m/s
P-wave	[0 1 0]	[0 1 0]	55.89 mm	0 MPa	2298±3 m/s
P-wave	[0 1 0]	[0 1 0]	55.89 mm	10 MPa	2353±3 m/s
P-wave	[0 1 0]	[0 1 0]	55.89 mm	20 MPa	2393±3 m/s
P-wave	$[0\ \frac{1}{\sqrt{2}}\ \frac{1}{\sqrt{2}}]$	$[0\ \frac{1}{\sqrt{2}}\ \frac{1}{\sqrt{2}}]$	50.28 mm	0 MPa	2168±3 m/s
P-wave	$[0\ \frac{1}{\sqrt{2}}\ \frac{1}{\sqrt{2}}]$	$[0\ \frac{1}{\sqrt{2}}\ \frac{1}{\sqrt{2}}]$	50.28 mm	10 MPa	2223±3 m/s
P-wave	$[0\ \frac{1}{\sqrt{2}}\ \frac{1}{\sqrt{2}}]$	$[0\ \frac{1}{\sqrt{2}}\ \frac{1}{\sqrt{2}}]$	50.28 mm	20 MPa	2257±3 m/s
P-wave	[0 0 1]	[0 0 1]	53.30 mm	0 MPa	2090±2 m/s
P-wave	[0 0 1]	[0 0 1]	53.30 mm	10 MPa	2127±2 m/s
P-wave	[0 0 1]	[0 0 1]	53.30 mm	20 MPa	2186±3 m/s
S-wave	[0 0 1]	[0 1 0]	55.89 mm	0 MPa	904±1 m/s
S-wave	[0 0 1]	[0 1 0]	55.89 mm	10 MPa	944±1 m/s
S-wave	[0 0 1]	[0 1 0]	55.89 mm	20 MPa	957±1 m/s
S-wave	[0 0 1]	[0 0 1]	59.47 mm	0 MPa	905±1 m/s
S-wave	[0 0 1]	[0 0 1]	59.47 mm	10 MPa	931±1 m/s
S-wave	[0 0 1]	[0 0 1]	59.47 mm	20 MPa	940±1 m/s
S-wave	[1 0 0]	[0 1 0]	55.89 mm	0 MPa	1059±1 m/s
S-wave	[1 0 0]	[0 1 0]	55.89 mm	10 MPa	1096±1 m/s
S-wave	[1 0 0]	[0 1 0]	55.89 mm	20 MPa	1109±1 m/s

Table 6.2: Distance travelled and phase velocities at 0, 10, and 20 MPa pressure for all 6 directions of propagation.

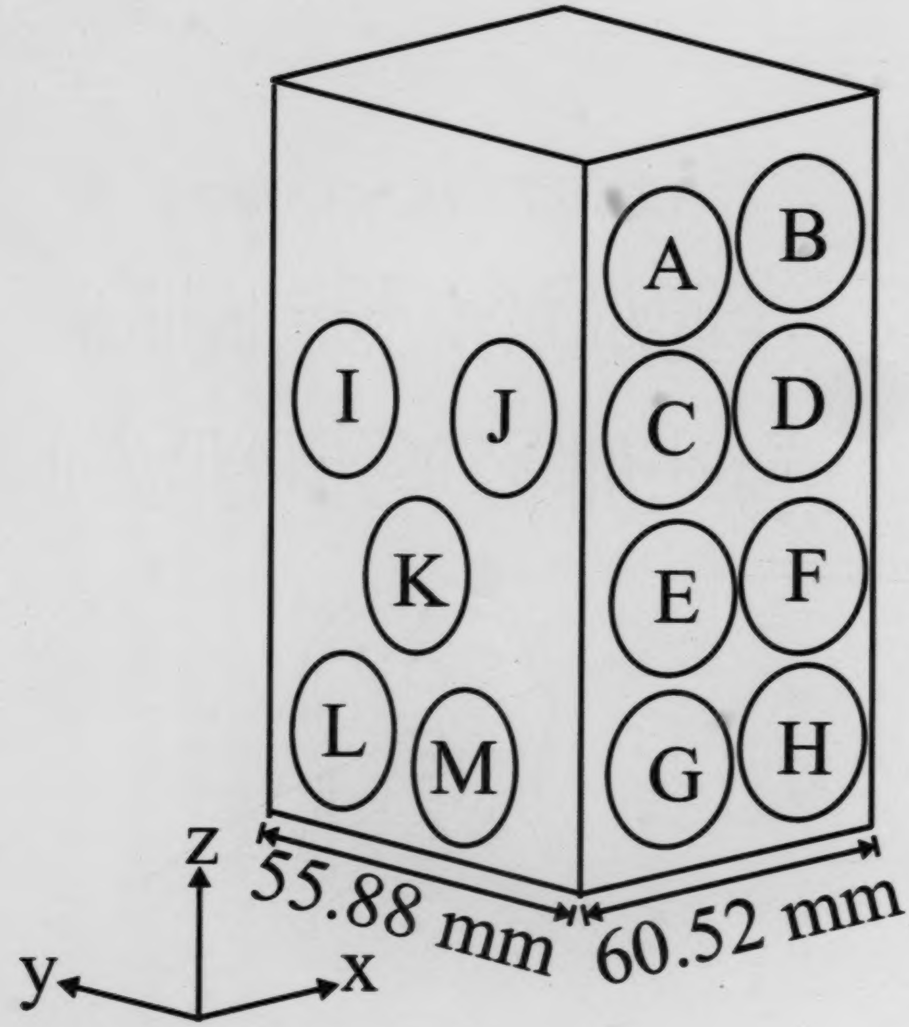
A
B
I
J
C
D
K
E
F
L
M
G
H
z
55.88 mm
60.52 mm
y
x

Figure 6.6: Locations A to M investigated in heterogeneity test.

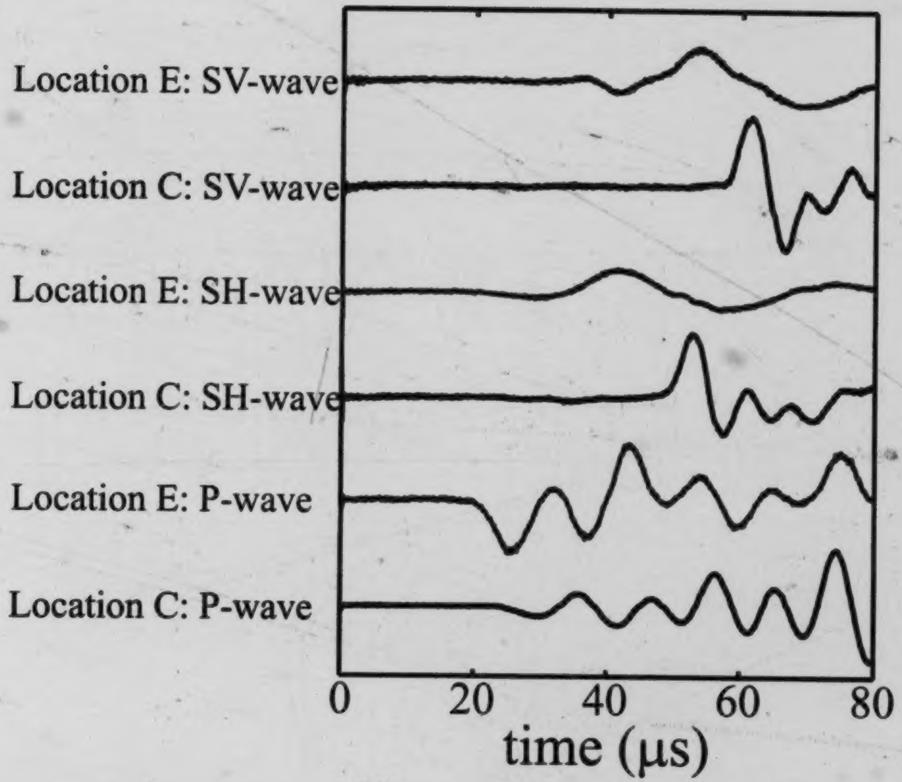

Figure 6.7: Waveforms acquired at locations C and E are shown in Figure 6.6. Waveforms acquired at location C are shown in blue while those acquired at location E are shown in red. All waveforms travelled a distance of 55.88 mm and were travelling in the $\vec{n}$ = (0 1 0) direction. SH-waves have a polarization of (1 0 0) and SV-waves have a polarization of (0 0 1).

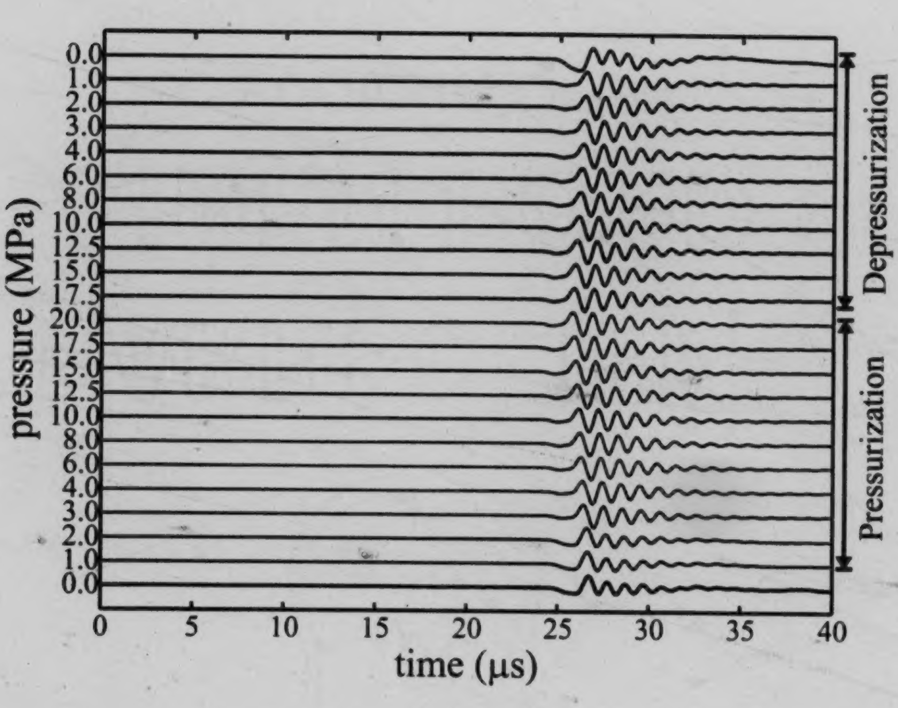

Figure 6.8: P-wave waveforms travelling in the $\vec{n}$ = (1 0 0) direction acquired as a function of pressure.

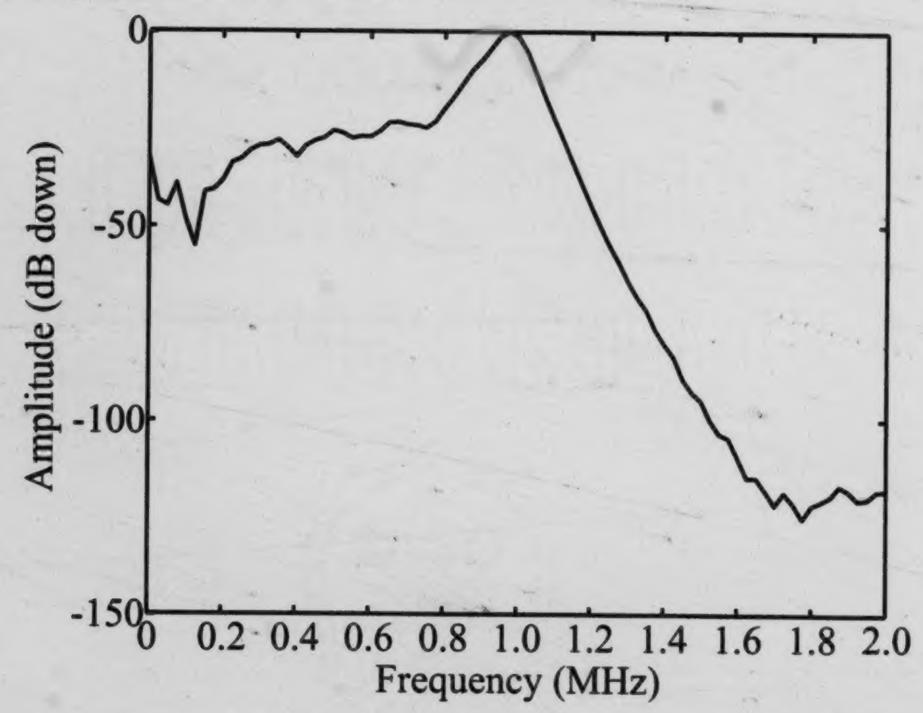

Figure 6.9: Average amplitude spectrum of P-wave waveforms in shown Figure 6.8.

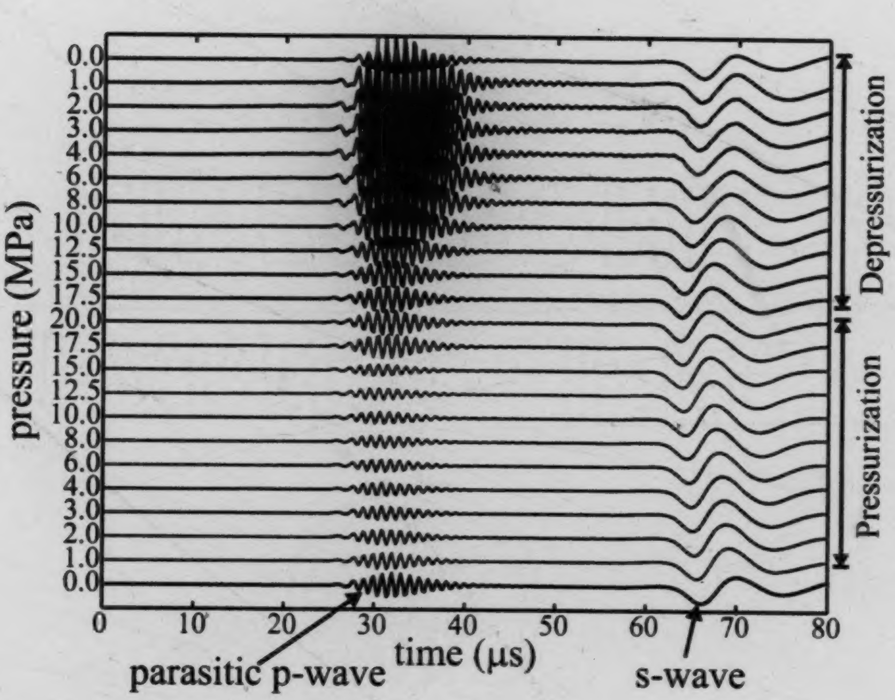

Figure 6.10: S-wave with polarization (0 0 1) waveforms travelling in the $\vec{n}$ = (1 0 0) acquired as a function of pressure.

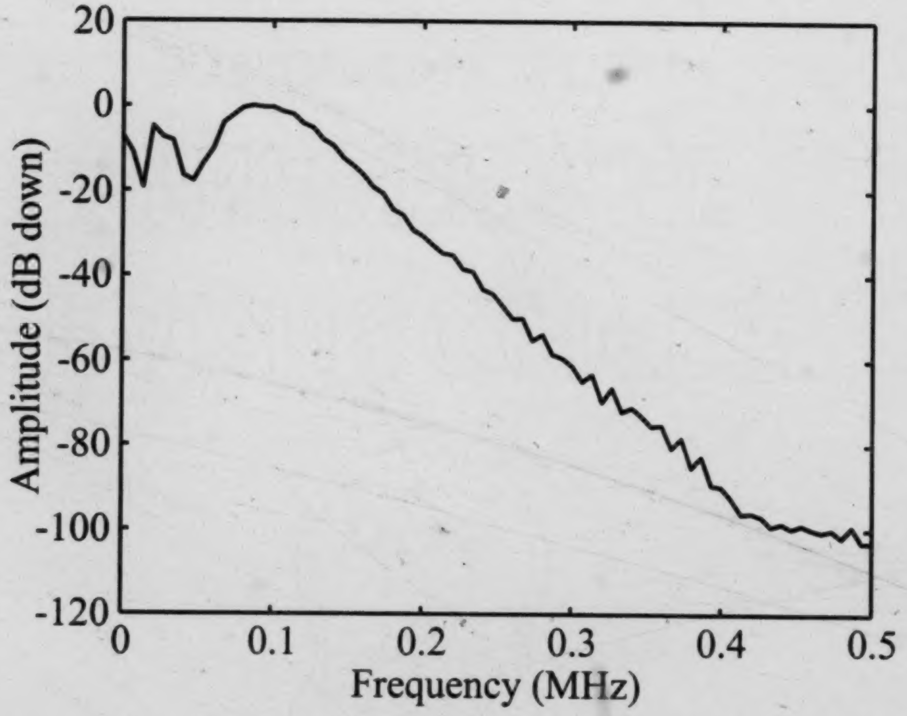

Figure 6.11: Average amplitude spectrum of S-wave waveforms shown in Figure 6.10.

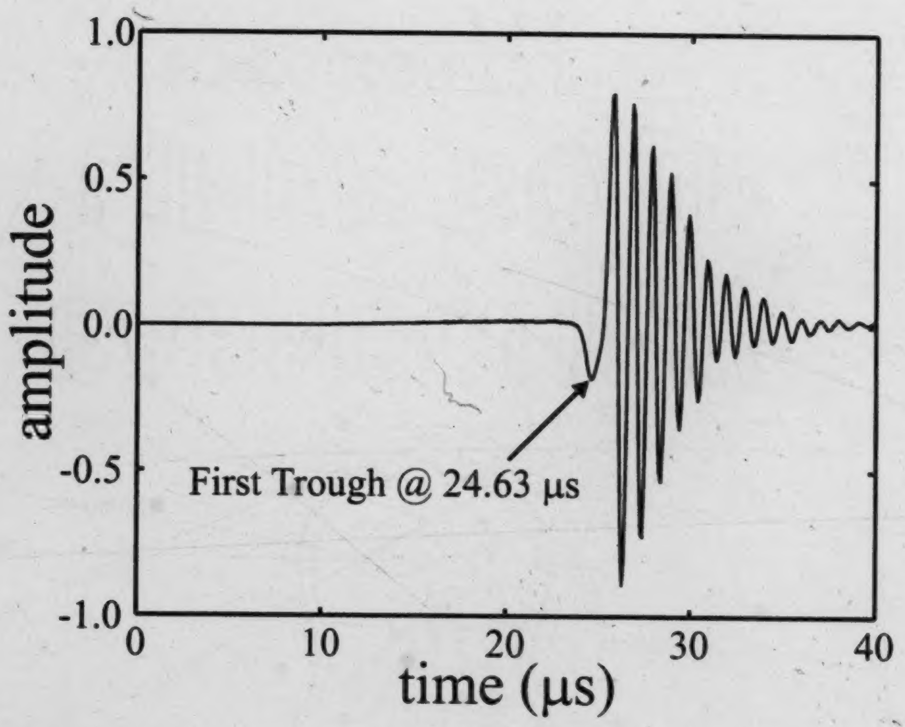

Figure 6.12: P-wave travelling in the $\vec{n}$ = (1 0 0) direction at 20 MPa (200 bar) confining pressure.

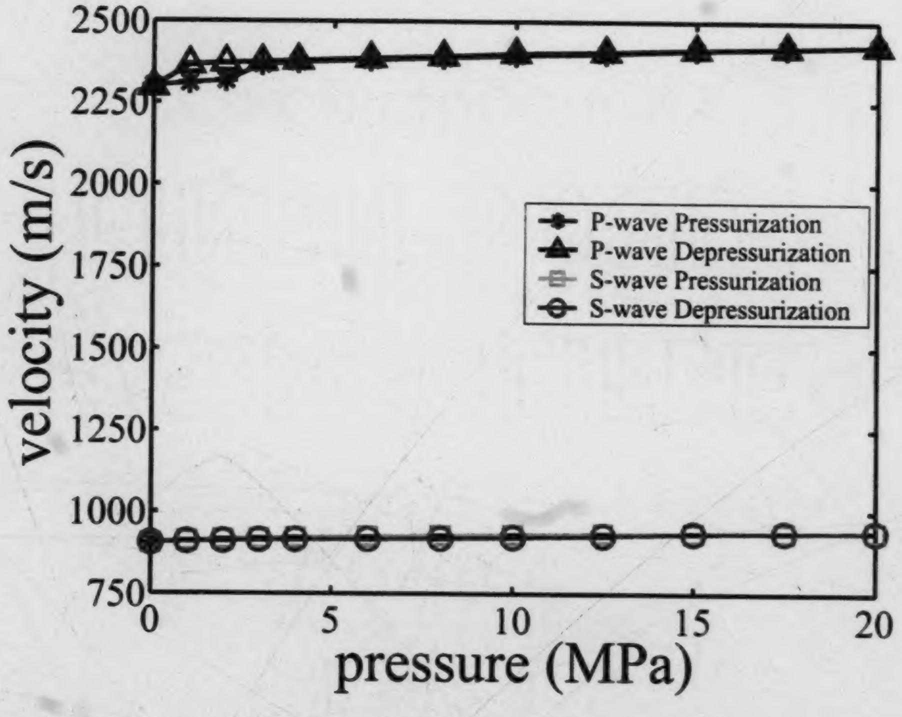

Figure 6.13: P-wave and S-wave with velocities are determined as a function of pressure in the $\vec{n} = (1\ 0\ 0)$ direction for both increasing and decreasing pressure. The S-wave has a polarization of (0 0 1) Due to the large difference in P-wave and S-wave velocities, velocity hysteresis and the error bars cannot be easily distinguished at this scale.

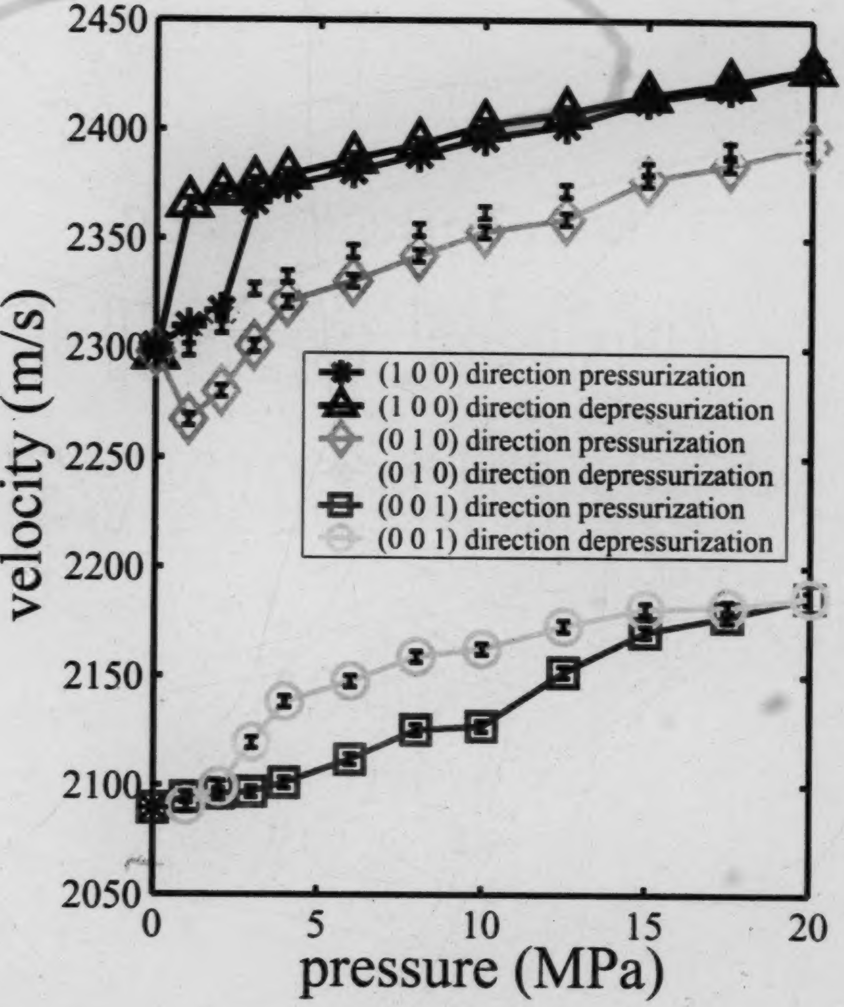

Figure 6.14: P-wave velocity versus pressure in the $\vec{n}$ = (1 0 0), $\vec{n}$ = (0 1 0), and $\vec{n}$ = (0 0 1) direction.

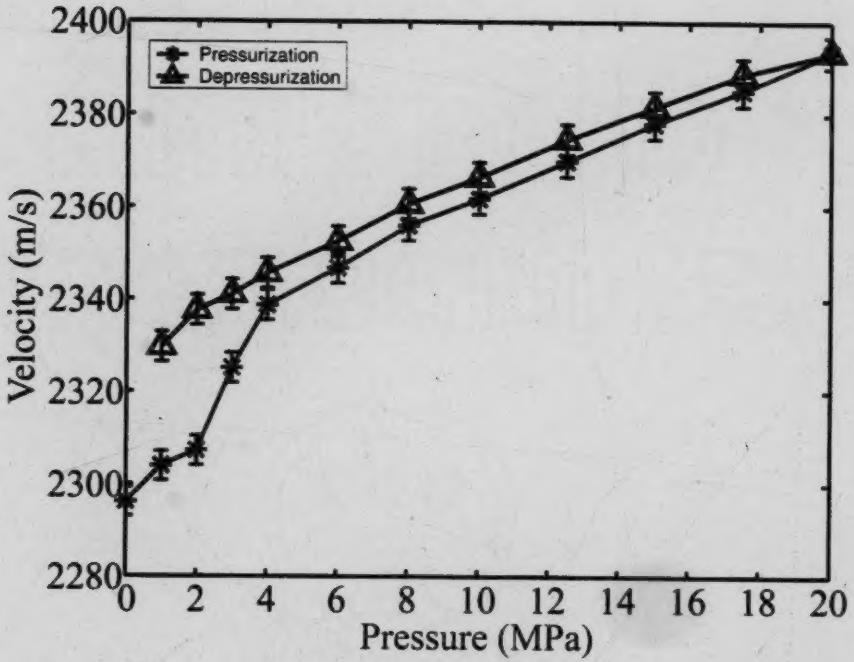

Figure 6.15: P-wave velocity versus pressure in the $\vec{n} = (\frac{1}{\sqrt{2}}\ \frac{1}{\sqrt{2}}\ 0)$ direction.

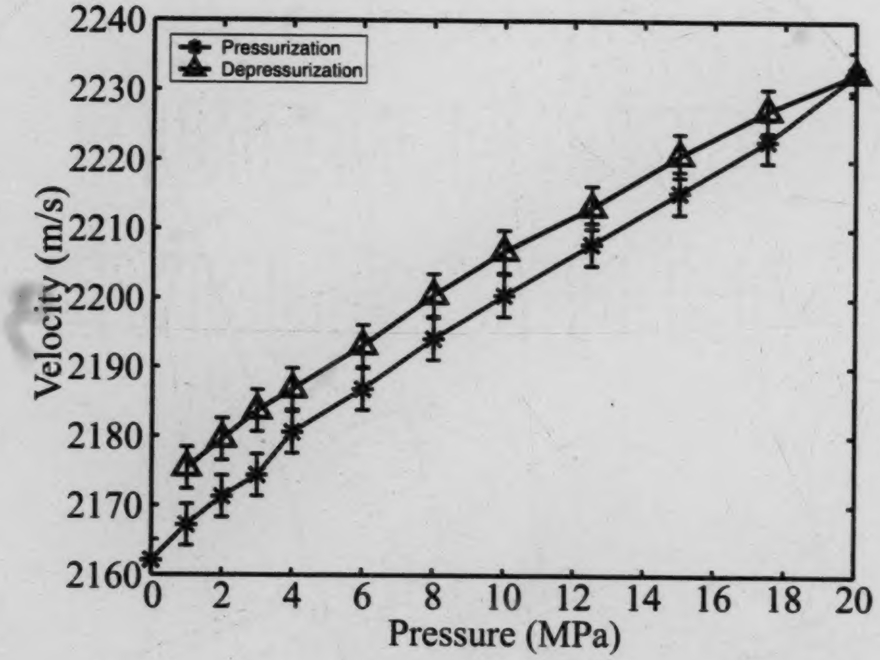

Figure 6.16: P-wave velocity versus pressure in the $\vec{n} = (\frac{1}{\sqrt{2}}\ 0\ \frac{1}{\sqrt{2}})$ direction.

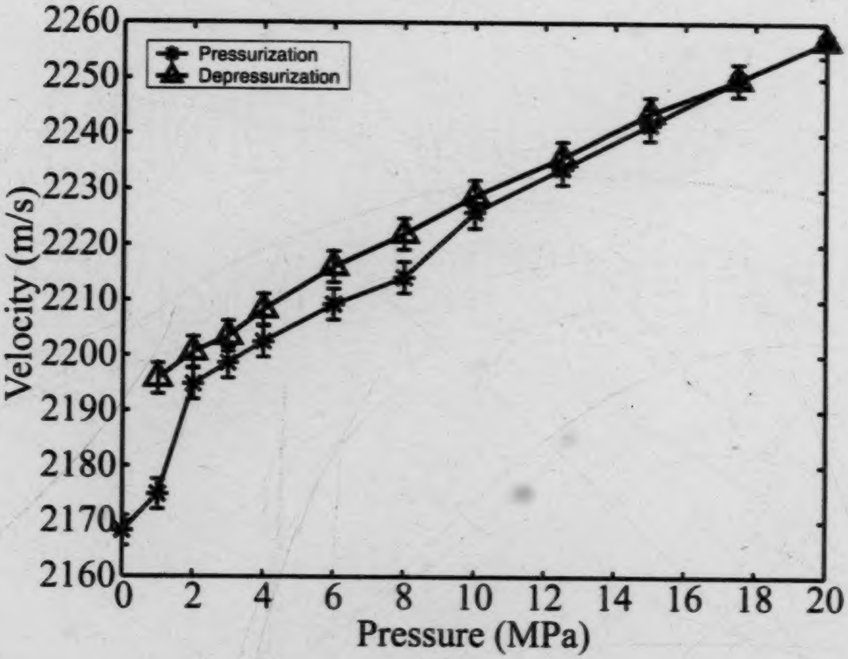

Figure 6.17: P-wave velocity versus pressure in the $\vec{n} = (0\ \frac{1}{\sqrt{2}}\ \frac{1}{\sqrt{2}})$ direction.

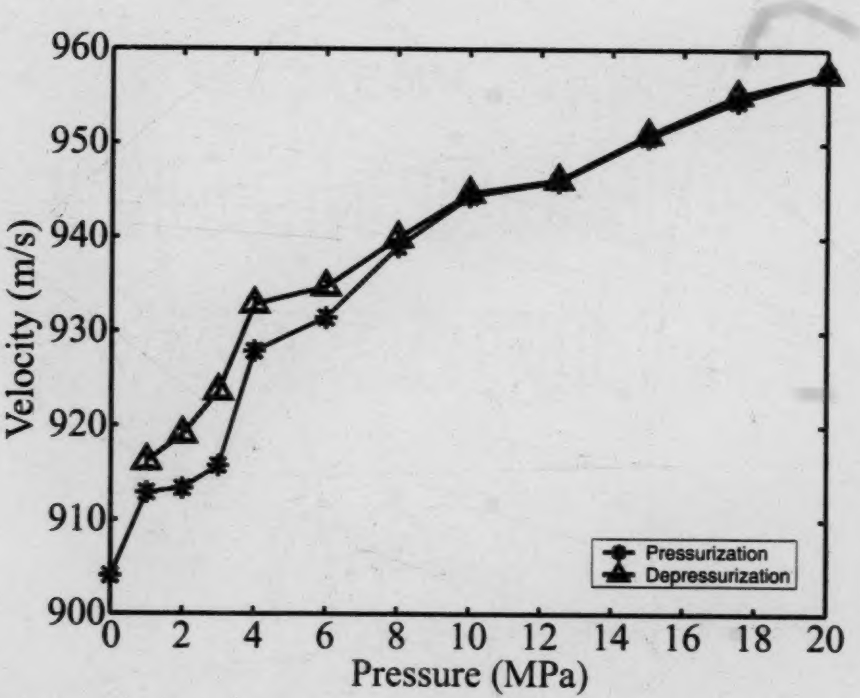

Figure 6.18: S-wave velocity versus pressure in the $\vec{n}$ = (0 1 0) direction with polarization (0 0 1).

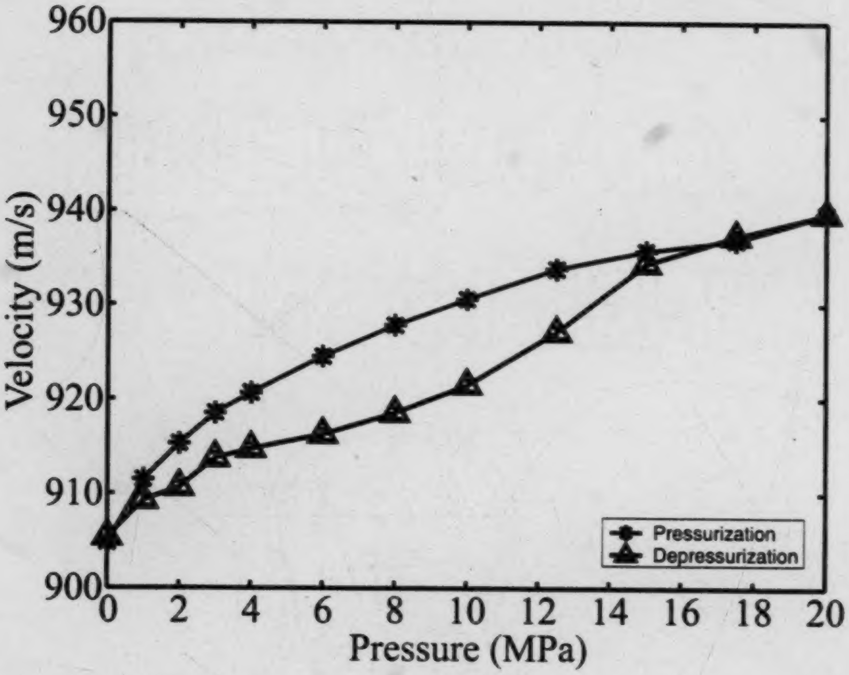

Figure 6.19: S-wave velocity versus pressure in the $\vec{n}$ = (1 0 0) direction with polarization (0 0 1).

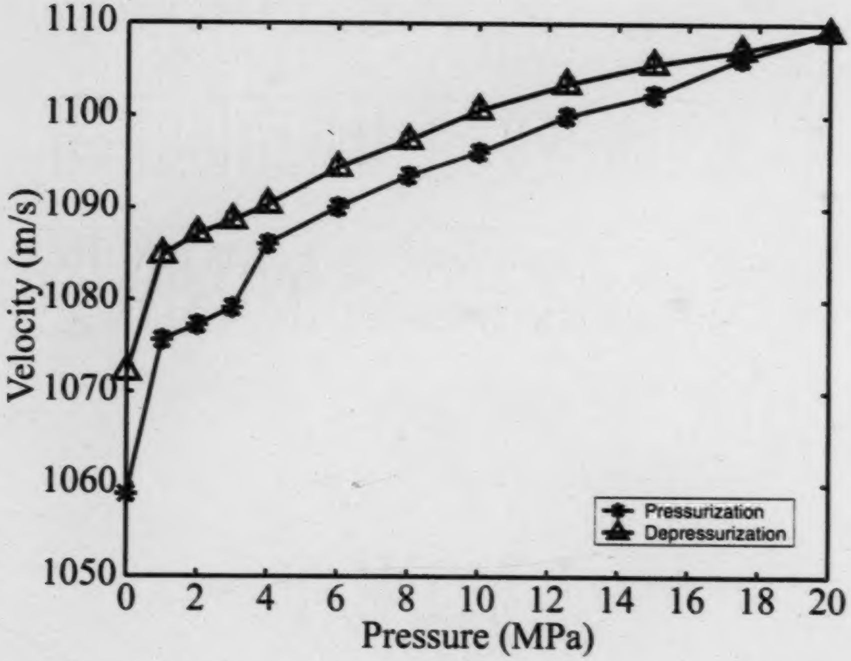

Figure 6.20: S-wave velocity versus pressure in the $\vec{n}$ = (1 0 0) direction with polarization (0 1 0).

6.6.3 Elastic Constants with Pressure

For an orthorhombic medium the elastic constants are:

$$C_{IJ} = \begin{bmatrix} C_{11} & C_{12} & C_{13} & 0 & 0 & 0 \\ & C_{22} & C_{23} & 0 & 0 & 0 \\ & & C_{33} & 0 & 0 & 0 \\ & & & C_{44} & 0 & 0 \\ & & & & C_{55} & 0 \\ & & & & & C_{66} \end{bmatrix} . \tag{6.1}$$

According to Appendix A, the following equations relating the elastic constants back to the phase velocities in the $\vec{n} = [1\ 0\ 0]$ direction are:

$$C_{11} = \rho\nu^2_{P[1\ 0\ 0]} , \tag{6.2}$$

$$C_{55} = \rho\nu^2_{S[0\ 0\ 1]} , \tag{6.3}$$

and

$$C_{66} = \rho\nu^2_{S[0\ 1\ 0]} \tag{6.4}$$

where ρ is the density and the vector given inside the square brackets, e.g. [1, 0, 0], refers to the polarization of the propagating plane wave. Similarly, elastic constants determined from phase velocities in the $\vec{n} = [0\ 1\ 0]$ direction are:

$$C_{22} = \rho\nu^2_{P[0\ 1\ 0]} , \tag{6.5}$$

$$C_{44} = \rho\nu^2_{S[0\ 0\ 1]} , \tag{6.6}$$

and

$$C_{66} = \rho\nu^2_{S[1\ 0\ 0]} . \tag{6.7}$$

As one can see, there is redundancy in the determination of the elastic constant C_{66}. This redundancy is seen in the elastic constants determined from phase velocities in the $\vec{n} = [0\ 0\ 1]$ direction:

$$C_{33} = \rho v^2_{P[0\ 0\ 1]}\ , \qquad (6.8)$$

$$C_{44} = \rho v^2_{S[0\ 1\ 0]}\ , \qquad (6.9)$$

and

$$C_{55} = \rho v^2_{S[1\ 0\ 0]} \qquad (6.10)$$

where the elastic constants C_{44} and C_{55} are redundantly determined.

Even with this overlap, these 3 directions allow only the 6 elastic constants of Equation 6.1 to be determined. Using the P-wave phase velocities in the off-axis directions $\vec{n} = \left[\frac{1}{\sqrt{2}}\ \frac{1}{\sqrt{2}}\ 0\right]$, $\vec{n} = \left[\frac{1}{\sqrt{2}}\ 0\ \frac{1}{\sqrt{2}}\right]$, and $\vec{n} = \left[0\ \frac{1}{\sqrt{2}}\ \frac{1}{\sqrt{2}}\right]$ allows:

$$C_{12} = -C_{66} - \sqrt{\left(C_{11} + C_{66} - 2\rho v^2_{P\left[\frac{1}{\sqrt{2}}\ \frac{1}{\sqrt{2}}\ 0\right]}\right)\left(C_{22} + C_{66} - 2\rho v^2_{P\left[\frac{1}{\sqrt{2}}\ \frac{1}{\sqrt{2}}\ 0\right]}\right)}\ , \qquad (6.11)$$

$$C_{13} = -C_{55} - \sqrt{\left(C_{11} + C_{55} - 2\rho v^2_{P\left[\frac{1}{\sqrt{2}}\ 0\ \frac{1}{\sqrt{2}}\right]}\right)\left(C_{33} + C_{55} - 2\rho v^2_{P\left[\frac{1}{\sqrt{2}}\ 0\ \frac{1}{\sqrt{2}}\right]}\right)}\ , \qquad (6.12)$$

and

$$C_{23} = -C_{44} - \sqrt{\left(C_{22} + C_{44} - 2\rho v^2_{P\left[0\ \frac{1}{\sqrt{2}}\ \frac{1}{\sqrt{2}}\right]}\right)\left(C_{33} + C_{44} - 2\rho v^2_{P\left[0\ \frac{1}{\sqrt{2}}\ \frac{1}{\sqrt{2}}\right]}\right)}\ , \qquad (6.13)$$

to be derived, respectively. See Appendix A for a more complete description.

Using Equations 6.2 through 6.13 for an orthorhombic medium, the elastic constants as functions of pressure were calculated. If the oil shale is transversely isotropic the C_{13} and C_{23} elastic constants should be equal but are noticeably different (Figure 6.21). The C_{11} and C_{22} elastic constants are expected to be the same for a transversely isotropic medium but are slightly different for the oil shale (Figure 6.22). As well, the C_{44} and C_{55} elastic constants are different for the oil shale (Figure 6.24). Assuming that this is not experimental error or heterogeneity, such observations suggest that the oil shale is not perfectly transversely isotropic but is more anisotropically complex being at least weakly orthorhombic.

Hysteresis has been observed previously in the velocity as a function of pressure data and this manifests itself as well in the changes in the elastic constants with pressure (Figures 6.22, 6.21, and 6.24). The elastic constants C_{11} and C_{22} seem to display a smaller degree of hysteresis compared with the C_{33} elastic constant. The C_{11} hysteresis is smaller than the C_{22} hysteresis (Figure 6.22). When the elastic constant hysteresis is shown as a percentage versus pressure, the C_{33} hysteresis is larger than the C_{11} and C_{22} hystereses for 4 MPa to 15 MPa even though at lower pressures it is smaller (Figure 6.23). The C_{44} and C_{55} elastic constant hystereses are different from each other and from the C_{66} hysteresis as well (Figure 6.24).

As mentioned previously, the oil shale is expected to be transversely isotropic due to its layered nature. However, it has been determined through ultrasonic measurements that the oil shale is weakly orthorhombic. If indeed the oil shale were transversely isotropic, one would expect C_{11} to be equal to C_{22} as shown in Figure 6.22. At 0 MPa confining pressure, there is no difference between C_{11} and C_{22} elastic constants (Figure 6.25). As the pressure increases, there is a sudden jump in the difference and then a gradual drop with increasing pressure. This may indicate that some of this "orthorhombicity" is caused by preferential orientation of the microcracks with planes normal either to the x-direction or to the y-direction.

Similarly, if the oil shale were transversely isotropic one would expect C_{13} to be equal to C_{23} as shown in Figure 6.21. Surprisingly, the difference between the

Elastic constant	Value at 0 MPa	Value at 10 MPa	Value at 20 MPa
C_{11}	8.31±0.07 GPa	9.01±0.07 GPa	9.26±0.07 GPa
C_{12}	-8.3±0.2 GPa	-8.7±0.2 GPa	-8.9±0.2 GPa
C_{13}	-7.0±0.1 GPa	-7.1±0.2 GPa	-7.2±0.2 GPa
C_{22}	8.29±0.07 GPa	8.69±0.07 GPa	8.99±0.07 GPa
C_{23}	-7.1±0.1 GPa	-7.6±0.2 GPa	-7.7±0.2 GPa
C_{33}	6.85±0.06 GPa	7.10±0.06 GPa	7.51±0.06 GPa
C_{44}	1.282±0.009 GPa	1.40±0.01 GPa	1.44±0.01 GPa
C_{55}	1.285±0.009 GPa	1.36±0.01 GPa	1.39±0.01 GPa
C_{66}	1.76±0.01 GPa	1.89±0.01 GPa	1.93±0.01 GPa

Table 6.3: Elastic constants for the oil shale at 0, 10, and 20 MPa pressure assuming orthorhombic symmetry.

C_{13} and C_{23} elastic constants (Figure 6.26) is relatively constant with pressure. The C_{44} and C_{55} elastic constants would also be the same if the oil shale is transversely isotropic (Figure 6.24) but are different as shown in Figure 6.27. The difference between C_{44} and C_{55} ranges from 2.3 MPa to 67.9 MPa and generally increases with pressure.

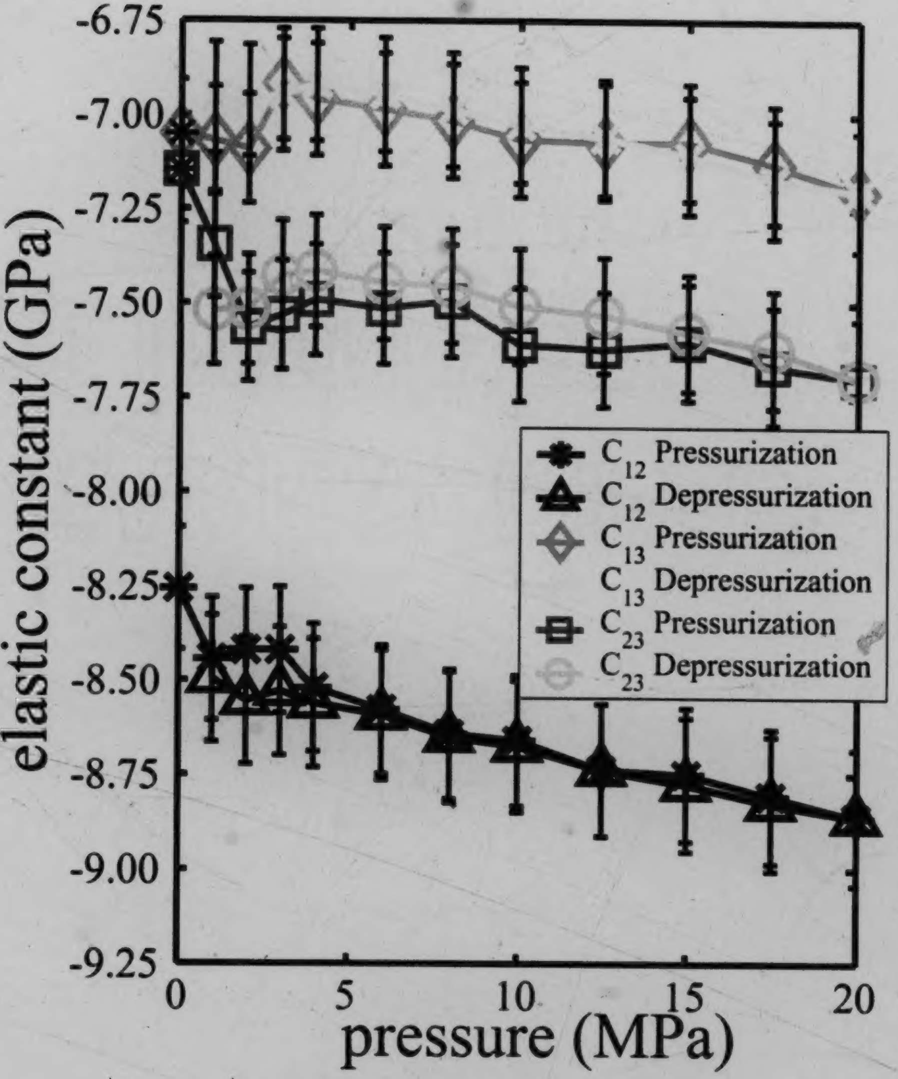

Figure 6.21: Elastic constant C_{12}, C_{13}, and C_{23} versus pressure.

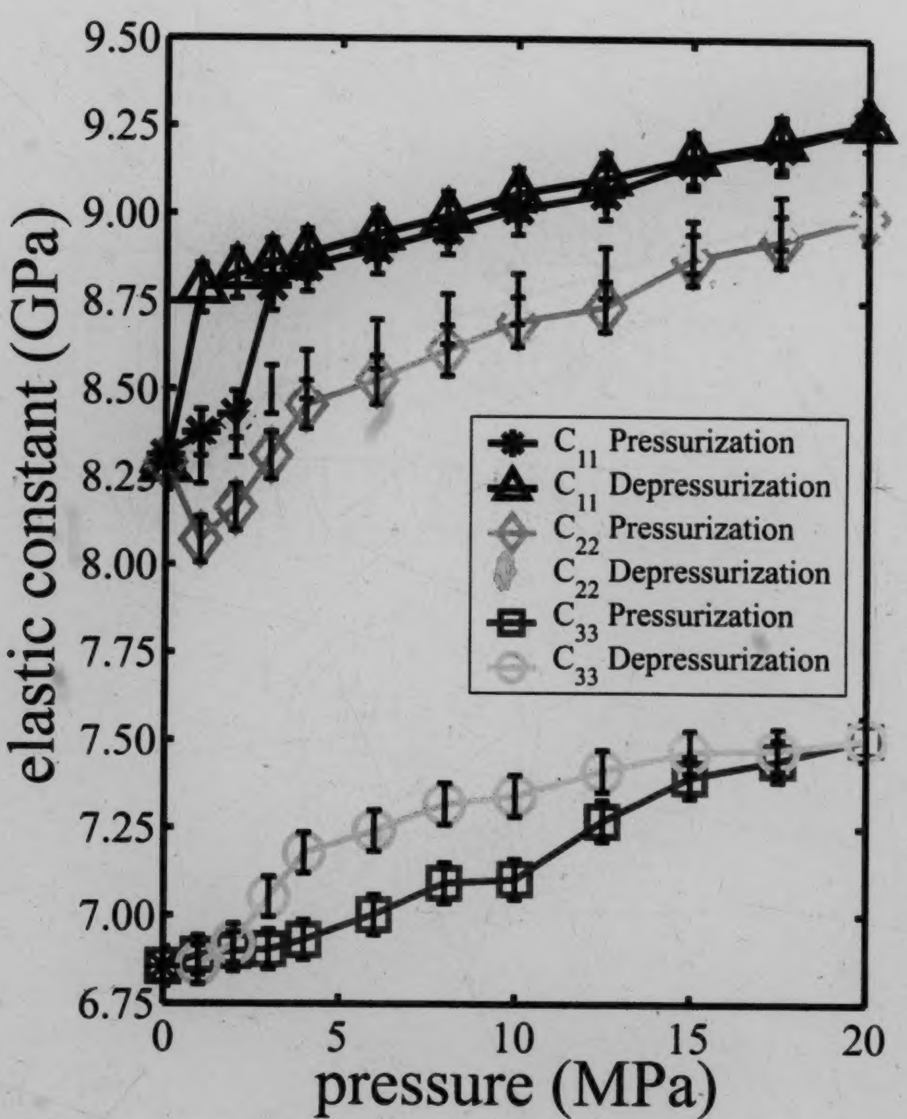

Figure 6.22: Elastic constant C_{11}, C_{22}, and C_{33} versus pressure.

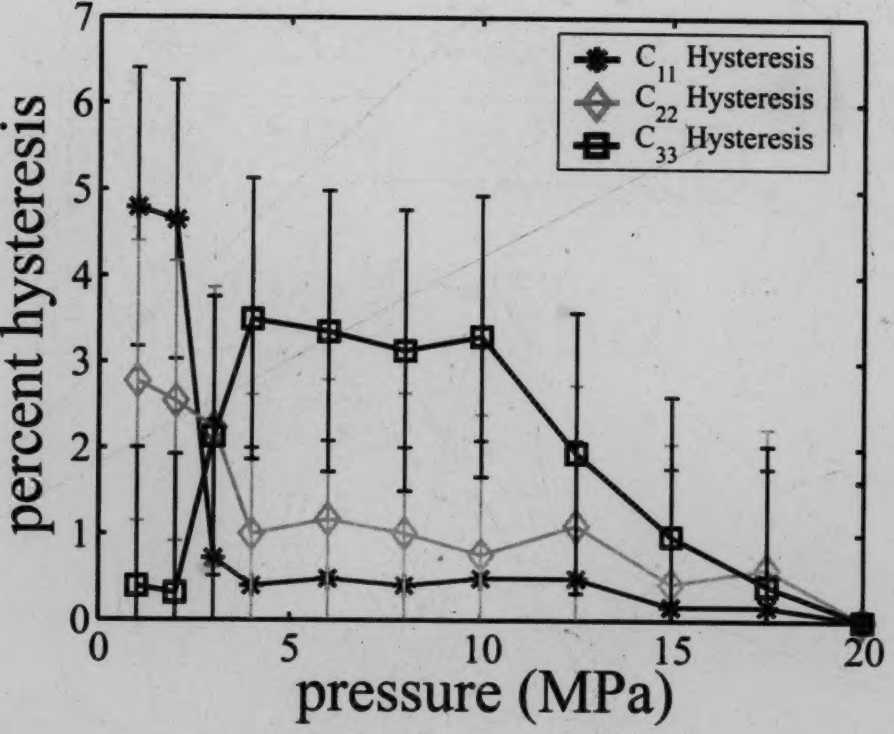

Figure 6.23: Hysteresis for elastic constants C_{11}, C_{22}, and C_{33} versus pressure.

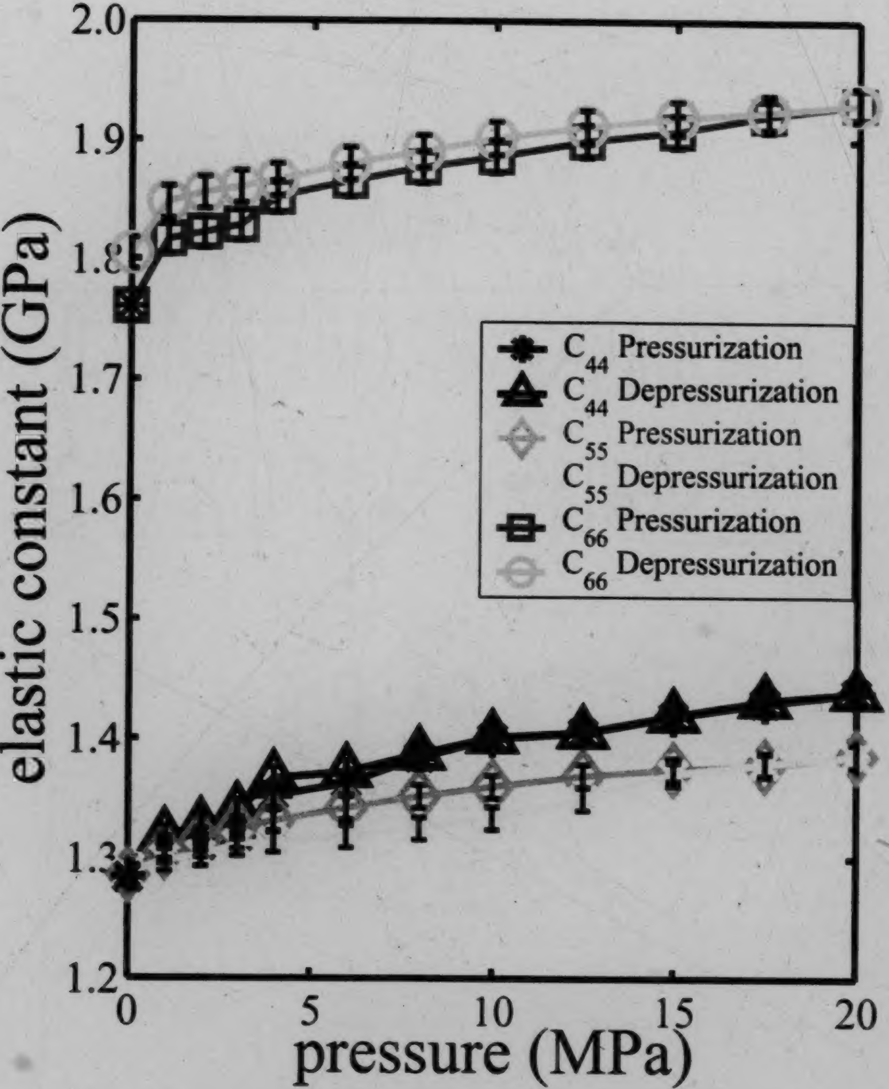

Figure 6.24: Elastic constant C_{44}, C_{55}, and C_{66} versus pressure.

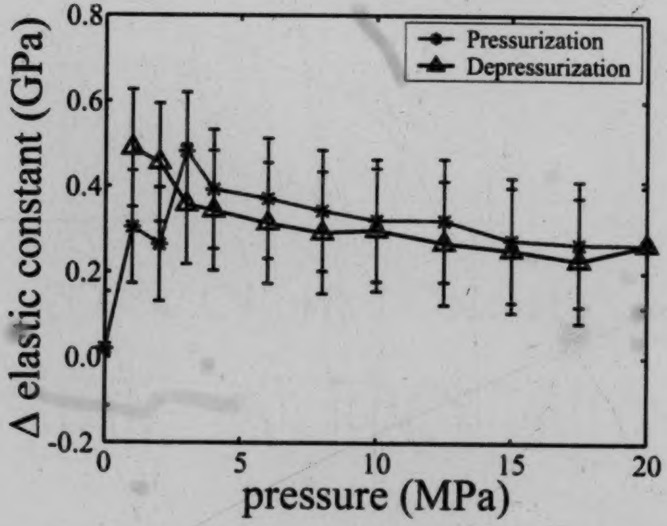

(a) Absolute difference.

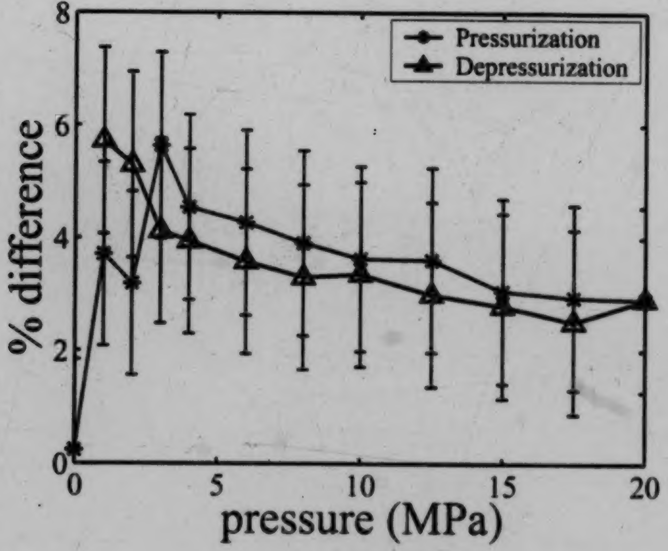

(b) Percentage difference.

Figure 6.25: Absolute and percentage differences between elastic constants C_{11} and C_{22} versus pressure.

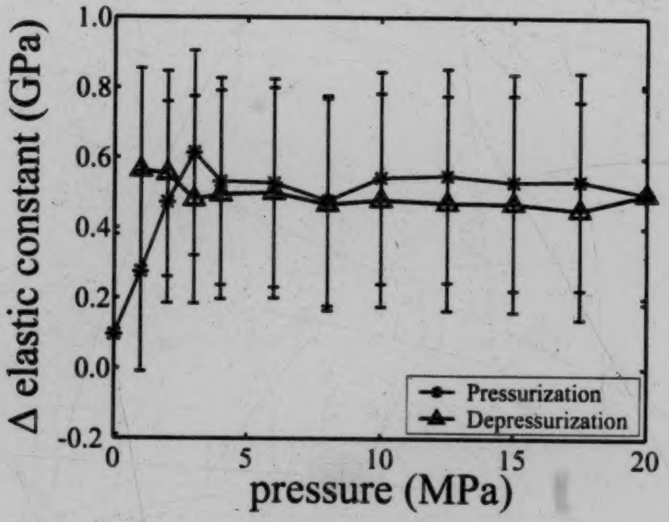

(a) Absolute difference.

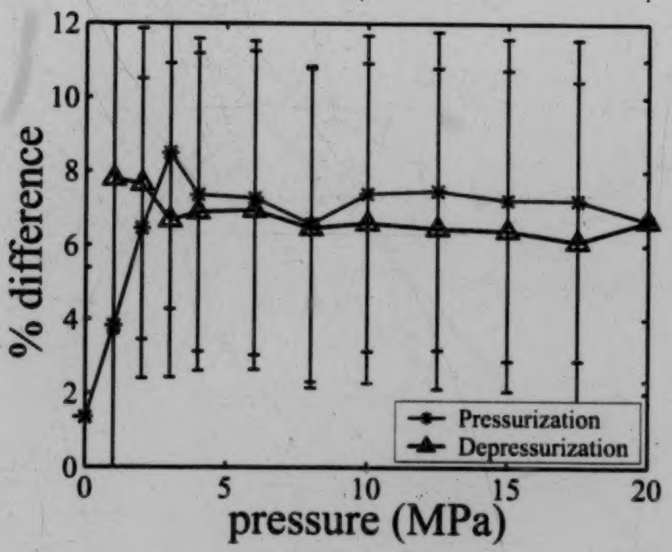

(b) Percentage difference.

Figure 6.26: Absolute and percentage differences between elastic constants C_{13} and C_{23} versus pressure.

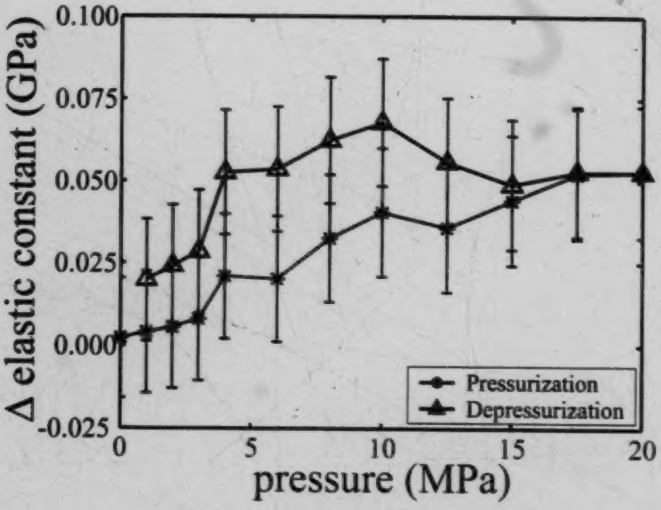

(a) Absolute difference.

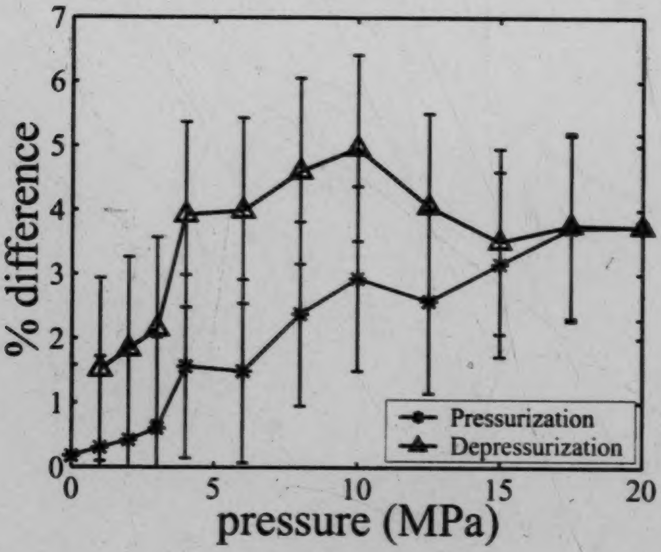

(b) Percentage difference.

Figure 6.27: Absolute and percentage differences between elastic constants C_{44} and C_{55} versus pressure.

6.6.4 Thomsen's parameters

Thomsen (1986) showed a method for linearizing the velocities for weakly anisotropic materials and describe them as functions of angle using just a few parameters such as ϵ, δ, and γ. According to Thomsen (1986) the parameters ϵ, δ, and γ in a transversely isotropic medium are:

$$\epsilon = \frac{C_{11} - C_{33}}{2C_{33}}, \tag{6.14}$$

$$\delta = \frac{(C_{13} + C_{44})^2 - (C_{33} - C_{44})^2}{2C_{33}(C_{33} - C_{44})}, \tag{6.15}$$

and

$$\gamma = \frac{C_{66} - C_{44}}{2C_{44}}, \tag{6.16}$$

respectively, where elastic constants C_{11}, C_{13}, C_{33}, C_{44}, and C_{66} are described in Appendix A.5. The Thomsen parameter ϵ essentially describes the relationship between the velocities parallel and perpendicular to layering while the Thomsen parameter δ describes the shape of the P-wave velocity surface at off-axis angles. Thomsen (1986) represented the P-wave velocity surface in a transversely isotropic medium as:

$$\nu_p(\theta) = \alpha_0 \left(1 + \delta \sin^2(\theta) \cos^2(\theta) + \epsilon \sin^4(\theta)\right) \tag{6.17}$$

where θ is the angle from the vertical axis of symmetry and α is P-wave velocity in the direction parallel to the vertical axis of symmetry. For the purpose of illustration, the normalized P-wave velocity surfaces are calculated for the isotropic case where δ and ϵ are 0, and two anisotropic cases where $\epsilon = 0.25$ and δ is either 0 or 0.25 (See Figure 6.28). The Thomsen parameter γ describes the relationship between the velocities of the two S-waves when travelling perpendicularly to the axis of symmetry.

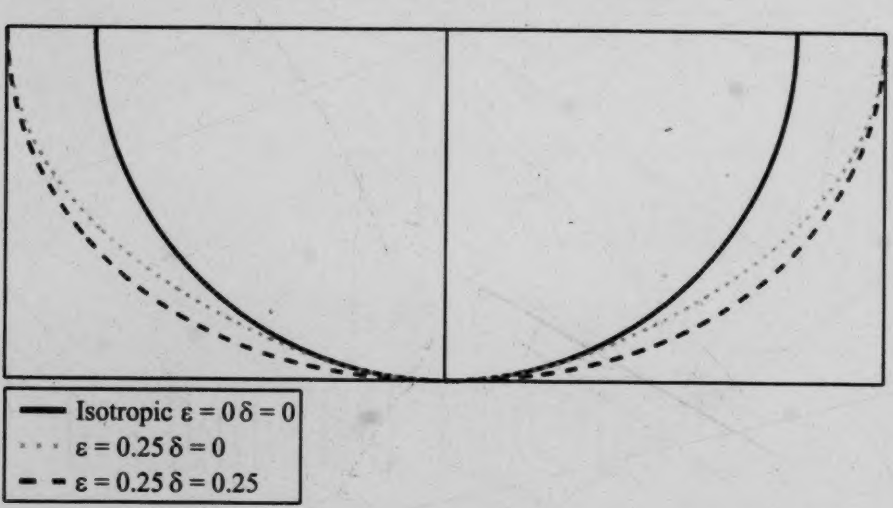

Figure 6.28: Velocity surfaces using various combinations of δ and ϵ.

While the layered nature of the oil shale would suggest transverse isotropy, differences in the ultrasonic velocities in the $\vec{n} = (1\ 0\ 0)$ direction as compared to the $\vec{n} = (0\ 1\ 0)$ direction would indicate that the oil shale is weakly orthorhombic in nature. Fortunately, Thomsen's parameters have also been calculated for an orthorhombic medium (Tsvankin, 1997). According to Tsvankin (1997), Thomsen's parameter ϵ can be calculated in the x and y-directions. The Thomsen parameter ϵ in the x-direction can be written as:

$$\begin{aligned} \epsilon^{(1)} &= \frac{C_{22} - C_{33}}{2C_{33}} \\ &= \frac{1}{2}\frac{C_{22}}{C_{33}} - \frac{1}{2} \end{aligned} \tag{6.18}$$

where $C_{22} = \rho\nu^2_{P[0\ 1\ 0]}$ and $C_{33} = \rho\nu^2_{P[0\ 0\ 1]}$ according to Equations A.130 and A.135, respectively. Consequently,

$$\epsilon^{(1)} = \frac{1}{2}\frac{\nu^2_{P[0\ 1\ 0]}}{\nu^2_{P[0\ 0\ 1]}} - \frac{1}{2}\ . \tag{6.19}$$

The subsequent uncertainty is:

$$\Delta\epsilon^{(1)} = \frac{\nu^2_{P[0\ 1\ 0]}}{\nu^2_{P[0\ 0\ 1]}} \left(\frac{\Delta\nu_{P[0\ 1\ 0]}}{\left|\nu_{P[0\ 1\ 0]}\right|} + \frac{\Delta\nu_{P[0\ 0\ 1]}}{\left|\nu_{P[0\ 0\ 1]}\right|} \right) \tag{6.20}$$

where $\Delta\nu_{P[0\ 1\ 0]}$ and $\Delta\nu_{P[0\ 0\ 1]}$ are the uncertainties in $\nu_{P[0\ 1\ 0]}$ and $\nu_{P[0\ 0\ 1]}$, respectively.

Similarly, the Thomsen parameter ϵ in the y-direction can be written as:

$$\begin{aligned} \epsilon^{(2)} &= \frac{C_{11} - C_{33}}{2C_{33}} \\ &= \frac{1}{2}\frac{C_{11}}{C_{33}} - \frac{1}{2} \end{aligned} \tag{6.21}$$

where $C_{11} = \rho\nu^2_{P[1\ 0\ 0]}$ and $C_{33} = \rho\nu^2_{P[0\ 0\ 1]}$ according to Equations A.125 and A.135, respectively. Consequently,

$$\epsilon^{(2)} = \frac{1}{2}\frac{\nu^2_{P[1\ 0\ 0]}}{\nu^2_{P[0\ 0\ 1]}} - \frac{1}{2} . \tag{6.22}$$

The subsequent uncertainty is:

$$\Delta\epsilon^{(2)} = \frac{\nu^2_{P[1\ 0\ 0]}}{\nu^2_{P[0\ 0\ 1]}} \left(\frac{\Delta\nu_{P[1\ 0\ 0]}}{\left|\nu_{P[1\ 0\ 0]}\right|} + \frac{\Delta\nu_{P[0\ 0\ 1]}}{\left|\nu_{P[0\ 0\ 1]}\right|} \right) \tag{6.23}$$

where $\Delta\nu_{P[1\ 0\ 0]}$ and $\Delta\nu_{P[0\ 0\ 1]}$ are the uncertainties in $\nu_{P[1\ 0\ 0]}$ and $\nu_{P[0\ 0\ 1]}$, respectively. The corresponding $\epsilon^{(1)}$ and $\epsilon^{(2)}$ were calculated for the oil shale as functions of pressure as shown in Figures 6.29 and 6.30, respectively.

In an orthorhombic medium, the Thomsen parameter δ can be calculated in 3 different directions. In the x-direction, the Thomsen parameter δ is:

$$\delta^{(1)} = \frac{(C_{23} + C_{44})^2 - (C_{33} - C_{44})^2}{2C_{33}\,(C_{33} - C_{44})} . \tag{6.24}$$

Then one makes the following substitutions:

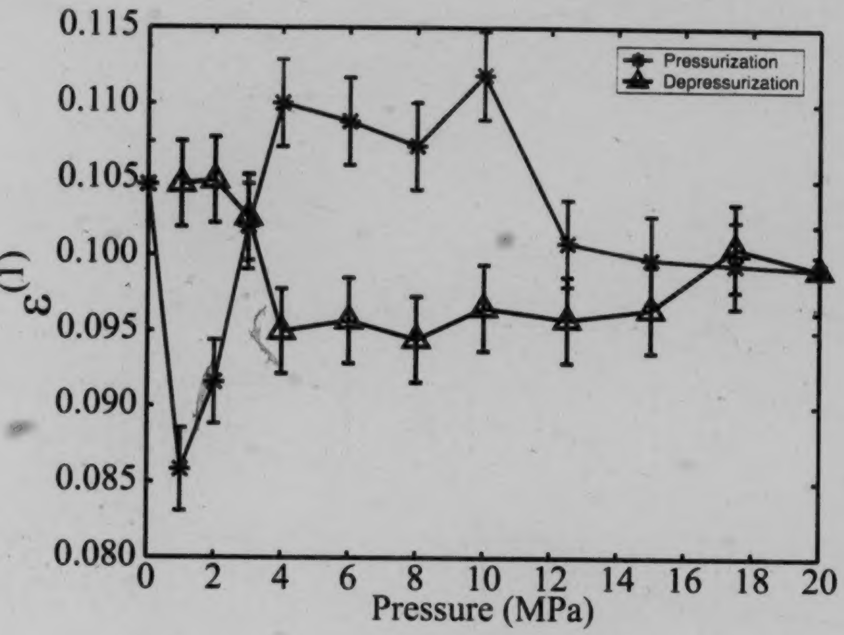

Figure 6.29: Elastic coefficient $\epsilon^{(1)}$ versus pressure.

$$C_{23} = -C_{44} - \sqrt{\left(C_{22} + C_{44} - 2\rho\nu^2_{P\left[0 \approx \frac{1}{\sqrt{2}} \approx \frac{1}{\sqrt{2}}\right]}\right)\left(C_{33} + C_{44} - 2\rho\nu^2_{P\left[0 \approx \frac{1}{\sqrt{2}} \approx \frac{1}{\sqrt{2}}\right]}\right)},$$

$C_{22} = \rho\nu^2_{P[0\ 1\ 0]}$,

$C_{33} = \rho\nu^2_{P[0\ 0\ 1]}$,

and $C_{44} = \rho\nu^2_{S[0\ 1\ 0]}$ in the $\vec{n} = [0\ 0\ 1]$ direction,

according to Equations A.152, A.130, A.135, and A.134, respectively. This implies:

$$\begin{aligned}\delta^{(1)} &= \frac{\left(\nu^2_{P[0\ 1\ 0]} + \nu^2_{S[0\ 1\ 0]} - 2\nu^2_{P\left[0 \approx \frac{1}{\sqrt{2}} \approx \frac{1}{\sqrt{2}}\right]}\right)}{2\left(\nu^2_{P[0\ 0\ 1]} - \nu^2_{S[0\ 1\ 0]}\right)} \\ &+ \frac{\left(\nu^4_{S[0\ 1\ 0]} + \nu^2_{P[0\ 1\ 0]}\nu^2_{S[0\ 1\ 0]} - 2\nu^2_{P[0\ 1\ 0]}\nu^2_{P\left[0 \approx \frac{1}{\sqrt{2}} \approx \frac{1}{\sqrt{2}}\right]}\right)}{2\nu^2_{P[0\ 0\ 1]}\left(\nu^2_{P[0\ 0\ 1]} - \nu^2_{S[0\ 1\ 0]}\right)}\end{aligned}$$

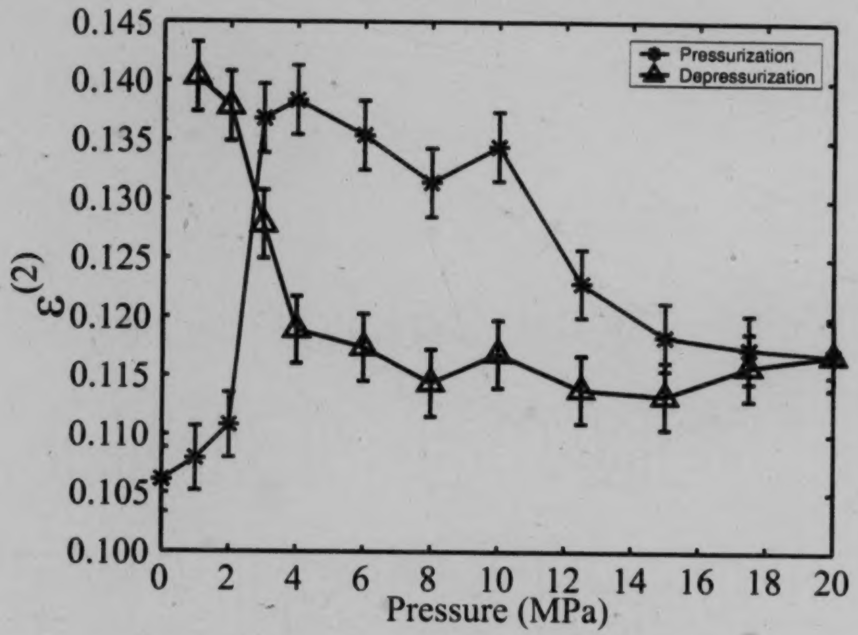

Figure 6.30: Elastic coefficient $\epsilon^{(2)}$ versus pressure.

$$
\begin{aligned}
& - \frac{\left(2\nu^2_{S[0\ 1\ 0]}\nu^2_{P\left[0\ \approx\frac{1}{\sqrt{2}}\ \approx\frac{1}{\sqrt{2}}\right]} - 2\nu^4_{P\left[0\ \approx\frac{1}{\sqrt{2}}\ \approx\frac{1}{\sqrt{2}}\right]}\right)}{\nu^2_{P[0\ 0\ 1]}\left(\nu^2_{P[0\ 0\ 1]} - \nu^2_{S[0\ 1\ 0]}\right)} \\
& - \frac{1}{2} + \frac{\nu^2_{S[0\ 1\ 0]}}{2\nu^2_{P[0\ 0\ 1]}}
\end{aligned}
\qquad (6.25)
$$

where $\nu^2_{S[0\ 1\ 0]}$ is in the $\overrightarrow{n} = [0\ 0\ 1]$ direction. The uncertainty in $\delta^{(1)}$ then becomes:

$$
\begin{aligned}
\Delta\delta^{(1)} &= \frac{\nu_{P[0\ 1\ 0]}\Delta\nu_{P[0\ 1\ 0]}}{\nu^2_{P[0\ 0\ 1]} - \nu^2_{S[0\ 1\ 0]}} \\
&+ \frac{\left(\nu^2_{S[0\ 1\ 0]} + 2\nu^2_{P\left[0\ \approx\frac{1}{\sqrt{2}}\ \approx\frac{1}{\sqrt{2}}\right]}\right)\nu_{P[0\ 1\ 0]}\Delta\nu_{P[0\ 1\ 0]}}{\nu^2_{P[0\ 0\ 1]}\left(\nu^2_{P[0\ 0\ 1]} - \nu^2_{S[0\ 1\ 0]}\right)}
\end{aligned}
$$

$$
\begin{aligned}
&+\frac{\left(\nu^{2}_{P[0\ 1\ 0]}+\nu^{2}_{S[0\ 1\ 0]}+2{\nu^{2}}_{P\left[0\ \approx\frac{1}{\sqrt{2}}\ \approx\frac{1}{\sqrt{2}}\right]}\right)\nu_{P[0\ 0\ 1]}\Delta\nu_{P[0\ 0\ 1]}}{\left(\nu^{2}_{P[0\ 0\ 1]}-\nu^{2}_{S[0\ 1\ 0]}\right)^{2}}\\
&+\frac{\left(\nu^{4}_{S[0\ 1\ 0]}+\nu^{2}_{P[0\ 1\ 0]}\nu^{2}_{S[0\ 1\ 0]}+2\nu^{2}_{P[0\ 1\ 0]}{\nu^{2}}_{P\left[0\ \approx\frac{1}{\sqrt{2}}\ \approx\frac{1}{\sqrt{2}}\right]}\right)\Delta\nu_{P[0\ 0\ 1]}}{\nu^{3}_{P[0\ 0\ 1]}\left(\nu^{2}_{P[0\ 0\ 1]}-\nu^{2}_{S[0\ 1\ 0]}\right)}\\
&+\frac{4\left(\nu^{2}_{S[0\ 1\ 0]}{\nu^{2}}_{P\left[0\ \approx\frac{1}{\sqrt{2}}\ \approx\frac{1}{\sqrt{2}}\right]}+{\nu^{4}}_{P\left[0\ \approx\frac{1}{\sqrt{2}}\ \approx\frac{1}{\sqrt{2}}\right]}\right)\Delta\nu_{P[0\ 0\ 1]}}{\nu^{3}_{P[0\ 0\ 1]}\left(\nu^{2}_{P[0\ 0\ 1]}-\nu^{2}_{S[0\ 1\ 0]}\right)}\\
&+\frac{\left(\nu^{4}_{S[0\ 1\ 0]}+\nu^{2}_{P[0\ 1\ 0]}\nu^{2}_{S[0\ 1\ 0]}+2\nu^{2}_{P[0\ 1\ 0]}{\nu^{2}}_{P\left[0\ \approx\frac{1}{\sqrt{2}}\ \approx\frac{1}{\sqrt{2}}\right]}\right)\Delta\nu_{P[0\ 0\ 1]}}{\nu_{P[0\ 0\ 1]}\left(\nu^{2}_{P[0\ 0\ 1]}-\nu^{2}_{S[0\ 1\ 0]}\right)^{2}}\\
&+\frac{4\left(\nu^{2}_{S[0\ 1\ 0]}{\nu^{2}}_{P\left[0\ \approx\frac{1}{\sqrt{2}}\ \approx\frac{1}{\sqrt{2}}\right]}+{\nu^{4}}_{P\left[0\ \approx\frac{1}{\sqrt{2}}\ \approx\frac{1}{\sqrt{2}}\right]}\right)\Delta\nu_{P[0\ 0\ 1]}}{\nu_{P[0\ 0\ 1]}\left(\nu^{2}_{P[0\ 0\ 1]}-\nu^{2}_{S[0\ 1\ 0]}\right)^{2}}\\
&+\frac{\nu^{2}_{S[0\ 1\ 0]}\Delta\nu_{P[0\ 0\ 1]}}{\nu^{3}_{P[0\ 0\ 1]}}+\frac{\nu_{S[0\ 1\ 0]}\Delta\nu_{S[0\ 1\ 0]}}{\nu^{2}_{P[0\ 0\ 1]}-\nu^{2}_{S[0\ 1\ 0]}}\\
&+\frac{\left(\nu^{2}_{P[0\ 1\ 0]}+\nu^{2}_{S[0\ 1\ 0]}+2{\nu^{2}}_{P\left[0\ \approx\frac{1}{\sqrt{2}}\ \approx\frac{1}{\sqrt{2}}\right]}\right)\nu_{S[0\ 1\ 0]}\Delta\nu_{S[0\ 1\ 0]}}{\left(\nu^{2}_{P[0\ 0\ 1]}-\nu^{2}_{S[0\ 1\ 0]}\right)^{2}}\\
&+\frac{\left(2\nu^{2}_{S[0\ 1\ 0]}+\nu^{2}_{P[0\ 1\ 0]}+4{\nu^{2}}_{P\left[0\ \approx\frac{1}{\sqrt{2}}\ \approx\frac{1}{\sqrt{2}}\right]}\right)\nu_{S[0\ 1\ 0]}\Delta\nu_{S[0\ 1\ 0]}}{\nu^{2}_{P[0\ 0\ 1]}\left(\nu^{2}_{P[0\ 0\ 1]}-\nu^{2}_{S[0\ 1\ 0]}\right)}\\
&+\frac{\left(\nu^{4}_{S[0\ 1\ 0]}+\nu^{2}_{P[0\ 1\ 0]}\nu^{2}_{S[0\ 1\ 0]}+2\nu^{2}_{P[0\ 1\ 0]}{\nu^{2}}_{P\left[0\ \approx\frac{1}{\sqrt{2}}\ \approx\frac{1}{\sqrt{2}}\right]}\right)\nu_{S[0\ 1\ 0]}\Delta\nu_{S[0\ 1\ 0]}}{\nu^{2}_{P[0\ 0\ 1]}\left(\nu^{2}_{P[0\ 0\ 1]}-\nu^{2}_{S[0\ 1\ 0]}\right)^{2}}\\
&+\frac{4\left(\nu^{2}_{S[0\ 1\ 0]}{\nu^{2}}_{P\left[0\ \approx\frac{1}{\sqrt{2}}\ \approx\frac{1}{\sqrt{2}}\right]}+{\nu^{4}}_{P\left[0\ \approx\frac{1}{\sqrt{2}}\ \approx\frac{1}{\sqrt{2}}\right]}\right)\nu_{S[0\ 1\ 0]}\Delta\nu_{S[0\ 1\ 0]}}{\nu^{2}_{P[0\ 0\ 1]}\left(\nu^{2}_{P[0\ 0\ 1]}-\nu^{2}_{S[0\ 1\ 0]}\right)^{2}}
\end{aligned}
$$

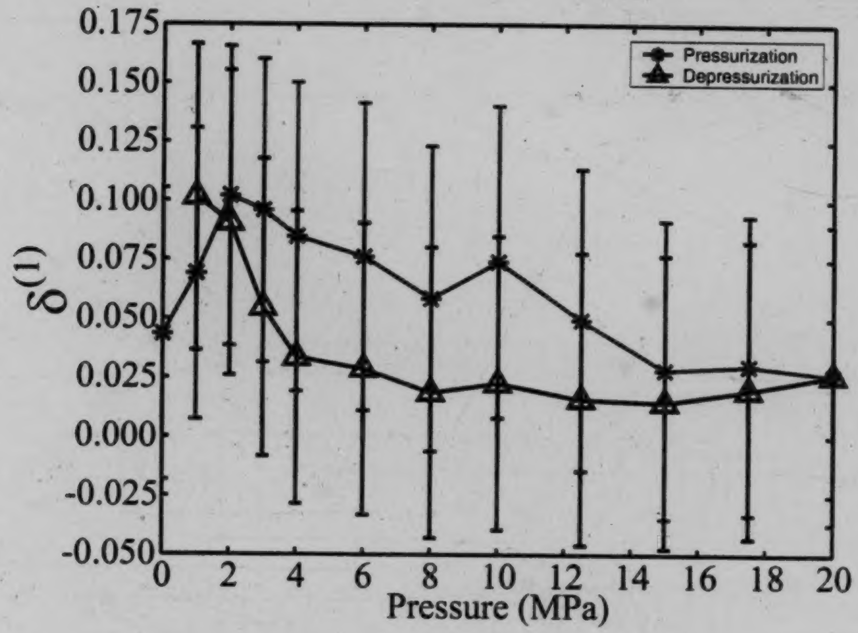

Figure 6.31: Elastic coefficient $\delta^{(1)}$ versus pressure.

$$+\ \frac{2\left(\nu^2_{P[0\ 1\ 0]}+2\nu^2_{S[0\ 1\ 0]}+4\nu^2_{P\left[0\ \approx\frac{1}{\sqrt{2}}\ \approx\frac{1}{\sqrt{2}}\right]}\right)\nu_{P\left[0\ \approx\frac{1}{\sqrt{2}}\ \approx\frac{1}{\sqrt{2}}\right]}\Delta\nu_{P\left[0\ \approx\frac{1}{\sqrt{2}}\ \approx\frac{1}{\sqrt{2}}\right]}}{\nu^2_{P[0\ 0\ 1]}\left(\nu^2_{P[0\ 0\ 1]}-\nu^2_{S[0\ 1\ 0]}\right)}$$

$$+\ \frac{\nu_{S[0\ 1\ 0]}\Delta\nu_{S[0\ 1\ 0]}}{\nu^2_{P[0\ 0\ 1]}} \tag{6.26}$$

where Δ is used to indicate that the uncertainty in the following symbol should be used. The $\delta^{(1)}$ was calculated for the oil shale and is shown in Figure 6.31.

In the $\hat{y}$-direction, the Thomsen parameter δ is:

$$\delta^{(2)}=\frac{\left(C_{13}+C_{55}\right)^2-\left(C_{33}-C_{55}\right)^2}{2C_{33}\left(C_{33}-C_{55}\right)}. \tag{6.27}$$

Then one makes the following substitutions:

$$C_{13}=-C_{55}-\sqrt{\left(C_{11}+C_{55}-2\rho\nu^2_{P\left[\approx\frac{1}{\sqrt{2}}\ 0\ \approx\frac{1}{\sqrt{2}}\right]}\right)\left(C_{33}+C_{55}-2\rho\nu^2_{P\left[\approx\frac{1}{\sqrt{2}}\ 0\ \approx\frac{1}{\sqrt{2}}\right]}\right)},$$

$C_{11} = \rho \nu^2_{P[1\ 0\ 0]}$,
$C_{33} = \rho \nu^2_{P[0\ 0\ 1]}$,
and $C_{55} = \rho \nu^2_{S[1\ 0\ 0]}$ in the $\vec{n} = [0\ 0\ 1]$ direction,
according to Equations A.146, A.125, A.135, and A.133, respectively. This implies:

$$\begin{aligned}
\delta^{(2)} \;=\;& \frac{\left(\nu^2_{P[1\ 0\ 0]} + \nu^2_{S[1\ 0\ 0]} - 2\nu^2_{P\left[\approx\frac{1}{\sqrt{2}}\ 0\ \approx\frac{1}{\sqrt{2}}\right]}\right)}{2\left(\nu^2_{P[0\ 0\ 1]} - \nu^2_{S[1\ 0\ 0]}\right)} \\
&+ \frac{\left(\nu^4_{S[1\ 0\ 0]} + \nu^2_{P[1\ 0\ 0]}\nu^2_{S[1\ 0\ 0]} - 2\nu^2_{P[1\ 0\ 0]}\nu^2_{P\left[\approx\frac{1}{\sqrt{2}}\ 0\ \approx\frac{1}{\sqrt{2}}\right]}\right)}{2\nu^2_{P[0\ 0\ 1]}\left(\nu^2_{P[0\ 0\ 1]} - \nu^2_{S[1\ 0\ 0]}\right)} \\
&- \frac{\left(2\nu^2_{S[1\ 0\ 0]}\nu^2_{P\left[\approx\frac{1}{\sqrt{2}}\ 0\ \approx\frac{1}{\sqrt{2}}\right]} - 2\nu^4_{P\left[\approx\frac{1}{\sqrt{2}}\ 0\ \approx\frac{1}{\sqrt{2}}\right]}\right)}{\nu^2_{P[0\ 0\ 1]}\left(\nu^2_{P[0\ 0\ 1]} - \nu^2_{S[1\ 0\ 0]}\right)} \\
&- \frac{1}{2} + \frac{\nu^2_{S[1\ 0\ 0]}}{2\nu^2_{P[0\ 0\ 1]}} \qquad (6.28)
\end{aligned}$$

where $\nu^2_{S[1\ 0\ 0]}$ is in the $\vec{n} = [0\ 0\ 1]$ direction. The uncertainty in $\delta^{(2)}$ then becomes:

$$\begin{aligned}
\Delta\delta^{(2)} \;=\;& \frac{\nu_{P[1\ 0\ 0]}\Delta\nu_{P[1\ 0\ 0]}}{\nu^2_{P[0\ 0\ 1]} - \nu^2_{S[1\ 0\ 0]}} \\
&+ \frac{\left(\nu^2_{S[1\ 0\ 0]} + 2\nu^2_{P\left[\approx\frac{1}{\sqrt{2}}\ 0\ \approx\frac{1}{\sqrt{2}}\right]}\right)\nu_{P[1\ 0\ 0]}\Delta\nu_{P[1\ 0\ 0]}}{\nu^2_{P[0\ 0\ 1]}\left(\nu^2_{P[0\ 0\ 1]} - \nu^2_{S[1\ 0\ 0]}\right)} \\
&+ \frac{\left(\nu^2_{P[1\ 0\ 0]} + \nu^2_{S[1\ 0\ 0]} + 2\nu^2_{P\left[\approx\frac{1}{\sqrt{2}}\ 0\ \approx\frac{1}{\sqrt{2}}\right]}\right)\nu_{P[0\ 0\ 1]}\Delta\nu_{P[0\ 0\ 1]}}{\left(\nu^2_{P[0\ 0\ 1]} - \nu^2_{S[1\ 0\ 0]}\right)^2} \\
&+ \frac{\left(\nu^4_{S[1\ 0\ 0]} + \nu^2_{P[1\ 0\ 0]}\nu^2_{S[1\ 0\ 0]} + 2\nu^2_{P[1\ 0\ 0]}\nu^2_{P\left[\approx\frac{1}{\sqrt{2}}\ 0\ \approx\frac{1}{\sqrt{2}}\right]}\right)\Delta\nu_{P[0\ 0\ 1]}}{\nu^3_{P[0\ 0\ 1]}\left(\nu^2_{P[0\ 0\ 1]} - \nu^2_{S[1\ 0\ 0]}\right)}
\end{aligned}$$

$$
\begin{aligned}
&+ \frac{4\left(\nu^2_{S[1\ 0\ 0]}\nu^2_{P\left[\approx\frac{1}{\sqrt{2}}\ 0\ \approx\frac{1}{\sqrt{2}}\right]} + \nu^4_{P\left[\approx\frac{1}{\sqrt{2}}\ 0\ \approx\frac{1}{\sqrt{2}}\right]}\right)\Delta\nu_{P[0\ 0\ 1]}}{\nu^3_{P[0\ 0\ 1]}\left(\nu^2_{P[0\ 0\ 1]} - \nu^2_{S[1\ 0\ 0]}\right)} \\
&+ \frac{\left(\nu^4_{S[1\ 0\ 0]} + \nu^2_{P[1\ 0\ 0]}\nu^2_{S[1\ 0\ 0]} + 2\nu^2_{P[1\ 0\ 0]}\nu^2_{P\left[\approx\frac{1}{\sqrt{2}}\ 0\ \approx\frac{1}{\sqrt{2}}\right]}\right)\Delta\nu_{P[0\ 0\ 1]}}{\nu_{P[0\ 0\ 1]}\left(\nu^2_{P[0\ 0\ 1]} - \nu^2_{S[1\ 0\ 0]}\right)^2} \\
&+ \frac{4\left(\nu^2_{S[1\ 0\ 0]}\nu^2_{P\left[\approx\frac{1}{\sqrt{2}}\ 0\ \approx\frac{1}{\sqrt{2}}\right]} + \nu^4_{P\left[\approx\frac{1}{\sqrt{2}}\ 0\ \approx\frac{1}{\sqrt{2}}\right]}\right)\Delta\nu_{P[0\ 0\ 1]}}{\nu_{P[0\ 0\ 1]}\left(\nu^2_{P[0\ 0\ 1]} - \nu^2_{S[1\ 0\ 0]}\right)^2} \\
&+ \frac{\nu^2_{S[1\ 0\ 0]}\Delta\nu_{P[0\ 0\ 1]}}{\nu^3_{P[0\ 0\ 1]}} + \frac{\nu_{S[1\ 0\ 0]}\Delta\nu_{S[1\ 0\ 0]}}{\nu^2_{P[0\ 0\ 1]} - \nu^2_{S[1\ 0\ 0]}} \\
&+ \frac{\left(\nu^2_{P[1\ 0\ 0]} + \nu^2_{S[1\ 0\ 0]} + 2\nu^2_{P\left[\approx\frac{1}{\sqrt{2}}\ 0\ \approx\frac{1}{\sqrt{2}}\right]}\right)\nu_{S[1\ 0\ 0]}\Delta\nu_{S[1\ 0\ 0]}}{\left(\nu^2_{P[0\ 0\ 1]} - \nu^2_{S[1\ 0\ 0]}\right)^2} \\
&+ \frac{\left(2\nu^2_{S[1\ 0\ 0]} + \nu^2_{P[1\ 0\ 0]} + 4\nu^2_{P\left[\approx\frac{1}{\sqrt{2}}\ 0\ \approx\frac{1}{\sqrt{2}}\right]}\right)\nu_{S[1\ 0\ 0]}\Delta\nu_{S[1\ 0\ 0]}}{\nu^2_{P[0\ 0\ 1]}\left(\nu^2_{P[0\ 0\ 1]} - \nu^2_{S[1\ 0\ 0]}\right)} \\
&+ \frac{\left(\nu^4_{S[1\ 0\ 0]} + \nu^2_{P[1\ 0\ 0]}\nu^2_{S[1\ 0\ 0]} + 2\nu^2_{P[1\ 0\ 0]}\nu^2_{P\left[\approx\frac{1}{\sqrt{2}}\ 0\ \approx\frac{1}{\sqrt{2}}\right]}\right)\nu_{S[1\ 0\ 0]}\Delta\nu_{S[1\ 0\ 0]}}{\nu^2_{P[0\ 0\ 1]}\left(\nu^2_{P[0\ 0\ 1]} - \nu^2_{S[1\ 0\ 0]}\right)^2} \\
&+ \frac{4\left(\nu^2_{S[1\ 0\ 0]}\nu^2_{P\left[\approx\frac{1}{\sqrt{2}}\ 0\ \approx\frac{1}{\sqrt{2}}\right]} + \nu^4_{P\left[\approx\frac{1}{\sqrt{2}}\ 0\ \approx\frac{1}{\sqrt{2}}\right]}\right)\nu_{S[1\ 0\ 0]}\Delta\nu_{S[1\ 0\ 0]}}{\nu^2_{P[0\ 0\ 1]}\left(\nu^2_{P[0\ 0\ 1]} - \nu^2_{S[1\ 0\ 0]}\right)^2} \\
&+ \frac{2\left(\nu^2_{P[1\ 0\ 0]} + 2\nu^2_{S[1\ 0\ 0]} + 4\nu^2_{P\left[\approx\frac{1}{\sqrt{2}}\ 0\ \approx\frac{1}{\sqrt{2}}\right]}\right)\nu_{P\left[\approx\frac{1}{\sqrt{2}}\ 0\ \approx\frac{1}{\sqrt{2}}\right]}\Delta\nu_{P\left[\approx\frac{1}{\sqrt{2}}\ 0\ \approx\frac{1}{\sqrt{2}}\right]}}{\nu^2_{P[0\ 0\ 1]}\left(\nu^2_{P[0\ 0\ 1]} - \nu^2_{S[1\ 0\ 0]}\right)} \\
&+ \frac{\nu_{S[1\ 0\ 0]}\Delta\nu_{S[1\ 0\ 0]}}{\nu^2_{P[0\ 0\ 1]}}
\end{aligned}
\tag{6.29}
$$

where Δ is used to indicate that the uncertainty in the following symbol should

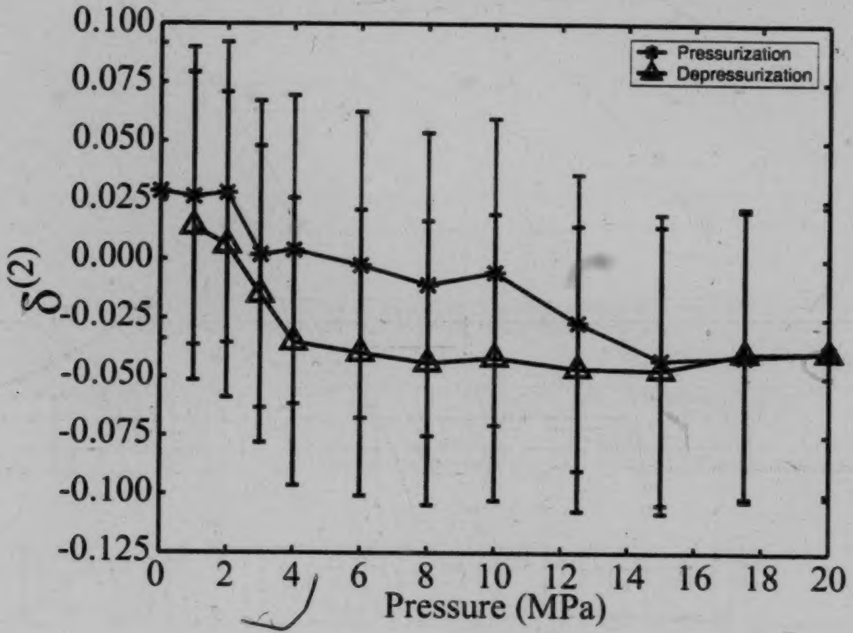

Figure 6.32: Elastic coefficient $\delta^{(2)}$ versus pressure.

be used. The $\delta^{(2)}$ was calculated for the oil shale and is shown in Figure 6.32.

In the z-direction, the Thomsen parameter δ is:

$$\delta^{(3)} = \frac{(C_{12}+C_{66})^2 - (C_{11}-C_{66})^2}{2C_{11}\,(C_{11}-C_{66})}. \tag{6.30}$$

Then one makes the following substitutions:

$C_{12} = -C_{66} - \sqrt{\left(C_{11} + C_{66} - 2\rho\nu^2_{P\left[\approx\frac{1}{\sqrt{2}}\ \approx\frac{1}{\sqrt{2}}0\ \right]}\right)\left(C_{22} + C_{66} - 2\rho\nu^2_{P\left[\approx\frac{1}{\sqrt{2}}\ \approx\frac{1}{\sqrt{2}}0\ \right]}\right)}$,
$C_{11} = \rho\nu^2_{P[1\ 0\ 0]}$,
$C_{22} = \rho\nu^2_{P[0\ 1\ 0]}$,
and $C_{66} = \rho\nu^2_{S[1\ 0\ 0]}$ in the $\vec{n} = [0\ 1\ 0]$ direction,
according to Equations A.140, A.125, A.130, and A.129, respectively.

This implies:

$$\begin{aligned}
\delta^{(3)} &= \frac{\left(\nu^2_{P[0\ 1\ 0]} + \nu^2_{S[1\ 0\ 0]} - 2\nu^2_{P\left[\approx\frac{1}{\sqrt{2}}\ \approx\frac{1}{\sqrt{2}}0\ \right]}\right)}{2\left(\nu^2_{P[1\ 0\ 0]} - \nu^2_{S[1\ 0\ 0]}\right)} \\
&+ \frac{\left(\nu^4_{S[1\ 0\ 0]} + \nu^2_{P[0\ 1\ 0]}\nu^2_{S[1\ 0\ 0]} - 2\nu^2_{P[0\ 1\ 0]}\nu^2_{P\left[\approx\frac{1}{\sqrt{2}}\ \approx\frac{1}{\sqrt{2}}0\ \right]}\right)}{2\nu^2_{P[1\ 0\ 0]}\left(\nu^2_{P[1\ 0\ 0]} - \nu^2_{S[1\ 0\ 0]}\right)} \\
&- \frac{\left(2\nu^2_{S[1\ 0\ 0]}\nu^2_{P\left[\approx\frac{1}{\sqrt{2}}\ \approx\frac{1}{\sqrt{2}}0\ \right]} - 2\nu^4_{P\left[\approx\frac{1}{\sqrt{2}}\ \approx\frac{1}{\sqrt{2}}0\ \right]}\right)}{\nu^2_{P[1\ 0\ 0]}\left(\nu^2_{P[1\ 0\ 0]} - \nu^2_{S[1\ 0\ 0]}\right)} \\
&- \frac{1}{2} + \frac{\nu^2_{S[1\ 0\ 0]}}{2\nu^2_{P[1\ 0\ 0]}} \qquad (6.31)
\end{aligned}$$

where $\nu^2_{S[1\ 0\ 0]}$ is in the $\vec{n} = [0\ 1\ 0]$ direction. The uncertainty in $\delta^{(3)}$ then becomes:

$$\begin{aligned}
\Delta\delta^{(3)} &= \frac{\nu_{P[0\ 1\ 0]}\Delta\nu_{P[0\ 1\ 0]}}{\nu^2_{P[1\ 0\ 0]} - \nu^2_{S[1\ 0\ 0]}} \\
&+ \frac{\left(\nu^2_{S[1\ 0\ 0]} + 2\nu^2_{P\left[\approx\frac{1}{\sqrt{2}}\ \approx\frac{1}{\sqrt{2}}0\ \right]}\right)\nu_{P[0\ 1\ 0]}\Delta\nu_{P[0\ 1\ 0]}}{\nu^2_{P[1\ 0\ 0]}\left(\nu^2_{P[1\ 0\ 0]} - \nu^2_{S[1\ 0\ 0]}\right)} \\
&+ \frac{\left(\nu^2_{P[0\ 1\ 0]} + \nu^2_{S[1\ 0\ 0]} + 2\nu^2_{P\left[\approx\frac{1}{\sqrt{2}}\ \approx\frac{1}{\sqrt{2}}0\ \right]}\right)\nu_{P[1\ 0\ 0]}\Delta\nu_{P[1\ 0\ 0]}}{\left(\nu^2_{P[1\ 0\ 0]} - \nu^2_{S[1\ 0\ 0]}\right)^2} \\
&+ \frac{\left(\nu^4_{S[1\ 0\ 0]} + \nu^2_{P[0\ 1\ 0]}\nu^2_{S[1\ 0\ 0]} + 2\nu^2_{P[0\ 1\ 0]}\nu^2_{P\left[\approx\frac{1}{\sqrt{2}}\ \approx\frac{1}{\sqrt{2}}0\ \right]}\right)\Delta\nu_{P[1\ 0\ 0]}}{\nu^3_{P[1\ 0\ 0]}\left(\nu^2_{P[1\ 0\ 0]} - \nu^2_{S[1\ 0\ 0]}\right)} \\
&+ \frac{4\left(\nu^2_{S[1\ 0\ 0]}\nu^2_{P\left[\approx\frac{1}{\sqrt{2}}\ \approx\frac{1}{\sqrt{2}}0\ \right]} + \nu^4_{P\left[\approx\frac{1}{\sqrt{2}}\ \approx\frac{1}{\sqrt{2}}0\ \right]}\right)\Delta\nu_{P[1\ 0\ 0]}}{\nu^3_{P[1\ 0\ 0]}\left(\nu^2_{P[1\ 0\ 0]} - \nu^2_{S[1\ 0\ 0]}\right)}
\end{aligned}$$

$$
\begin{aligned}
&+ \frac{\left(\nu^4_{S[1\ 0\ 0]} + \nu^2_{P[0\ 1\ 0]}\nu^2_{S[1\ 0\ 0]} + 2\nu^2_{P[0\ 1\ 0]}\nu^2_{P\left[\approx\frac{1}{\sqrt{2}}\ \approx\frac{1}{\sqrt{2}}0\ \right]}\right)\Delta\nu_{P[1\ 0\ 0]}}{\nu_{P[1\ 0\ 0]}\left(\nu^2_{P[1\ 0\ 0]} - \nu^2_{S[1\ 0\ 0]}\right)^2} \\
&+ \frac{4\left(\nu^2_{S[1\ 0\ 0]}\nu^2_{P\left[\approx\frac{1}{\sqrt{2}}\ \approx\frac{1}{\sqrt{2}}0\ \right]} + \nu^4_{P\left[\approx\frac{1}{\sqrt{2}}\ \approx\frac{1}{\sqrt{2}}0\ \right]}\right)\Delta\nu_{P[1\ 0\ 0]}}{\nu_{P[1\ 0\ 0]}\left(\nu^2_{P[1\ 0\ 0]} - \nu^2_{S[1\ 0\ 0]}\right)^2} \\
&+ \frac{\nu^2_{S[1\ 0\ 0]}\Delta\nu_{P[1\ 0\ 0]}}{\nu^3_{P[1\ 0\ 0]}} + \frac{\nu_{S[1\ 0\ 0]}\Delta\nu_{S[1\ 0\ 0]}}{\nu^2_{P[1\ 0\ 0]} - \nu^2_{S[1\ 0\ 0]}} \\
&+ \frac{\left(\nu^2_{P[0\ 1\ 0]} + \nu^2_{S[1\ 0\ 0]} + 2\nu^2_{P\left[\approx\frac{1}{\sqrt{2}}\ \approx\frac{1}{\sqrt{2}}0\ \right]}\right)\nu_{S[1\ 0\ 0]}\Delta\nu_{S[1\ 0\ 0]}}{\left(\nu^2_{P[1\ 0\ 0]} - \nu^2_{S[1\ 0\ 0]}\right)^2} \\
&+ \frac{\left(2\nu^2_{S[1\ 0\ 0]} + \nu^2_{P[0\ 1\ 0]} + 4\nu^2_{P\left[\approx\frac{1}{\sqrt{2}}\ \approx\frac{1}{\sqrt{2}}0\ \right]}\right)\nu_{S[1\ 0\ 0]}\Delta\nu_{S[1\ 0\ 0]}}{\nu^2_{P[1\ 0\ 0]}\left(\nu^2_{P[1\ 0\ 0]} - \nu^2_{S[1\ 0\ 0]}\right)} \\
&+ \frac{\left(\nu^4_{S[1\ 0\ 0]} + \nu^2_{P[0\ 1\ 0]}\nu^2_{S[1\ 0\ 0]} + 2\nu^2_{P[0\ 1\ 0]}\nu^2_{P\left[\approx\frac{1}{\sqrt{2}}\ \approx\frac{1}{\sqrt{2}}0\ \right]}\right)\nu_{S[1\ 0\ 0]}\Delta\nu_{S[1\ 0\ 0]}}{\nu^2_{P[1\ 0\ 0]}\left(\nu^2_{P[1\ 0\ 0]} - \nu^2_{S[1\ 0\ 0]}\right)^2} \\
&+ \frac{4\left(\nu^2_{S[1\ 0\ 0]}\nu^2_{P\left[\approx\frac{1}{\sqrt{2}}\ \approx\frac{1}{\sqrt{2}}0\ \right]} + \nu^4_{P\left[\approx\frac{1}{\sqrt{2}}\ \approx\frac{1}{\sqrt{2}}0\ \right]}\right)\nu_{S[1\ 0\ 0]}\Delta\nu_{S[1\ 0\ 0]}}{\nu^2_{P[1\ 0\ 0]}\left(\nu^2_{P[1\ 0\ 0]} - \nu^2_{S[1\ 0\ 0]}\right)^2} \\
&+ \frac{2\left(\nu^2_{P[0\ 1\ 0]} + 2\nu^2_{S[1\ 0\ 0]} + 4\nu^2_{P\left[\approx\frac{1}{\sqrt{2}}\ \approx\frac{1}{\sqrt{2}}0\ \right]}\right)\nu_{P\left[\approx\frac{1}{\sqrt{2}}\ \approx\frac{1}{\sqrt{2}}0\ \right]}\Delta\nu_{P\left[\approx\frac{1}{\sqrt{2}}\ \approx\frac{1}{\sqrt{2}}0\ \right]}}{\nu^2_{P[1\ 0\ 0]}\left(\nu^2_{P[1\ 0\ 0]} - \nu^2_{S[1\ 0\ 0]}\right)} \\
&+ \frac{\nu_{S[1\ 0\ 0]}\Delta\nu_{S[1\ 0\ 0]}}{\nu^2_{P[1\ 0\ 0]}} \qquad (6.32)
\end{aligned}
$$

where Δ is used to indicate that the uncertainty in the following symbol should be used. The $\delta^{(3)}$ was calculated for the oil shale and is shown in Figure 6.33.

According to Tsvankin (1997), Thomsen's parameter γ can calculated in the $x - z$ and $y - z$ planes. The Thomsen parameter γ in the x-direction can be

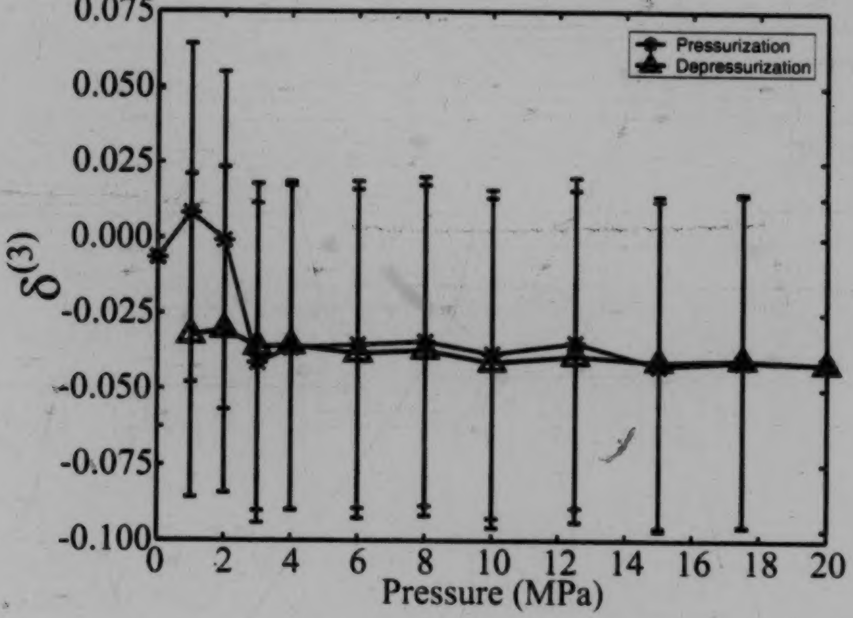

Figure 6.33: Elastic coefficient $\delta^{(3)}$ versus pressure.

written as:

$$\begin{aligned}\gamma^{(1)} &= \frac{C_{66}-C_{55}}{2C_{55}} \\ &= \frac{1}{2}\frac{C_{66}}{C_{55}} - \frac{1}{2}\end{aligned} \tag{6.33}$$

where $C_{55} = \rho\nu^2_{S[0\ 0\ 1]}$ and $C_{66} = \rho\nu^2_{S[0\ 1\ 0]}$ in the $\overrightarrow{n} = [1\ 0\ 0]$ direction according to Equations A.127 and A.126, respectively.

$$\gamma^{(1)} = \frac{1}{2}\frac{\nu^2_{S[0\ 1\ 0]}}{\nu^2_{S[0\ 0\ 1]}} - \frac{1}{2} \tag{6.34}$$

The subsequent uncertainty is:

$$\Delta\gamma^{(1)} = \frac{\nu^2_{S[0\ 1\ 0]}}{\nu^2_{S[0\ 0\ 1]}}\left(\frac{\Delta\nu_{S[0\ 1\ 0]}}{\left|\nu_{S[0\ 1\ 0]}\right|} + \frac{\Delta\nu_{S[0\ 0\ 1]}}{\left|\nu_{S[0\ 0\ 1]}\right|}\right) \tag{6.35}$$

where $\Delta\nu_{S[0\ 1\ 0]}$ and $\Delta\nu_{S[0\ 0\ 1]}$ are the uncertainties in $\nu_{S[0\ 1\ 0]}$ and $\nu_{S[0\ 0\ 1]}$, respectively. The Thomsen parameter γ in the y-direction can be written as:

$$\begin{aligned}\gamma^{(2)} &= \frac{C_{66}-C_{44}}{2C_{44}}\\ &= \frac{1}{2}\frac{C_{66}}{C_{44}}-\frac{1}{2}\end{aligned}\tag{6.36}$$

where $C_{44}=\rho\nu^2_{S[0\ 0\ 1]}$ and $C_{66}=\rho\nu^2_{S[1\ 0\ 0]}$ in the $\vec{n}=[0\ 1\ 0]$ direction according to Equations A.131 and A.129, respectively.

$$\gamma^{(2)}=\frac{1}{2}\frac{\nu^2_{S[1\ 0\ 0]}}{\nu^2_{S[0\ 0\ 1]}}-\frac{1}{2}\tag{6.37}$$

The subsequent uncertainty is:

$$\Delta\gamma^{(2)}=\frac{\nu^2_{S[1\ 0\ 0]}}{\nu^2_{S[0\ 0\ 1]}}\left(\frac{\Delta\nu_{S[1\ 0\ 0]}}{\left|\nu_{S[1\ 0\ 0]}\right|}+\frac{\Delta\nu_{S[0\ 0\ 1]}}{\left|\nu_{S[0\ 0\ 1]}\right|}\right)\tag{6.38}$$

where $\Delta\nu_{S[0\ 0\ 1]}$ and $\Delta\nu_{S[1\ 0\ 0]}$ are the uncertainties in $\nu_{S[0\ 0\ 1]}$ and $\nu_{S[1\ 0\ 0]}$, respectively. The $\gamma^{(1)}$ and $\gamma^{(2)}$ were calculated for the oil shale and are shown in Figures 6.31 and 6.32, respectively.

In Thomsen (1986) once ϵ and δ are determined the P-wave velocity can be determined as a function of angle. The same can be done with $\epsilon^{(1)}$, $\epsilon^{(2)}$, $\delta^{(1)}$, $\delta^{(2)}$, and $\delta^{(3)}$. The P-wave velocity in the $x-z$ plane was defined by Tsvankin (1997) as:

$$V_P(\theta)=V_{P0}\left(1+\delta^{(2)}\sin^2\theta\cos^2\theta+\epsilon^{(2)}\sin^4\theta\right)\tag{6.39}$$

where V_{P0} is the P-wave velocity in the $\vec{n}=(0\ 0\ 1)$ direction and θ is the angle from the z-axis. Similarly the P-wave velocity in the $y-z$ plane can be defined as:

$$V_P(\theta)=V_{P0}\left(1+\delta^{(1)}\sin^2\theta\cos^2\theta+\epsilon^{(1)}\sin^4\theta\right)\ .\tag{6.40}$$

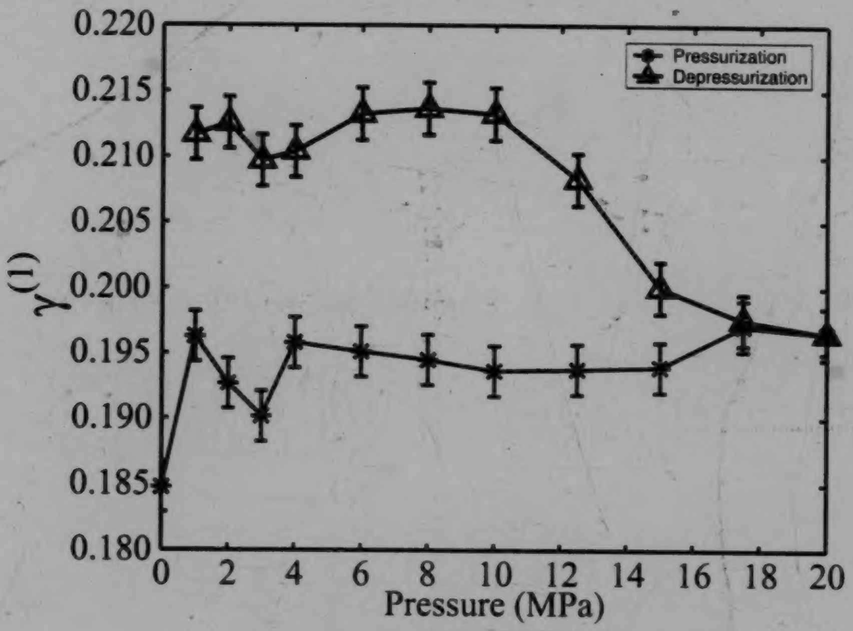

Figure 6.34: Elastic coefficient $\gamma^{(1)}$ versus pressure.

As the pressure is increased from 0 to 4 MPa (40 bar), both $\epsilon^{(1)}$ and $\epsilon^{(2)}$ initially increase. This may be caused by the initial closure of the microcracks (Figures 6.29 and 6.30). However, the gradual decrease in $\epsilon^{(1)}$ and $\epsilon^{(2)}$ as the pressure is increased from 6 MPa (60 bar) to 20 MPa (200 bar) indicates the oil shale is more isotropic with increased pressure (Figures 6.29 and 6.30). This may indicate that the microcracks are almost completely closed. However, at 20 MPa (200 bar) both $\epsilon^{(1)}$ and $\epsilon^{(2)}$ are non-zero and not equal to each other indicating that the oil shale is indeed orthorhombic. As the pressure decreases from 20 MPa (200 bar) to 4 MPa (40 bar), there is no significant change in either $\epsilon^{(1)}$ or $\epsilon^{(2)}$ indicating that the orthorhombicity of the oil shale sample does not change. This may indicate that some of the orthorhombicity of the sample is controlled by microcracks and that the oil shale may be overall orthorhombic or

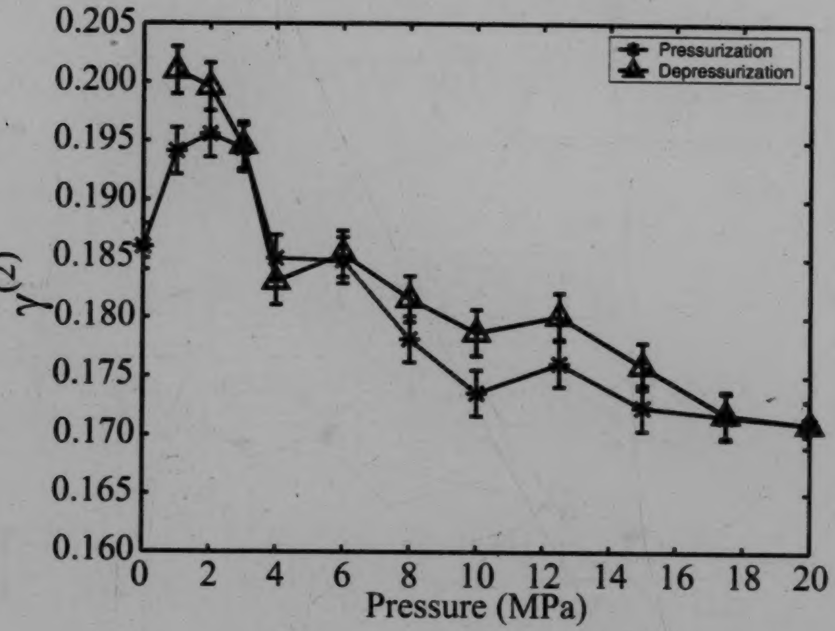

Figure 6.35: Elastic coefficient $\gamma^{(2)}$ versus pressure.

that heterogeneity is present.

6.7 Conclusions

P-wave and S-wave waveforms were recorded in 6 well-chosen directions using the long established pulse-transmission methodology for pressures up to 20 MPa (200 bar). The arrival times of these waveforms were measured and the P-wave and S-wave velocities were determined as functions of pressure. Velocity hysteresis was observed indicating the possible presence of microcracks. Unexpected differences in the velocities indicate the oil shale is, at face value, weakly orthorhombic and not transversely isotropic as expected. The resultant elastic constants as functions of pressure also showed this hysteresis and indicated that the oil shale was orthorhombic. Thomsen/Tsvankin parameters were calculated as functions of pressure and it was found that at higher confining pressure, the oil shale appeared more isotropic but was still overall at least orthorhombic. Barring experimental error or heterogeneity in the oil shale, the orthorhombicity of the sample was partially controlled by microcracks or oriented void spaces but was still dominated by the intrinsic anisotropy or layering.

References

Backus, G. E., 1962, Long-wave elastic anisotropy produced by horizontal layering: Journal of Geophysical Research, **67**, 4427-4440.

Banik, N. C., 1984, Velocity anisotropy of shales and depth estimation in the North Sea Basin: Geophysics, **49**, 1411-1419.

Bass, J. D., 1995, Elasticity of minerals, glasses, and melts, in Ahrens, T. J., ed., Minerals physics and crystallography: A handbook of physical constants: American Geophysical Union, 45-63.

Birch, F., 1960, The velocity of compressional waves in rocks to 10 kilobars, part 1: Journal of Geophysical Research, **65**, 1083-1102.

Bishop, R. S., 1979, Calculated compaction states of thick abnormally pressured shales: American Association of Petroleum Geologists Bulletin, **63**, 918-933.

Brocher, T. M., and Christensen, N. I., 1990, Seismic anisotropy due to preferred mineral orientation observed in shallow crustal rocks in southern Alaska: Geology, **18**, 737-740.

Carcione, J. M., Kosloff, D., and Behle, A., 1991, Long-wave anisotropy in stratified media: A numerical test: Geophysics, **56**, 245-254.

Carlson, R. L., Schaftenaar, C. H., and Moore, R. P., 1984, Causes of compressional-wave anisotropy in carbonate-bearing, deep-sea sediments: Geophysics, **49**, 525-532.

Chang, Y., and Chang, C., 2001, Laboratory results for the feature of body-wave propagation in a transversely isotropic media: Geophysics, **66**, 1921-1924.

Cheadle, S. P., Brown, R. J., and Lawton, D. C., 1991, Orthorhombic anisotropy: A physical seismic modeling study: Geophysics, **56**, 1603-1613.

Cholach, P., 1994, The elasticity of intrinsically anisotropic rocks, Ph. D. thesis, Univ. of Alberta, Edmonton, Alberta.

Claerbout, J. F., 1985, Imaging the earth's interior: Blackwell Scientific Publications, Inc.

Dellinger, J., and Vernik, L., 1994, Do traveltimes in pulse-transmission experiments yield group or phase velocities?: Geophysics, **59**, 1774-1779.

Domnesteanu, P. R., Domnesteanu, R., and McCann, C., 2001, The anisotropic response of shale elastic coefficients to overpressure: 71st Ann. Internat. Mtg., Soc. Expl. Geophys., Expanded Abstracts, 1744-1747.

Faust, L. Y., 1951, Seismic velocity as a function of depth of geological time:

Geophysics, **16**, 192-206.

Freund, D., 1992, Ultrasonic compressional and shear velocities in dry clastic rocks as a function of porosity, clay content, and confining pressure: Geophysical Journal International, **108**, 126-135.

Gardner, G. H. F., Wyllie, M. R. J., and Droschak, D. M., 1965, Hysteresis in the velocity-pressure characteristics of rocks: Geophysics, **30**, 111-116.

Hornby, B. E., 1995, Experimental determination of the anisotropic elastic properties of shales, in Fjaer, E., Holt, R. M., and Rathore, J. S., eds., Seismic anisotropy: Soc. Expl. Geophysics., 238-296.

Hornby, B. E., 1998, Experimental laboratory determinations of the dynamic elastic properties of wet, drained shales: Journal of Geophysical Research, **103**, No. B12, 29945-29964.

Isaac, J. J., and Lawton, D. C., 1999, Image mispositioning due to dipping TI media: a physical seismic modeling study: Geophysics, **64**, 1230-1238.

Johnston, D. H., 1987, Physical properties of shale at temperature and pressure: Geophysics, **52**, 1391-1401.

Johnston, J. E., and Christensen, N. I., 1995, Seismic anisotropy of shales: Journal of Geophysical Research, **100**, 5991-6003.

Jones, L. E. A., and Wang, H. F., 1981, Ultrasonic velocities in Cretaceous shales from the Williston basin: Geophysics, **46**, 288-297.

Kaarsberg, E. A., 1959, Introductory studies of natural and artificial argillaceous aggregates by sound propagation and X-ray diffraction,: Journal of Geology, **67**, 447-472.

Karayaka, M., and Kurath, P., 1994, Deformation and failure behaviour of woven composite laminates: J. Eng. Mat. and Technol., **116**, 222-232.

Katahara, K., 1996, Clay mineral elastic properties: 66th Ann. Internat. Mtg., Soc. Expl. Geophys., Expanded Abstract, 1691-1694.

Kebaili, A., and Schmitt, D. R., 1997, Ultrasonic anisotropic phase velocity determination with the Radon transform, Journal of the Acoustical Society of America, **101**, 3278-3286.

Kim, J. W., Bryant, W. R., Watkins, J. S., and Tieh, T. T., 1998, Mineralogical and fabric changes of shale during burial diagenesis and their effects on petrophysical properties: Gulf Coast Association of Geological Societies Transactions, **XLVIII**, 139-150.

Kim, J. W., Bryant, W. R., Watkins, J. S., and Tieh, T. T., 1999, Electron microscopic observations of shale diagenesis, offshore Louisiana, USA, Gulf of Mexico: Geo-Marine Letters, **18**, 234-240.

Liu, Y. and Schmitt, D., 2000, Quantitative analysis of thin layer effects: Transmission coefficients and seismograms: 70th Ann. Internat. Mtg: Soc. of Expl.

Geophys., Expanded Abstracts, 2464-2467.

Lo, T., Coyner, K. B., and Toksoz, M. N., 1986, Experimental determination of elastic anisotropy of Berea sandstone, Chicopee shale, and Chelmsford granite: Geophysics, **51**, 164-171.

Mah, M., and Schmitt, D. R., 2001a, Experimental determination of the elastic coefficients of an orthorhombic material: Geophysics, **66**, 1217-1225.

Mah, M., and Schmitt, D. R., 2001b, Near point-source longitudinal and transverse mode ultrasonic arrays for material characterization, IEEE Transactions on Ultrasonics, Ferroelectrics, and Frequency Control, **48**, 691-698.

Mah, M., and Schmitt, D. R., 2003, Determination of the complete elastic stiffnesses from ultrasonic phase velocity determination: J. Geophys. Res., **108(B1)** art. no. 2016.

Marion, D., Mukerji, T., and Mavko, G., 1994, Scale effects on velocity dispersion: From ray to effective medium theories in stratified media: Geophysics, **59**, 1613-1619.

Markham, M. F., 1957, Measurement of elastic constants by the ultrasonic pulse method: Brit. J. Appl. Phys., **6**, 56-63.

Melia, P. J., and Carlson, R. L., 1984, An experimental test of P-wave anisotropy in stratified media: Geophysics, **49**, 374-378.

Musgrave, M. J. P., 1970, Crystal Acoustics: Holden-Day.

Neighbours, J. R., and Schacher, G. E., 1967, Determination of elastic constants from sound-velocity measurements in crystals of general symmetry: J. Appl. Phys., **38**, 5366-5375.

Okoye, P. N., Uren, N. F., MacDonald, J. A., and Ebrom, D. A., 1996a, Variation of spatial resolution with orientation of symmetry axis in anisotropic media, in Fjaer, D., Holt, R. M., and Rathore, J. S., Eds., Seismic anisotropy: Soc. Expl. Geophys., 76-99.

Okoye, P. N., Zhao, P., and Uren, N. F., 1996b, Inversion technique for recovering the elastic constants of transversely isotropic materials: Geophysics, **61**, 1247-1257.

Podio, A. L., Gregory, A. R., and Gray, K. E., 1968, Dynamic properties of dry and water-saturated Green River shale under stress: Society of Petroleum Engineers Journal, **8**, 389-404.

Rumpker, G., Brown, R. J., and Thomson, C. J., 1996, Shear wave propagation in orthorhombic phenolic: A comparison of numerical and physical modeling: J. Geophys. Res., **101**, 27765-27777.

Sayers, C. M., 1994, The elastic anisotropy of shales: Journal of Geophysical Research, **99**, 767-774.

Sayers, C. M., 1999, Stress-dependent seismic anisotropy of shales: Geophysics,

64, 93-98.

Schaftenaar, C. H., and Carlson, R. L., 1984, Calcite fabric and acoustic anisotropy in deep-sea carbonates: Journal of Geophysical Research, **89**, 503-510.

Smith, J. E., 1971, The dynamics of shale compaction and evolution of pore-fluid pressures: Mathematical Geology, **3**, 239-263.

Snarskiy, A. N., 1961, Relationship between primary migration and compaction of rocks: Petroleum Geology, **5**, 362-365.

Thomsen, L., 1986, Weak elastic anisotropy: Geophysics, **51**, 1954-1966.

Tosaya, C., and Nur, A., 1982, Effects of diagenesis and clays on compressional velocities in rocks: Geophysical Research Letters, **9**, 5-8.

Tsvankin, I., 1997, Anisotropic parameters and P-wave velocity for orthorhombic media: Geophysics, **62**, 1292-1309.

Tutunca, A. N.; Podio, A. L., and Sharma, M. M., 1998, Nonlinear viscoelastic behavior of sedimentary rocks, Part II: Hysteresis effects and influence of type of fluid on elastic moduli: Geophysics, **63**, 195-203.

Vernik, L., 1993, Microcrack-induced versus intrinsic elastic anisotropy in mature HC-source shales: Geophysics, **58**, 1703-1706.

Vernik, L., 1994, Hydrocarbon-generation-induced microcracking of source rocks:

Geophysics, **59**, 555-563.

Vernik, L., and Landis, C., 1996, Elastic anisotropy of source rocks: Implications for hydrocarbon generation and primary migration: American Association of Petroleum Geologists Bulletin, **80**, 531-544.

Vernik, L., and Liu, X., 1997, Velocity anisotropy in shales: A petrophysical study : Geophysics, **62**, 521-532.

Vernik, L., and Nur, A., 1992, Ultrasonic velocity and anisotropy of hydrocarbon source rocks: Geophysics, **57**, 727-735.

Vestrum, R. W., 1994, Group and phase-velocity inversions for the general isotropic stiffness tensor, M. Sc. thesis, Univ. of Calgary, Calgary, Alberta.

Vestrum, R., and Lawton, D., 1999, Anisotropic depth migration: Reducing lateral-position uncertainty of subsurface structures in thrust-belt environments, 69th Ann. Internat. Mtg., Soc. of Expl. Geophys., Expanded Abstracts, 1107-1109.

Wang, Z., Wang, H., and Cates, M. E., 2001, Effective elastic properites of solid clays: Geophysics, **66**, 428-440.

Wild, P., and Crampin, S., 1991, The range of effects of azimuthal isotropy and EDA anisotropy in sedimentary basins: Geophysical Journal International, **107**, 513-529.

Chapter 7

Conclusions

7.1 Summary

The purpose of this work was to investigate the anisotropy of orthorhombic and transversely isotropic materials with experimental application to a real rock. The $\tau - p$ methodology was applied to an isotropic glass block in Chapter 3 which was previously published in Mah & Schmitt (2001b). Previous work by Kebaili & Schmitt (1997) used only P-waves. It was found that phase velocities could be determined as functions of the phase propagation angle for P-wave and S-wave propagation using the $\tau - p$ methodology to within 1 % when compared with the conventional pulse-transmission methodology. This allowed the elastic constants for an isotropic material to be determined.

The $\tau - p$ methodology was then applied to phenolic which is canvas held together by a phenol resin (Chapter 4; Mah & Schmitt, 2001a; Mah & Schmitt, 2003). Clean P-wave and SH-wave waveforms were achieved and the resultant phase velocities as functions of angle were calculated. However, problems were encountered in acquiring clean SV-wave data due to the coupled nature of P-waves and SV-waves. Due to the weave and layering of the canvas, the phenolic was expected to have an orthorhombic symmetry. The $\tau - p$ methodology was used to determine the phase velocities with phase propagation angle in an anisotropic medium. Numerous sets of waveforms were acquired in a variety of well chosen directions allowing for the phase velocities to be determined in a variety of directions that were not symmetry dependent. Using a non-linear iterative inversion, assuming orthorhombic, monoclinic, and triclinic symmetry, up to all 21 elastic constants were determined for the phenolic. It was found that phenolic is predominantly orthorhombic in nature and that the $\tau - p$ methodology as able to determine phase velocities as functions of propagation direction in anisotropic media. Phase velocities were also calculated in a forward manner from the 21 elastic constants derived from the inversion and it was found that they were in good agreement with the observed phase velocities.

An oil shale was chosen for indepth study using thin section, pyrolysis, whole-rock analysis, X-ray diffraction, scanning electron microscopy, and electron microprobing (Chapter 5; Mah & Schmitt, 2002) in order to determine its composition since the seismic properties of rocks are controlled by their composition and structure. Albite, calcite, dawsonite, dolomite, kerogen, pyrite, and quartz were positively identified as being present in the oil shale and other minerals such as anorthoclase, illite, and ilmenite are thought to be present. However, the material is predominantly kerogen which contributes almost 50 % by weight. The relative concentration of these minerals has been identified. It has also been determined that the oil shale is layered at scales from a few microns to a few millimetres. Further, there may be some preferential distribution or preferential orientation of these minerals. There are also some indications that the dolomite in the oil shale may have been deposited by direct precipitation as opposed to diagenesis of calcite. The composition and structure of the oil shale has been determined.

Preliminary application of the $\tau - p$ methodology yielded poor quality data on the oil shale. Consequently, conventional pulse-transmission tests were performed on the oil shale instead (Chapter 6; Mah & Schmitt, 2002). P-wave and S-wave waveforms were recorded as a function of pressure up to 20 MPa (200 bar) in a pressure vessel. The velocities were measured as functions of pressure and the elastic constants as functions of pressure were calculated. Even though the oil shale was expected to be transversely isotropic on the basis of its layering, it was found to be at least transversely isotropic if not weakly orthorhombic in nature. Velocity and elastic constant hysteresis with pressure shows that there may be microcracks or oriented void spaces present in the oil shale and that there may be a preferential orientation to these. Thomsen/Tsvankin parameters were calculated and showed the anisotropy of the oil shale slightly decreased with pressure.

7.2 Future Work

7.2.1 $\tau - p$ methodology

As has been previously discussed, the $\tau - p$ methodology has allowed the phase velocities to be determined in a variety of directions that are not symmetry dependent on both isotropic and anisotropic materials (Mah & Schmitt, 2001a; Mah & Schmitt, 2001b; Mah & Schmitt, 2003). This has allowed the full anisotropy of the synthetic materials to be determined. However, the $\tau - p$ methodology has been unexpectedly unsuccessfully in determining phase velocities in an oil shale due to its attenuative nature. The $\tau - p$ methodology should be applied to a more suitable sample allowing all 21 elastic constants to be determined. This will also allow more indepth studies of dispersion and scaling effects in real rocks. Once the $\tau - p$ methodology is perfected at room pressure, it should be applied to a sample under confining pressure to allow the elastic constants of the material to be determined as functions of pressure. This would not be to difficult since the $\tau - p$ methodology is readily applicable to cylinders and rectangular prisms.

7.2.2 3rd order elastic constants

The generalized Hooke's law is described in Appendix A in detail where the stress is related to the strain by the elasticity tensor c_{ijkl} and the 2nd order equation A.21:

$$\rho\ddot{U}_i = c_{ijkl}U_{l,jk} \tag{7.1}$$

is derived. This equation does not take into account the change in elastic constants with pressure as observed in the oil shale. Work done by Breazeale (2001) and Thurston & Brugger (1964) has allowed Equation A.21 as:

$$\rho\ddot{U}_i = c^s_{ijkl}U_{l,jk} \tag{7.2}$$

where ρ is the density, U is the displacement, and the tensor c^s_{ijkl} is determined by not only velocities or the stress-strain relationships but also by the deformation gradients or the changes in the stress-strain relationships with pressure. It is possible that 3rd order elastic constants may be calculated for pressure regimes where the elastic constants of the oil shale are changing linearly with pressure. This will allow for more accurate modelling and processing using non-linear wave equations for seismic waves travelling through rocks at deeper depths. The study of nonlinear propagation of elastic waves, particularly through the earth, is only in its nascent stage. However, studying this nonlinearity may provide some new useful insights into materials at depth in the earth in coming years.

7.2.3 Backus modelling

Seismic waves passing through a series of layers do not see the individual layers when the wavelength is larger than the individual layers (Backus, 1962; Carcione et al., 1991). This has been studied in the laboratory using isotropic layers of glass and epoxy or plastic and steel disks that overall have a transversely isotropic response (Marion et al., 1994; Melia & Carlson, 1984). The oil shale is composed of layers that will behave as an effective anisotropic medium. Since the composition of the oil shale has been relatively well quantified and the elastic constants of the individual minerals are well studied in the literature, numerical models can be built attempting to describe the anisotropic response of the oil shale and comparisons made with the observed oil shale response.

7.2.4 Anisotropic turning ray

In an isotropic medium, Snell's law is simply:

$$\frac{\sin(\theta_1)}{v_1} = \frac{\sin(\theta_2)}{v_2} \tag{7.3}$$

where θ_1 and θ_2 are the angles at which the seismic wave enters and leaves the interface between the velocity contrast, respectively. v_1 and v_2 are the velocities above and below the interface between the velocity contrast, respectively. As seismic waves travel through an isotropic material with a linear velocity gradient that increases with depth the seismic waves tend to turn back towards the surface (Shearer, 1999). Turning rays have also been theoretically and numerically described for an anisotropic medium with a linear velocity gradient by Shearer & Chapman (1988). These turning rays have been investigated in snow and ice using data from laboratory studies on cores (Bennett, 1968). The oil shale measurements have shown that the velocity in the oil shale increases with pressure and hence for increasing depth. Numerical simulations could possibly describe turning rays in an oil shale formation. This will be of interest because ray paths so produced are substantially more complex than those for isotropic media. Such results will be important in tomographic inversions in areas with an anisotropic overburden.

References

Backus, G. E., 1962, Long-wave elastic anisotropy produced by horizontal layering: Journal of Geophysical Research, **67**, 4427-4440.

Bennett, H. F., 1968, An investigation into velocity anisotropy through measurements of ultrasonic wave velocities in snow and ice cores from Greenland and Antarctica, Ph. D. thesis., Univ. of Wisconsin, Madison, Wisconsin.

Breazeale, M. A., 2001, Third-order elastic constants of cubic crystals, in Levy, M., Bass, H. E., and Stern, R. R., eds., Handbook of elastic properties of solids, liquids, and gases: Volume I - Dynamic methods for measuring the elastic properties of solids: Academic Press, 489-510.

Carcione, J. M., Kosloff, D., and Behle, A., 1991, Long-wave anisotropy in stratified media: A numerical test: Geophysics, **56**, 245-254.

Kebaili, A. M., and Schmitt, D. R.,1997, Ultrasonic anisotropic phase velocity determination with the Radon transform: J. Acoust. Soc. Am., **101**, 3278-3286.

Mah, M., and Schmitt, D. R., 2001a, Experimental determination of the elastic coefficients of an orthorhombic material: Geophysics, **66**, 1217-1225.

Mah, M., and Schmitt, D. R., 2001b, Near point-source longitudinal and transverse mode ultrasonic arrays for material characterization, IEEE Transactions on Ultrasonics, Ferroelectrics, and Frequency Control, **48**, 691-698.

Mah, M., and Schmitt, D.R., 2002, Determination of the complete elastic stiffnesses from ultrasonic phase velocity measurements: 2002 CSEG National Convention Abstract.

Mah, M., and Schmitt, D. R., 2003, Determination of the complete elastic stiffnesses from ultrasonic phase velocity determination: J. Geophys. Res., **108(B1)** art. no. 2016.

Marion, D., Mukerji, T., and Mavko, G., 1994, Scale effects on velocity dispersion: From ray to effective medium theories in stratified media: Geophysics, **59**, 1613-1619.

Markham, M. F., 1957, Measurement of elastic constants by the ultrasonic pulse method: Brit. J. Appl. Phys., **6**, 56-63.

Melia, P. J., and Carlson, R. L., 1984, An experimental test of P-wave anisotropy in stratified media: Geophysics, **49**, 374-378.

Shearer, P. M., 1999, Introduction to seismology, Cambridge University Press, New York, NY.

Shearer, P. M., and Chapman, C. H., 1988, Ray tracing in anisotropic media with a linear gradient: Geophysical Journal, **94**, 575-580.

Thurston, R. N., and Brugger, K., 1964, Third-order elastic constants and the velocity of small amplitude elastic waves in homogeneously stressed media: Physical Review, **1333**, No. 6A, A1604-A1610.

Appendix A

Elastic constant formula derivation

A.1 Theory

The following is a brief summary of the mathematical work and a more complete description can be found in Lay & Wallace (1995) and Musgrave (1970). It is important to discuss the underlying theory of elasticity as it applies to elastic wave anisotropy.

To begin, the stress is related to strain by the stress-strain relationship which is given by the generalized Hooke's Law where the Einstein summation convention will be used:

$$\sigma_{ij} = c_{ijkl}\epsilon_{kl} \tag{A.1}$$

where

$i = 1, 2, 3;$

$j = 1, 2, 3;$

$k = 1, 2, 3;$

$l = 1, 2, 3;$

σ_{ij} is the second order stress tensor,

ϵ_{kl} is the second order strain tensor, and

c_{ijkl} is the fourth rank elasticity tensor with components of stiffness.

Since the elasticity tensor c_{ijkl} has 4 indices, each of which goes from 1 to 3, the elasticity tensor has 81 elements present.

If one takes the unit cube as an example then σ_{ij} is the stress or pressure on the i^{th} face in the x_j direction as shown in Figure A.1. The i^{th} face is the face on the unit cube whose outward normal is parallel to the x_i direction as can be seen in Figure A.2. For convenience, in this thesis x, y, and z will be used for x_1, x_2, and x_3, respectively.

The strain ϵ_{kl} is defined in a similar manner to the stress σ_{ij}. The strain ϵ_{kl} is the strain on the k^{th} surface in the x_l direction and will be defined by the following formula (Lay & Wallace, 1995) as:

$$\epsilon_{kl} = \frac{1}{2}\left(\frac{\partial U_k}{\partial x_l} + \frac{\partial U_l}{\partial x_k}\right) \tag{A.2}$$

where U_k is the displacement in the x_k direction.

A closer look at ϵ_{11}, ϵ_{22}, and ϵ_{33} shows that these strains are distortions in the size of the unit cube.

These are strains normal to the surface.
(i.e. compression or elongation)

$\epsilon_{11} = \frac{\partial U_1}{\partial x_1}$ which is an elongation of the unit cube in the x_1 direction
$\epsilon_{22} = \frac{\partial U_2}{\partial x_2}$ which is an elongation of the unit cube in the x_2 direction
$\epsilon_{33} = \frac{\partial U_3}{\partial x_3}$ which is an elongation of the unit cube in the x_3 direction

A closer look at ϵ_{12}, ϵ_{13}, and ϵ_{23} shows that these are distortions in the shape of

2

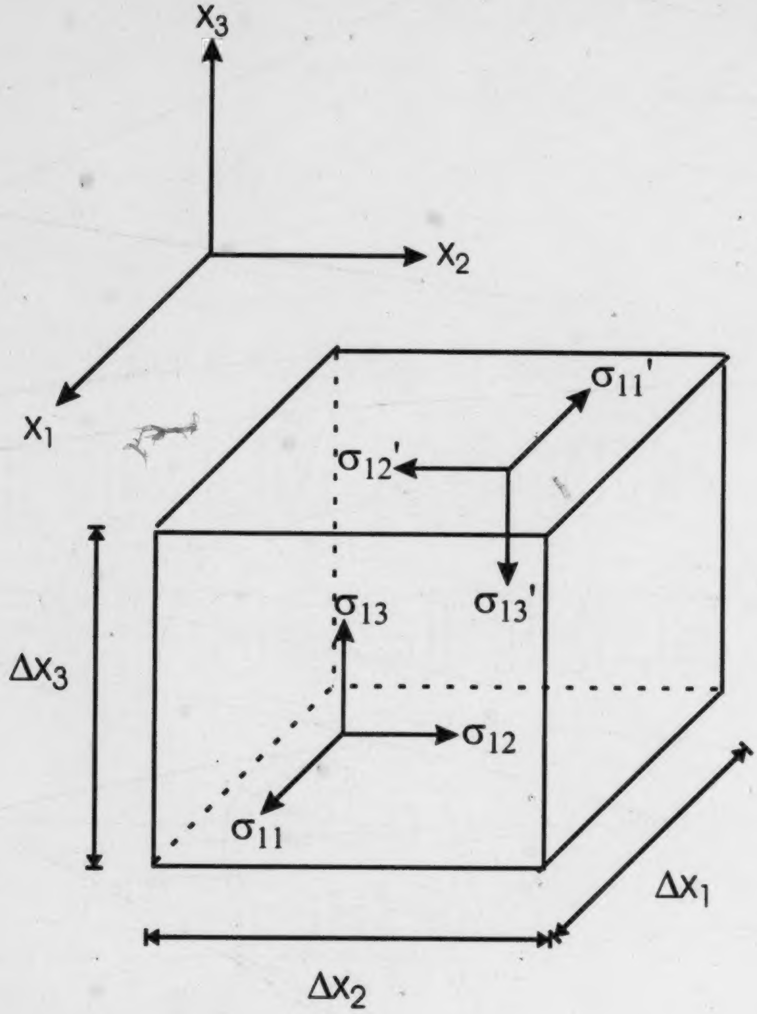
X3
X2
X1
σ11'
σ12'
σ13'
σ13
σ12
σ11
ΔX3
ΔX1
ΔX2

Figure A.1: σ_{ij} is the stress on the i^{th} face in the x_j direction. σ'_{ij} is the stress on the face opposite the i^{th} face on the unit cube and is defined as $\sigma_{ij} + \frac{\partial \sigma_{ij}}{\partial x_i}(-\Delta x_i)$. Δx_i is the width of the unit cube in the x_i direction.

the unit cube.

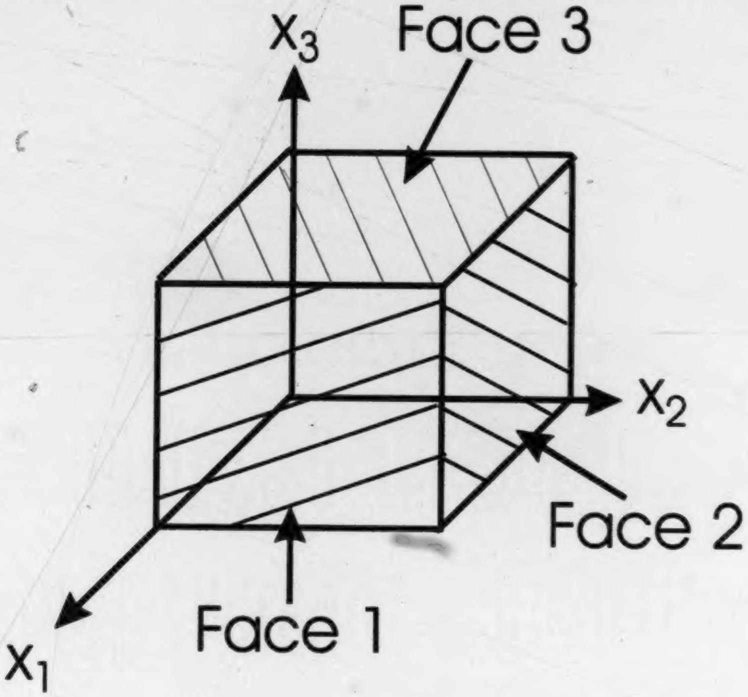

Figure A.2: Face 1 is the face on the unit cube whose outward normal is parallel to direction x_1. Face 2 is the face on the unit cube whose outward normal is parallel to direction x_2. Face 3 is the face on the unit cube whose outward normal is parallel to direction x_3.

These are strains parallel to the surface.(i.e. shear)

$\epsilon_{12} = \frac{1}{2}\left(\frac{\partial U_1}{\partial x_2} + \frac{\partial U_2}{\partial x_1}\right)$ is the shearing on surface 1 in the x$_2$ direction

$\epsilon_{13} = \frac{1}{2}\left(\frac{\partial U_1}{\partial x_3} + \frac{\partial U_3}{\partial x_1}\right)$ is the shearing on surface 1 in the x$_3$ direction

$\epsilon_{23} = \frac{1}{2}\left(\frac{\partial U_2}{\partial x_3} + \frac{\partial U_3}{\partial x_2}\right)$ is the shearing on surface 2 in the x$_3$ direction

As can be easily seen from Equation A.2, ϵ_{kl} is equal to ϵ_{lk}. (i.e., ϵ_{12}=ϵ_{21} and so forth.) This symmetry implies:

$$c_{ijkl} = c_{ijlk} \ . \tag{A.3}$$

A similar symmetry exists for the stress tensor as well where σ_{ij} is equal to σ_{ji}. This symmetry of stresses implies:

$$c_{ijkl} = c_{jikl} \ . \tag{A.4}$$

Using the symmetries in the stress and strain tensors reduces the 81 element stress-strain tensor c_{ijkl} to only 36 independent elements.

Arguments of symmetry and thermodynamics (i.e., internal energy of the material must increase with a strain) reduces from 81 to 21 the components of stiffness (Musgrave, 1970). For the sake of convenience, the c_{ijkl} stiffness tensor can be represented as a symmetric 6 × 6 matrix C_{mn}.

The stiffness c_{ijkl} can be transformed to C_{MN} according to the rule (Vestrum, 1994):

$$M = \begin{cases} i & \text{if i=j} \\ 9-(i+j) & \text{if i} \neq \text{j} \end{cases} \quad \text{and} \tag{A.5}$$

$$N = \begin{cases} k & \text{if k=l} \\ 9-(k+l) & \text{if k} \neq \text{l} \end{cases} \ . \tag{A.6}$$

Using this formula translates the generalized Hooke's Law from $\sigma_{ij} = c_{ijkl}\epsilon_{kl}$ to the following form:

$$\begin{bmatrix} \sigma_{11} \\ \sigma_{22} \\ \sigma_{33} \\ \sigma_{23} \\ \sigma_{13} \\ \sigma_{12} \end{bmatrix} = \begin{bmatrix} C_{11} & C_{12} & C_{13} & C_{14} & C_{15} & C_{16} \\ C_{21} & C_{22} & C_{23} & C_{24} & C_{25} & C_{26} \\ C_{31} & C_{32} & C_{33} & C_{34} & C_{35} & C_{36} \\ C_{41} & C_{42} & C_{43} & C_{44} & C_{45} & C_{46} \\ C_{51} & C_{52} & C_{53} & C_{54} & C_{55} & C_{56} \\ C_{61} & C_{62} & C_{63} & C_{64} & C_{65} & C_{66} \end{bmatrix} \begin{bmatrix} \epsilon_{11} \\ \epsilon_{22} \\ \epsilon_{33} \\ 2\epsilon_{23} \\ 2\epsilon_{13} \\ 2\epsilon_{12} \end{bmatrix} \tag{A.7}$$

where $C_{MN} = C_{NM}$ and by examination it may be noted that only 21 independent stiffnesses exist. However, this is the most general case where there is no symmetry. It is useful to examine briefly how the elastic tensor C_{mn} appears with decreasing symmetry. For cubic symmetry, 3 independent constants are required (Musgrave, 1970).

$$C_{IJ} = \begin{bmatrix} a & b & b & 0 & 0 & 0 \\ b & a & b & 0 & 0 & 0 \\ b & b & a & 0 & 0 & 0 \\ 0 & 0 & 0 & c & 0 & 0 \\ 0 & 0 & 0 & 0 & c & 0 \\ 0 & 0 & 0 & 0 & 0 & c \end{bmatrix} . \tag{A.8}$$

For hexagonal symmetry (transverse isotropy), 5 independent constants are required (Musgrave, 1970).

$$C_{IJ} = \begin{bmatrix} a & b & c & 0 & 0 & 0 \\ b & a & c & 0 & 0 & 0 \\ c & c & d & 0 & 0 & 0 \\ 0 & 0 & 0 & e & 0 & 0 \\ 0 & 0 & 0 & 0 & e & 0 \\ 0 & 0 & 0 & 0 & 0 & x \end{bmatrix} \tag{A.9}$$

where $x = \frac{a-b}{2}$.

Orthorhombic symmetry is characterized by 3 mutually orthogonal planes of symmetry and 9 independent elastic constants (Musgrave, 1970).

$$C_{IJ} = \begin{bmatrix} a & b & c & 0 & 0 & 0 \\ b & d & e & 0 & 0 & 0 \\ c & e & f & 0 & 0 & 0 \\ 0 & 0 & 0 & g & 0 & 0 \\ 0 & 0 & 0 & 0 & h & 0 \\ 0 & 0 & 0 & 0 & 0 & i \end{bmatrix} \tag{A.10}$$

In contrast to the previous cases, if no symmetry is present the material is treated as triclinic which is characterized by 21 independent elastic constants (Musgrave, 1970).

$$C_{IJ} = \begin{bmatrix} a & b & c & d & e & f \\ b & g & h & i & j & k \\ c & h & l & m & n & o \\ d & i & m & p & q & r \\ e & j & n & q & s & t \\ f & k & o & r & t & u \end{bmatrix} \tag{A.11}$$

For a variety of reasons, one might expect the symmetry of many rocks to be rather low, with orthorhombic symmetry being that of the lowest symmetry. However in natural crystals less symmetry can exist, as in the cases of calcite and plagioclase feldspar in order of symmetry and requiring an increasing number of elastic constants of 7 and 21, respectively.

Determining the stiffness tensor directly by actually applying large pressures and shears to the sample and determining the infinitesimal compressions can be difficult. Instead, it is often simpler to determine these properties indirectly by measuring the elastic wave velocities and densities of the material.

A.2 Relationship between stiffness and anisotropic velocities

Newton's second law states that the sum of the forces applied to the unit cube will be equal to the mass times the acceleration. In other words, the mass multiplied by the acceleration in the x_i direction is equal to the sum of the forces in the x_i direction:

$$\vec{F} = m\vec{a} \tag{A.12}$$

Take for example in the x_1 direction $\sum F_{x_1} = ma_{x_1} = m\ddot{U}_1$.

$$\begin{aligned}\sum F_{x_1} &= \left[\sigma_{11} - \left(\sigma_{11} + \frac{\partial \sigma_{11}}{\partial x_1}(-\Delta x_1)\right)\right] \Delta x_2 \Delta x_3 \\ &+ \left[\sigma_{21} - \left(\sigma_{21} + \frac{\partial \sigma_{21}}{\partial x_2}(-\Delta x_2)\right)\right] \Delta x_1 \Delta x_3 \\ &+ \left[\sigma_{31} - \left(\sigma_{31} + \frac{\partial \sigma_{31}}{\partial x_3}(-\Delta x_3)\right)\right] \Delta x_1 \Delta x_2\end{aligned} \tag{A.13}$$

This equation simplifies to the following:

$$\begin{aligned}\sum F_{x_1} &= \left(\frac{\partial \sigma_{11}}{\partial x_1} + \frac{\partial \sigma_{21}}{\partial x_2} + \frac{\partial \sigma_{31}}{\partial x_3}\right) \Delta x_1 \Delta x_2 \Delta x_3 \\ &= \left[\frac{\partial (c_{11kl}\epsilon_{kl})}{\partial x_1} + \frac{\partial (c_{21kl}\epsilon_{kl})}{\partial x_2} + \frac{\partial (c_{31kl}\epsilon_{kl})}{\partial x_3}\right] \Delta x_1 \Delta x_2 \Delta x_3\end{aligned} \tag{A.14}$$

But $\frac{\partial c_{ijkl}}{\partial x_m} = 0$ for m=1,2,3 since the material is assumed to be homogeneous and the elastic constants cannot change with position.

This means:

$$\sum F_{x_1} = \left[c_{11kl}\frac{\partial \epsilon_{kl}}{\partial x_1} + c_{21kl}\frac{\partial \epsilon_{kl}}{\partial x_2} + c_{31kl}\frac{\partial \epsilon_{kl}}{\partial x_3}\right] \Delta x_1 \Delta x_2 \Delta x_3\ . \tag{A.15}$$

However,

$$\sum F_{x_1} = m\ddot{U}_1 = \rho \Delta x_1 \Delta x_2 \Delta x_3 \ddot{U}_1 \tag{A.16}$$

where ρ is the density for the unit cube.

When Equation A.15 and Equation A.16 are combined, one obtains the following:

$$\rho \Delta x_1 \Delta x_2 \Delta x_3 \ddot{U}_1 = c_{i1kl}\epsilon_{kl,i} \Delta x_1 \Delta x_2 \Delta x_3 \tag{A.17}$$

which can be simplified to:

$$\rho \ddot{U}_i = c_{ijkl}\epsilon_{kl,j} \ . \tag{A.18}$$

But, as defined before:

$$\begin{aligned} \epsilon_{kl} &= \frac{1}{2}\left(\frac{\partial U_k}{\partial x_l} + \frac{\partial U_l}{\partial x_k}\right) \\ &= \frac{1}{2}\left(U_{k,l} + U_{l,k}\right) \ , \end{aligned} \tag{A.19}$$

which implies:

$$\begin{aligned} \epsilon_{kl,j} &= \frac{1}{2}\left(\frac{\partial^2 U_k}{\partial x_l \partial x_j} + \frac{\partial^2 U_l}{\partial x_k \partial x_j}\right) \\ &= \frac{1}{2}\left(U_{k,lj} + U_{l,kj}\right) \ . \end{aligned} \tag{A.20}$$

So, when Equation A.20 is substituted into Equation A.18, one obtains the following:

$$\begin{aligned} \rho \ddot{U}_i &= c_{ijkl}\left(\frac{1}{2}\left(U_{k,lj} + U_{l,kj}\right)\right) \\ &= \frac{1}{2}\left(c_{ijlk}U_{k,lj} + c_{ijkl}U_{l,kj}\right) \\ &= c_{ijkl}U_{l,jk} \ . \end{aligned} \tag{A.21}$$

Due to the simplicity of using plane waves, if one assumes that the plane wave solutions to this equation are of the form:

$$U_i = A_i e^{i\frac{2\pi}{\lambda}(n_r x_r - \nu t)} \tag{A.22}$$

where ν is the phase velocity, $\overrightarrow{n} = (n_1, n_2, n_3)$ is the wave front normal, $\overrightarrow{A} = (A_1, A_2, A_3)$ is the amplitude vector, and $\overrightarrow{x} = (x_1, x_2, x_3)$ is the position vector.

From this ansatz

$$\dot{U}_i = \left(-\nu\left(i\frac{2\pi}{\lambda}\right)\right) A_i e^{i\frac{2\pi}{\lambda}(n_r x_r - \nu t)} \tag{A.23}$$

and

$$\begin{aligned}\ddot{U}_i &= \left(-\nu\left(i\frac{2\pi}{\lambda}\right)\right)^2 A_i e^{i\frac{2\pi}{\lambda}(n_r x_r - \nu t)} \\ &= -\left(\nu\frac{2\pi}{\lambda}\right)^2 A_i e^{i\frac{2\pi}{\lambda}(n_r x_r - \nu t)} . \end{aligned} \tag{A.24}$$

Similarly,

$$U_l = A_l e^{i\frac{2\pi}{\lambda}(n_r x_r - \nu t)} , \tag{A.25}$$

$$U_{l,j} = i\frac{2\pi}{\lambda} n_j A_l e^{i\frac{2\pi}{\lambda}(n_r x_r - \nu t)} , \text{ and} \tag{A.26}$$

$$\begin{aligned}U_{l,jk} &= \left(i\frac{2\pi}{\lambda}\right)^2 n_j n_k A_l e^{i\frac{2\pi}{\lambda}(n_r x_r - \nu t)} \\ &= -\left(\frac{2\pi}{\lambda}\right)^2 n_j n_k A_l e^{i\frac{2\pi}{\lambda}(n_r x_r - \nu t)} . \end{aligned} \tag{A.27}$$

When Equation A.24 and Equation A.27 are substituted in Equation A.21 one gets the following:

$$-\rho\left(\nu\frac{2\pi}{\lambda}\right)^2 A_i e^{i\frac{2\pi}{\lambda}(n_r x_r - \nu t)} = -c_{ijkl}\left(\frac{2\pi}{\lambda}\right)^2 n_j n_k A_l e^{i\frac{2\pi}{\lambda}(n_r x_r - \nu t)} \tag{A.28}$$

Equation A.28 simplifies to:

$$\rho\nu^2 A_i = c_{ijkl} n_j n_k A_l \tag{A.29}$$

The following substitution $\Gamma_{il} = c_{ijkl} n_j n_k$ is used where Γ_{il} are the Christoffel equations (Musgrave, 1970). When this substitution is made into Equation A.29 one obtains the following:

$$\rho\nu^2 A_i = \Gamma_{il} A_l \tag{A.30}$$

which implies

$$\left(\Gamma_{il} - \rho\nu^2\delta_{il}\right) A_l = 0\ . \tag{A.31}$$

When written in matrix form, this equation is an eigenvalue problem, $Bx = \lambda x$, where the eigenvalues and eigenvectors of the system are equivalent to the phase velocities and amplitude vectors respectively.

$$\begin{bmatrix} \Gamma_{11} & \Gamma_{12} & \Gamma_{13} \\ \Gamma_{21} & \Gamma_{22} & \Gamma_{23} \\ \Gamma_{31} & \Gamma_{32} & \Gamma_{33} \end{bmatrix} \begin{bmatrix} A_1 \\ A_2 \\ A_3 \end{bmatrix} = \rho\nu^2 \begin{bmatrix} A_1 \\ A_2 \\ A_3 \end{bmatrix}\ . \tag{A.32}$$

For example, the case of the orthorhombic medium has the following 2-dimensional stiffness matrix:

$$C_{IJ} = \begin{bmatrix} a & b & c & 0 & 0 & 0 \\ b & d & e & 0 & 0 & 0 \\ c & e & f & 0 & 0 & 0 \\ 0 & 0 & 0 & g & 0 & 0 \\ 0 & 0 & 0 & 0 & h & 0 \\ 0 & 0 & 0 & 0 & 0 & i \end{bmatrix}$$

where the letters a through i represent the 9 independent elastic constants.

For the direction $\vec{n} = (1, 0, 0)$ Equation A.32 becomes:

$$\begin{bmatrix} a & 0 & 0 \\ 0 & i & 0 \\ 0 & 0 & h \end{bmatrix} \begin{bmatrix} A_1 \\ A_2 \\ A_3 \end{bmatrix} = \rho\nu^2 \begin{bmatrix} A_1 \\ A_2 \\ A_3 \end{bmatrix} \tag{A.33}$$

Three eigenvectors and corresponding eigenvalues are determined as follows:

$\vec{A_1} = (1, 0, 0) \quad \rho{\nu_1}^2 = a$

$\vec{A_2} = (0, 1, 0) \quad \rho{\nu_2}^2 = i$

$\vec{A_3} = (0, 0, 1) \quad \rho{\nu_3}^2 = h$

where $\overrightarrow{A_1}$ is the P-wave or compressional wave polarization while $\overrightarrow{A_2}$ and $\overrightarrow{A_3}$ are the two S-wave or shear wave polarizations.

By being able to forward calculate the phase velocities from the elastic constants one is able to determine the elastic constants from the phase velocities. However, one must still be able to calculate the phase velocities from the group velocity data. In order to do this operation, the Radon transform will be employed.

A.3 Isotropic case: 2 elastic constants

The elastic constants for an isotropic solid is:

$$C_{IJ} = \begin{bmatrix} C_{11} & C_{12} & C_{12} & 0 & 0 & 0 \\ & C_{11} & C_{12} & 0 & 0 & 0 \\ & & C_{11} & 0 & 0 & 0 \\ & & & C_{44} & 0 & 0 \\ & & & & C_{44} & 0 \\ & & & & & C_{44} \end{bmatrix} \tag{A.34}$$

where $C_{12} = C_{11} - 2C_{44}$.

For $\overrightarrow{n} = [1\ 0\ 0]$, the Christoffel matrix (according to Appendix B) is:

$$\begin{bmatrix} C_{11} & 0 & 0 \\ 0 & C_{44} & 0 \\ 0 & 0 & C_{44} \end{bmatrix} \begin{bmatrix} A_1 \\ A_2 \\ A_3 \end{bmatrix} = \rho\nu^2 \begin{bmatrix} A_1 \\ A_2 \\ A_3 \end{bmatrix} . \tag{A.35}$$

This implies:

$$\rho\nu^2_{P[1\ 0\ 0]} = C_{11} \tag{A.36}$$

$$\rho\nu^2_{S[0\ 1\ 0]} = C_{44} \tag{A.37}$$

$$\rho \nu^2_{S[0\ 0\ 1]} = C_{44} \tag{A.38}$$

where $\nu_{P[1\ 0\ 0]}$ is the P-wave with particle motion [1 0 0], $\nu_{S[0\ 1\ 0]}$ is the S-wave with particle motion [0 1 0], and $\nu_{S[0\ 0\ 1]}$ is the S-wave with particle motion [0 0 1].

A.4 Cubic case: 3 elastic constants

The elastic constants for a cubic solid is:

$$C_{IJ} = \begin{bmatrix} C_{11} & C_{12} & C_{12} & 0 & 0 & 0 \\ & C_{11} & C_{12} & 0 & 0 & 0 \\ & & C_{11} & 0 & 0 & 0 \\ & & & C_{44} & 0 & 0 \\ & & & & C_{44} & 0 \\ & & & & & C_{44} \end{bmatrix}. \tag{A.39}$$

For $\vec{n} = [1\ 0\ 0]$, the Christoffel matrix (according to Appendix B) is:

$$\begin{bmatrix} C_{11} & 0 & 0 \\ 0 & C_{44} & 0 \\ 0 & 0 & C_{44} \end{bmatrix} \begin{bmatrix} A_1 \\ A_2 \\ A_3 \end{bmatrix} = \rho \nu^2 \begin{bmatrix} A_1 \\ A_2 \\ A_3 \end{bmatrix}. \tag{A.40}$$

This implies:

$$\rho \nu^2_{P[1\ 0\ 0]} = C_{11} \tag{A.41}$$

$$\rho \nu^2_{S[0\ 1\ 0]} = C_{44} \tag{A.42}$$

$$\rho \nu^2_{S[0\ 0\ 1]} = C_{44} \tag{A.43}$$

For $\overrightarrow{n} = [0\ 1\ 0]$, the Christoffel matrix (according to Appendix B) is:

$$\begin{bmatrix} C_{44} & 0 & 0 \\ 0 & C_{11} & 0 \\ 0 & 0 & C_{44} \end{bmatrix} \begin{bmatrix} A_1 \\ A_2 \\ A_3 \end{bmatrix} = \rho\nu^2 \begin{bmatrix} A_1 \\ A_2 \\ A_3 \end{bmatrix}. \tag{A.44}$$

This implies:

$$\rho\nu^2_{S[1\ 0\ 0]} = C_{44} \tag{A.45}$$

$$\rho\nu^2_{P[0\ 1\ 0]} = C_{11} \tag{A.46}$$

$$\rho\nu^2_{S[0\ 0\ 1]} = C_{44} \tag{A.47}$$

For $\overrightarrow{n} = [0\ 0\ 1]$, the Christoffel matrix (according to Appendix B) is:

$$\begin{bmatrix} C_{44} & 0 & 0 \\ 0 & C_{44} & 0 \\ 0 & 0 & C_{11} \end{bmatrix} \begin{bmatrix} A_1 \\ A_2 \\ A_3 \end{bmatrix} = \rho\nu^2 \begin{bmatrix} A_1 \\ A_2 \\ A_3 \end{bmatrix}. \tag{A.48}$$

This implies:

$$\rho\nu^2_{S[1\ 0\ 0]} = C_{44} \tag{A.49}$$

$$\rho\nu^2_{S[0\ 1\ 0]} = C_{44} \tag{A.50}$$

$$\rho\nu^2_{P[0\ 0\ 1]} = C_{11} \tag{A.51}$$

For $\overrightarrow{n} = \left[\frac{1}{\sqrt{2}}\ \frac{1}{\sqrt{2}}\ 0\right]$, the Christoffel matrix (according to Appendix B) is:

$$\begin{bmatrix} \frac{1}{2}(C_{11}+C_{44}) & \frac{1}{2}(C_{12}+C_{44}) & 0 \\ \frac{1}{2}(C_{12}+C_{44}) & \frac{1}{2}(C_{11}+C_{44}) & 0 \\ 0 & 0 & C_{44} \end{bmatrix} \begin{bmatrix} A_1 \\ A_2 \\ A_3 \end{bmatrix} = \rho\nu^2 \begin{bmatrix} A_1 \\ A_2 \\ A_3 \end{bmatrix}. \tag{A.52}$$

This implies:

$$\rho\nu^2_{P\left[\frac{1}{\sqrt{2}}\ \frac{1}{\sqrt{2}}\ 0\right]} = C_{44} + \frac{1}{2}C_{11} + \frac{1}{2}C_{12} \tag{A.53}$$

$$\rho\nu^2_{S\left[\frac{1}{\sqrt{2}}\ \frac{-1}{\sqrt{2}}\ 0\right]} = \frac{1}{2}\left(C_{11} - C_{12}\right) \tag{A.54}$$

$$\rho\nu^2_{S[0\ 0\ 1]} = C_{44} \tag{A.55}$$

Equation A.53 can be transformed into the following form:

$$C_{12} = 2\rho\nu^2_{P\left[\frac{1}{\sqrt{2}}\ \frac{1}{\sqrt{2}}\ 0\right]} - 2C_{44} - C_{11}\ . \tag{A.56}$$

A.5 Hexagonal case: 5 elastic constants

The elastic constants for an transversely isotropic solid with a vertical axis of symmetry is:

$$C_{IJ} = \begin{bmatrix} C_{11} & C_{12} & C_{13} & 0 & 0 & 0 \\ & C_{11} & C_{13} & 0 & 0 & 0 \\ & & C_{33} & 0 & 0 & 0 \\ & & & C_{44} & 0 & 0 \\ & & & & C_{44} & 0 \\ & & & & & C_{66} \end{bmatrix} \tag{A.57}$$

where $C_{12} = C_{11} - 2C_{66}$.

For $\vec{n} = [1\ 0\ 0]$, the Christoffel matrix (according to Appendix B) is:

$$\begin{bmatrix} C_{11} & 0 & 0 \\ 0 & C_{66} & 0 \\ 0 & 0 & C_{44} \end{bmatrix} \begin{bmatrix} A_1 \\ A_2 \\ A_3 \end{bmatrix} = \rho\nu^2 \begin{bmatrix} A_1 \\ A_2 \\ A_3 \end{bmatrix}. \tag{A.58}$$

This implies:

$$\rho\nu^2_{P[1\ 0\ 0]} = C_{11} \tag{A.59}$$

$$\rho\nu^2_{S[0\ 1\ 0]} = C_{66} \tag{A.60}$$

$$\rho\nu^2_{S[0\ 0\ 1]} = C_{44} \tag{A.61}$$

For $\overrightarrow{n} = [0\ 1\ 0]$, the Christoffel matrix (according to Appendix B) is:

$$\begin{bmatrix} C_{66} & 0 & 0 \\ 0 & C_{11} & 0 \\ 0 & 0 & C_{44} \end{bmatrix} \begin{bmatrix} A_1 \\ A_2 \\ A_3 \end{bmatrix} = \rho\nu^2 \begin{bmatrix} A_1 \\ A_2 \\ A_3 \end{bmatrix} . \tag{A.62}$$

This implies:

$$\rho\nu^2_{S[1\ 0\ 0]} = C_{66} \tag{A.63}$$

$$\rho\nu^2_{P[0\ 1\ 0]} = C_{11} \tag{A.64}$$

$$\rho\nu^2_{S[0\ 0\ 1]} = C_{44} \tag{A.65}$$

For $\overrightarrow{n} = [0\ 0\ 1]$, the Christoffel matrix (according to Appendix B) is:

$$\begin{bmatrix} C_{44} & 0 & 0 \\ 0 & C_{44} & 0 \\ 0 & 0 & C_{33} \end{bmatrix} \begin{bmatrix} A_1 \\ A_2 \\ A_3 \end{bmatrix} = \rho\nu^2 \begin{bmatrix} A_1 \\ A_2 \\ A_3 \end{bmatrix} . \tag{A.66}$$

This implies:

$$\rho\nu^2_{S[1\ 0\ 0]} = C_{44} \tag{A.67}$$

$$\rho\nu^2_{S[0\ 1\ 0]} = C_{44} \tag{A.68}$$

$$\rho\nu^2_{P[0\ 0\ 1]} = C_{33} \tag{A.69}$$

For $\vec{n} = \left[\frac{1}{\sqrt{2}}\ 0\ \frac{1}{\sqrt{2}}\right]$, the Christoffel matrix (according to Appendix B) is:

$$\begin{bmatrix} \frac{1}{2}(C_{11}+C_{44}) & 0 & \frac{1}{2}(C_{13}+C_{44}) \\ 0 & \frac{1}{2}(C_{44}+C_{66}) & 0 \\ \frac{1}{2}(C_{13}+C_{44}) & 0 & \frac{1}{2}(C_{33}+C_{44}) \end{bmatrix} \begin{bmatrix} A_1 \\ A_2 \\ A_3 \end{bmatrix} = \rho\nu^2 \begin{bmatrix} A_1 \\ A_2 \\ A_3 \end{bmatrix}. \tag{A.70}$$

This implies:

$$\rho\nu^2_{P\left[\approx\frac{1}{\sqrt{2}}\ 0\ \approx\frac{1}{\sqrt{2}}\right]} = \frac{1}{4}(C_{11}+C_{33}+2C_{44}) + \frac{1}{2}\sqrt{\frac{1}{4}(C_{11}-C_{33})^2 + (C_{13}+C_{44})^2} \tag{A.71}$$

$$\rho\nu^2_{S[0\ 1\ 0]} = \frac{1}{2}(C_{44}+C_{66}) \tag{A.72}$$

$$\rho\nu^2_{S\left[\approx\frac{1}{\sqrt{2}}\ 0\ \approx\frac{-1}{\sqrt{2}}\right]} = \frac{1}{4}(C_{11}+C_{33}+2C_{44}) - \frac{1}{2}\sqrt{\frac{1}{4}(C_{11}-C_{33})^2 + (C_{13}+C_{44})^2} \tag{A.73}$$

Equation A.71 can be transformed into the following form:

$$C_{13} = -C_{44} - \sqrt{\left(C_{11}+C_{44}-2\rho\nu^2_{P\left[\approx\frac{1}{\sqrt{2}}\ 0\ \approx\frac{1}{\sqrt{2}}\right]}\right)\left(C_{33}+C_{44}-2\rho\nu^2_{P\left[\approx\frac{1}{\sqrt{2}}\ 0\ \approx\frac{1}{\sqrt{2}}\right]}\right)}. \tag{A.74}$$

N.B. $\approx \frac{1}{\sqrt{2}}$ means that the particle motions are only approximately in this direction due to the particle motions not being exactly parallel or perpendicular to the dirction of propagation.

A.5.1 Proof of hexagonal symmetry is equivalent to transverse isotropy

Hexagonal symmetry is thought to be representative of transverse isotropy where transverse isotropy is when all the properties in a given plane are equivalent. This can be shown by rotating the elastic constants of a hexagonal medium with a vertical axis of symmetry around the $z - axis$. According to Chou & Pagano (1967) the elastic constants of an anisotropic medium can be rotated by the following formula:

$$c'_{mpqr} = a_{mi}a_{pj}a_{qk}a_{rl}c_{ijkl} \ , \tag{A.75}$$

where c'_{mpqr} is the 4^{th} order tensor representing the elastic constants in the new coordinate system, c_{ijkl} is the 4^{th} order tensor representing the elastic constants in the original coordinate system, a_{ij} is the direction cosines of the new coordinate axes with respect to the original coordinate axes. So for an arbitrary rotation θ around the $z - axis$:

$$a_{ij} = \begin{bmatrix} \cos(\theta) & -\sin(\theta) & 0 \\ \sin(\theta) & \cos(\theta) & 0 \\ 0 & 0 & 1 \end{bmatrix} . \tag{A.76}$$

Since Equation A.76 uses the 4^{th} order tensor instead of the 2^{nd} order Voigt notation tensor, one must define the relations in both:

$$C_{11} = C_{22} = c_{1111} = c_{2222} \tag{A.77}$$

$$C_{12} = c_{1122} = c_{2211} = C_{11} - 2C_{66} = c_{1111} - 2c_{1212} \tag{A.78}$$

$$C_{13} = C_{23} = c_{1133} = c_{3311} = c_{2233} = c_{3322} \tag{A.79}$$

$$C_{33} = c_{3333} \tag{A.80}$$

$$\begin{aligned} C_{44} = C_{55} &= c_{2323} = c_{2332} = c_{3223} = c_{3232} \\ &= c_{1313} = c_{1331} = c_{3113} = c_{3131} \end{aligned} \tag{A.81}$$

$$C_{66} = c_{1212} = c_{1221} = c_{2112} = c_{2121} \tag{A.82}$$

According to Equations A.75, A.76, and A.77, C'_{11} after an arbitrary rotation would be:

$$\begin{aligned} C'_{11} = c'_{1111} &= a_{1i}a_{1j}a_{1k}a_{1l}c_{ijkl} \\ &= a_{11}a_{11}a_{11}a_{11}c_{1111} + a_{11}a_{11}a_{11}a_{12}c_{1112} \\ &+ a_{11}a_{11}a_{12}a_{11}c_{1121} + a_{11}a_{11}a_{12}a_{12}c_{1122} \\ &+ a_{11}a_{12}a_{11}a_{11}c_{1211} + a_{11}a_{12}a_{11}a_{12}c_{1212} \\ &+ a_{11}a_{12}a_{12}a_{11}c_{1221} + a_{11}a_{12}a_{12}a_{12}c_{1222} \\ &+ a_{12}a_{11}a_{11}a_{11}c_{2111} + a_{12}a_{11}a_{11}a_{12}c_{2112} \\ &+ a_{12}a_{11}a_{12}a_{11}c_{2121} + a_{12}a_{11}a_{12}a_{12}c_{2122} \\ &+ a_{12}a_{12}a_{11}a_{11}c_{2211} + a_{12}a_{12}a_{11}a_{12}c_{2212} \\ &+ a_{12}a_{12}a_{12}a_{11}c_{2221} + a_{12}a_{12}a_{12}a_{12}c_{2222} \end{aligned} \tag{A.83}$$

With the incorporation of Equations A.77, A.78, and A.82:

$$\begin{aligned} C'_{11} = c'_{1111} &= a_{11}a_{11}a_{11}a_{11}c_{1111} + 2a_{11}a_{11}a_{12}a_{12}c_{1122} \\ &+ 4a_{11}a_{12}a_{11}a_{12}c_{1212} + a_{12}a_{12}a_{12}a_{12}c_{1111} \end{aligned} \tag{A.84}$$

However from Equation A.76, $a_{11} = \cos\theta$ and $a_{12} = -\sin\theta$:

$$\begin{aligned} C'_{11} = c'_{1111} &= \cos^4\theta c_{1111} + 2\cos^2\theta\sin^2\theta c_{1122} \\ &+ 4\cos^2\theta\sin^2\theta c_{1212} + \sin^4\theta c_{1111} \end{aligned} \tag{A.85}$$

From Equation A.78, $c_{1122} = c_{1111} - 2c_{1212}$:

$$\begin{aligned} C'_{11} = c'_{1111} &= \left(\cos^4\theta + 2\cos^2\theta\sin^2\theta + \sin^4\theta\right) c_{1111} \\ &= \left(\cos^2\theta + \sin^2\theta\right)\left(\cos^2\theta + \sin^2\theta\right) c_{1111} \\ &= c_{1111} = C_{11} \end{aligned} \tag{A.86}$$

This proves that after an arbitrary rotation around the $z-axis$ there is no change in the C_{11} elastic constant.

According to Equations A.75, A.76, and A.78, C_{12}' after an arbitrary rotation would be:

$$\begin{aligned}
C_{12}' = c_{1122}' &= a_{1i}a_{1j}a_{2k}a_{2l}c_{ijkl} \\
&= a_{11}a_{11}a_{21}a_{21}c_{1111} + a_{11}a_{11}a_{21}a_{22}c_{1112} \\
&+ a_{11}a_{11}a_{22}a_{21}c_{1121} + a_{11}a_{11}a_{22}a_{22}c_{1122} \\
&+ a_{11}a_{12}a_{21}a_{21}c_{1211} + a_{11}a_{12}a_{21}a_{22}c_{1212} \\
&+ a_{11}a_{12}a_{22}a_{21}c_{1221} + a_{11}a_{12}a_{22}a_{22}c_{1222} \\
&+ a_{12}a_{11}a_{21}a_{21}c_{2111} + a_{12}a_{11}a_{21}a_{22}c_{2112} \\
&+ a_{12}a_{11}a_{22}a_{21}c_{2121} + a_{12}a_{11}a_{22}a_{22}c_{2122} \\
&+ a_{12}a_{12}a_{21}a_{21}c_{2211} + a_{12}a_{12}a_{21}a_{22}c_{2212} \\
&+ a_{12}a_{12}a_{22}a_{21}c_{2221} + a_{12}a_{12}a_{22}a_{22}c_{2222} \qquad \text{(A.87)}
\end{aligned}$$

With the incorporation of Equations A.77, A.78, and A.82:

$$\begin{aligned}
C_{12}' = c_{1122}' &= a_{11}a_{11}a_{21}a_{21}c_{1111} + \left(a_{11}a_{11}a_{22}a_{22} + a_{12}a_{12}a_{21}a_{21}\right)c_{1122} \\
&+ \left(a_{11}a_{12}a_{21}a_{22} + a_{11}a_{12}a_{22}a_{21} + a_{12}a_{11}a_{21}a_{22} + a_{12}a_{11}a_{22}a_{21}\right)c_{1212} \\
&+ a_{12}a_{12}a_{22}a_{22}c_{1111} \\
&= 2\cos^2\theta\sin^2\theta c_{1111} + \left(\cos^4\theta + \sin^4\theta\right)c_{1122} \\
&- 4\cos^2\theta\sin^2\theta c_{1212} \\
&= 2\cos^2\theta\sin^2\theta\left(c_{1111} - 2c_{1212}\right) + \left(\cos^4\theta + \sin^4\theta\right)c_{1122} \qquad \text{(A.88)}
\end{aligned}$$

From Equation A.78, $c_{1122} = c_{1111} - 2c_{1212}$:

$$\begin{aligned}
C_{12}' = c_{1122}' &= \left(\cos^4\theta + 2\cos^2\theta\sin^2\theta + \sin^4\theta\right)c_{1122} \\
&= \left(\cos^2\theta + \sin^2\theta\right)\left(\cos^2\theta + \sin^2\theta\right)c_{1122} \\
&= c_{1122} = C_{12} \qquad \text{(A.89)}
\end{aligned}$$

This proves that after an arbitrary rotation around the $z - axis$ there is no change in the C_{12} elastic constant.

According to Equations A.75, A.76, and A.79, C'_{13} after an arbitrary rotation would be:

$$\begin{aligned} C'_{13} = c'_{1133} &= a_{1i}a_{1j}a_{3k}a_{3l}c_{ijkl} \\ &= a_{11}a_{11}a_{33}a_{33}c_{1133} + a_{11}a_{12}a_{33}a_{33}c_{1233} \\ &+ a_{12}a_{11}a_{33}a_{33}c_{2133} + a_{12}a_{12}a_{33}a_{33}c_{2233} \end{aligned} \tag{A.90}$$

With the incorporation of Equation A.79 and with $c_{1233} = 0$ and $c_{2133} = 0$:

$$\begin{aligned} C'_{13} = c'_{1133} &= a_{11}a_{11}a_{33}a_{33}c_{1133} + a_{12}a_{12}a_{33}a_{33}c_{2233} \\ &= \left(\cos^2\theta + \sin^2\theta\right) c_{1133} \\ &= c_{1133} = C_{13} \end{aligned} \tag{A.91}$$

This proves that after an arbitrary rotation around the $z - axis$ there is no change in the C_{13} elastic constant.

According to Equations A.75, A.76, and A.77, C'_{22} after an arbitrary rotation would be:

$$\begin{aligned} C'_{22} = c'_{2222} &= a_{2i}a_{2j}a_{2k}a_{2l}c_{ijkl} \\ &= a_{21}a_{21}a_{21}a_{21}c_{1111} + a_{21}a_{21}a_{21}a_{22}c_{1112} \\ &+ a_{21}a_{21}a_{22}a_{21}c_{1121} + a_{21}a_{21}a_{22}a_{22}c_{1122} \\ &+ a_{21}a_{22}a_{21}a_{21}c_{1211} + a_{21}a_{22}a_{21}a_{22}c_{1212} \\ &+ a_{21}a_{22}a_{22}a_{21}c_{1221} + a_{21}a_{22}a_{22}a_{22}c_{1222} \\ &+ a_{22}a_{21}a_{21}a_{21}c_{2111} + a_{22}a_{21}a_{21}a_{22}c_{2112} \\ &+ a_{22}a_{21}a_{22}a_{21}c_{2121} + a_{22}a_{21}a_{22}a_{22}c_{2122} \end{aligned}$$

$$\begin{aligned}
&+ \quad a_{22}a_{22}a_{21}a_{21}c_{2211} + a_{22}a_{22}a_{21}a_{22}c_{2212} \\
&+ \quad a_{22}a_{22}a_{22}a_{21}c_{2221} + a_{22}a_{22}a_{22}a_{22}c_{2222} \qquad \text{(A.92)}
\end{aligned}$$

With the incorporation of Equations A.77, A.78, and A.82:

$$\begin{aligned}
C'_{22} = c'_{2222} &= a_{21}a_{21}a_{21}a_{21}c_{1111} + 2a_{21}a_{21}a_{22}a_{22}c_{1122} \\
&+ 4a_{21}a_{22}a_{21}a_{22}c_{1212} + a_{22}a_{22}a_{22}a_{22}c_{1111} \\
&= \sin^4\theta c_{1111} + 2\cos^2\theta\sin^2\theta c_{1122} \\
&+ 4\cos^2\theta\sin^2\theta c_{1212} + \cos^4\theta c_{1111} \qquad \text{(A.93)}
\end{aligned}$$

From Equation A.78, $c_{1122} = c_{1111} - 2c_{1212}$:

$$\begin{aligned}
C'_{22} = c'_{2222} &= \left(\cos^4\theta + 2\cos^2\theta\sin^2\theta + \sin^4\theta\right) c_{1111} \\
&= \left(\cos^2\theta + \sin^2\theta\right)\left(\cos^2\theta + \sin^2\theta\right) c_{1111} \\
&= c_{1111} = C_{11} \qquad \text{(A.94)}
\end{aligned}$$

This proves that after an arbitrary rotation around the $z - axis$ there is no change in the C_{22} elastic constant.

According to Equations A.75, A.76, and A.79, C'_{23} after an arbitrary rotation would be:

$$\begin{aligned}
C'_{23} = c'_{2233} &= a_{2i}a_{2j}a_{3k}a_{3l}c_{ijkl} \\
&= a_{21}a_{21}a_{33}a_{33}c_{1133} + a_{21}a_{22}a_{33}a_{33}c_{1233} \\
&+ a_{22}a_{21}a_{33}a_{33}c_{2133} + a_{22}a_{22}a_{33}a_{33}c_{2233} \qquad \text{(A.95)}
\end{aligned}$$

With the incorporation of Equation A.79 and with $c_{1233} = 0$ and $c_{2133} = 0$:

$$\begin{aligned}
C'_{23} = c'_{2233} &= a_{21}a_{21}a_{33}a_{33}c_{1133} + a_{22}a_{22}a_{33}a_{33}c_{2233} \\
&= \left(\cos^2\theta + \sin^2\theta\right) c_{1133} \\
&= c_{1133} = C_{13} \qquad \text{(A.96)}
\end{aligned}$$

This proves that after an arbitrary rotation around the $z - axis$ there is no change in the C_{23} elastic constant.

According to Equations A.75, A.76, and A.79, C'_{33} after an arbitrary rotation would be:

$$\begin{aligned} C'_{33} = c'_{3333} &= a_{3i}a_{3j}a_{3l}a_{3k}c_{ijkl} \\ &= a_{33}a_{33}a_{33}a_{33}c_{3333} \\ &= c_{3333} = C_{33} \end{aligned} \tag{A.97}$$

This proves that after an arbitrary rotation around the $z - axis$ there is no change in the C_{33} elastic constant.

According to Equations A.75, A.76, and A.81, C'_{44} after an arbitrary rotation would be:

$$\begin{aligned} C'_{44} = c'_{2323} &= a_{2i}a_{3j}a_{2k}a_{3l}c_{ijkl} \\ &= a_{21}a_{33}a_{21}a_{33}c_{1313} + a_{21}a_{33}a_{22}a_{33}c_{1323} \\ &+ a_{22}a_{33}a_{21}a_{33}c_{2313} + a_{22}a_{33}a_{22}a_{33}c_{2323} \end{aligned} \tag{A.98}$$

With the incorporation of Equation A.81 and with $c_{1323} = 0$ and $c_{2313} = 0$:

$$\begin{aligned} C'_{44} = c'_{2323} &= (a_{21}a_{21} + a_{22}a_{22})\, a_{33}a_{33}c_{2323} \\ &= \left(\cos^2\theta + \sin^2\theta\right) c_{2323} \\ &= c_{2323} = C_{44} \end{aligned} \tag{A.99}$$

This proves that after an arbitrary rotation around the $z - axis$ there is no change in the C_{44} elastic constant.

According to Equations A.75, A.76, and A.81, C'_{55} after an arbitrary rotation would be:

$$\begin{aligned} C'_{55} = c'_{1313} &= a_{1i}a_{3j}a_{1k}a_{3l}c_{ijkl} \\ &= a_{11}a_{33}a_{11}a_{33}c_{1313} + a_{11}a_{33}a_{12}a_{33}c_{1323} \\ &+ a_{12}a_{33}a_{11}a_{33}c_{2313} + a_{12}a_{33}a_{12}a_{33}c_{2323} \end{aligned} \tag{A.100}$$

With the incorporation of Equation A.81 and with $c_{1323} = 0$ and $c_{2313} = 0$:

$$\begin{aligned} C'_{55} = c'_{1313} &= (a_{11}a_{11} + a_{12}a_{12})\, a_{33}a_{33}c_{2323} \\ &= \left(\cos^2\theta + \sin^2\theta\right) c_{2323} \\ &= c_{2323} = C_{44} \end{aligned} \tag{A.101}$$

This proves that after an arbitrary rotation around the $z - axis$ there is no change in the C_{55} elastic constant.

According to Equations A.75, A.76, and A.82, C'_{66} after an arbitrary rotation would be:

$$\begin{aligned} C'_{66} = c'_{1212} &= a_{1i}a_{2j}a_{1k}a_{2l}c_{ijkl} \\ &= a_{11}a_{21}a_{11}a_{21}c_{1111} + a_{11}a_{21}a_{11}a_{22}c_{1112} \\ &+ a_{11}a_{21}a_{12}a_{21}c_{1121} + a_{11}a_{21}a_{12}a_{22}c_{1122} \\ &+ a_{11}a_{22}a_{11}a_{21}c_{1211} + a_{11}a_{22}a_{11}a_{22}c_{1212} \\ &+ a_{11}a_{22}a_{12}a_{21}c_{1221} + a_{11}a_{22}a_{12}a_{22}c_{1222} \\ &+ a_{12}a_{21}a_{11}a_{21}c_{2111} + a_{12}a_{21}a_{11}a_{22}c_{2112} \\ &+ a_{12}a_{21}a_{12}a_{21}c_{2121} + a_{12}a_{21}a_{12}a_{22}c_{2122} \\ &+ a_{12}a_{22}a_{11}a_{21}c_{2211} + a_{12}a_{22}a_{11}a_{22}c_{2212} \\ &+ a_{12}a_{22}a_{12}a_{21}c_{2221} + a_{12}a_{22}a_{12}a_{22}c_{2222} \end{aligned} \tag{A.102}$$

With the incorporation of Equations A.77, A.78, and A.82:

$$\begin{aligned} C'_{66} = c'_{1212} &= (a_{11}a_{21}a_{11}a_{21} + a_{12}a_{22}a_{12}a_{22})\, c_{1111} \\ &+ (a_{11}a_{21}a_{12}a_{22} + a_{12}a_{22}a_{11}a_{21})\, c_{1122} \\ &+ (a_{11}a_{22}a_{11}a_{22} + a_{11}a_{22}a_{12}a_{21} + a_{12}a_{21}a_{11}a_{22} + a_{12}a_{21}a_{12}a_{21})\, c_{1212} \\ &= 2\cos^2\theta \sin^2\theta c_{1111} - 2\cos^2\theta\sin^2\theta c_{1122} \\ &+ \left(\cos^4\theta - 2\cos^2\theta\sin^2\theta + \sin^4\theta\right) c_{1212} \qquad \text{(A.103)} \end{aligned}$$

From Equation A.78:

$$\begin{aligned} C'_{66} = c'_{1212} &= \left(\cos^4\theta + 2\cos^2\theta\sin^2\theta + \sin^4\theta\right) c_{1212} \\ &= \left(\cos^2\theta + \sin^2\theta\right)\left(\cos^2\theta + \sin^2\theta\right) c_{1212} \\ &= c_{1212} = C_{66} \qquad \text{(A.104)} \end{aligned}$$

This proves that after an arbitrary rotation around the $z - axis$ there is no change in the C_{66} elastic constant.

According to Equations A.75 and A.76, C'_{14} after an arbitrary rotation would be:

$$\begin{aligned} C'_{14} = c'_{1123} &= a_{1i}a_{1j}a_{2k}a_{3l}c_{ijkl} \\ &= 0 \textit{ by inspection} \qquad \text{(A.105)} \end{aligned}$$

This proves that after an arbitrary rotation around the $z - axis$ there is no change in the C_{14} elastic constant.

According to Equations A.75 and A.76, C'_{15} after an arbitrary rotation would be:

$$\begin{aligned} C'_{15} = c'_{1113} &= a_{1i}a_{1j}a_{1k}a_{3l}c_{ijkl} \\ &= 0 \textit{ by inspection} \qquad \text{(A.106)} \end{aligned}$$

This proves that after an arbitrary rotation around the $z-axis$ there is no change in the C_{15} elastic constant.

According to Equations A.75 and A.76, C'_{16} after an arbitrary rotation would be:

$$\begin{aligned}
C'_{16} = c'_{1112} &= a_{1i}a_{1j}a_{1k}a_{2l}c_{ijkl} \\
&= a_{11}a_{11}a_{11}a_{21}c_{1111} + a_{11}a_{11}a_{11}a_{22}c_{1112} \\
&+ a_{11}a_{11}a_{12}a_{21}c_{1121} + a_{11}a_{11}a_{12}a_{22}c_{1122} \\
&+ a_{11}a_{12}a_{11}a_{21}c_{1211} + a_{11}a_{12}a_{11}a_{22}c_{1212} \\
&+ a_{11}a_{12}a_{12}a_{21}c_{1221} + a_{11}a_{12}a_{12}a_{22}c_{1222} \\
&+ a_{12}a_{11}a_{11}a_{21}c_{2111} + a_{12}a_{11}a_{11}a_{22}c_{2112} \\
&+ a_{12}a_{11}a_{12}a_{21}c_{2121} + a_{12}a_{11}a_{12}a_{22}c_{2122} \\
&+ a_{12}a_{12}a_{11}a_{21}c_{2211} + a_{12}a_{12}a_{11}a_{22}c_{2212} \\
&+ a_{12}a_{12}a_{12}a_{21}c_{2221} + a_{12}a_{12}a_{12}a_{22}c_{2222} \qquad (A.107)
\end{aligned}$$

With the incorporation of Equations A.77, A.78, and A.82:

$$\begin{aligned}
C'_{16} = c'_{1112} &= \left(a_{11}a_{11}a_{11}a_{21} + a_{12}a_{12}a_{12}a_{22}\right)c_{1111} \\
&+ \left(a_{11}a_{11}a_{12}a_{22} + a_{12}a_{12}a_{11}a_{21}\right)c_{1122} \\
&+ \left(a_{11}a_{12}a_{11}a_{22} + a_{11}a_{12}a_{12}a_{21} + a_{12}a_{11}a_{11}a_{22} + a_{12}a_{11}a_{12}a_{21}\right)c_{1212} \\
&= \left(\cos^3\theta\sin\theta - \cos\theta\sin^3\theta\right)c_{1111} \\
&- \left(\cos^3\theta\sin\theta - \cos\theta\sin^3\theta\right)c_{1122} \\
&- 2\left(\cos^3\theta\sin\theta - \cos\theta\sin^3\theta\right)c_{1212} \\
&= \left(\cos^3\theta\sin\theta - \cos\theta\sin^3\theta\right)\left(c_{1111} - c_{1122} - 2c_{1212}\right) \qquad (A.108)
\end{aligned}$$

From Equation A.78, $c_{1122} = c_{1111} - 2c_{1212}$:

$$C'_{16} = c'_{1112} = 0 \qquad (A.109)$$

This proves that after an arbitrary rotation around the $z - axis$ there is no change in the C_{16} elastic constant.

According to Equations A.75 and A.76, C_{24}' after an arbitrary rotation would be:

$$\begin{aligned} C_{24}' = c_{2223}' &= a_{2i}a_{2j}a_{2k}a_{3l}c_{ijkl} \\ &= 0 \; by \; inspection \end{aligned} \tag{A.110}$$

This proves that after an arbitrary rotation around the $z - axis$ there is no change in the C_{24} elastic constant.

According to Equations A.75 and A.76, C_{25}' after an arbitrary rotation would be:

$$\begin{aligned} C_{25}' = c_{2213}' &= a_{2i}a_{2j}a_{1k}a_{3l}c_{ijkl} \\ &= 0 \; by \; inspection \end{aligned} \tag{A.111}$$

This proves that after an arbitrary rotation around the $z - axis$ there is no change in the C_{25} elastic constant.

According to Equations A.75 and A.76, C_{26}' after an arbitrary rotation would be:

$$\begin{aligned} C_{26}' = c_{2212}' &= a_{2i}a_{2j}a_{1k}a_{2l}c_{ijkl} \\ &= a_{21}a_{21}a_{11}a_{21}c_{1111} + a_{21}a_{21}a_{11}a_{22}c_{1112} \\ &+ a_{21}a_{21}a_{12}a_{21}c_{1121} + a_{21}a_{21}a_{12}a_{22}c_{1122} \\ &+ a_{21}a_{22}a_{11}a_{21}c_{1211} + a_{21}a_{22}a_{11}a_{22}c_{1212} \\ &+ a_{21}a_{22}a_{12}a_{21}c_{1221} + a_{21}a_{22}a_{12}a_{22}c_{1222} \\ &+ a_{22}a_{21}a_{11}a_{21}c_{2111} + a_{22}a_{21}a_{11}a_{22}c_{2112} \end{aligned}$$

$$\begin{aligned}
&+ a_{22}a_{21}a_{12}a_{21}c_{2121} + a_{22}a_{21}a_{12}a_{22}c_{2122} \\
&+ a_{22}a_{22}a_{11}a_{21}c_{2211} + a_{22}a_{22}a_{11}a_{22}c_{2212} \\
&+ a_{22}a_{22}a_{12}a_{21}c_{2221} + a_{22}a_{22}a_{12}a_{22}c_{2222} \qquad \text{(A.112)}
\end{aligned}$$

With the incorporation of Equations A.77, A.78, and A.82:

$$\begin{aligned}
C'_{26} = c'_{2212} &= \left(a_{21}a_{21}a_{11}a_{21} + a_{22}a_{22}a_{12}a_{22}\right) c_{1111} \\
&+ \left(a_{21}a_{21}a_{12}a_{22} + a_{22}a_{22}a_{11}a_{21}\right) c_{1122} \\
&+ \left(a_{21}a_{22}a_{11}a_{22} + a_{21}a_{22}a_{12}a_{21} + a_{22}a_{21}a_{11}a_{22} + a_{22}a_{21}a_{12}a_{21}\right) c_{1212} \\
&= \left(-\cos^3\theta \sin\theta + \cos\theta \sin^3\theta\right) c_{1111} \\
&+ \left(\cos^3\theta \sin\theta - \cos\theta \sin^3\theta\right) c_{1122} \\
&+ 2\left(\cos^3\theta \sin\theta - \cos\theta \sin^3\theta\right) c_{1212} \\
&= \left(-\cos^3\theta \sin\theta + \cos\theta \sin^3\theta\right)\left(c_{1111} - c_{1122} - 2c_{1212}\right) \qquad \text{(A.113)}
\end{aligned}$$

From Equation A.78, $c_{1122} = c_{1111} - 2c_{1212}$:

$$C'_{26} = c'_{2212} = 0 \qquad \text{(A.114)}$$

This proves that after an arbitrary rotation around the $z - axis$ there is no change in the C_{26} elastic constant.

According to Equations A.75 and A.76, C'_{34} after an arbitrary rotation would be:

$$\begin{aligned}
C'_{34} = c'_{3323} &= a_{3i}a_{3j}a_{2k}a_{3l}c_{ijkl} \\
&= 0 \; \textit{by inspection} \qquad \text{(A.115)}
\end{aligned}$$

This proves that after an arbitrary rotation around the $z - axis$ there is no change in the C_{34} elastic constant.

According to Equations A.75 and A.76, C'_{35} after an arbitrary rotation would be:

$$\begin{aligned} C'_{35} = c'_{3313} &= a_{3i}a_{3j}a_{1k}a_{3l}c_{ijkl} \\ &= 0 \textit{ by inspection} \end{aligned} \tag{A.116}$$

This proves that after an arbitrary rotation around the $z - axis$ there is no change in the C_{35} elastic constant.

According to Equations A.75 and A.76, C'_{36} after an arbitrary rotation would be:

$$\begin{aligned} C'_{36} = c'_{3312} &= a_{3i}a_{3j}a_{1k}a_{2l}c_{ijkl} \\ &= a_{33}a_{33}a_{11}a_{21}c_{3311} + a_{33}a_{33}a_{11}a_{22}c_{3312} \\ &+ a_{33}a_{33}a_{12}a_{21}c_{3321} + a_{33}a_{33}a_{12}a_{22}c_{3322} \end{aligned} \tag{A.117}$$

With the incorporation of Equation A.79, and with $c_{3312} = 0$ and $c_{3321} = 0$:

$$\begin{aligned} C'_{36} = c'_{3312} &= (a_{33}a_{33}a_{11}a_{21} + a_{33}a_{33}a_{12}a_{22})\, c_{1133} \\ &= (\cos\theta \sin\theta - \cos\theta \sin\theta)\, c_{1133} \\ &= 0 \end{aligned} \tag{A.118}$$

This proves that after an arbitrary rotation around the $z - axis$ there is no change in the C_{36} elastic constant.

According to Equations A.75 and A.76, C'_{45} after an arbitrary rotation would be:

$$\begin{aligned} C'_{45} = c'_{2313} &= a_{2i}a_{3j}a_{1k}a_{3l}c_{ijkl} \\ &= a_{21}a_{33}a_{11}a_{33}c_{1313} + a_{21}a_{33}a_{12}a_{33}c_{1323} \\ &+ a_{22}a_{33}a_{11}a_{33}c_{2313} + a_{22}a_{33}a_{12}a_{33}c_{2323} \end{aligned} \tag{A.119}$$

With the incorporation of Equation A.81, and with $c_{1323} = 0$ and $c_{2313} = 0$:

$$\begin{aligned} C'_{45} = c'_{2313} &= \left(a_{21}a_{33}a_{11}a_{33} + a_{22}a_{33}a_{12}a_{33}\right) c_{1313} \\ &= \left(\cos^3\theta \sin\theta - \cos^3\theta \sin\theta\right) c_{1313} \\ &= 0 \end{aligned} \tag{A.120}$$

This proves that after an arbitrary rotation around the $z - axis$ there is no change in the C_{45} elastic constant.

According to Equations A.75 and A.76, C'_{46} after an arbitrary rotation would be:

$$\begin{aligned} C'_{46} = c'_{2312} &= a_{2i}a_{3j}a_{1k}a_{2l}c_{ijkl} \\ &= 0 \; by \; inspection \end{aligned} \tag{A.121}$$

This proves that after an arbitrary rotation around the $z - axis$ there is no change in the C_{46} elastic constant.

According to Equations A.75 and A.76, C'_{56} after an arbitrary rotation would be:

$$\begin{aligned} C'_{56} = c'_{1312} &= a_{1i}a_{3j}a_{1k}a_{2l}c_{ijkl} \\ &= 0 \; by \; inspection \end{aligned} \tag{A.122}$$

This proves that after an arbitrary rotation around the $z - axis$ there is no change in the C_{56} elastic constant.

In conclusion, from Equations A.86, A.89, A.91, A.94, A.96, A.97, A.99, A.101, A.104, A.105, A.106, A.109, A.110, A.111, A.114, A.115, A.116, A.118, A.120, A.121, and A.122, one can see that after an arbitrary rotation about the $z - axis$ there is no change in the elastic constants of the hexagonal medium. This implies that hexagonal symmetry is equivalent to transverse isotropy with a vertical axis of symmetry.

A.6 Orthorhombic case: 9 elastic constants

The elastic constants for an orthorhombic solid is:

$$C_{IJ} = \begin{bmatrix} C_{11} & C_{12} & C_{13} & 0 & 0 & 0 \\ & C_{22} & C_{23} & 0 & 0 & 0 \\ & & C_{33} & 0 & 0 & 0 \\ & & & C_{44} & 0 & 0 \\ & & & & C_{55} & 0 \\ & & & & & C_{66} \end{bmatrix}. \tag{A.123}$$

For $\vec{n} = [1\ 0\ 0]$, the Christoffel matrix (according to Appendix B) is:

$$\begin{bmatrix} C_{11} & 0 & 0 \\ 0 & C_{66} & 0 \\ 0 & 0 & C_{55} \end{bmatrix} \begin{bmatrix} A_1 \\ A_2 \\ A_3 \end{bmatrix} = \rho\nu^2 \begin{bmatrix} A_1 \\ A_2 \\ A_3 \end{bmatrix}. \tag{A.124}$$

This implies:

$$\rho\nu^2_{P[1\ 0\ 0]} = C_{11} \tag{A.125}$$

$$\rho\nu^2_{S[0\ 1\ 0]} = C_{66} \tag{A.126}$$

$$\rho\nu^2_{S[0\ 0\ 1]} = C_{55} \tag{A.127}$$

For $\vec{n} = [0\ 1\ 0]$, the Christoffel matrix (according to Appendix B) is:

$$\begin{bmatrix} C_{66} & 0 & 0 \\ 0 & C_{22} & 0 \\ 0 & 0 & C_{44} \end{bmatrix} \begin{bmatrix} A_1 \\ A_2 \\ A_3 \end{bmatrix} = \rho\nu^2 \begin{bmatrix} A_1 \\ A_2 \\ A_3 \end{bmatrix}. \tag{A.128}$$

This implies:

$$\rho\nu^2_{S[1\ 0\ 0]} = C_{66} \tag{A.129}$$

$$\rho\nu^2_{P[0\ 1\ 0]} = C_{22} \tag{A.130}$$

$$\rho\nu^2_{S[0\ 0\ 1]} = C_{44} \tag{A.131}$$

For $\overrightarrow{n} = [0\ 0\ 1]$, the Christoffel matrix (according to Appendix B) is:

$$\begin{bmatrix} C_{55} & 0 & 0 \\ 0 & C_{44} & 0 \\ 0 & 0 & C_{33} \end{bmatrix} \begin{bmatrix} A_1 \\ A_2 \\ A_3 \end{bmatrix} = \rho\nu^2 \begin{bmatrix} A_1 \\ A_2 \\ A_3 \end{bmatrix}. \tag{A.132}$$

This implies:

$$\rho\nu^2_{S[1\ 0\ 0]} = C_{55} \tag{A.133}$$

$$\rho\nu^2_{S[0\ 1\ 0]} = C_{44} \tag{A.134}$$

$$\rho\nu^2_{P[0\ 0\ 1]} = C_{33} \tag{A.135}$$

For $\overrightarrow{n} = \left[\frac{1}{\sqrt{2}}\ \frac{1}{\sqrt{2}}\ 0\right]$, the Christoffel matrix (according to Appendix B) is:

$$\begin{bmatrix} \frac{1}{2}(C_{11}+C_{66}) & \frac{1}{2}(C_{12}+C_{66}) & 0 \\ \frac{1}{2}(C_{12}+C_{66}) & \frac{1}{2}(C_{22}+C_{66}) & 0 \\ 0 & 0 & \frac{1}{2}(C_{44}+C_{55}) \end{bmatrix} \begin{bmatrix} A_1 \\ A_2 \\ A_3 \end{bmatrix} = \rho\nu^2 \begin{bmatrix} A_1 \\ A_2 \\ A_3 \end{bmatrix}. \tag{A.136}$$

This implies:

$$\rho\nu^2_{P\left[\approx\frac{1}{\sqrt{2}}\ \approx\frac{1}{\sqrt{2}}\ 0\right]} = \frac{1}{4}\left(C_{11}+C_{22}+2C_{66}\right)+\frac{1}{2}\sqrt{\frac{1}{4}\left(C_{11}-C_{22}\right)^2+\left(C_{12}+C_{66}\right)^2} \tag{A.137}$$

$$\rho\nu^2_{S\left[\approx\frac{1}{\sqrt{2}}\ \approx\frac{-1}{\sqrt{2}}\ 0\right]} = \frac{1}{4}\left(C_{11}+C_{22}+2C_{66}\right)-\frac{1}{2}\sqrt{\frac{1}{4}\left(C_{11}-C_{22}\right)^2+\left(C_{12}+C_{66}\right)^2} \tag{A.138}$$

$$\rho\nu^2_{S[0\ 0\ 1]} = \frac{1}{2}\left(C_{44}+C_{55}\right) \tag{A.139}$$

Equation A.137 can be transformed into the following form:

$$C_{12} = -C_{66}-\sqrt{\left(C_{11}+C_{66}-2\rho\nu^2_{P\left[\approx\frac{1}{\sqrt{2}}\ \approx\frac{1}{\sqrt{2}}\ 0\right]}\right)\left(C_{22}+C_{66}-2\rho\nu^2_{P\left[\approx\frac{1}{\sqrt{2}}\ \approx\frac{1}{\sqrt{2}}\ 0\right]}\right)}. \tag{A.140}$$

The corresponding error in Equation A.140 is:

$$\begin{aligned}\delta C_{12} \;=\;& \delta C_{66}+\frac{1}{2}\left(\delta C_{66}+\delta C_{11}+2\delta\left(\rho\nu^2_{P[\approx\frac{1}{\sqrt{2}}\ \approx\frac{1}{\sqrt{2}}\ 0\ ]}\right)\right)\Bigg(C_{11}+C_{66}\\ &-2\rho\nu^2_{P[\approx\frac{1}{\sqrt{2}}\ \approx\frac{1}{\sqrt{2}}\ 0\ ]}\Bigg)^{-1/2}\left(C_{22}+C_{66}-2\rho\nu^2_{P[\approx\frac{1}{\sqrt{2}}\ \approx\frac{1}{\sqrt{2}}\ 0\ ]}\right)^{1/2}\\ &+\frac{1}{2}\left(\delta C_{66}+\delta C_{22}+2\delta\left(\rho\nu^2_{P[\approx\frac{1}{\sqrt{2}}\ \approx\frac{1}{\sqrt{2}}\ 0\ ]}\right)\right)\Bigg(C_{11}+C_{66}\\ &-2\rho\nu^2_{P[\approx\frac{1}{\sqrt{2}}\ \approx\frac{1}{\sqrt{2}}\ 0\ ]}\Bigg)^{1/2}\left(C_{22}+C_{66}-2\rho\nu^2_{P[\approx\frac{1}{\sqrt{2}}\ \approx\frac{1}{\sqrt{2}}\ 0\ ]}\right)^{-1/2}\end{aligned} \tag{A.141}$$

For $\vec{n} = \left[\frac{1}{\sqrt{2}}\ 0\ \frac{1}{\sqrt{2}}\right]$, the Christoffel matrix (according to Appendix B) is:

$$\begin{bmatrix}\frac{1}{2}\left(C_{11}+C_{55}\right) & 0 & \frac{1}{2}\left(C_{13}+C_{55}\right)\\ 0 & \frac{1}{2}\left(C_{44}+C_{66}\right) & 0\\ \frac{1}{2}\left(C_{13}+C_{55}\right) & 0 & \frac{1}{2}\left(C_{33}+C_{55}\right)\end{bmatrix}\begin{bmatrix}A_1\\ A_2\\ A_3\end{bmatrix} = \rho\nu^2\begin{bmatrix}A_1\\ A_2\\ A_3\end{bmatrix}. \tag{A.142}$$

This implies:

$$\rho\nu^2_{P\left[\approx\frac{1}{\sqrt{2}}\ 0\ \approx\frac{1}{\sqrt{2}}\right]} = \frac{1}{4}\left(C_{11} + C_{33} + 2C_{55}\right) + \frac{1}{2}\sqrt{\frac{1}{4}\left(C_{11} - C_{33}\right)^2 + \left(C_{13} + C_{55}\right)^2} \tag{A.143}$$

$$\rho\nu^2_{S[0\ 1\ 0]} = \frac{1}{2}\left(C_{44} + C_{66}\right) \tag{A.144}$$

$$\rho\nu^2_{S\left[\approx\frac{1}{\sqrt{2}}\ 0\ \approx\frac{-1}{\sqrt{2}}\right]} = \frac{1}{4}\left(C_{11} + C_{33} + 2C_{55}\right) - \frac{1}{2}\sqrt{\frac{1}{4}\left(C_{11} - C_{33}\right)^2 + \left(C_{13} + C_{55}\right)^2} \tag{A.145}$$

Equation A.143 can be transformed into the following form:

$$C_{13} = -C_{55} - \sqrt{\left(C_{11} + C_{55} - 2\rho\nu^2_{P\left[\approx\frac{1}{\sqrt{2}}\ 0\ \approx\frac{1}{\sqrt{2}}\right]}\right)\left(C_{33} + C_{55} - 2\rho\nu^2_{P\left[\approx\frac{1}{\sqrt{2}}\ 0\ \approx\frac{1}{\sqrt{2}}\right]}\right)}. \tag{A.146}$$

The corresponding error in Equation A.146 is:

$$\begin{aligned}\delta C_{13} \;=\;& \delta C_{55} + \frac{1}{2}\left(\delta C_{55} + \delta C_{11} + 2\delta\left(\rho\nu^2_{P\left[\approx\frac{1}{\sqrt{2}}\ 0\ \approx\frac{1}{\sqrt{2}}\right]}\right)\right)\Bigg(C_{11} + C_{55} \\ & -2\rho\nu^2_{P\left[\approx\frac{1}{\sqrt{2}}\ 0\ \approx\frac{1}{\sqrt{2}}\right]}\Bigg)^{-1/2}\left(C_{33} + C_{55} - 2\rho\nu^2_{P\left[\approx\frac{1}{\sqrt{2}}\ 0\ \approx\frac{1}{\sqrt{2}}\right]}\right)^{1/2} \\ & +\frac{1}{2}\left(\delta C_{55} + \delta C_{33} + 2\delta\left(\rho\nu^2_{P\left[\approx\frac{1}{\sqrt{2}}\ 0\ \approx\frac{1}{\sqrt{2}}\right]}\right)\right)\Bigg(C_{11} + C_{55} \\ & -2\rho\nu^2_{P\left[\approx\frac{1}{\sqrt{2}}\ 0\ \approx\frac{1}{\sqrt{2}}\right]}\Bigg)^{1/2}\left(C_{33} + C_{55} - 2\rho\nu^2_{P\left[\approx\frac{1}{\sqrt{2}}\ 0\ \approx\frac{1}{\sqrt{2}}\right]}\right)^{-1/2}\end{aligned} \tag{A.147}$$

For $\vec{n} = \left[0\ \frac{1}{\sqrt{2}}\ \frac{1}{\sqrt{2}}\right]$, the Christoffel matrix (according to Appendix B) is:

$$\begin{bmatrix} \frac{1}{2}\left(C_{55} + C_{66}\right) & 0 & 0 \\ 0 & \frac{1}{2}\left(C_{22} + C_{44}\right) & \frac{1}{2}\left(C_{23} + C_{44}\right) \\ 0 & \frac{1}{2}\left(C_{23} + C_{44}\right) & \frac{1}{2}\left(C_{33} + C_{44}\right) \end{bmatrix}\begin{bmatrix} A_1 \\ A_2 \\ A_3 \end{bmatrix} = \rho\nu^2\begin{bmatrix} A_1 \\ A_2 \\ A_3 \end{bmatrix}. \tag{A.148}$$

This implies:

$$\rho\nu^2_{S[1\ 0\ 0]} = \frac{1}{2}\left(C_{55} + C_{66}\right) \tag{A.149}$$

$$\rho\nu^2_{P\left[0\ \approx\frac{1}{\sqrt{2}}\ \approx\frac{1}{\sqrt{2}}\right]} = \frac{1}{4}\left(C_{22} + C_{33} + 2C_{44}\right) + \frac{1}{2}\sqrt{\frac{1}{4}\left(C_{22} - C_{33}\right)^2 + \left(C_{23} + C_{44}\right)^2} \tag{A.150}$$

$$\rho\nu^2_{S\left[0\ \approx\frac{1}{\sqrt{2}}\ \approx\frac{-1}{\sqrt{2}}\right]} = \frac{1}{4}\left(C_{22} + C_{33} + 2C_{44}\right) - \frac{1}{2}\sqrt{\frac{1}{4}\left(C_{22} - C_{33}\right)^2 + \left(C_{23} + C_{44}\right)^2} \tag{A.151}$$

Equation A.150 can be transformed into the following form:

$$C_{23} = -C_{44} - \sqrt{\left(C_{22} + C_{44} - 2\rho\nu^2_{P\left[0\ \approx\frac{1}{\sqrt{2}}\ \approx\frac{1}{\sqrt{2}}\right]}\right)\left(C_{33} + C_{44} - 2\rho\nu^2_{P\left[0\ \approx\frac{1}{\sqrt{2}}\ \approx\frac{1}{\sqrt{2}}\right]}\right)}. \tag{A.152}$$

The corresponding error in Equation A.152 is:

$$\begin{aligned}
\delta C_{23} \;=\;& \delta C_{44} + \frac{1}{2}\left(\delta C_{44} + \delta C_{22} + 2\delta\left(\rho\nu^2_{P[0\ \approx\frac{1}{\sqrt{2}}\ \approx\frac{1}{\sqrt{2}}]}\right)\right)\Bigg(C_{22} + C_{44} \\
& -2\rho\nu^2_{P[0\ \approx\frac{1}{\sqrt{2}}\ \approx\frac{1}{\sqrt{2}}]}\Bigg)^{-1/2}\left(C_{33} + C_{44} - 2\rho\nu^2_{P[0\ \approx\frac{1}{\sqrt{2}}\ \approx\frac{1}{\sqrt{2}}]}\right)^{1/2} \\
& +\frac{1}{2}\left(\delta C_{44} + \delta C_{33} + 2\delta\left(\rho\nu^2_{P[0\ \approx\frac{1}{\sqrt{2}}\ \approx\frac{1}{\sqrt{2}}]}\right)\right)\Bigg(C_{22} + C_{44} \\
& -2\rho\nu^2_{P[0\ \approx\frac{1}{\sqrt{2}}\ \approx\frac{1}{\sqrt{2}}]}\Bigg)^{1/2}\left(C_{33} + C_{44} - 2\rho\nu^2_{P[0\ \approx\frac{1}{\sqrt{2}}\ \approx\frac{1}{\sqrt{2}}]}\right)^{-1/2}
\end{aligned} \tag{A.153}$$

A.7 Monoclinic case: 13 elastic constants

The elastic constants for a monoclinic solid is:

$$C_{IJ} = \begin{bmatrix} C_{11} & C_{12} & C_{13} & 0 & C_{15} & 0 \\ & C_{22} & C_{23} & 0 & C_{25} & 0 \\ & & C_{33} & 0 & C_{35} & 0 \\ & & & C_{44} & 0 & C_{46} \\ & & & & C_{55} & 0 \\ & & & & & C_{66} \end{bmatrix} . \tag{A.154}$$

For $\overrightarrow{n} = [1\ 0\ 0]$, the Christoffel matrix (according to Appendix B) is:

$$\begin{bmatrix} C_{11} & 0 & C_{15} \\ 0 & C_{66} & 0 \\ C_{15} & 0 & C_{55} \end{bmatrix} \begin{bmatrix} A_1 \\ A_2 \\ A_3 \end{bmatrix} = \rho\nu^2 \begin{bmatrix} A_1 \\ A_2 \\ A_3 \end{bmatrix} . \tag{A.155}$$

This implies:

$$\rho\nu^2_{P[\approx 1\ 0\ 0]} = \frac{1}{2}\left(C_{11} + C_{55}\right) + \sqrt{\frac{1}{4}\left(C_{11} - C_{55}\right)^2 + C_{15}} \tag{A.156}$$

$$\rho\nu^2_{S[0\ 1\ 0]} = C_{66} \tag{A.157}$$

$$\rho\nu^2_{S[0\ 0\ \approx 1]} = \frac{1}{2}\left(C_{11} + C_{55}\right) - \sqrt{\frac{1}{4}\left(C_{11} - C_{55}\right)^2 + C_{15}} \tag{A.158}$$

For $\overrightarrow{n} = [0\ 1\ 0]$, the Christoffel matrix (according to Appendix B) is:

$$\begin{bmatrix} C_{66} & 0 & C_{46} \\ 0 & C_{22} & 0 \\ C_{46} & 0 & C_{44} \end{bmatrix} \begin{bmatrix} A_1 \\ A_2 \\ A_3 \end{bmatrix} = \rho\nu^2 \begin{bmatrix} A_1 \\ A_2 \\ A_3 \end{bmatrix} . \tag{A.159}$$

This implies:

$$\rho\nu^2_{S[\approx 1\ 0\ 0]} = \frac{1}{2}\left(C_{44} + C_{66}\right) - \sqrt{\frac{1}{4}\left(C_{44} - C_{66}\right)^2 + C_{46}} \tag{A.160}$$

$$\rho\nu^2_{P[0\ 1\ 0]} = C_{22} \tag{A.161}$$

$$\rho\nu^2_{S[0\ 0\ \approx 1]} = \frac{1}{2}\left(C_{44} + C_{66}\right) + \sqrt{\frac{1}{4}\left(C_{44} - C_{66}\right)^2 + C_{46}} \tag{A.162}$$

For $\vec{n} = [0\ 0\ 1]$, the Christoffel matrix (according to Appendix B) is:

$$\begin{bmatrix} C_{55} & 0 & C_{35} \\ 0 & C_{44} & 0 \\ C_{35} & 0 & C_{33} \end{bmatrix} \begin{bmatrix} A_1 \\ A_2 \\ A_3 \end{bmatrix} = \rho\nu^2 \begin{bmatrix} A_1 \\ A_2 \\ A_3 \end{bmatrix} . \tag{A.163}$$

This implies:

$$\rho\nu^2_{S[\approx 1\ 0\ 0]} = \frac{1}{2}\left(C_{33} + C_{55}\right) - \sqrt{\frac{1}{4}\left(C_{33} - C_{55}\right)^2 + C_{35}} \tag{A.164}$$

$$\rho\nu^2_{S[0\ 1\ 0]} = C_{44} \tag{A.165}$$

$$\rho\nu^2_{P[0\ 0\ \approx 1]} = \frac{1}{2}\left(C_{33} + C_{55}\right) + \sqrt{\frac{1}{4}\left(C_{33} - C_{55}\right)^2 + C_{35}} \tag{A.166}$$

For $\vec{n} = \left[\frac{1}{\sqrt{2}}\ \frac{1}{\sqrt{2}}\ 0\right]$, the Christoffel matrix (according to Appendix B) is:

$$\begin{bmatrix} \frac{1}{2}\left(C_{11} + C_{66}\right) & \frac{1}{2}\left(C_{12} + C_{66}\right) & \frac{1}{2}C_{46} \\ \frac{1}{2}\left(C_{12} + C_{66}\right) & \frac{1}{2}\left(C_{22} + C_{66}\right) & \frac{1}{2}\left(C_{25} + C_{56}\right) \\ \frac{1}{2}C_{46} & \frac{1}{2}\left(C_{25} + C_{56}\right) & \frac{1}{2}\left(C_{44} + C_{55}\right) \end{bmatrix} \begin{bmatrix} A_1 \\ A_2 \\ A_3 \end{bmatrix} = \rho\nu^2 \begin{bmatrix} A_1 \\ A_2 \\ A_3 \end{bmatrix} . \tag{A.167}$$

However, unlike the previous directions of propagation, there are no short solutions to the eigenvalue problem to give us useful equations for the determination of the phase velocities.

For $\vec{n} = \left[\frac{1}{\sqrt{2}}\ 0\ \frac{1}{\sqrt{2}}\right]$, the Christoffel matrix (according to Appendix B) is:

$$\begin{bmatrix} \frac{1}{2}(C_{11} + 2C_{15} & 0 & \frac{1}{2}(C_{13} + C_{15} \\ +C_{55}) & & +C_{35} + C_{55}) \\ 0 & \frac{1}{2}(C_{44} + 2C_{46} & 0 \\ & +C_{66}) & \\ \frac{1}{2}(C_{13} + C_{15} & 0 & \frac{1}{2}(C_{33} + C_{55}) \\ +C_{35} + C_{55}) & & +2C_{35} \end{bmatrix} \begin{bmatrix} A_1 \\ \\ A_2 \\ \\ A_3 \end{bmatrix} = \rho\nu^2 \begin{bmatrix} A_1 \\ \\ A_2 \\ \\ A_3 \end{bmatrix} . \tag{A.168}$$

This implies:

$$\rho \nu^2_{S[0\ 1\ 0]} = C_{46} + \frac{1}{2}\left(C_{44} + C_{66}\right) \ . \tag{A.169}$$

However, the other 2 polarizations cannot be easily determined. The previous equation implies that C_{46} can be determined once C_{44} and C_{66} are determined. For $\vec{n} = \left[0\ \frac{1}{\sqrt{2}}\ \frac{1}{\sqrt{2}}\right]$, the Christoffel matrix (according to Appendix B) is:

$$\begin{bmatrix} \frac{1}{2}\left(C_{55}+C_{66}\right) & \frac{1}{2}\left(C_{25}+C_{46}\right) & \frac{1}{2}\left(C_{35}+C_{46}\right) \\ \frac{1}{2}\left(C_{25}+C_{46}\right) & \frac{1}{2}\left(C_{22}+C_{44}\right) & \frac{1}{2}\left(C_{23}+C_{44}\right) \\ \frac{1}{2}\left(C_{25}+C_{46}\right) & \frac{1}{2}\left(C_{23}+C_{44}\right) & \frac{1}{2}\left(C_{33}+C_{44}\right) \end{bmatrix} \begin{bmatrix} A_1 \\ A_2 \\ A_3 \end{bmatrix} = \rho \nu^2 \begin{bmatrix} A_1 \\ A_2 \\ A_3 \end{bmatrix} . \tag{A.170}$$

However, unlike the previous directions of propagation, there are no short solutions to the eigenvalue problem to give us useful equations for the determination of the phase velocities.

References

Chou, P. C., and Pagano, N. J., 1967, Elasticity: Tensor, Dyadic, and Engineering Approaches, Dover Publication, Inc., New York, New York.

Lay, T., and Wallace, T. C., 1995, Modern Global Seismology, Academic Press., San Diego, California.

Musgrave, M. J. P., 1970, Crystal acoustics, Holden-Day, San Francisco, California.

Appendix B

Christoffel Symbols

B.1 Theory

$$\Gamma_{il} = c_{ijkl} n_j n_k \tag{B.1}$$

is used where Γ_{il} are the Christoffel equations, c_{ijkl} are the elastic stiffnesses, and n_j and n_k represent various components of the direction vector $\overrightarrow{n}$ (Musgrave, 1970).

So when expanded for Γ_{11}

$$\begin{aligned} \Gamma_{11} &= c_{1111} n_1 n_1 + c_{1121} n_1 n_2 + c_{1131} n_1 n_3 \\ &+ c_{1211} n_2 n_1 + c_{1221} n_2 n_2 + c_{1231} n_2 n_3 \\ &+ c_{1311} n_3 n_1 + c_{1321} n_3 n_2 + c_{1331} n_3 n_3 \end{aligned} \tag{B.2}$$

or in Voigt notation

$$\begin{aligned} \Gamma_{11} &= C_{11} n_1^2 + C_{66} n_2^2 + C_{55} n_3^2 \\ &+ 2C_{16} n_1 n_2 + 2C_{15} n_1 n_3 + 2C_{56} n_2 n_3 \end{aligned} \tag{B.3}$$

Similarly Γ_{12}, Γ_{13}, Γ_{22}, Γ_{23}, and Γ_{33} are listed for completeness.

$$\Gamma_{12} = c_{1112} n_1 n_1 + c_{1122} n_1 n_2 + c_{1132} n_1 n_3 \tag{B.4}$$

$$\begin{aligned} &+ c_{1212} n_2 n_1 + c_{1222} n_2 n_2 + c_{1232} n_2 n_3 \\ &+ c_{1312} n_3 n_1 + c_{1322} n_3 n_2 + c_{1332} n_3 n_3 \end{aligned}$$

$$\begin{aligned} \Gamma_{12} &= C_{16} n_1^2 + C_{26} n_2^2 + C_{45} n_3^2 + \left(C_{12} + C_{66}\right) n_1 n_2 \\ &+ \left(C_{14} + C_{56}\right) n_1 n_3 + \left(C_{25} + C_{46}\right) n_2 n_3 \end{aligned} \tag{B.5}$$

$$\begin{aligned} \Gamma_{13} &= c_{1113} n_1 n_1 + c_{1123} n_1 n_2 + c_{1133} n_1 n_3 \\ &+ c_{1213} n_2 n_1 + c_{1223} n_2 n_2 + c_{1233} n_2 n_3 \\ &+ c_{1313} n_3 n_1 + c_{1323} n_3 n_2 + c_{1333} n_3 n_3 \end{aligned} \tag{B.6}$$

$$\begin{aligned} \Gamma_{13} &= C_{15} n_1^2 + C_{46} n_2^2 + C_{35} n_3^2 + \left(C_{14} + C_{56}\right) n_1 n_2 \\ &+ \left(C_{13} + C_{55}\right) n_1 n_3 + \left(C_{36} + C_{45}\right) n_2 n_3 \end{aligned} \tag{B.7}$$

$$\begin{aligned} \Gamma_{22} &= c_{2112} n_1 n_1 + c_{2122} n_1 n_2 + c_{2132} n_1 n_3 \\ &+ c_{2212} n_2 n_1 + c_{2222} n_2 n_2 + c_{2232} n_2 n_3 \\ &+ c_{2312} n_3 n_1 + c_{2322} n_3 n_2 + c_{2332} n_3 n_3 \end{aligned} \tag{B.8}$$

$$\begin{aligned} \Gamma_{22} &= C_{66} n_1^2 + C_{22} n_2^2 + C_{44} n_3^2 \\ &+ 2C_{26} n_1 n_2 + 2C_{46} n_1 n_3 + 2C_{24} n_2 n_3 \end{aligned} \tag{B.9}$$

$$\begin{aligned} \Gamma_{23} &= c_{2113} n_1 n_1 + c_{2123} n_1 n_2 + c_{2133} n_1 n_3 \\ &+ c_{2213} n_2 n_1 + c_{2223} n_2 n_2 + c_{2233} n_2 n_3 \\ &+ c_{2313} n_3 n_1 + c_{2323} n_3 n_2 + c_{2333} n_3 n_3 \end{aligned} \tag{B.10}$$

$$\begin{aligned}\Gamma_{23} &= C_{56}n_1^2 + C_{24}n_2^2 + C_{34}n_3^2 + (C_{25} + C_{46})\, n_1 n_2 \\ &+ (C_{36} + C_{45})\, n_1 n_3 + (C_{23} + C_{44})\, n_2 n_3\end{aligned} \tag{B.11}$$

$$\begin{aligned}\Gamma_{33} &= c_{3113}n_1 n_1 + c_{3123}n_1 n_2 + c_{3133}n_1 n_3 \\ &+ c_{3213}n_2 n_1 + c_{3223}n_2 n_2 + c_{3233}n_2 n_3 \\ &+ c_{3313}n_3 n_1 + c_{3323}n_3 n_2 + c_{3333}n_3 n_3\end{aligned} \tag{B.12}$$

$$\begin{aligned}\Gamma_{33} &= C_{55}n_1^2 + C_{44}n_2^2 + C_{33}n_3^2 \\ &+ 2C_{45}n_1 n_2 + 2C_{35}n_1 n_3 + 2C_{34}n_2 n_3\end{aligned} \tag{B.13}$$

B.2 Expanded Christoffel terms for a few example directions

For $\vec{n} = [1\ 0\ 0]$

$\Gamma_{11} = c_{1111}$

$\Gamma_{12} = c_{1112}$

$\Gamma_{13} = c_{1113}$

$\Gamma_{22} = c_{2112}$

$\Gamma_{23} = c_{2113}$

$\Gamma_{33} = c_{3113}$

For $\vec{n} = [0\ 1\ 0]$

$\Gamma_{11} = c_{1221}$

$\Gamma_{12} = c_{1222}$

$\Gamma_{13} = c_{1223}$

$\Gamma_{22} = c_{2222}$

$\Gamma_{23} = c_{2223}$

$\Gamma_{33} = c_{3223}$

For $\vec{n} = [0\ 0\ 1]$

$\Gamma_{11} = c_{1331}$

$\Gamma_{12} = c_{1332}$

$\Gamma_{13} = c_{1333}$

$\Gamma_{22} = c_{2332}$

$\Gamma_{23} = c_{2333}$

$\Gamma_{33} = c_{3333}$

For $\vec{n} = \left[\frac{1}{\sqrt{2}}\ \frac{1}{\sqrt{2}}\ 0\right]$

$\Gamma_{11} = \frac{1}{2}c_{1111} + \frac{1}{2}c_{1121} + \frac{1}{2}c_{1211} + \frac{1}{2}c_{1221}$

$\Gamma_{12} = \frac{1}{2}c_{1112} + \frac{1}{2}c_{1122} + \frac{1}{2}c_{1212} + \frac{1}{2}c_{1222}$

$\Gamma_{13} = \frac{1}{2}c_{1113} + \frac{1}{2}c_{1123} + \frac{1}{2}c_{1213} + \frac{1}{2}c_{1223}$

$\Gamma_{22} = \frac{1}{2}c_{2112} + \frac{1}{2}c_{2122} + \frac{1}{2}c_{2212} + \frac{1}{2}c_{2222}$

$\Gamma_{23} = \frac{1}{2}c_{2113} + \frac{1}{2}c_{2123} + \frac{1}{2}c_{2213} + \frac{1}{2}c_{2223}$

$\Gamma_{33} = \frac{1}{2}c_{3113} + \frac{1}{2}c_{3123} + \frac{1}{2}c_{3213} + \frac{1}{2}c_{3223}$

For $\vec{n} = \left[\frac{1}{\sqrt{2}}\ \frac{-1}{\sqrt{2}}\ 0\right]$

$\Gamma_{11} = \frac{1}{2}c_{1111} - \frac{1}{2}c_{1121} - \frac{1}{2}c_{1211} + \frac{1}{2}c_{1221}$

$$\begin{aligned}
\Gamma_{12} &= \tfrac{1}{2}c_{1112} - \tfrac{1}{2}c_{1122} - \tfrac{1}{2}c_{1212} + \tfrac{1}{2}c_{1222}\\
\Gamma_{13} &= \tfrac{1}{2}c_{1113} - \tfrac{1}{2}c_{1123} - \tfrac{1}{2}c_{1213} + \tfrac{1}{2}c_{1223}\\
\Gamma_{22} &= \tfrac{1}{2}c_{2112} - \tfrac{1}{2}c_{2122} - \tfrac{1}{2}c_{2212} + \tfrac{1}{2}c_{2222}\\
\Gamma_{23} &= \tfrac{1}{2}c_{2113} - \tfrac{1}{2}c_{2123} - \tfrac{1}{2}c_{2213} + \tfrac{1}{2}c_{2223}\\
\Gamma_{33} &= \tfrac{1}{2}c_{3113} - \tfrac{1}{2}c_{3123} - \tfrac{1}{2}c_{3213} + \tfrac{1}{2}c_{3223}
\end{aligned}$$

For $\vec{n} = \left[0\ \frac{1}{\sqrt{2}}\ \frac{1}{\sqrt{2}}\right]$

$$\begin{aligned}
\Gamma_{11} &= \tfrac{1}{2}c_{1221} + \tfrac{1}{2}c_{1231} + \tfrac{1}{2}c_{1321} + \tfrac{1}{2}c_{1331}\\
\Gamma_{12} &= \tfrac{1}{2}c_{1222} + \tfrac{1}{2}c_{1232} + \tfrac{1}{2}c_{1322} + \tfrac{1}{2}c_{1332}\\
\Gamma_{13} &= \tfrac{1}{2}c_{1223} + \tfrac{1}{2}c_{1233} + \tfrac{1}{2}c_{1323} + \tfrac{1}{2}c_{1333}\\
\Gamma_{22} &= \tfrac{1}{2}c_{2222} + \tfrac{1}{2}c_{2232} + \tfrac{1}{2}c_{2322} + \tfrac{1}{2}c_{2332}\\
\Gamma_{23} &= \tfrac{1}{2}c_{2223} + \tfrac{1}{2}c_{2233} + \tfrac{1}{2}c_{2323} + \tfrac{1}{2}c_{2333}\\
\Gamma_{33} &= \tfrac{1}{2}c_{3223} + \tfrac{1}{2}c_{3233} + \tfrac{1}{2}c_{3323} + \tfrac{1}{2}c_{3333}
\end{aligned}$$

For $\vec{n} = \left[0\ \frac{1}{\sqrt{2}}\ \frac{-1}{\sqrt{2}}\right]$

$$\begin{aligned}
\Gamma_{11} &= \tfrac{1}{2}c_{1221} - \tfrac{1}{2}c_{1231} - \tfrac{1}{2}c_{1321} + \tfrac{1}{2}c_{1331}\\
\Gamma_{12} &= \tfrac{1}{2}c_{1222} - \tfrac{1}{2}c_{1232} - \tfrac{1}{2}c_{1322} + \tfrac{1}{2}c_{1332}\\
\Gamma_{13} &= \tfrac{1}{2}c_{1223} - \tfrac{1}{2}c_{1233} - \tfrac{1}{2}c_{1323} + \tfrac{1}{2}c_{1333}\\
\Gamma_{22} &= \tfrac{1}{2}c_{2222} - \tfrac{1}{2}c_{2232} - \tfrac{1}{2}c_{2322} + \tfrac{1}{2}c_{2332}\\
\Gamma_{23} &= \tfrac{1}{2}c_{2223} - \tfrac{1}{2}c_{2233} - \tfrac{1}{2}c_{2323} + \tfrac{1}{2}c_{2333}\\
\Gamma_{33} &= \tfrac{1}{2}c_{3223} - \tfrac{1}{2}c_{3233} - \tfrac{1}{2}c_{3323} + \tfrac{1}{2}c_{3333}
\end{aligned}$$

For $\vec{n} = \left[\frac{1}{\sqrt{2}}\ 0\ \frac{1}{\sqrt{2}}\right]$

$$\Gamma_{11} = \tfrac{1}{2}c_{1111} + \tfrac{1}{2}c_{1131} + \tfrac{1}{2}c_{1311} + \tfrac{1}{2}c_{1331}$$

$$\Gamma_{12} = \tfrac{1}{2}c_{1112} + \tfrac{1}{2}c_{1132} + \tfrac{1}{2}c_{1312} + \tfrac{1}{2}c_{1332}$$
$$\Gamma_{13} = \tfrac{1}{2}c_{1113} + \tfrac{1}{2}c_{1133} + \tfrac{1}{2}c_{1313} + \tfrac{1}{2}c_{1333}$$
$$\Gamma_{22} = \tfrac{1}{2}c_{2112} + \tfrac{1}{2}c_{2132} + \tfrac{1}{2}c_{2312} + \tfrac{1}{2}c_{2332}$$
$$\Gamma_{23} = \tfrac{1}{2}c_{2113} + \tfrac{1}{2}c_{2133} + \tfrac{1}{2}c_{2313} + \tfrac{1}{2}c_{2333}$$
$$\Gamma_{33} = \tfrac{1}{2}c_{3113} + \tfrac{1}{2}c_{3133} + \tfrac{1}{2}c_{3313} + \tfrac{1}{2}c_{3333}$$

For $\overrightarrow{n} = \left[\frac{1}{\sqrt{2}}\ 0\ \frac{-1}{\sqrt{2}}\right]$

$$\Gamma_{11} = \tfrac{1}{2}c_{1111} - \tfrac{1}{2}c_{1131} - \tfrac{1}{2}c_{1311} + \tfrac{1}{2}c_{1331}$$
$$\Gamma_{12} = \tfrac{1}{2}c_{1112} - \tfrac{1}{2}c_{1132} - \tfrac{1}{2}c_{1312} + \tfrac{1}{2}c_{1332}$$
$$\Gamma_{13} = \tfrac{1}{2}c_{1113} - \tfrac{1}{2}c_{1133} - \tfrac{1}{2}c_{1313} + \tfrac{1}{2}c_{1333}$$
$$\Gamma_{22} = \tfrac{1}{2}c_{2112} - \tfrac{1}{2}c_{2132} - \tfrac{1}{2}c_{2312} + \tfrac{1}{2}c_{2332}$$
$$\Gamma_{23} = \tfrac{1}{2}c_{2113} - \tfrac{1}{2}c_{2133} - \tfrac{1}{2}c_{2313} + \tfrac{1}{2}c_{2333}$$
$$\Gamma_{33} = \tfrac{1}{2}c_{3113} - \tfrac{1}{2}c_{3133} - \tfrac{1}{2}c_{3313} + \tfrac{1}{2}c_{3333}$$

For $\overrightarrow{n} = \left[\frac{1}{\sqrt{3}}\ \frac{1}{\sqrt{3}}\ \frac{1}{\sqrt{2}}\right]$

$$\Gamma_{11} = \tfrac{1}{3}c_{1111} + \tfrac{2}{3}c_{1121} + \tfrac{2}{3}c_{1131} + \tfrac{1}{3}c_{1221} + \tfrac{2}{3}c_{1231} + \tfrac{1}{3}c_{1331}$$
$$\Gamma_{12} = \tfrac{1}{3}c_{1112} + \tfrac{2}{3}c_{1122} + \tfrac{2}{3}c_{1132} + \tfrac{1}{3}c_{1222} + \tfrac{2}{3}c_{1232} + \tfrac{1}{3}c_{1332}$$
$$\Gamma_{13} = \tfrac{1}{3}c_{1113} + \tfrac{2}{3}c_{1123} + \tfrac{2}{3}c_{1133} + \tfrac{1}{3}c_{1223} + \tfrac{2}{3}c_{1233} + \tfrac{1}{3}c_{1333}$$
$$\Gamma_{22} = \tfrac{1}{3}c_{2112} + \tfrac{2}{3}c_{2122} + \tfrac{2}{3}c_{2132} + \tfrac{1}{3}c_{2222} + \tfrac{2}{3}c_{2232} + \tfrac{1}{3}c_{2332}$$
$$\Gamma_{23} = \tfrac{1}{3}c_{2113} + \tfrac{2}{3}c_{2123} + \tfrac{2}{3}c_{2133} + \tfrac{1}{3}c_{2223} + \tfrac{2}{3}c_{2233} + \tfrac{1}{3}c_{2333}$$
$$\Gamma_{33} = \tfrac{1}{3}c_{3113} + \tfrac{2}{3}c_{3123} + \tfrac{2}{3}c_{3133} + \tfrac{1}{3}c_{3223} + \tfrac{2}{3}c_{3233} + \tfrac{1}{3}c_{3333}$$

For $\overrightarrow{n} = \left[\frac{-1}{\sqrt{3}}\ \frac{1}{\sqrt{3}}\ \frac{1}{\sqrt{2}}\right]$

$$\Gamma_{11} = \tfrac{1}{3}c_{1111} - \tfrac{2}{3}c_{1121} - \tfrac{2}{3}c_{1131} + \tfrac{1}{3}c_{1221} + \tfrac{2}{3}c_{1231} + \tfrac{1}{3}c_{1331}$$

$$\Gamma_{12} = \tfrac{1}{3}c_{1112} - \tfrac{2}{3}c_{1122} - \tfrac{2}{3}c_{1132} + \tfrac{1}{3}c_{1222} + \tfrac{2}{3}c_{1232} + \tfrac{1}{3}c_{1332}$$
$$\Gamma_{13} = \tfrac{1}{3}c_{1113} - \tfrac{2}{3}c_{1123} - \tfrac{2}{3}c_{1133} + \tfrac{1}{3}c_{1223} + \tfrac{2}{3}c_{1233} + \tfrac{1}{3}c_{1333}$$
$$\Gamma_{22} = \tfrac{1}{3}c_{2112} - \tfrac{2}{3}c_{2122} - \tfrac{2}{3}c_{2132} + \tfrac{1}{3}c_{2222} + \tfrac{2}{3}c_{2232} + \tfrac{1}{3}c_{2332}$$
$$\Gamma_{23} = \tfrac{1}{3}c_{2113} - \tfrac{2}{3}c_{2123} - \tfrac{2}{3}c_{2133} + \tfrac{1}{3}c_{2223} + \tfrac{2}{3}c_{2233} + \tfrac{1}{3}c_{2333}$$
$$\Gamma_{33} = \tfrac{1}{3}c_{3113} - \tfrac{2}{3}c_{3123} - \tfrac{2}{3}c_{3133} + \tfrac{1}{3}c_{3223} + \tfrac{2}{3}c_{3233} + \tfrac{1}{3}c_{3333}$$

For $\vec{n} = \left[\frac{1}{\sqrt{3}}\ \frac{-1}{\sqrt{3}}\ \frac{1}{\sqrt{2}}\right]$

$$\Gamma_{11} = \tfrac{1}{3}c_{1111} - \tfrac{2}{3}c_{1121} + \tfrac{2}{3}c_{1131} + \tfrac{1}{3}c_{1221} - \tfrac{2}{3}c_{1231} + \tfrac{1}{3}c_{1331}$$
$$\Gamma_{12} = \tfrac{1}{3}c_{1112} - \tfrac{2}{3}c_{1122} + \tfrac{2}{3}c_{1132} + \tfrac{1}{3}c_{1222} - \tfrac{2}{3}c_{1232} + \tfrac{1}{3}c_{1332}$$
$$\Gamma_{13} = \tfrac{1}{3}c_{1113} - \tfrac{2}{3}c_{1123} + \tfrac{2}{3}c_{1133} + \tfrac{1}{3}c_{1223} - \tfrac{2}{3}c_{1233} + \tfrac{1}{3}c_{1333}$$
$$\Gamma_{22} = \tfrac{1}{3}c_{2112} - \tfrac{2}{3}c_{2122} + \tfrac{2}{3}c_{2132} + \tfrac{1}{3}c_{2222} - \tfrac{2}{3}c_{2232} + \tfrac{1}{3}c_{2332}$$
$$\Gamma_{23} = \tfrac{1}{3}c_{2113} - \tfrac{2}{3}c_{2123} + \tfrac{2}{3}c_{2133} + \tfrac{1}{3}c_{2223} - \tfrac{2}{3}c_{2233} + \tfrac{1}{3}c_{2333}$$
$$\Gamma_{33} = \tfrac{1}{3}c_{3113} - \tfrac{2}{3}c_{3123} + \tfrac{2}{3}c_{3133} + \tfrac{1}{3}c_{3223} - \tfrac{2}{3}c_{3233} + \tfrac{1}{3}c_{3333}$$

For $\vec{n} = \left[\frac{1}{\sqrt{3}}\ \frac{1}{\sqrt{3}}\ \frac{-1}{\sqrt{2}}\right]$

$$\Gamma_{11} = \tfrac{1}{3}c_{1111} + \tfrac{2}{3}c_{1121} - \tfrac{2}{3}c_{1131} + \tfrac{1}{3}c_{1221} - \tfrac{2}{3}c_{1231} + \tfrac{1}{3}c_{1331}$$
$$\Gamma_{12} = \tfrac{1}{3}c_{1112} + \tfrac{2}{3}c_{1122} - \tfrac{2}{3}c_{1132} + \tfrac{1}{3}c_{1222} - \tfrac{2}{3}c_{1232} + \tfrac{1}{3}c_{1332}$$
$$\Gamma_{13} = \tfrac{1}{3}c_{1113} + \tfrac{2}{3}c_{1123} - \tfrac{2}{3}c_{1133} + \tfrac{1}{3}c_{1223} - \tfrac{2}{3}c_{1233} + \tfrac{1}{3}c_{1333}$$
$$\Gamma_{22} = \tfrac{1}{3}c_{2112} + \tfrac{2}{3}c_{2122} - \tfrac{2}{3}c_{2132} + \tfrac{1}{3}c_{2222} - \tfrac{2}{3}c_{2232} + \tfrac{1}{3}c_{2332}$$
$$\Gamma_{23} = \tfrac{1}{3}c_{2113} + \tfrac{2}{3}c_{2123} - \tfrac{2}{3}c_{2133} + \tfrac{1}{3}c_{2223} - \tfrac{2}{3}c_{2233} + \tfrac{1}{3}c_{2333}$$
$$\Gamma_{33} = \tfrac{1}{3}c_{3113} + \tfrac{2}{3}c_{3123} - \tfrac{2}{3}c_{3133} + \tfrac{1}{3}c_{3223} - \tfrac{2}{3}c_{3233} + \tfrac{1}{3}c_{3333}$$